



Danish Space Research Institute

**DSRI Report 2/2004**

ISSN 1602-527X



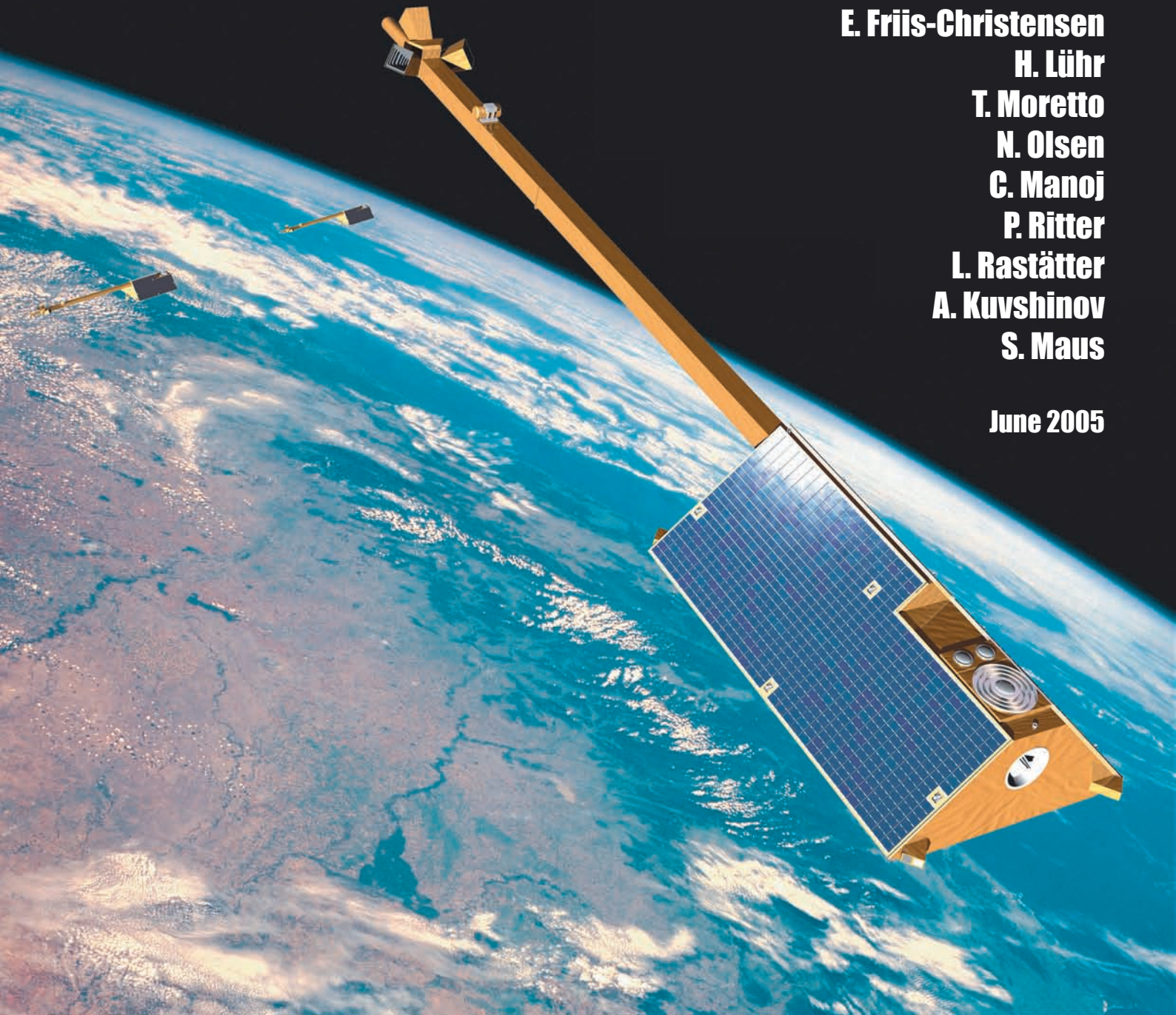
# Swarm

**The Impact of Combined  
Magnetic and Electric  
Field Analysis and of  
Ocean Circulation Effects on  
Swarm Mission Performance**

**Final Report**

**S. Vennerstrom  
E. Friis-Christensen  
H. Lühr  
T. Moretto  
N. Olsen  
C. Manoj  
P. Ritter  
L. Rastätter  
A. Kuvshinov  
S. Maus**

**June 2005**



This page is intentionally left blank

# **The Impact of Combined Magnetic and Electric Field Analysis and of Ocean Circulation Effects on *Swarm* Mission Performance**

by

Vennerstrom S., E. Friis-Christensen, H. Lühr,  
T. Moretto, N. Olsen, C. Manoj, P. Ritter, L. Rastätter,  
A. Kuvshinov, S. Maus

## **Final Report**

---

**Doc. No. (Issue):** SWSC/DSRI/MIS/TN/0001(2)

**Date:** 2005-06-24

**Prepared by:** Susanne Vennerstrøm

**Authorized by:** Eigil Friis-Christensen

**Classification:** Public

This page is intentionally left blank

## Classification Codes

<b>Confidential</b>	The document shall be circulated only to those positively identified on the distribution list.
<b>Restricted</b>	The document may be circulated to anybody working on the project and, if deemed necessary, within the involved institutions or companies, but not outside.
<b>Open</b>	There are no restrictions in circulation, but the document will only be disseminated upon request to a named person.
<b>Public</b>	There are no restrictions in circulation, and the document will be made generally available on the World Wide Web.

## PAGE ISSUE RECORD

Document	Page	Issue	Filename and Format
SWSC/DSRI/MIS/TN/0001	131	1	Science Study_Final_Report_Draft.pdf
SWSC/DSRI/MIS/TN/0001	138	2	Science Study_Final_Report.pdf

## DOCUMENT CHANGE LOG

Issue	Change References	Issue Date	Pages Affected	Remarks	Init.
1		2004-06-15	All	Initial Issue	SV
2		2005-06-24	All	Final Issue	SV

### © 2005, Danish National Space Center

This document contains information proprietary to Danish National Space Center. The information, whether in the form of text, schematics, tables, drawings or illustrations, must not be duplicated or used for other purposes than evaluation, or disclosed outside the recipient institution without the prior, written permission of Danish National Space Center. The restriction does not limit the recipient's right to use information contained in the document if such information is received from another source without restriction, provided that such source is not in breach of an obligation of confidentiality towards Danish National Space Center.

The Danish National Space Center (DNSC) is a new research center under the Ministry of Science, Technology and Innovation. The center is the result of the Danish Space Research center merging with a part of The National Survey and Cadastre (KMS). The research activities include astrophysics, solar system physics, geodesy and space technology.

This page is intentionally left blank

## ESA STUDY CONTRACT REPORT

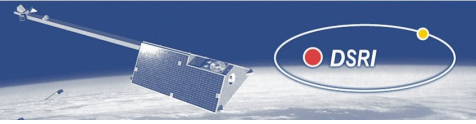
No ESA Study Contract Report will be accepted unless this sheet is inserted at the beginning of each volume of the Report.

<b>ESA CONTRACT No</b> <b>18045/04/NL/CB</b>	<b>SUBJECT</b> <b>The Impact of Combined Magnetic and Electric Field Analysis and of Ocean Circulation Effects on <i>Swarm</i> Mission Performance</b>		<b>CONTRACTOR</b> <b>Danish Space Research Institute</b>
<b>* ESA CR( )No</b> <b>18045</b>	<b>* STAR CODE</b>	<b>No of volumes</b> <b>1</b> <b>This is Volume No</b> <b>1</b>	<b>CONTRACTOR'S REFERENCE</b> <b>SWSC/DSRI/MIS/TN/0001</b>
<b>ABSTRACT:</b>  This report describes the outcome of the <i>Swarm</i> Science Study on <i>The Impact of Combined Magnetic and Electric Field Analysis and of Ocean Circulation Effects on Swarm Mission Performance</i> (ESTEC Contract No. 18045/04/NL/CB).			
The work described in this report was done under ESA Contract. Responsibility for the contents resides in the author or organisation that prepared it.			
Names of authors: Vennerstrøm S., E. Friis-Christensen, H. Lühr, T. Moretto, N. Olsen, C. Manoj, P. Ritter, L. Rastätter, A. Kuvshinov, S. Maus			
<b>** NAME OF ESA STUDY MANAGER</b> <b>Roger Haagmans</b> <b>DIV:</b> Science and Applications Department <b>DIRECTORATE:</b> Directorate of Earth Observation Programmes	<b>** ESA BUDGET HEADING</b>		

This page is intentionally left blank

# Contents

<b>1</b>	<b>Introduction</b>	<b>10</b>
<b>2</b>	<b>External Electric and Magnetic Field Contributions</b>	<b>11</b>
2.1	Introduction . . . . .	12
2.2	Magnetospheric and Ionospheric Currents from Global MHD Simulations . . . . .	13
2.2.1	The UCLA GGCM Model at the CCMC . . . . .	13
2.2.2	Tailored Output for the Swarm Study . . . . .	15
2.2.3	Products . . . . .	20
2.3	<i>Swarm</i> Study Simulations . . . . .	21
2.3.1	Slowly Changing IMF $B_Z$ . . . . .	22
2.3.2	Slowly Changing IMF $B_Z$ With Dipole Tilt . . . . .	25
2.3.3	Real Event . . . . .	25
2.3.4	Products . . . . .	30
2.4	Computation of magnetic fields within source regions of ionospheric and magnetospheric currents . . . . .	33
2.4.1	Poloidal–Toroidal Decomposition Method . . . . .	33
2.4.2	Implementation of the Poloidal – Toroidal Approach . . . . .	36
2.4.3	Biot-Savart Integration . . . . .	36
2.4.4	Tests . . . . .	37
2.4.5	Products . . . . .	39
2.5	Results of the Forward Modelling . . . . .	41
2.5.1	The Main Contributions - Ionospheric and Field-Aligned Currents . . . . .	41
2.5.2	The Contributions From the Distant Magnetosphere . . . . .	44
2.6	Comparison with observations . . . . .	46
2.7	Summary and conclusions of the forward modeling . . . . .	54
2.8	Retrieval of Ionospheric Currents. Physical interpretation and assumptions . . . . .	55
2.9	Determination of the field-aligned currents . . . . .	57
2.10	Retrieval of horizontal ionospheric currents . . . . .	71
2.11	New Auroral Region Index for Improved Data Selection . . . . .	78
2.12	Assessment of current estimates and conclusions . . . . .	89
2.13	Suggestions for further studies . . . . .	94
<b>3</b>	<b>Magnetic Field Contributions Produced by Ocean Flow</b>	<b>97</b>
3.1	Introduction . . . . .	98
3.2	Ocean circulation model . . . . .	98
3.2.1	The ECCO 1 (1992 – 2002) model run . . . . .	98
3.2.2	Input data to the model . . . . .	99
3.2.3	The outputs from the model . . . . .	99



3.2.4	Modifications of the output for <i>Swarm</i> study . . . . .	99
3.2.5	General description of the data . . . . .	100
3.3	Numerical approach to calculate electromagnetic field due to ocean flow . . . . .	100
3.3.1	Governing equations . . . . .	100
3.3.2	Green's tensors of the reference radially-symmetric section . . . . .	103
3.3.3	Validation of numerical solution . . . . .	106
3.3.4	3-D conductivity model . . . . .	108
3.3.5	Computational aspects . . . . .	109
3.4	Results of simulation . . . . .	109
3.4.1	Seasonal variation . . . . .	112
3.4.2	El Niño / Interannual variability . . . . .	112
3.5	Conclusions and scope for future work . . . . .	117
3.6	Introduction . . . . .	118
3.7	Simulations with high resolution ocean circulation data . . . . .	118
3.7.1	OCCAM Model . . . . .	118
3.7.2	OCCAM velocity data . . . . .	119
3.7.3	Forward Computation of ocean magnetic fields . . . . .	119
3.7.4	Results of simulation . . . . .	120
3.7.5	Comparison of results using ECCO and OCCAM models . . . . .	121
3.8	Sensitivity analysis . . . . .	124
3.9	Recovery of the ocean circulation from satellite magnetic signals . . . . .	129
3.10	Conclusions . . . . .	131
3.11	Suggestions for further studies . . . . .	132
<b>A</b>	<b>Coordinate systems</b>	<b>133</b>
A.1	Geocentric Solar Magnetic (GSM) Frame . . . . .	133
A.2	Solar Magnetic (SM) Frame . . . . .	133
A.3	IERS Conventional Terrestrial Reference Frame (ITRF) . . . . .	133
A.4	Velocity Zenith (VZ) Frame . . . . .	133
A.5	Mean Field Aligned (MFA) Frame . . . . .	134
	Bibliography	

# Chapter 1

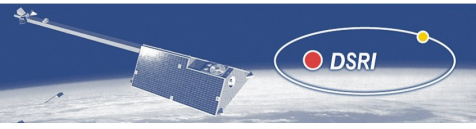
## Introduction

This report describes the outcome of the Study on the Impact of Combined Magnetic and Electric Field Analysis and of Ocean Circulation Effects on *Swarm* Mission Performance (ESTEC Contract No. 18045/04/NL/CB), which concerns the modeling of external and oceanographic contributions to *swarm* observations.

Each of the two topics was divided into two tasks: Forward modeling and inversion. The study was performed by GeoForschungsZentrum Potsdam (GFZ) and Danish Space Research Institute (DSRI) In collaboration with The Community Coordinated Modeling Center (CCMC) at Goddard Space Flight Center. For the combined electric and magnetic field analysis the forward modeling was performed by the DSRI in a collaboration with the CCMC (WP 1100 and WP 1200), while the inversion was performed by GFZ (WP 1300 and WP 1400). For the ocean circulation effects the forward modeling was performed mainly by DSRI (WP 2200) with input from GFZ (WP2100) while the inversion was performed by GFZ (WP 2300).

## Chapter 2

# External Electric and Magnetic Field Contributions



## 2.1 Introduction

The forward modeling effort of the combined magnetic and electric field analysis is described in sections 2.2 - 2.7. The contributions to the *Swarm* magnetic and electric field measurements from sources external to the Earth, in the ionosphere and magnetosphere, have been estimated. Specifically, we have developed a capability to produce realistic estimates of the external sources during a variety of conditions based on the results of global magnetospheric simulations and to calculate the contributions hereof to the magnetic and electric fields at *Swarm* altitudes.

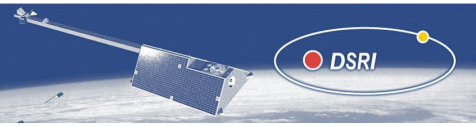
Interrelated results for the three-dimensional electric potential distribution at *Swarm* altitudes, the height-integrated horizontal ionospheric current distribution, the three-dimensional distribution of field-aligned currents flowing between the inner magnetosphere and the ionosphere, and the three-dimensional distribution of the current density in the near-Earth magnetosphere have all been obtained from global Magneto-Hydro-Dynamics (MHD) simulation runs. The models and algorithms involved are described in Section 2.2. Three different simulations representing quiet and moderately disturbed geomagnetic conditions have been performed and analyzed. This effort is described in Section 2.3. The work described in sections 2.2 and 2.3 was performed in a collaboration between T. Moretto, L. Rastätter and S. Vennerstrom. The resulting magnetic and electric fields have been calculated on a global grid at satellite altitudes using two different methods. The two magnetic field methods, the implementation and test results are described in Section 2.4. This work was performed by N. Olsen, S. Vennerstrom and T. Moretto. Resulting magnetic signatures at *Swarm* altitudes are presented and discussed in Section 2.5. In addition these results have been compared with Ørsted and CHAMP data. This effort, which was performed by S. Vennerstrom and T. Moretto, is described in section 2.6. Section 2.7 contains a summary of the forward modeling effort.

The following sections contain a description of the inversion effort. Here the efforts to estimate the ionospheric and field-aligned currents from *Swarm* synthetic magnetic and electric field data is described. Two tasks were identified:

- Investigate the relationship/correlation between the simulated electric and magnetic field data;
- Derive models of the magnetic signature due to external current systems to correct *Swarm* magnetic observations for field modeling. Test this facility.

These two tasks have been treated in one run without special differentiation. In Section 2.8 we discuss the physical properties of the various quantities in the synthetic data set. The determination of field-aligned currents is given special attention in Section 2.9. The *Swarm* constellation is particularly well suited to determine this important current component accurately. Field-aligned currents are of paramount importance for the high-latitude ionospheric physics, since they carry the energy and momentum from the magnetosphere into the upper atmosphere. Attempts to retrieve the horizontal currents in the ionospheric E-layer are presented in Section 2.10. Section 2.11 reflects our efforts to construct a new auroral region activity index. An assessment of the obtained results is given in Section 2.12. The work described in sections 2.8 - 2.12 was performed by P. Ritter and H. Lühr.

Finally in section 2.13 we outline some suggestions for further studies.



## 2.2 Magnetospheric and Ionospheric Currents from Global MHD Simulations

Realistic estimates of the currents in the ionosphere and magnetosphere responsible for the external magnetic field contributions to geomagnetic satellite measurements are provided for the current study by global MHD simulations run at the Community Coordinated Modeling Center (CCMC) at NASA Goddard Space Flight Center (<http://ccmc.gsfc.nasa.gov>). For the results presented here, we have used the UCLA Geospace General Circulation Model (GGCM).

### 2.2.1 The UCLA GGCM Model at the CCMC

The UCLA GGCM was originally developed as a MHD model of Earth's magnetosphere at UCLA in the early 1990's by J. Raeder [Raeder and Angelopoulos, 1998]. The model solves the resistive MHD equations in the magnetosphere and includes a magnetosphere-ionosphere coupling module that not only maps the field-aligned currents into the ionosphere and the potential back into the magnetosphere, but also computes electron precipitation parameters and the ionospheric Hall and Pedersen conductances using empirical relations in a self-consistent manner [Raeder et al., 1998].

#### Basic model concept

The magnetospheric part solves the MHD equations on a stretched Cartesian grid using second order explicit time integration with conservative and flux-limited spatial finite differences [Raeder, 2003]. A Yee grid is used to preserve the magnetic field divergence to round-off error. The code is parallelized using the message passing interface (MPI) and runs on a large variety of computers that support MPI. Currently the code is used on IBM-SP2, IBM-p690, SGI-Origin2000, HP/alpha based machines, and on a variety of Intel or AMD based Beowulf clusters. The numerical grid is adaptable and can have from a few times  $10^5$  to more than  $10^7$  cells. Correspondingly, the resolution in the MHD grid near the sub-solar magnetopause can be as small as 500 km or as large as  $0.5 R_E$ . The simulation results used for this study are from the implementation of the code run at the CCMC on their Beowulf cluster. The code has been run on a grid  $160 \times 60 \times 60$  in size, spanning from  $-255 R_E$  to  $33 R_E$  in the geocentric solar ecliptic (GSE) X direction and from  $-48 R_E$  to  $48 R_E$  in the GSE Y and Z directions. The GSE system has its X-axis pointing from the Earth towards the Sun, and its Y-axis in the ecliptic plane towards dusk. The grid has finest resolution of  $0.4 R_E$  close to the inner magnetospheric boundary.

#### Principal limitations and caveats

The model does not include the energetic particle drift and ring current physics. Likewise, there is no plasmasphere. This should not affect the dynamics of the magnetosphere much, though wave propagation through the inner magnetosphere is affected. Also, the model uses a "Boris correction" to keep time steps manageable. As a consequence wave propagation in the inner magnetosphere is artificially slowed. In the context of the present study objectives the most serious result of these limitations is a limited modeling of the high-latitude region 2 currents. The region 2 currents, on the other hand, are believed to be rather weak during quiet conditions, which is the condition of primary interest in the present context.

## The ionospheric solver

Field-aligned currents are calculated close to the inner boundary of the magnetospheric part of the simulation (at  $4 R_E$ ) and are used as input to solve the ionospheric potential equation. The field-aligned currents are mapped from points in the magnetosphere  $(r_M, \vartheta_M, \lambda)$  into points in the ionosphere  $(r_I, \vartheta_I, \lambda)$  along dipole field lines:

$$j_{par}(r_I, \vartheta_I, \lambda) = j_{par}(r_M, \vartheta_M, \lambda) \left( \frac{r_M}{r_I} \right)^3 \sqrt{\frac{4 - 3 \sin^2 \vartheta_I}{4 - 3 \sin^2 \vartheta_I (r_M/r_I)}} \quad (2.1)$$

with

$$\sin \vartheta_I = \sin \vartheta_M \sqrt{\frac{r_I}{r_M}}$$

The polar ionosphere is treated as a two-dimensional spherical shell, thus the ionospheric potential equation reads:

$$\nabla \cdot \underline{\underline{\Sigma}} \cdot \nabla \Phi = -j_{par} \sin I \quad (2.2)$$

with the boundary condition for the electric potential:  $\Phi = 0$  at the magnetic equator.  $\underline{\underline{\Sigma}}$  is the ionospheric conductance tensor, given by:

$$\underline{\underline{\Sigma}} = \begin{pmatrix} \Sigma_{\vartheta\vartheta} & \Sigma_{\vartheta\lambda} \\ \Sigma_{\vartheta\lambda} & -\Sigma_{\lambda\lambda} \end{pmatrix}; \Sigma_{\vartheta\vartheta} = \frac{\Sigma_P}{\sin^2 I}; \Sigma_{\vartheta\lambda} = \frac{\Sigma_H}{\sin I}; \Sigma_{\lambda\lambda} = \Sigma_P$$

where  $\Sigma_H$  is the Hall conductance,  $\Sigma_P$  is the Pedersen conductance,  $(r, \vartheta, \lambda)$  are spherical coordinates centered on the magnetic dipole axis and  $I$  is the magnetic field inclination angle. Correspondingly, the horizontal ionospheric current is given by:

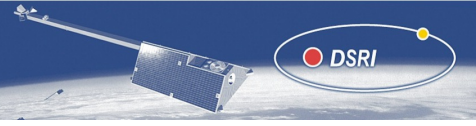
$$j_{\perp} = \begin{pmatrix} j_{\vartheta} \\ j_{\lambda} \end{pmatrix} = \underline{\underline{\Sigma}} \cdot (-\nabla \Phi) = \underline{\underline{\Sigma}} \cdot E_{horiz} = \underline{\underline{\Sigma}} \cdot \begin{pmatrix} E_{\vartheta} \\ E_{\lambda} \end{pmatrix} \quad (2.3)$$

where  $E$  is the ionospheric electric field.

The ionospheric Hall and Pedersen conductances play a large role in determining the ionospheric electrodynamics of the model. In the implementation of the model used for this study, they are computed from empirical formulas. The conductances are proportional to the ionospheric electron energy density (mostly dominated by the E-region), which is mainly determined by solar EUV irradiance and precipitation of magnetospheric electrons. The contribution to the conductance from the former is reliably parameterized by the solar radio flux parameter,  $F_{10.7}$ , together with the solar zenith angle [Moen and Brekke, 1993]. The contributions to the conductance from magnetospheric electron precipitation are parameterized by the energy flux and mean energy of the precipitating electrons [Robinson et al., 1987]. For the diffuse precipitation (from pitch angle scattering of hot magnetospheric electrons) these are parameterized, in turn, by the magnetospheric electron temperature and density, which are approximated by the density and temperature values from the magnetospheric part of the simulation. Additional discrete electron precipitation (auroral electrons accelerated by field-aligned potential drops) is parameterized by the field-aligned current density through the Knight relation [Knight, 1972].

## Model Input Parameters

Inputs to UCLA-GGCM are solar wind plasma and magnetic field conditions in GSE coordinates at the upstream simulation box boundary at  $33 R_E$ . For the simulation of real events, the solar wind observations must be propagated from a solar wind monitor satellite to this input position.



The Earth magnetic field is approximated by a dipole with fixed orientation during the entire simulation run. The orientation angle can be specified independently from the time interval simulated.

## Model Outputs

Standard outputs from the model simulation include the magnetospheric plasma parameters (density  $N$ , plasma pressure  $P$ , velocity  $V_x, V_y, V_z$ , magnetic field  $B_x, B_y, B_z$ , current densities,  $J_x, J_y, J_z$ ), and ionospheric parameters (electric potential, field-aligned currents, Hall and Pedersen conductances  $\Sigma_H, \Sigma_P$ ), electron precipitation mean energy and energy flux.

### 2.2.2 Tailored Output for the Swarm Study

For the Swarm external fields simulation study the standard output of ionospheric and magnetospheric parameters from the simulations has been supplemented by costume-designed outputs produced as part of this study.

#### Current distributions

The three-dimensional distribution of the field-aligned currents in the “gap” between the inner boundary of the magnetospheric part of the simulation (at  $4 R_E$ ) and the ionosphere (at 90 km altitude) is calculated by mapping of the field-aligned current density as described by eq. (2.1). This is done on a spherical grid that is equi-angular and has a distribution in the radial component given by:

$$r_n = r_0 + \frac{r_1 - r_0}{\exp(1) - 1} \left[ \exp\left(\frac{n^2}{(n_r - 1)^2}\right) - 1 \right] \quad (2.4)$$

where  $r_0$  is the lower radius ( $1.014 R_E$ ),  $r_1$  is the upper radius ( $4 R_E$ ), and  $n_r$  is the number of grid points in the radial direction. This routine has been tested by verifying that the resulting current vectors are aligned along the dipole field and satisfy  $\nabla \bullet \mathbf{j} = \mathbf{0}$  within numerical accuracy (except at the boundaries). The former feature is illustrated for two different conditions of magnetospheric activity in Figure 2.1 (more quiet) and Figure 2.2 (more active), respectively. The horizontal ionospheric (sheath) current distribution (on the corresponding grid in  $\vartheta$  and  $\lambda$ ) is calculated from the ionospheric electric potential and conductances. This routine has been tested by verifying that the resulting ionospheric current distributions satisfy  $\nabla_{\perp} \bullet \mathbf{j}_{\perp} = j_r$  where  $j_r$  is the radial component of the field-aligned current density flowing into and out of the ionosphere (cf. (2.3) above). This is illustrated in Figure 2.3 and Figure 2.4 for the same two sets of results used in Figures 2.1 and 2.2. Finally, the magnetospheric current distribution is obtained on the continuation of the spherical grid with equidistant spacing of  $0.5 R_E$  in the radial component from  $4.5 R_E$  out to  $20 R_E$  (32 grid points). All together, these contributions provide the global three-dimensional (3D) current distribution that is needed as input to the forward modeling modules for the magnetic field measurements. The size of the spherical grid was determined based on considerations of the resolution of the simulation results as well as tests of its effect on performance of the forward modeling modules. The grid size of 110 points in the radial direction up to  $4 R_E$  and (129,128) for  $(\vartheta, \lambda)$  has been used. A convenient binary data format has been defined for exchange and storage of the resulting data. One file, of roughly 29 Mbyte, is produced for each time-step of the simulation output.

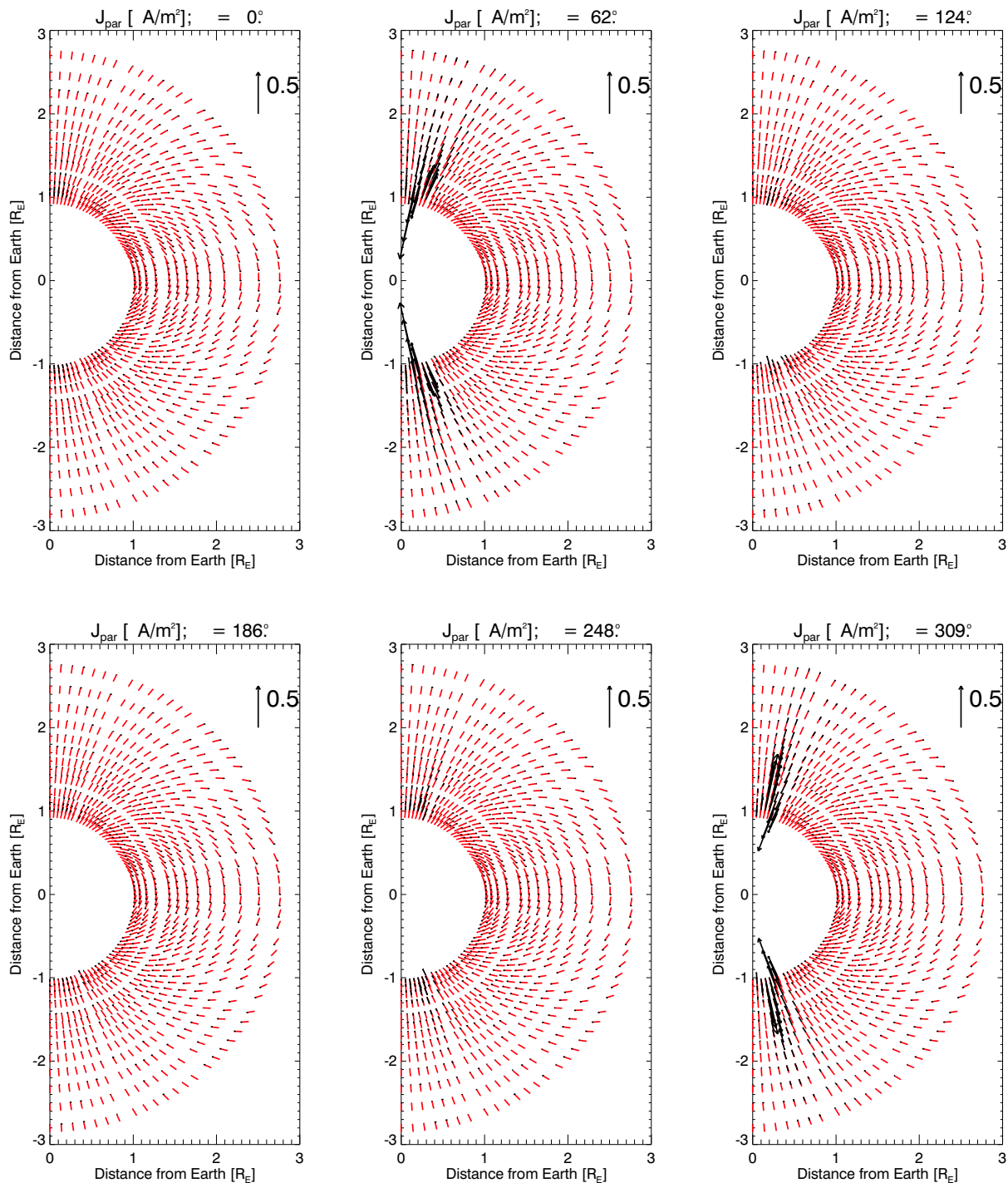


Figure 2.1: Parallel current vectors (black arrows) near the ionosphere are shown in meridional slices of the spherical grid (for clarity only a sub-sample of grid points are display). In the background, red arrows represent the dipole field unit vectors at each point. The results are for the UCLA run SV\_012804.1 at time 000000.

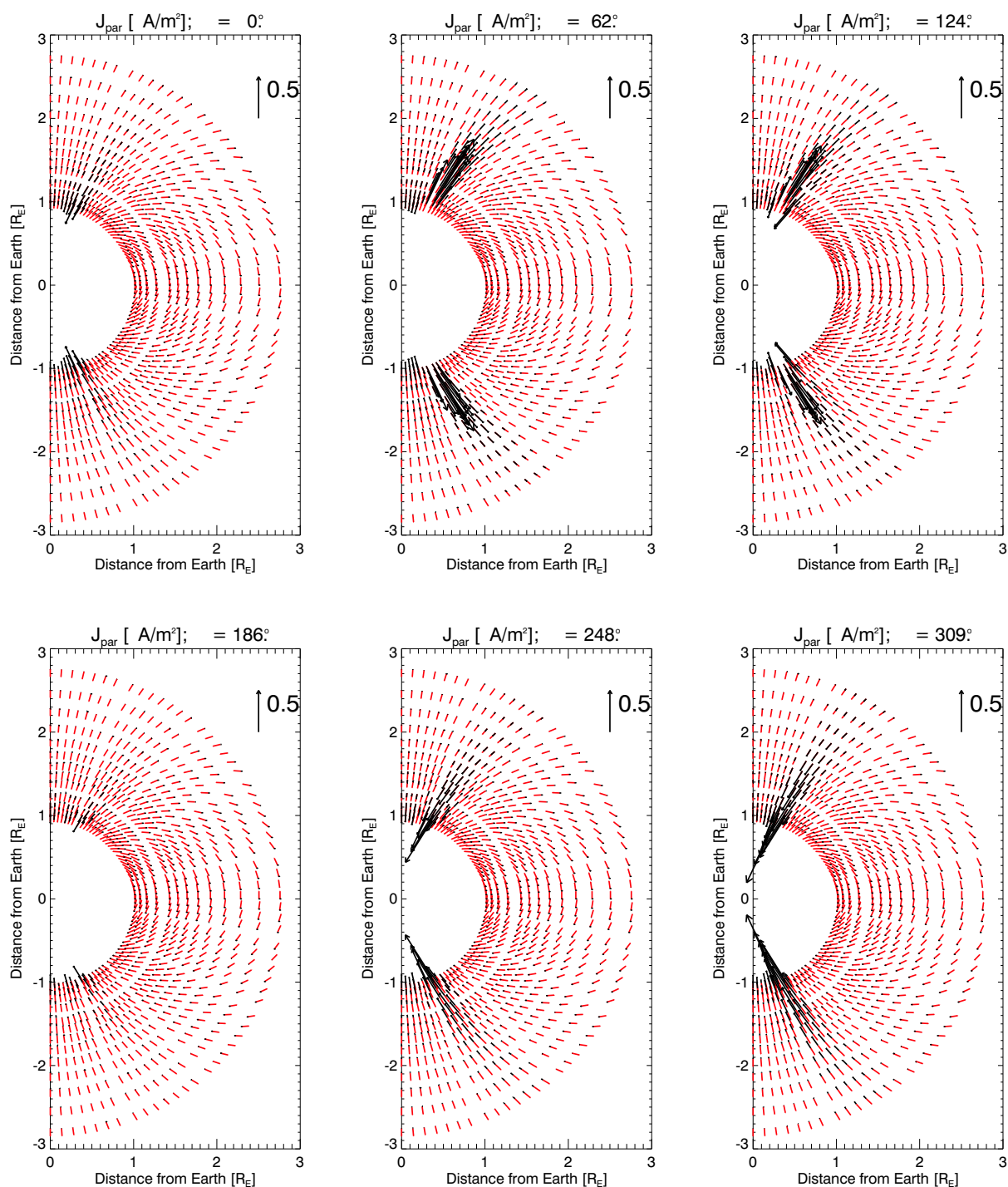


Figure 2.2: Parallel current vectors (black arrows) near the ionosphere are shown in meridional slices of the spherical grid (for clarity only a sub-sample of grid points are displayed). In the background, red arrows represent the dipole field unit vectors at each point. The results are for the UCLA run SV\_012804.1 at time 080000.

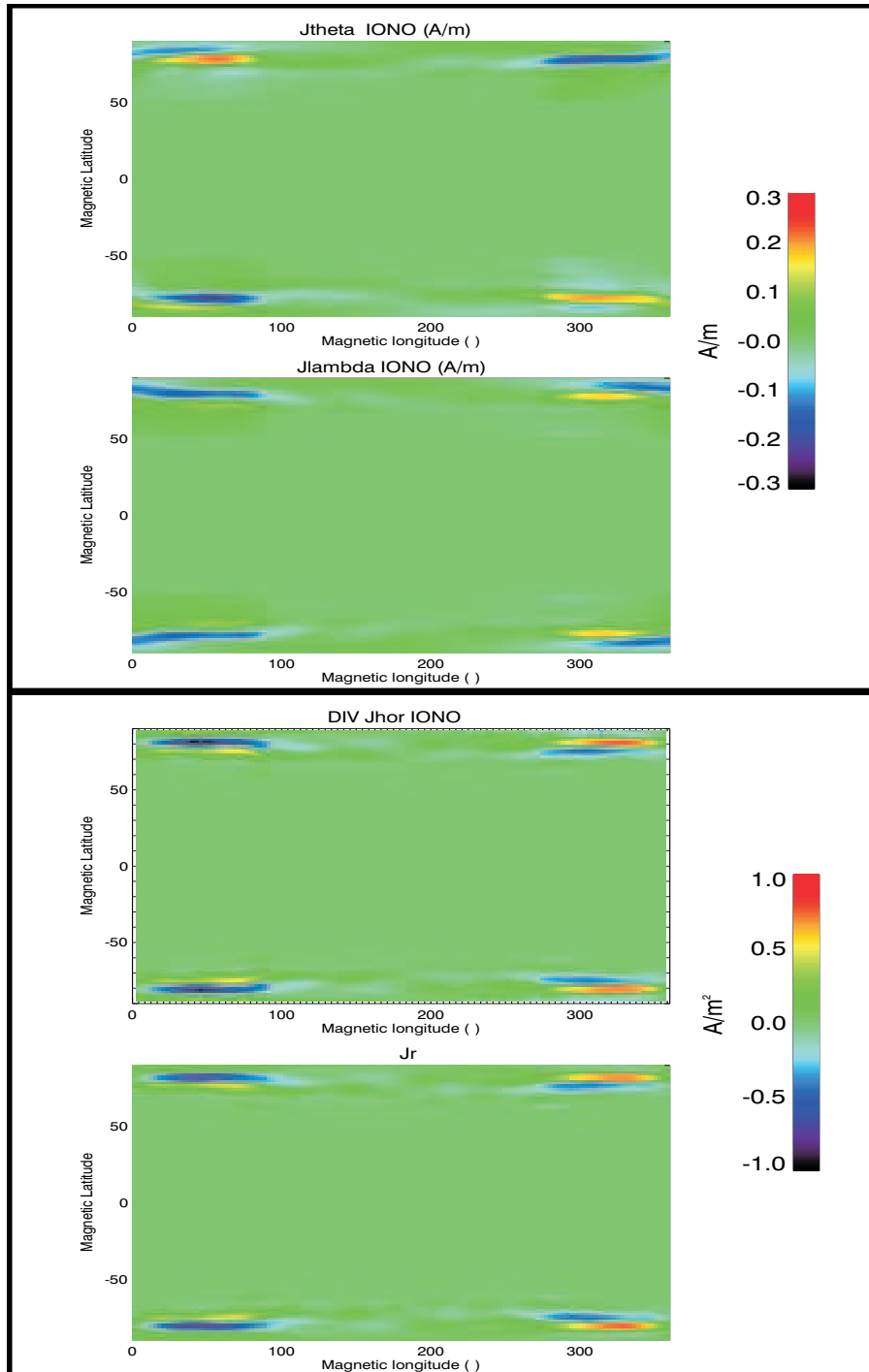


Figure 2.3: The top two panels show the ionospheric sheath current distribution,  $j_\theta$  (top) and  $j_\lambda$ , respectively. The bottom two panels show the comparison between the horizontal divergence (top) and  $j_r$ . The results are for the UCLA run SV\_012804.1 at time 000000.

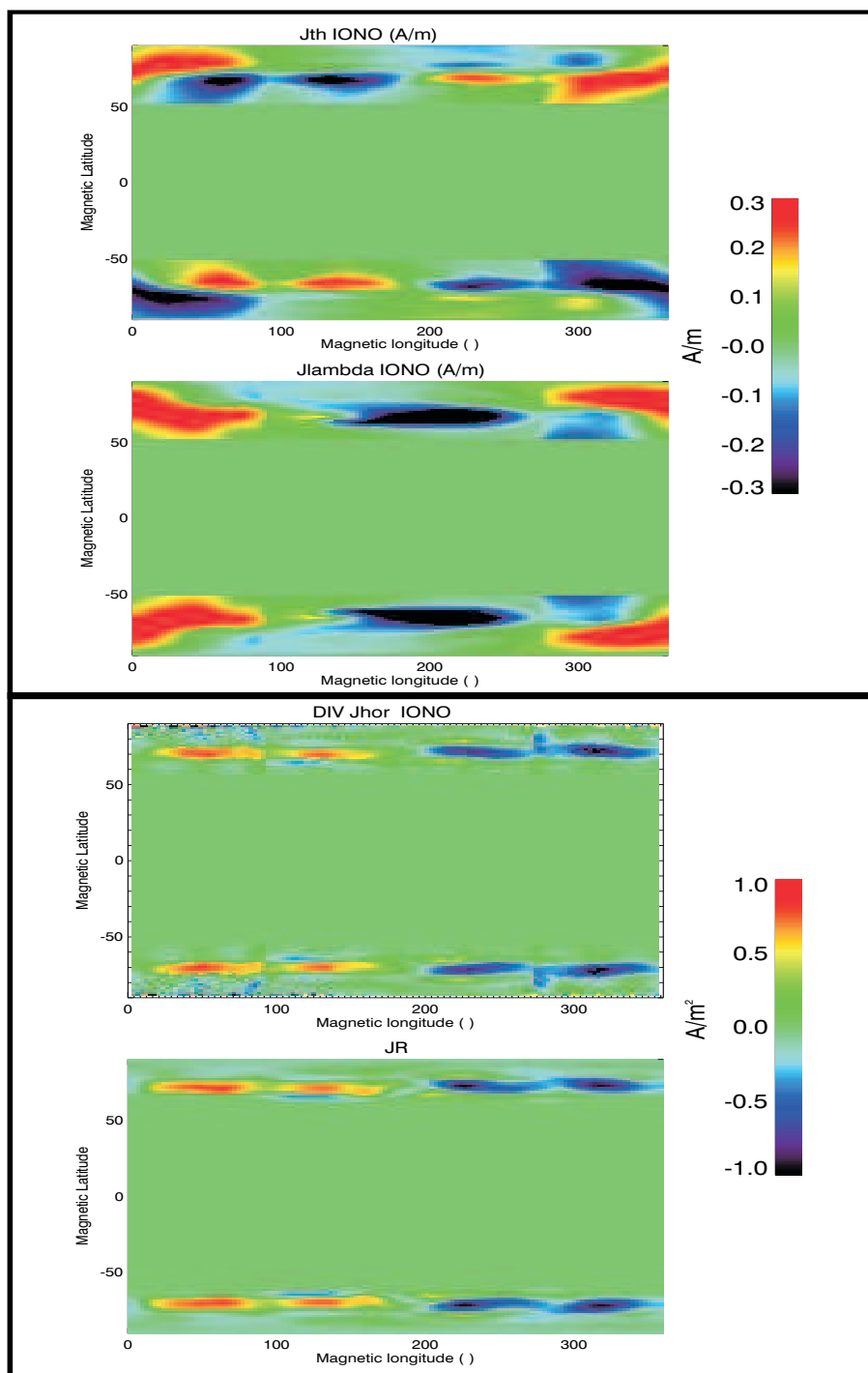
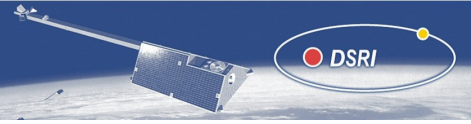


Figure 2.4: The top two panels show the ionospheric sheath current distribution,  $j_{\theta}$  (top) and  $j_{\lambda}$ , respectively. The bottom two panels show the comparison between the horizontal divergence (top) and  $j_r$ . The results are for the UCLA run SV\_012804.1 at time 080000.



Product	Description	Implementation	Use
Ionospheric Currents Tool	Calculates the horizontal ionospheric current on the specified polar grid	CCMC	Input to forward module for magnetic field measurement calculation
Field-Aligned Currents Tool	Calculates the distribution of field-aligned currents between the inner magnetosphere and the ionosphere on the specified spherical grid	CCMC	Input to forward module for magnetic field measurement calculation
Magnetospheric Currents Tool	Provides the magnetospheric current distribution on the specified spherical grid	CCMC	Input to forward module for magnetic field measurement calculation
Binary Data Files	Defines the binary format of the current-data files	DSRI, CCMC	Data Exchange
Test Field-Aligned Currents	Tests that resulting field-aligned current densities are really field aligned and are divergence free	DSRI	Validation
Test Ionospheric Currents	Verifies the consistency between the horizontal and radial currents at the ionosphere	DSRI	Validation

Table 2.1:

## Electric Potential Distributions

The three-dimensional distribution of the electric potential at Swarm satellite heights has been calculated by mapping of the ionospheric electric potential along magnetic field lines, with the assumption that these are equipotentials. This is done on a spherical grid from the model ionosphere (90 km altitude) out to 1700 km altitude and provides the input needed for the modeling of the electric field measurements at the Swarm satellites. This grid has the same number of points for the  $\vartheta$  and  $\lambda$  components and has 33 points in the radial direction (grid point spacing of 50 km), to allow for accurate estimation of the derivatives giving the electric field components.

### 2.2.3 Products

The tools and products developed under this part of the study are summarized in Table 2.1.

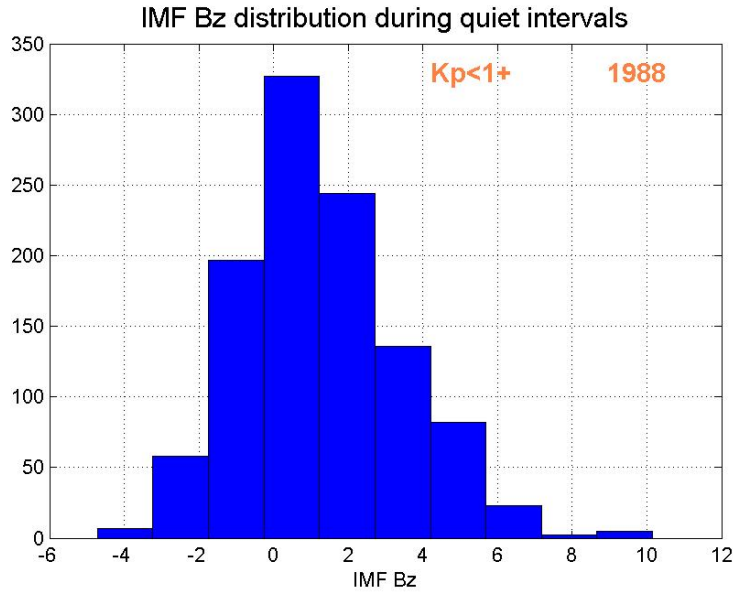
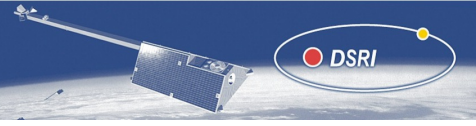


Figure 2.5: Distribution of intervals with  $K_P \leq 1^+$  as a function of the hourly average value of the IMF  $B_Z$  component for the interval.

## 2.3 *Swarm* Study Simulations

While geomagnetic activity is driven by the combination of a wide variety of conditions in the solar wind and magnetosphere, including their time-history, the single most decisive parameter is the north-south component ( $B_Z$ ) of the interplanetary magnetic field (IMF). Keeping all other parameters at average values, a small, positive (northward) IMF  $B_Z$  component generally will produce very low levels of geomagnetic activity. A small negative IMF  $B_Z$  component, in contrast, is generally associated with moderate geomagnetic activity. A common criterion for identifying geomagnetic quiet intervals is a small value of the  $K_P$  index. Figure 2.5 shows the distribution for the year 1988 of all 1 hour time intervals with  $K_P$  values less than or equal to  $1^+$  as a function of the average value of the IMF  $B_Z$  during the interval.

Following the objective of the *Swarm* mission, the focus in this study is on geomagnetic quiet and moderately disturbed conditions. Three separate simulations have been performed to obtain appropriate current density and electric potential data for use in the forward modeling of magnetic and electric field measurements by the *Swarm* satellites. One simulation was driven by average density and solar wind values with the IMF  $B_Z$  component changing slowly from a small positive to a small negative value over 8 hours. Another simulation was performed with the same solar wind driving conditions but applying a tilt of the dipole axis. This allows for comparative analyses of the results for winter and summer conditions at the two polar regions. Finally, a simulation driven by actual solar wind observations for a moderately quiet period was performed to allow for the comparison of the model results with magnetic field measurements from the Ørsted and CHAMP satellites.



### 2.3.1 Slowly Changing IMF $B_Z$

#### Set-up

The solar wind conditions used as input for the first simulation are: constant density, velocity, and temperature of  $7 \text{ cm}^{-3}$ ,  $400 \text{ km/s}$  (along the Sun-Earth axis), and  $1.4 \cdot 10^5 \text{ K}$ , respectively; IMF with zero  $B_Y$  and  $B_X$  components and  $B_Z$  component that changes linearly from  $+5.5 \text{ nT}$  to  $-5.5 \text{ nT}$  (cf. Figure 2.5) over the 8 hours of the simulation. The IMF-components are given in the geocentric solar magnetospheric (GSM) coordinate system, where the X-axis points from the Earth towards the Sun, and the Y-axis is perpendicular to the Earth's magnetic dipole, so that the X-Z plane contains the dipole-axis. A standard value of 150 has been used for the  $F_{10.7}$  parameter. Dipole tilt is zero making the model output exactly symmetric between the Northern and Southern hemispheres. Output is provided from the simulation every 10 minutes giving a total of 49 individual results.

#### Magnetosphere results

Figure 2.6 displays a set of images that illustrates the evolution of magnetospheric configuration and general conditions during the first simulation. In each column are shown four images at the times (top to bottom): 000000 (start of the simulation), 023000 (2.5 hours into the simulation), 053000 (5.5 hours into the simulation), and 080000 (at the end of the 8 hour long simulation). These times correspond to solar wind conditions of significant northward IMF, small amplitude northward IMF, small amplitude southward IMF, and significant southward IMF, respectively. Each image displays, in the  $Y=0$  plane (X-Z plane), the current density (background colour image), flow velocity (black arrows), and the projection of selected magnetic field lines originating in that plane (blue, black, and red lines). Only the near-Earth part of the simulation box, which extends to  $-255 R_E$  in the X-direction, is shown. The right column displays the same set of images, but with only a few field lines (drawn in green) to allow for a better view of the current distribution.

From top to bottom in Figure 2.6, the magnetosphere changes from being closed (no flaring) with reconnection occurring at high latitudes poleward of the cusps to being clearly open (large flaring) with reconnection occurring at the subsolar magnetopause. The changes in magnetospheric driving are also reflected in the current distribution. Both the location and amplitude of the most intense currents undergo considerable variations as a result of the IMF changes.

#### Ionosphere results

The changes in ionospheric parameters during the course of the simulation are illustrated in Figure 2.7. The results for the same four times as in Figure 2.6 are shown in each column from top to bottom. The two columns at the left show the ionospheric electric potential distribution (colour scale) and the open-closed field line boundary (black curve) for the Northern (left) and Southern (right) polar regions. The images are polar images with the magnetic pole at the center and showing 40 degrees of co-latitude (latitude circles are drawn for every 10 degrees). Magnetic local noon (direction to the Sun) is at the top of each image and dusk is to the left for both hemispheres (i.e. the Southern polar region is plotted as viewed from the North pole through the Earth). The two columns on the right display the Pedersen conductance (colour scale) together with the electric field vectors (black arrows) for the Northern and Southern polar regions in the same polar plot format. For both electric potential and Pedersen conductance the colour scale is kept constant throughout the figure, but the scale of the electric field vectors varies from row to row.

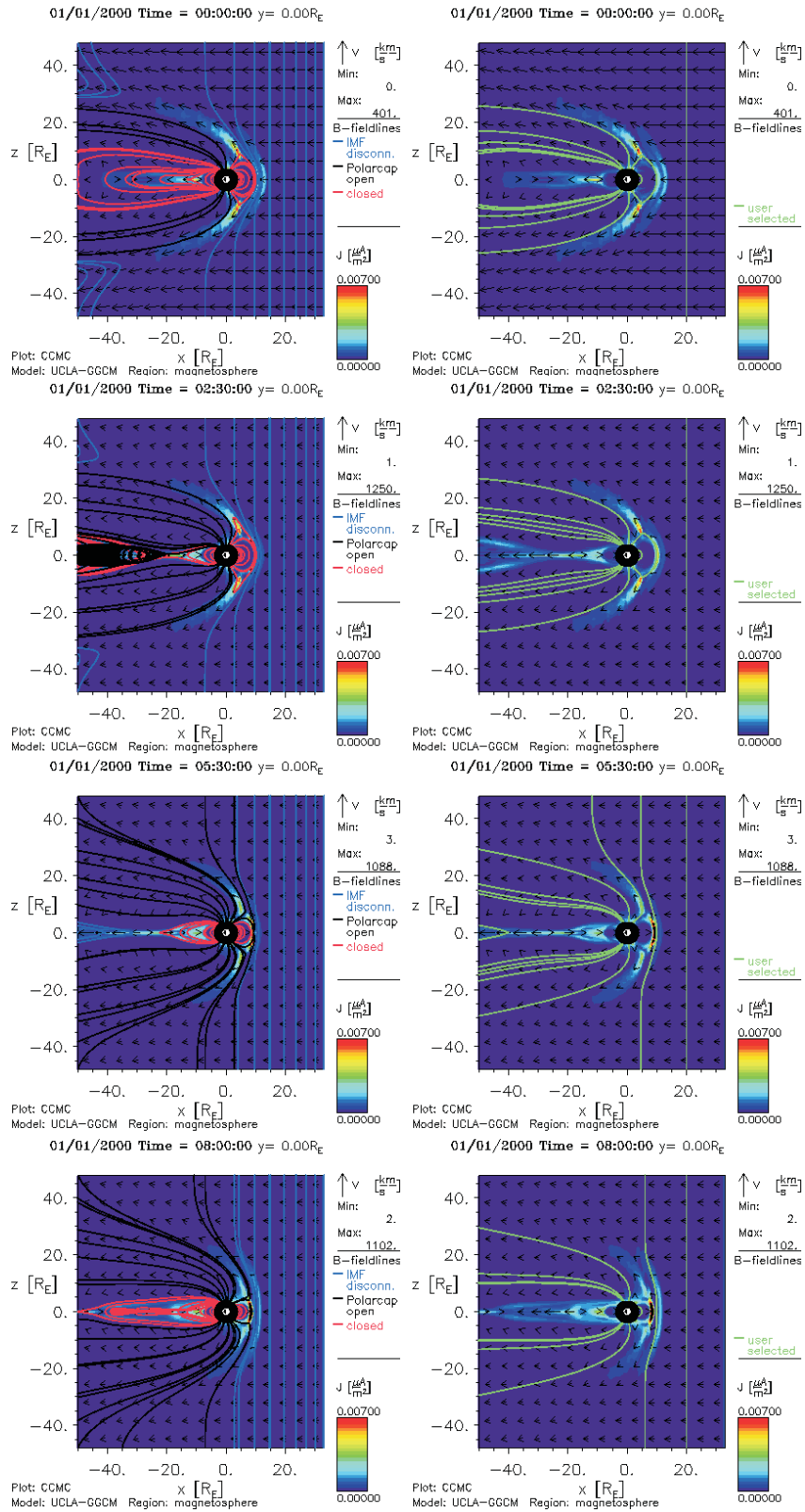


Figure 2.6: Magnetospheric conditions during the UCLA run SV\_012804.1 at times 000000, 023000, 053000, and 080000.

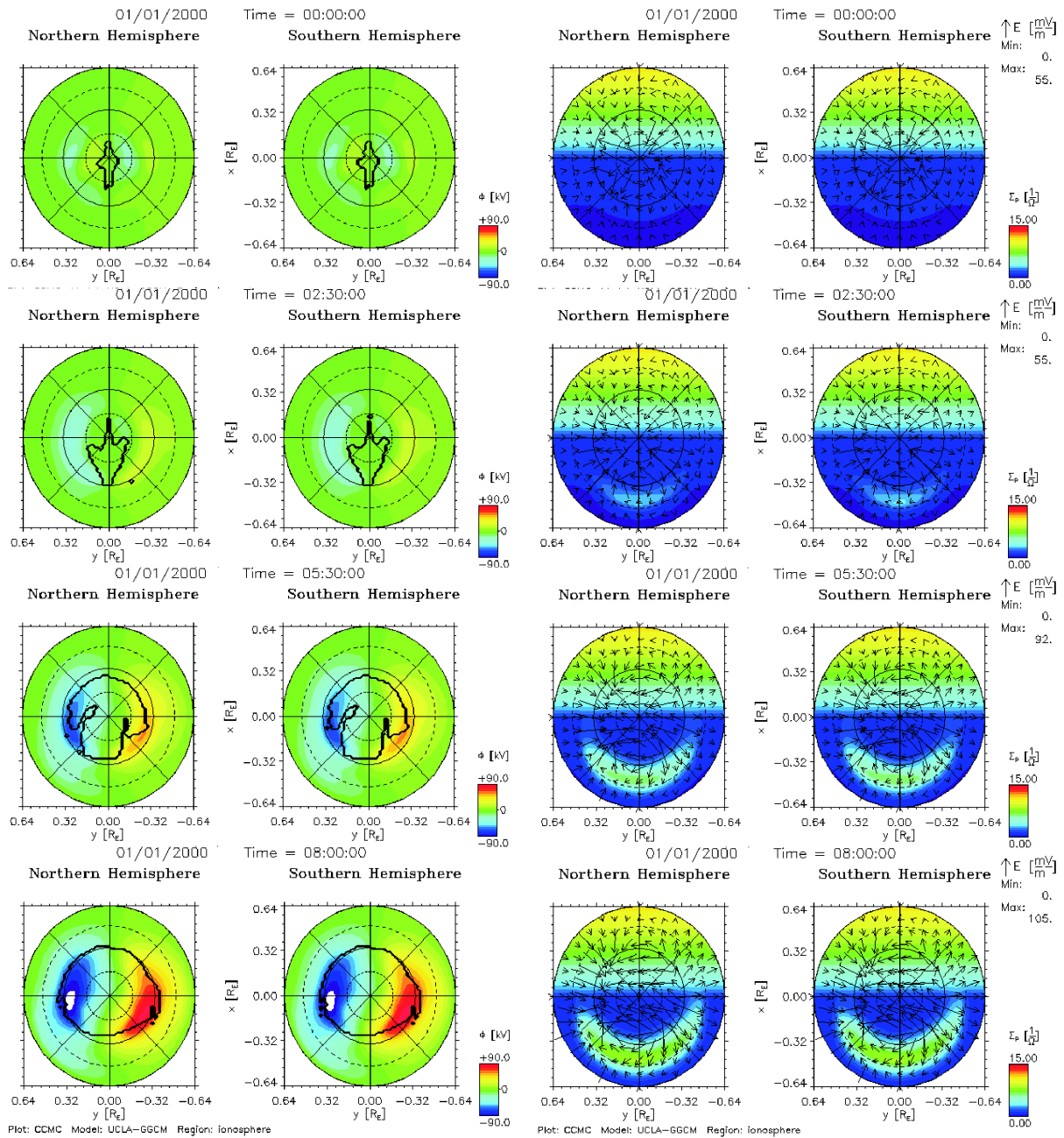
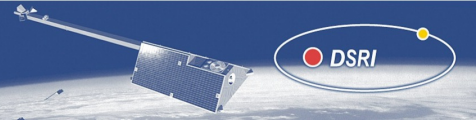


Figure 2.7: Ionospheric conditions during the UCLA run SV\_012804\_1 at times 000000, 023000, 053000, and 080000.



The change in ionospheric conditions from quiet to active as the IMF changes from northward to southward is evident in Figure 2.7. It is reflected most prominently in the expansion of the polar cap (area of open field-lines bounded by the black curve) and the strong increase in potential difference across the polar cap. However, the increase in activity also affects the conductance pattern, particularly on the night-side.

### 2.3.2 Slowly Changing IMF $B_Z$ With Dipole Tilt

#### Set-up

The same solar wind conditions as above is used for the second simulation, but a dipole tilt of -25 degrees in the X-Z plane has been included, simulating winter conditions for the Northern hemisphere and summer conditions for the Southern hemisphere. Again, output is provided from the simulation every 10 minutes giving a total of 49 individual results.

#### Magnetosphere results

Figure 2.8 illustrates the evolution of the magnetospheric conditions for this simulation. The format of the figure is the same as for Figure 2.6. The effects of the dipole tilt on the magnetic field configuration are clearly seen both for quiet and more active conditions. Strong asymmetries between the magnetopause currents in the Northern and Southern hemispheres are observed and the near-Earth tail current sheet is structured and tilted.

#### Ionosphere results

The changes in ionospheric parameters during the course of the simulation are illustrated in Figure 2.9. The format of the figure is the same as for Figure 2.7. Most prominently are the big differences between the Northern and Southern polar regions. The winter (Northern) hemisphere, naturally, is characterized by very low conductance levels for all levels of activity, though the effect of increased night-side conductance associated with stronger activity can be seen. In addition, very strong electric potentials are observed in the winter ionosphere as activity increases.

### 2.3.3 Real Event

In addition to the simulations result driven by modeled solar wind conditions presented above we present here the results of simulating an actual quiet-time interval driven by solar wind observations. The quiet day of March 9, 2002, was chosen for the simulation. The solar wind observations from the ACE spacecraft together with the  $K_P$  parameter for the entire day are displayed in Figure 2.10.

#### Set-up

The time interval modeled here is March 9, 2002 06-12 UT. Solar wind observations from the ACE spacecraft are propagated to the simulation inflow boundary at  $33 R_E$  upstream of the Earth. The resulting solar wind input parameters for the simulation are shown in Figure 2.11. They exhibit fairly stable values for all parameters with density, velocity, and temperature of approximately  $5 \text{ cm}^{-3}$ , 430 km/s (along the Sun-Earth axis), and  $5 \cdot 10^4 \text{ K}$ , respectively. The IMF has a steady positive  $B_Y$  component of roughly 4 nT and a slightly more variable  $B_Z$  component with values between +5 nT and -2 nT. The measured IMF  $B_X$  component also

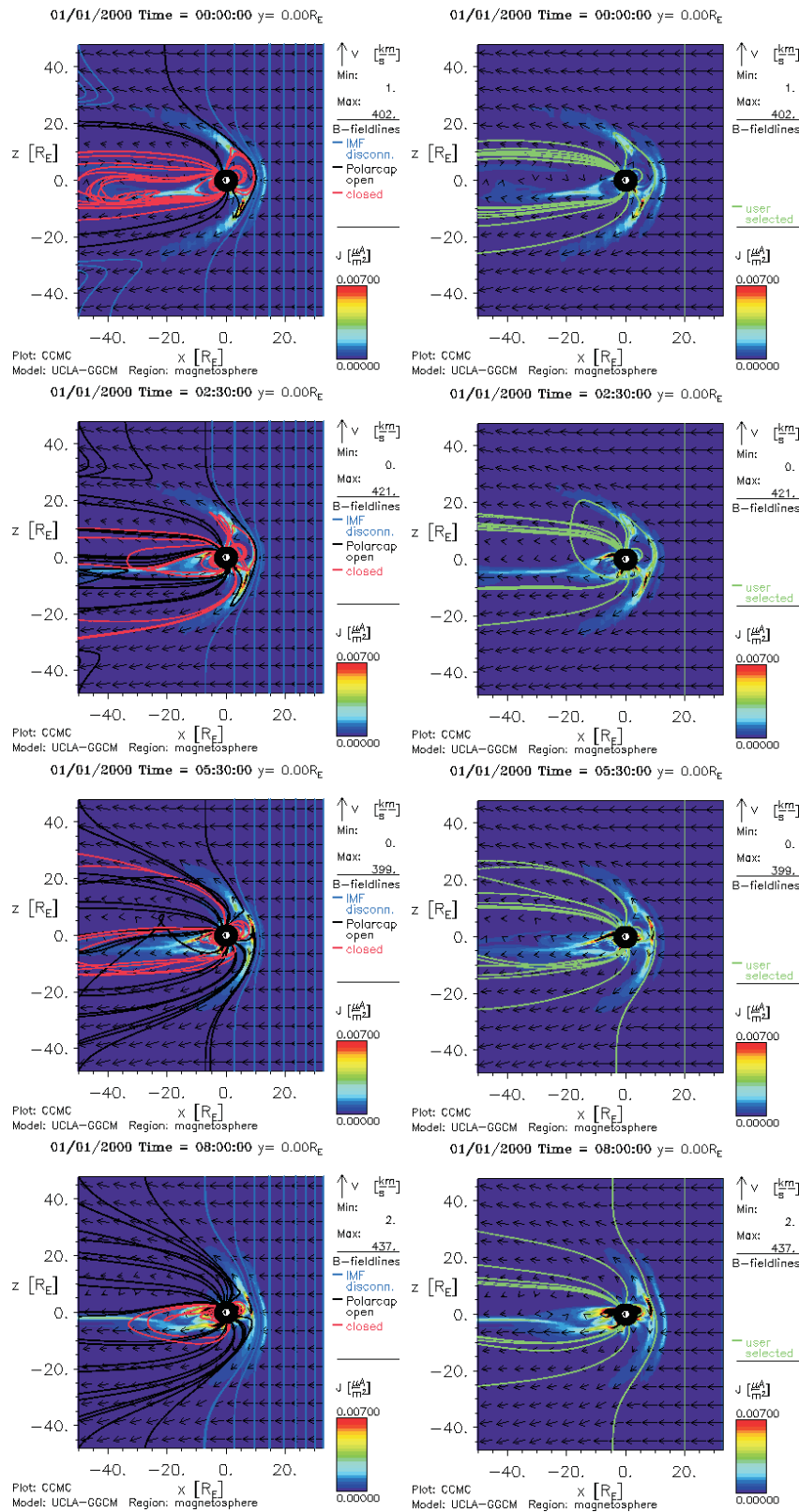


Figure 2.8: Magnetospheric conditions during the UCLA run SV\_021704.1 at times 000000, 023000, 053000, and 080000.

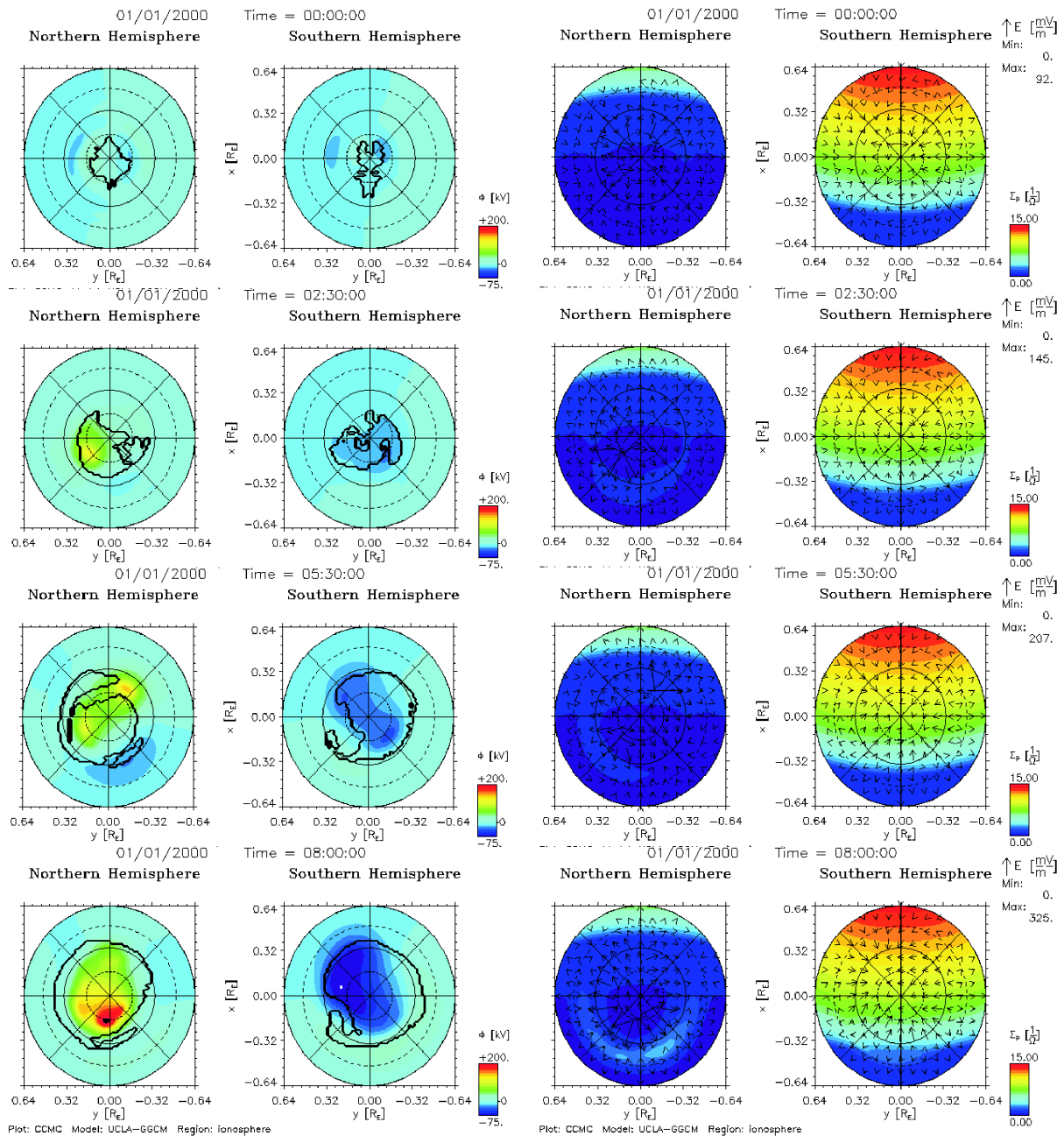


Figure 2.9: Ionospheric conditions during the UCLA run SV\_021704\_1 at times 000000, 023000, 053000, and 080000.

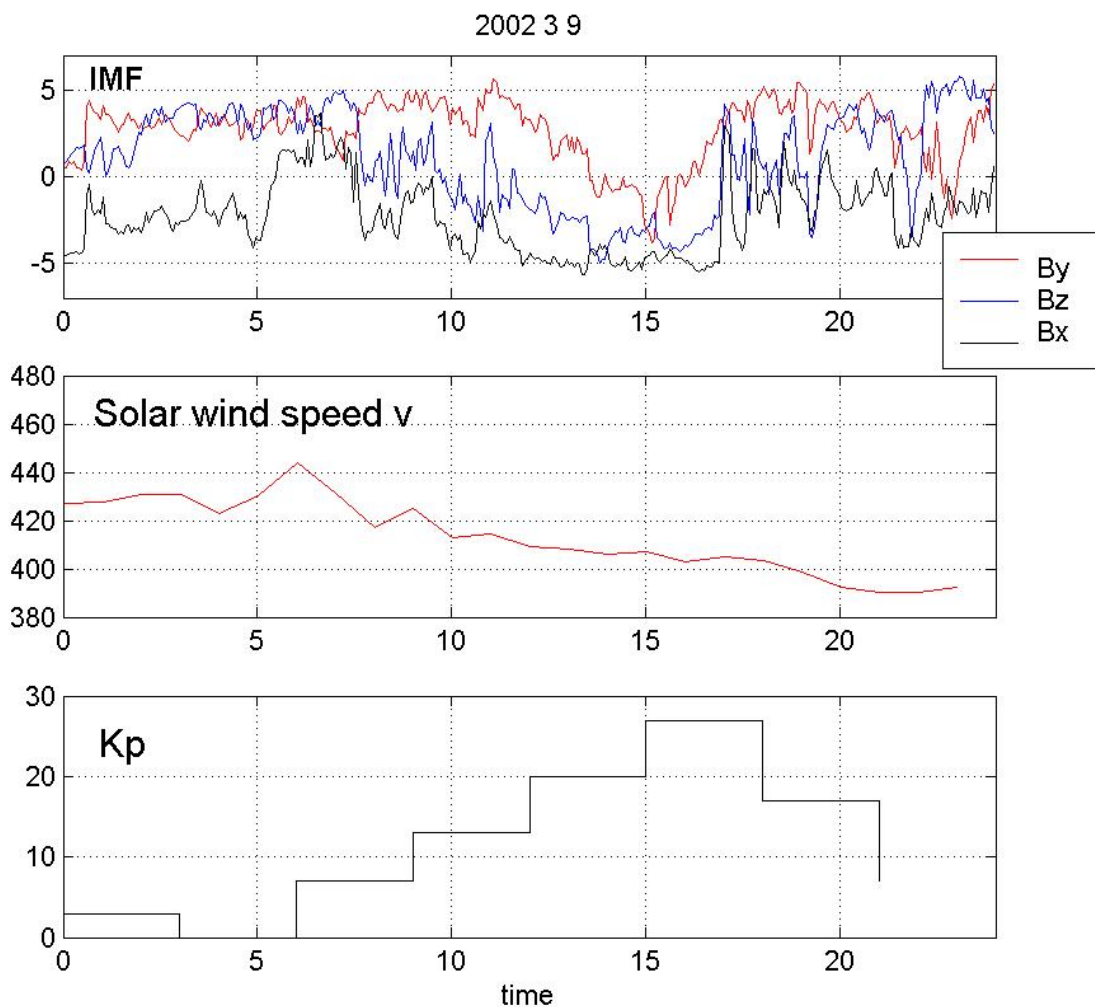


Figure 2.10: Top two panels show the IMF and Solar wind speed observations from the ACE spacecraft for the day March 9, 2002. The bottom panel displays the three-hour  $K_P$  index (a value of 10 in the figure equals  $1^0$ , a value of 13.3 equals  $1^+$  etc.).

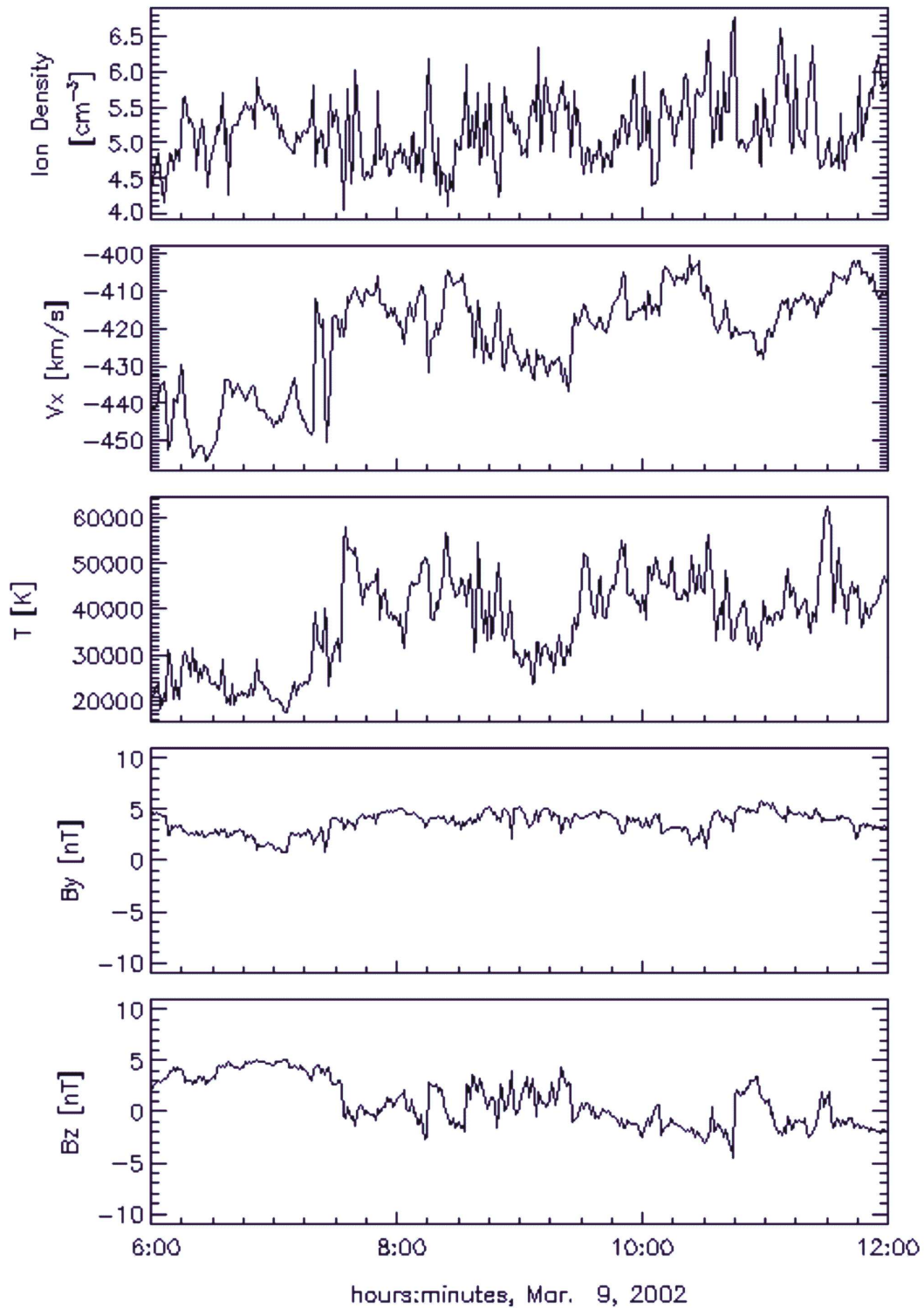


Figure 2.11: Solar wind input parameters measured by the ACE satellite for March 09, 2002 06-12 UT. The observations have been propagated to the simulation inflow boundary.

Product	Description	Implementation	Use
Simulation of Slowly Changing IMF $B_Z$	Global MHD simulation of IMF changing slowly from northward to southward over 8 hours	CCMC, DSRI	Provide input for current and electric potential derivations
Simulation of Slowly Changing IMF $B_Z$ and Non-zero Dipole Tilt	Global MHD simulation as above but with a tilted dipole, representing Northern winter conditions	CCMC, DSRI	Provide input for current and electric potential derivations
Simulation of Real Period	Global MHD simulation of actual solar wind conditions	CCMC, DSRI	Provide input for current and electric potential derivations

Table 2.2:

varies during the course of the event with values between +3 nT and -4 nT. For the simulation, however, the input IMF  $B_X$  is assumed 0 throughout. A dipole tilt appropriate for the date and time is applied (-16.1° in the GSE X-Z plane and 19.8° in the Y-Z plane). A major difference as compared to the previous simulations is the presence of a considerable IMF  $B_Y$  component in the solar wind driver. Output is provided from the simulation every 10 minutes giving a total of 37 individual results.

### Magnetosphere results

Figure 2.12 illustrates the magnetospheric configuration and general condition during the real event simulation. Results are shown for the times 060000 UT, 080000 UT, 100000 UT, and 1200000 UT. The presence of a strong  $B_Y$  component in the IMF means that it is not possible to depict the main magnetic field configuration by projecting onto a simple plane. Therefore the left column in Figure 2.12 displays a three-dimensional view of the magnetic field. A twisted and complex magnetosphere configuration prevails throughout the interval. The right column displays the current density (background colour scale), flow velocity (black arrows), and a few magnetic field lines (colored lines) in the  $Z=0$  (X-Y) plane. A strong dawn-dusk asymmetry can be seen in the tail-current structures.

### Ionosphere results

The ionospheric parameters during the course of the simulation are illustrated in Figure 2.13. The format of the figure is the same as for Figure 2.7. The dipole tilt for this UT time means that ionospheric conductance levels are almost as for Northern winter conditions (cf. Figure 2.9). The electric potential patterns exhibit the asymmetric (round/crescent) two-cell pattern typical for IMF  $B_Y$  dominated conditions.

#### 2.3.4 Products

The tools and products developed under this part of the study are summarized in Table 2.2.



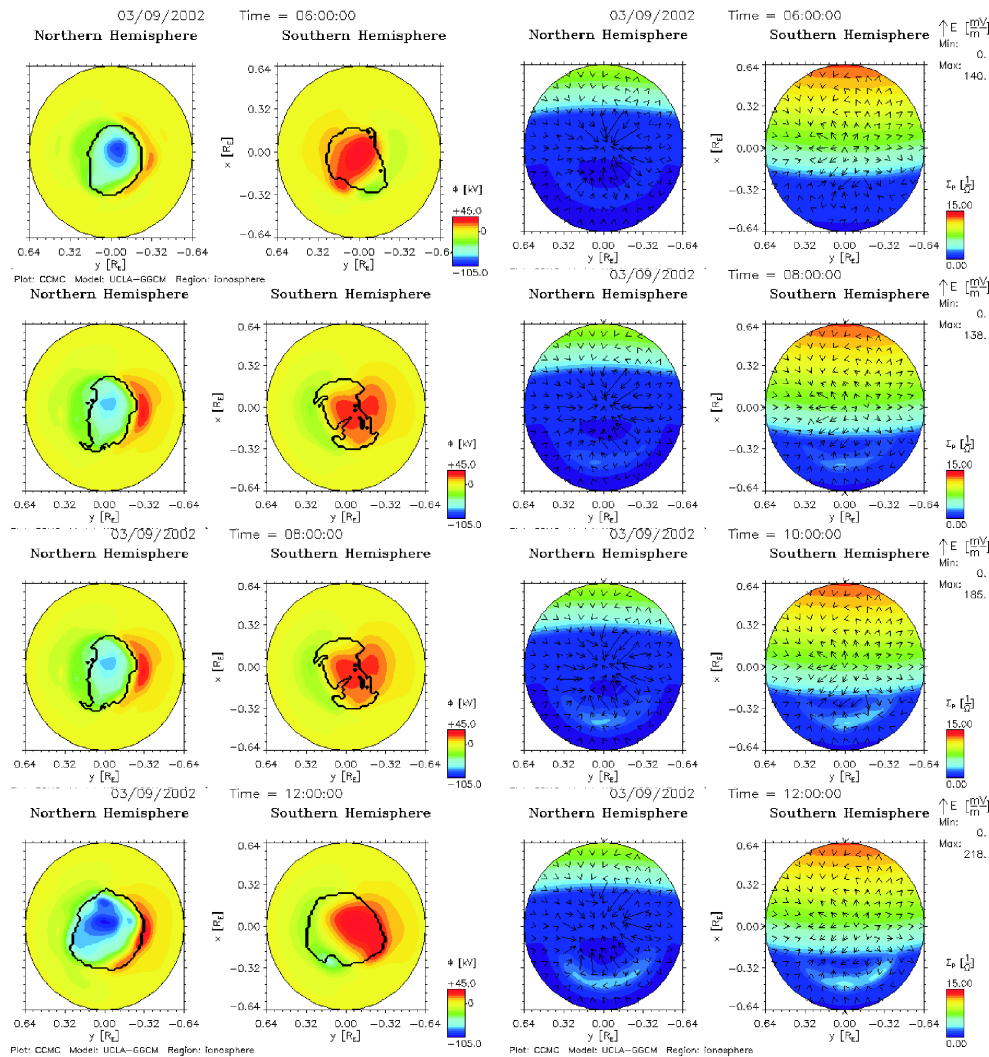


Figure 2.13: Ionospheric conditions during the UCLA run for March 09, 2002 06-12 UT at times 060000, 080000, 100000, and 120000.

## 2.4 Computation of magnetic fields within source regions of ionospheric and magnetospheric currents

Magnetic fields of external origin are of considerable interest for the analysis of magnetic fields of internal origin using satellite observations. A particular difficulty arises from the fact that satellites pass through source regions of external fields, and thus accurate modelling requires the determination of the magnetic field  $\mathbf{B}$  in the presence of a given ionospheric–magnetospheric current density  $\mathbf{J}$ . Several methods are in use for computing the magnetic field  $\mathbf{B}$  caused by a given ionospheric or magnetospheric current density  $\mathbf{J}$ . Most of them are based on Biot–Savart’s law:

$$\mathbf{B}(\mathbf{r}) = \frac{\mu_0}{4\pi} \int \frac{\mathbf{J}(\mathbf{r}') \times (\mathbf{r} - \mathbf{r}')}{|\mathbf{r} - \mathbf{r}'|^3} dV' \quad (2.5)$$

As the three–dimensional integral must be evaluated over the whole source region, these methods are useful mainly for small–scale current systems. In this study, two algorithms for the magnetic field computation have been developed independently and tested against each other. One is based on a poloidal–toroidal decomposition, as described below, and the other on direct Biot–Savart integration.

### 2.4.1 Poloidal–Toroidal Decomposition Method

The method described here follows closely the approach of [Engels and Olsen \[1998\]](#).

The time and length scales of the current density and magnetic fields considered are such that displacement currents can be neglected, which is equivalent to a non-divergent current flow. Because of  $\text{div } \mathbf{J} = 0$  and  $\text{div } \mathbf{B} = 0$  everywhere, it is always possible to decompose the current density  $\mathbf{J}$  and the associated magnetic field  $\mathbf{B}$  into poloidal and toroidal parts [[Stern, 1976](#), [Backus, 1986](#)].

In a spherical coordinate system  $(r, \vartheta, \lambda)$  with radius  $r$ , colatitude  $\vartheta$  and longitude  $\lambda$ , this decomposition reads as follows:

$$\begin{aligned} \mathbf{B} &= \mathbf{B}_{\text{tor}} + \mathbf{B}_{\text{pol}} \\ &= \text{curl } \mathbf{r}\Phi + \text{curl curl } \mathbf{r}\Psi \\ &= \begin{pmatrix} 0 \\ \frac{1}{\sin \vartheta} \frac{\partial}{\partial \lambda} \Phi \\ -\frac{\partial}{\partial \vartheta} \Phi \end{pmatrix} + \begin{pmatrix} -\nabla_{\text{s}}^2(r\Psi) \\ \frac{1}{r} \frac{\partial}{\partial \vartheta} (r\Psi)' \\ \frac{1}{r \sin \vartheta} \frac{\partial}{\partial \lambda} (r\Psi)' \end{pmatrix} \end{aligned} \quad (2.6)$$

with  $(r\Psi)' = d(r\Psi)/dr$  and

$$\nabla_{\text{s}}^2 = \frac{1}{r^2 \sin \vartheta} \frac{\partial}{\partial \vartheta} \left( \sin \vartheta \frac{\partial}{\partial \vartheta} \right) + \frac{1}{r^2 \sin^2 \vartheta} \frac{\partial^2}{\partial \lambda^2}$$

as the transverse part of the Laplacian.

$\Phi$  and  $\Psi$  are the toroidal and poloidal scalars for  $\mathbf{B}$ . Following [Backus \[1986\]](#), they are determined uniquely by the additional requirement that their mean value over each sphere vanishes, i.e.  $\int \Phi d\Omega = \int \Psi d\Omega = 0$  with  $d\Omega = \sin \vartheta d\vartheta d\lambda$ .

From Ampere's law, it follows for the current density:

$$\begin{aligned}
 \mu_0 \mathbf{J} &= \mu_0 \mathbf{J}_{\text{pol}} + \mu_0 \mathbf{J}_{\text{tor}} \\
 &= \text{curl } \mathbf{B} \\
 &= \text{curl curl } \mathbf{r}\Phi + \text{curl curl curl } \mathbf{r}\Psi \\
 &= \text{curl curl } \mathbf{r}\Phi - \text{curl } \mathbf{r}\nabla^2 \Psi \\
 &= \text{curl curl } \mathbf{r}\Phi + \text{curl } \mathbf{r}Q
 \end{aligned} \tag{2.7}$$

where  $Q$  and  $\Psi$  are connected by the equation

$$\text{curl}(\mathbf{r}[Q + \nabla^2 \Psi]) = \mathbf{0} \quad . \tag{2.8}$$

Then  $Q + \nabla^2 \Psi = (1/r) d\chi/dr$ , and  $\Psi$  is the sum of two functions, the general solution of

$$Q = -\nabla^2 \Psi \tag{2.9}$$

and some function of  $r$  alone, solving  $\nabla^2 \Psi = (1/r) d\chi/dr$ . However, any part of  $\Psi$  which depends on  $r$  alone does not contribute to (2.6) and may be omitted, leaving only the solution of (2.9). The scalar fields  $\Phi$ ,  $\Psi$  and  $Q$  are expanded into series of spherical harmonics

$$\Phi(r, \vartheta, \lambda) = \sum_{n,m} \phi_n^m(r) P_n^m(\cos \vartheta) e^{im\lambda} \tag{2.10}$$

$$\Psi(r, \vartheta, \lambda) = R \sum_{n,m} \psi_n^m(r) P_n^m(\cos \vartheta) e^{im\lambda} \tag{2.11}$$

$$Q(r, \vartheta, \lambda) = \frac{1}{R} \sum_{n,m} q_n^m(r) P_n^m(\cos \vartheta) e^{im\lambda} \tag{2.12}$$

where  $P_n^m(\cos \vartheta)$  are the Schmidt normalized Legendre functions.  $R$  is a reference radius, e.g. the Earth's radius  $a = 6371$  km. In this formulation the scalars  $\phi_n^m$ ,  $\psi_n^m$  and  $q_n^m$  have the units of  $\mathbf{B}$ , e. g. nanoteslas.

The components of the magnetic field and current density follow from the expansion coefficients  $\phi_n^m$ ,  $\psi_n^m$  and  $q_n^m$  as

$$\begin{aligned}
 \mathbf{B} &= \mathbf{B}_{\text{tor}} + \mathbf{B}_{\text{pol}} \\
 &= \sum_{n,m} \begin{pmatrix} 0 \\ \frac{im}{\sin \vartheta} \phi_n^m P_n^m e^{im\lambda} \\ -\phi_n^m \frac{d}{d\vartheta} P_n^m e^{im\lambda} \end{pmatrix} \\
 &\quad + \left(\frac{R}{r}\right) \sum_{n,m} \begin{pmatrix} n(n+1)\psi_n^m P_n^m e^{im\lambda} \\ (r\psi_n^m)' \frac{d}{d\vartheta} P_n^m e^{im\lambda} \\ \frac{im}{\sin \vartheta} (r\psi_n^m)' P_n^m e^{im\lambda} \end{pmatrix}
 \end{aligned} \tag{2.13}$$

and

$$\begin{aligned}
 \mu_0 \mathbf{J} &= \mu_0 \mathbf{J}_{\text{pol}} + \mu_0 \mathbf{J}_{\text{tor}} \\
 &= \frac{1}{r} \sum_{n,m} \begin{pmatrix} n(n+1)\phi_n^m P_n^m e^{im\lambda} \\ (r\phi_n^m)' \frac{d}{d\vartheta} P_n^m e^{im\lambda} \\ \frac{im}{\sin \vartheta} (r\phi_n^m)' P_n^m e^{im\lambda} \end{pmatrix} \\
 &\quad + \frac{1}{R} \sum_{n,m} \begin{pmatrix} 0 \\ \frac{im}{\sin \vartheta} q_n^m P_n^m e^{im\lambda} \\ -q_n^m \frac{d}{d\vartheta} P_n^m e^{im\lambda} \end{pmatrix}
 \end{aligned} \tag{2.14}$$

with  $(r\phi_n^m)' = d(r\phi_n^m)/dr$  and a corresponding equation for  $\psi_n^m$ . Note that the radial component of the current density is given by the expansion coefficients  $\phi_n^m$  only and, therefore, these coefficients can, in principle, be found from a spherical harmonic expansion of  $J_r$  alone.

The toroidal magnetic field  $\mathbf{B}_{\text{tor}} = \text{curl } \mathbf{r}\Phi$  is directly related to the poloidal current density  $\mu_0 \mathbf{J}_{\text{pol}} = \text{curl } \text{curl } \mathbf{r}\Phi$ . However, in order to obtain the poloidal magnetic field  $\mathbf{B}_{\text{pol}} = \text{curl } \text{curl } \mathbf{r}\Psi$  from a given toroidal current density  $\mu_0 \mathbf{J}_{\text{tor}} = \text{curl } \mathbf{r}Q$ , the Poisson equation  $\nabla^2 \Psi = -Q$  has to be solved. Due to the spherical harmonic expansion and the fact that  $r^2 \nabla_s^2 (P_n^m e^{im\lambda}) = -n(n+1)P_n^m e^{im\lambda}$ , the three-dimensional equation  $\nabla^2 \Psi = -Q$  reduces to an ordinary differential equation in  $r$ :

$$\frac{d}{dr} \left( r^2 \frac{d\psi_n^m}{dr} \right) - n(n+1)\psi_n^m = - \left( \frac{r}{R} \right)^2 q_n^m. \quad (2.15)$$

It can be solved by means of

$$\psi_n^m(r) = \int_0^\infty G_n(r, s) \left( \frac{s}{R} \right)^2 q_n^m(s) ds \quad (2.16)$$

with Green's function [cf. [Arfken, 1985](#), chapter 16.5]

$$G_n(r, s) = \frac{1}{2n+1} \begin{cases} \frac{r^n}{s^{n+1}}, & r < s \\ \frac{s^n}{r^{n+1}}, & r > s \end{cases}. \quad (2.17)$$

A short discussion of eq. (2.16) might be helpful. Let us assume that the currents only flow in the spherical shell  $r_1 < r < r_2$ . The magnetic field in the region  $r < r_1$  is a Laplacian potential field  $\mathbf{B} = -\text{grad } V^e = \text{curl } \text{curl } \mathbf{r}\Psi^e$  where the potential

$$V^e(r, \vartheta, \lambda) = R \sum_{n,m} \left( \frac{r}{R} \right)^n \epsilon_n^m P_n^m e^{im\lambda} \quad (2.18)$$

describes external sources only. The expansion coefficients of  $V^e$  and  $\Psi^e$  are connected as

$$\epsilon_n^m = -(n+1) \left( \frac{R}{r} \right)^n \psi_n^{m,e}(r) \quad (2.19)$$

and, using eq. (2.16), this yields

$$\epsilon_n^m = -\frac{n+1}{2n+1} \frac{1}{R} \int_{r_1}^{r_2} q_n^m(s) \left( \frac{R}{s} \right)^{n-1} ds. \quad (2.20)$$

The magnetic field  $\mathbf{B} = -\text{grad } V^i$  in the region  $r > r_2$  is a potential field, too, but representing internal sources only:

$$V^i(r, \vartheta, \lambda) = R \sum_{n,m} \left( \frac{R}{r} \right)^{n+1} \iota_n^m P_n^m e^{im\lambda} \quad (2.21)$$

with

$$\iota_n^m = n \left( \frac{r}{R} \right)^{n+1} \psi_n^{m,i}(r) \quad (2.22)$$

$$= \frac{n}{2n+1} \frac{1}{R} \int_{r_1}^{r_2} q_n^m(s) \left( \frac{s}{R} \right)^{n+2} ds. \quad (2.23)$$

One can choose any value of  $R$ , however, a suitable choice for practical applications is the Earth's radius.

Note that  $\epsilon_n^m$  and  $\iota_n^m$  do not depend on  $r$  (since the radial dependence is included in the expansion of the potential  $V$ , cf. eqs. (2.18) and (2.21)). Therefore the magnetic field on any sphere of radius  $r < r_1$  or  $r > r_2$  is given by the same coefficients  $\epsilon_n^m$  or  $\iota_n^m$ , respectively. However, in the current region  $r_1 < r < r_2$ , eq. (2.16) has to be solved for every  $r$  for which the magnetic field is sought.

The integrals in eqs. (2.20) and (2.23) give the height-integrated current function, weighted by  $(R/s)^{n-1}$  and  $(s/R)^{n+2}$ , respectively. In the case of a sheet current at  $r = R$ , this integral yields the expansion coefficients of the equivalent current function, and eqs. (2.20) and (2.23) merge into the well-known relationship between the expansion coefficients of the magnetic potential and of the equivalent current function [for example Chapman and Bartels, 1940, p. 630].

## 2.4.2 Implementation of the Poloidal – Toroidal Approach

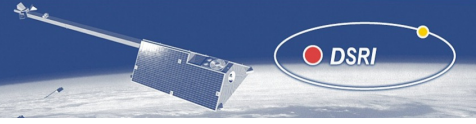
The approach described above has been implemented in MATLAB using the following scheme:

- The electric current density,  $\mathbf{J}(r_i, \theta_k, \phi_l)$  is given on a spherical grid,  $r_i, i = 1, \dots, N_r$ ;  $\theta_k, k = 1, \dots, N_\theta$ ;  $\phi_l, l = 1, \dots, N_\phi$ . The grid in  $\theta$ - and  $\phi$ -direction has to be equidistant, with  $\theta_1 = 0^\circ, \theta_{N_\theta} = 180^\circ, \phi_1 = 0^\circ, \phi_{N_\phi} = 360^\circ - \Delta\phi, \Delta\phi = 360^\circ/N_\phi$ . The radial grid may have arbitrary spacing, but has to cover the entire current region.
- For each spherical shell (i.e., each radius  $r_i$ ), a Spherical Harmonic Transformation (SHT) is performed and the expansion coefficients  $(r\phi_n^m)'$  and  $q_n^m$  are calculated up to degree and order  $n, m = 60$  from the magnetic horizontal components  $(B_\theta, B_\phi)$ . The transformation in longitudinal direction is done using Fourier Transform; for the latitudinal direction we use an integral approach (Simpson integration).
- $\phi_n^m$  is obtained from  $(r\psi_n^m)'$  by numerical integration in  $r$ -direction (Trapezoidal rule).
- $\psi_n^m$  is found from  $q_n^m$  according to Eq. 2.16 by numerical spline integration.
- Finally, the magnetic field,  $\mathbf{B}$ , is calculated from the expansion coefficients  $\psi_n^m$  and  $\phi_n^m$  for that part of the radial grid that covers *Swarm* altitudes.

## 2.4.3 Biot-Savart Integration

An algorithm for integrating the right-hand side of eq. (2.5) on a spherical grid was developed. The main problem with this approach is that the computation is very time-consuming if the number grid-points is large. In an attempt to reduce the computation time the algorithm was divided into three parts: calculations solely related to the chosen grid, calculations related to the current-system, and the actual B-field calculation at a specific position. In the first two parts, the volume of the grid-points are determined and the grid-positions and currents are transformed into Cartesian coordinates, in order to allow for a vectorized computation of the cross-product  $(\mathbf{J}(\mathbf{r}') \times (\mathbf{r} - \mathbf{r}'))$  in step 3.

Some difficulty arise due to a singularity of the integrand if  $\mathbf{B}$  is to be determined within the source region, where  $\mathbf{J}$  is non-zero and a source-point  $\mathbf{r}'$  may be identical with the field-point  $\mathbf{r}$ . Given a dense grid, this problem can be overcome with good results simply by omitting this point in the integration. This is possible because the contribution from this point, due to the



symmetry, is actually very small (identically zero for a vertical current). In order to solve the requirements for a dense grid, and at the same time minimize the computation time, a routine was developed, to divide selected grid-points into a number of smaller volume elements. This approach enables the grid resolution to vary with distance from the point where the magnetic field has to be computed. As the criterion for applying a smaller grid-size, an estimate of the magnitude of the B-field contribution of a given grid point to the integrand was used. In the results presented below, we used the value 10 nT as the limit above which a subdivision of a grid-point was performed. This value was incorporated as a variable parameter into the program, and a lower value can be chosen to obtain a higher accuracy at the cost of an increased computation time. In addition, the capability to down-sample the original grid in the  $\lambda$  and  $\vartheta$  direction with a variable factor was incorporated.

#### 2.4.4 Tests

The algorithms have been tested with two models of ionospheric–magnetospheric currents. The first example has the purpose to demonstrate, how the numerical results for a special spatially smooth current system can be verified by an analytical solution. Although the assumed current distribution is presumably not very realistic, it is chosen here for test purposes because it is one of the few current systems with an elementary analytical solution for the magnetic field. For the second example, in which the current density varies rapidly as a function of latitude and height, the two methods are compared

#### Comparison with an analytical solution

The details of the first example are quite complicated so only an outline shall be presented here. The full treatment of the first analytic part is due to *Siebert* [1996, *private communication*]. The basis of this model is a current distribution  $\mathbf{J} = \mathbf{J}_{\parallel} + \mathbf{K} \cdot \delta(r - b)$  consisting of a field-aligned current density  $\mathbf{J}_{\parallel}$  (dimension amp/m<sup>2</sup>) in the region  $r > b$ , and a horizontal sheet current density  $\mathbf{K}$  (amp/m) in the infinitesimally thin shell at  $r = b$ . The current  $\mathbf{J}$  flows between the two hemispheres along all dipole field lines outside a sphere  $r = b$ , and its strength on any such line is determined by the divergence of the sheet current  $\mathbf{K}$  which closes the circuit on  $r = b$ ;  $\mathbf{K}$  has only a  $\vartheta$ -component and is given by

$$\mathbf{K}(\vartheta, \lambda) = \begin{pmatrix} 0 \\ -J_0 \frac{b}{4} \sin^3 \vartheta e^{2i\lambda} \\ 0 \end{pmatrix}, r = b \quad (2.24)$$

which allows a solution in closed form;  $J_0$  (dimension amp/m<sup>2</sup>) is an amplitude factor. This sheet current has nonvanishing divergence, and hence the radial current density  $J_r(b_+, \vartheta, \lambda)$  just above  $r = b$  can be determined as  $J_r = -\text{div} \mathbf{K} \delta(r - b) = J_0 \sin^2 \vartheta \cos \vartheta e^{2i\lambda}$ . Assuming the currents in the region  $r > b$  flowing along the field lines of a dipole, the current density is given by

$$\mathbf{J}_{\parallel}(r, \vartheta, \lambda) = \begin{pmatrix} J_0 \left(\frac{b}{r}\right)^4 \sin^2 \vartheta \cos \vartheta e^{2i\lambda} \\ \frac{1}{2} J_0 \left(\frac{b}{r}\right)^4 \sin^3 \vartheta e^{2i\lambda} \\ 0 \end{pmatrix}, r > b. \quad (2.25)$$

There are no currents in the region  $r < b$ .

According to *Siebert*, this current distribution generates a magnetic field  $\mathbf{B}$ , which can be derived in a somewhat tricky direct way:

$$\mathbf{B} = \mathbf{B}_1 - \text{grad } V_1 = \begin{cases} \frac{i\mu_0 J_0 b}{4\sqrt{3}} \begin{pmatrix} -2 \left[ \left(\frac{b}{r}\right)^3 - \frac{6}{5} \left(\frac{b}{r}\right)^4 \right] P_2^2 e^{2i\lambda} \\ \left[ \left(\frac{b}{r}\right)^3 - \frac{4}{5} \left(\frac{b}{r}\right)^4 \right] \frac{dP_2^2}{d\vartheta} e^{2i\lambda} \\ \left[ \left(\frac{b}{r}\right)^3 \cos^2 \vartheta - \frac{4}{5} \left(\frac{b}{r}\right)^4 \right] \frac{2i}{\sin \vartheta} P_2^2 e^{2i\lambda} \end{pmatrix}, & r \geq b \\ \frac{i\mu_0 J_0 b}{20\sqrt{3}} \begin{pmatrix} 2 \left(\frac{r}{b}\right) P_2^2 e^{2i\lambda} \\ \left(\frac{r}{b}\right) \frac{dP_2^2}{d\vartheta} e^{2i\lambda} \\ \left(\frac{r}{b}\right) \frac{2i}{\sin \vartheta} P_2^2 e^{2i\lambda} \end{pmatrix}, & r < b \end{cases} \quad (2.26)$$

where  $\mathbf{B}_1$  is a particular solution of  $\text{curl } \mathbf{B}_1 = \mu_0 \mathbf{J}$  and  $V_1$  is chosen so as to guarantee the boundary conditions at  $r = b$  (continuity of  $B_r$  and  $B_\vartheta$ , jump of  $B_\lambda$  as given by  $\mathbf{K}$ ).

Eq. (2.26) can be verified by decomposing the current density of eqs. (2.25) and (2.24) into toroidal and poloidal parts according to eqs. (2.10) and (2.12) with reference radius  $R = b$ . It turns out that the only non-vanishing expansion coefficients are  $\phi_3^2$  and  $q_2^2$ :

$$\phi_3^2(r) = \begin{cases} \frac{\mu_0 J_0 b}{6\sqrt{15}} \left(\frac{b}{r}\right)^3, & r \geq b \\ 0, & r < b \end{cases} \quad (2.27)$$

$$q_2^2(r) = \begin{cases} \frac{-i\mu_0 J_0 b}{3\sqrt{3}} \left[ \left(\frac{b}{r}\right)^4 - \frac{b}{2} \delta(r - b) \right], & r \geq b \\ 0, & r < b. \end{cases} \quad (2.28)$$

The poloidal scalar  $\Phi$  changes discontinuously at  $r = b$ , which leads to a horizontal sheet current density ( $K_\vartheta, K_\lambda$ ) at  $r = b$ , while the  $\lambda$ -component of the total sheet current vanishes due to the contribution of the toroidal part, cf. the delta function in eq. (2.28).

Integrating eq. (2.28) according to eq. (2.16) yields

$$\psi_2^2(r) = \begin{cases} \frac{-i\mu_0 J_0 b}{12\sqrt{3}} \left[ \left(\frac{b}{r}\right)^2 - \frac{6}{5} \left(\frac{b}{r}\right)^3 \right], & r \geq b \\ \frac{+i\mu_0 J_0 b}{60\sqrt{3}} \left(\frac{r}{b}\right)^2, & r < b. \end{cases} \quad (2.29)$$

The resulting magnetic field, determined via eqs. (2.13), (2.27) and (2.29), is identical to that of eq. (2.26), as expected. In the current-free region  $r < b$ , the magnetic field is a Laplacian potential field  $\mathbf{B} = -\text{grad } V$  with  $V = b\epsilon_2^2(r/b)^2 P_2^2 \exp(2i\lambda)$  and  $\epsilon_2^2 = -i\mu_0 J_0 b / (20\sqrt{3})$  according to eq. (2.20). Both methods were applied to the current system defined by eq. (2.25), and found to be in good agreement with the analytical solution for the magnetic field given by eq. (2.26).

### Comparison between the two methods applied to MHD- model output

The two methods were tested against each other on the 3-dimensional current distribution from a global MHD simulation provided by the CCMC for the first model run. Figure 2.14 shows the magnetic field computed from the two methods at *Swarm* altitudes. Apart from a small deviation in  $B_\vartheta$  close to the pole, the overall agreement is excellent. Since the two methods were developed independently and are based on completely different numerical schemes, this provides a very strong validation of both algorithms.

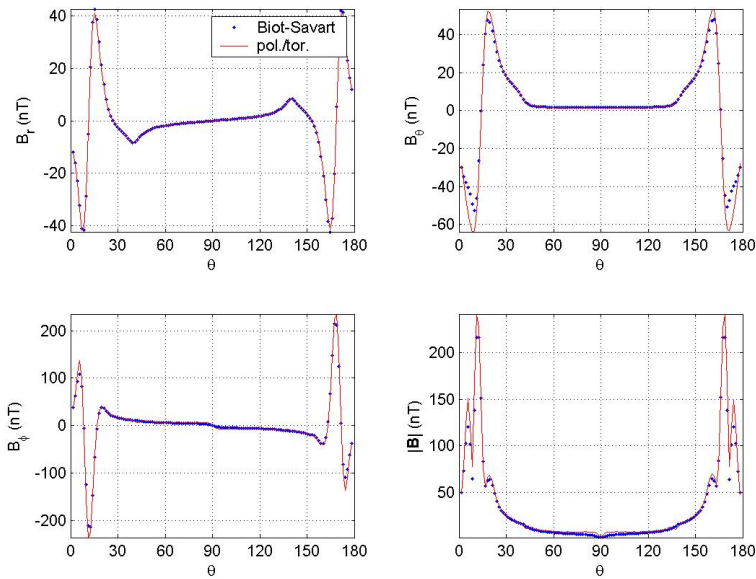


Figure 2.14: The magnetic field estimated by the two methods at time 000000 of the first CCMC run at *Swarm* altitudes as a function of north polar distance  $\vartheta$ .

The computation times used by the two methods are dramatically different. While it takes only a few minutes to compute the magnetic field on the spherical grid for a given 3D-current distribution using the poloidal–toroidal decomposition, it takes many hours using the Biot–Savart integration. Consequently, it was decided to use the poloidal–toroidal decomposition algorithm for the data processing. The Biot–Savart algorithm, on the other hand, is used for testing and for estimating the relative contributions from individual parts of the 3D-current system.

The estimated magnetic fields are delivered in the same binary data format as the input currents.

### Test of consistency with Amperes law

The estimated magnetic fields were tested for consistency with Amperes law (cf. eq. (2.7)). The rotation of the estimated magnetic fields where computed numerically at each grid point, and the results were compared with the input currents. As can be seen from Figure 2.15 the agreement was satisfactory. The rms of the difference between the input currents and the currents computed from the magnetic field through Amperes law amounts to  $0.14 \cdot 10^{(-7)}$  A/m<sup>2</sup>.

### 2.4.5 Products

The tools and products developed under this part of the study are summarized in Table 2.3.

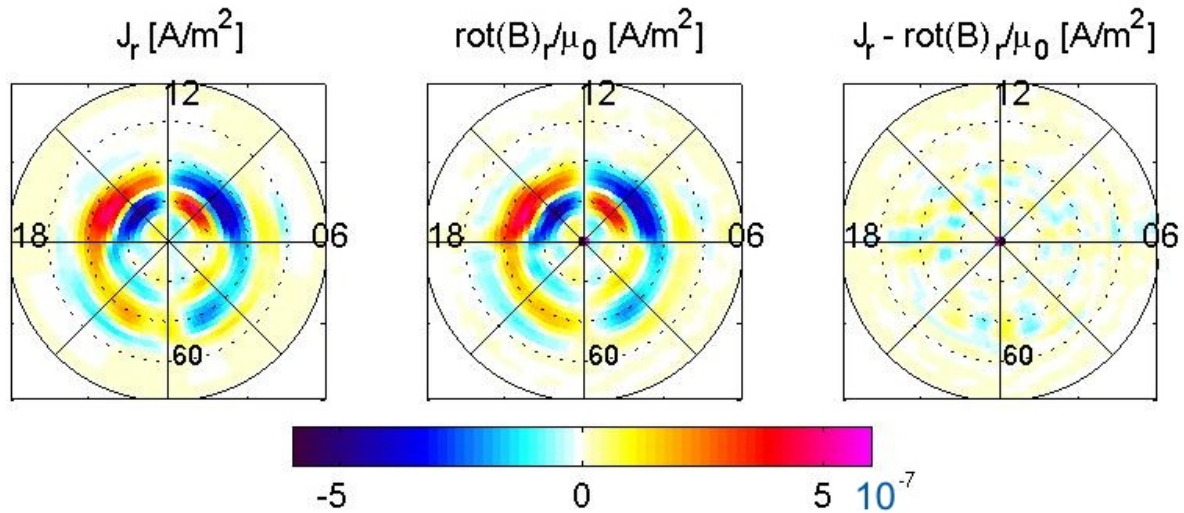


Figure 2.15:

Product	Description	Implementation	Use
Magnetic Field Algorithm Poloidal– Toroidal Decomposition	Calculates the magnetic field on the specified grid	DSRI	Selected for data-processing of the three CCMC-runs
Magnetic Field Algorithm Biot–Savart	Calculates the magnetic field on the specified grid	DSRI	Validation and analysis of individual current systems
Test Magnetic Fields	Calculates analytical solution for special example	DSRI	Validation
Test Amperes Law	Verifies that the rotation of the magnetic field fulfills Amperes law	DSRI	Validation
Output Data	Binary files containing estimated currents and B-field on a spherical grid up to 600 km altitude	DSRI	Task 1 Data product

Table 2.3:

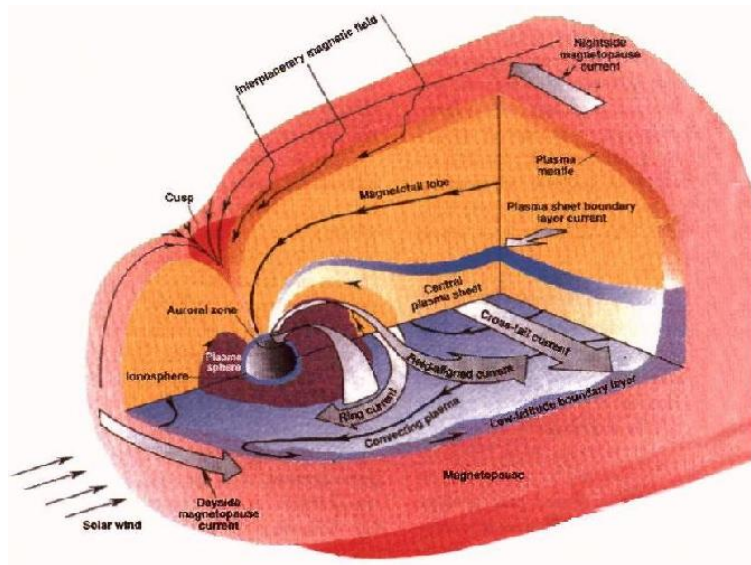


Figure 2.16: Schematic illustrating the various magnetospheric current systems.

## 2.5 Results of the Forward Modelling

The external currents that are generated in the interaction between the solar wind and the Earth's magnetosphere and ionosphere are the combination of a number of different current systems, including magnetopause currents, tail current, ring-current, field-aligned currents (FAC) and ionospheric current. The typical locations of these currents are illustrated schematically in Figure (2.16). Most of these current sources are included in the global MHD simulations, with the important exception of the ring current. The results of the study, that is the calculated current densities and magnetic field perturbations at *Swarm* altitudes are here presented by a number of illustrative examples.

### 2.5.1 The Main Contributions - Ionospheric and Field-Aligned Currents

At *Swarm* altitudes, the magnetic perturbations from the high latitude ionospheric and field-aligned currents are by far the largest of the external contributions to the magnetic field measurements. Figure (2.17) illustrates the calculated horizontal and field-aligned currents in the polar region at three times during the first simulation. The Figure shows the northern polar ionosphere seen from above in a (latitude-local time)-coordinate system centered on the geomagnetic pole. The three times are at the start of the run when IMF  $B_Z$  is significantly positive, at a time when it is slightly positive and at a time when it is slightly negative. It is clearly seen how the character of the current system changes from intense but localized currents in the near-pole region, to a more distributed current system with more intense currents at lower latitudes. The former currents are the so-called northward IMF  $B_Z$  (NBZ) currents, which are driven by reconnection between the IMF and magnetospheric field lines poleward of the cusp-region. The latter distribution, meanwhile, corresponds to build-up of the region 1 currents associated with reconnection near the subsolar magnetopause.

Figure (2.18) shows the resulting perturbations in the magnetic field, computed at the altitude of 300 km. During the course of the simulation, the perturbations clearly develop from being localized in the dayside near-pole region, to a stronger and more distributed system with

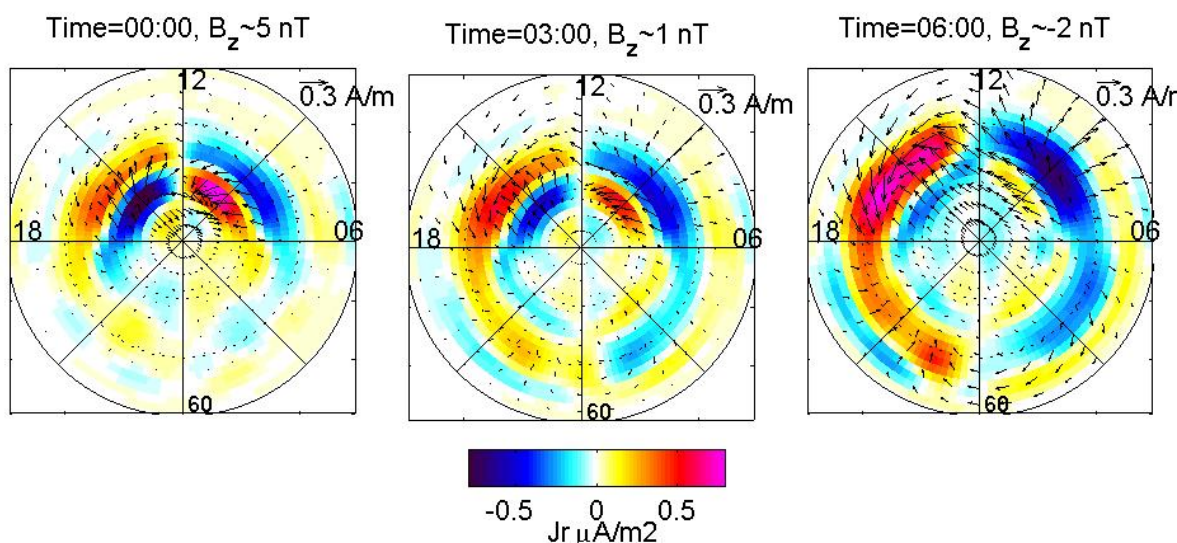


Figure 2.17: Horizontal ionospheric current densities (arrows) and vertical ionospheric current densities (colorscale) at three selected times during the first run.

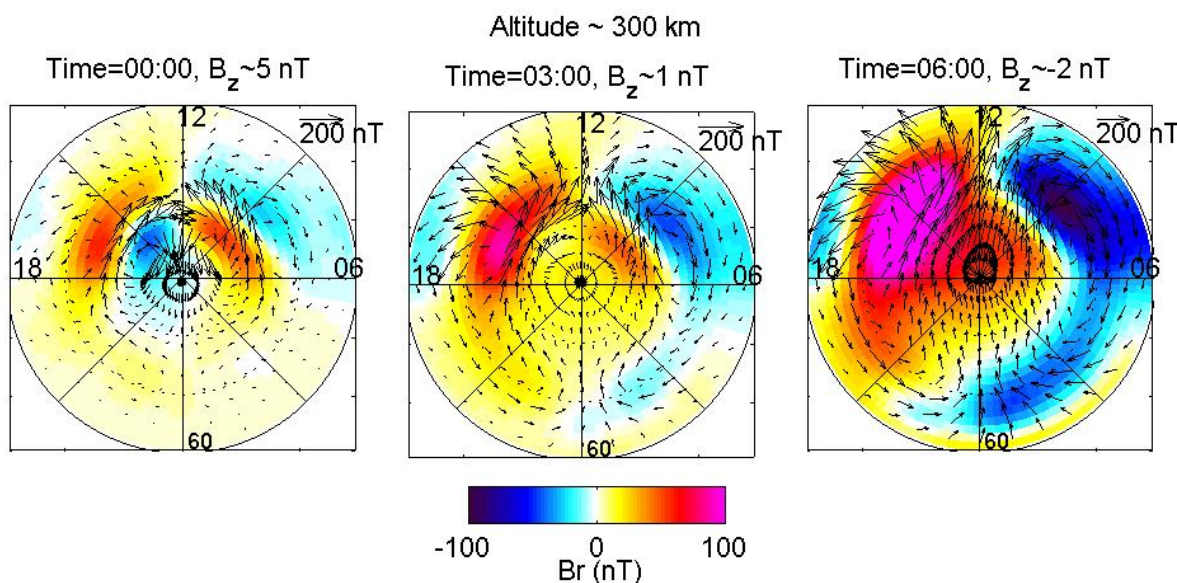


Figure 2.18: Magnetic perturbations (in nT) at 300 km's altitude due to the ionospheric and field-aligned currents shown in Figure (2.17)

significant perturbations also on the night-side. Throughout the three snapshots all three components of the magnetic field increase significantly in the auroral region at magnetic latitudes roughly below  $75^\circ$ . In the near-pole region, on the other hand, the character of the perturbations completely changes from rather complex to relatively simple during the course of the event.

Figure (2.19) is similar to Figure (2.18) but is calculated at 600 km's altitude. As expected,

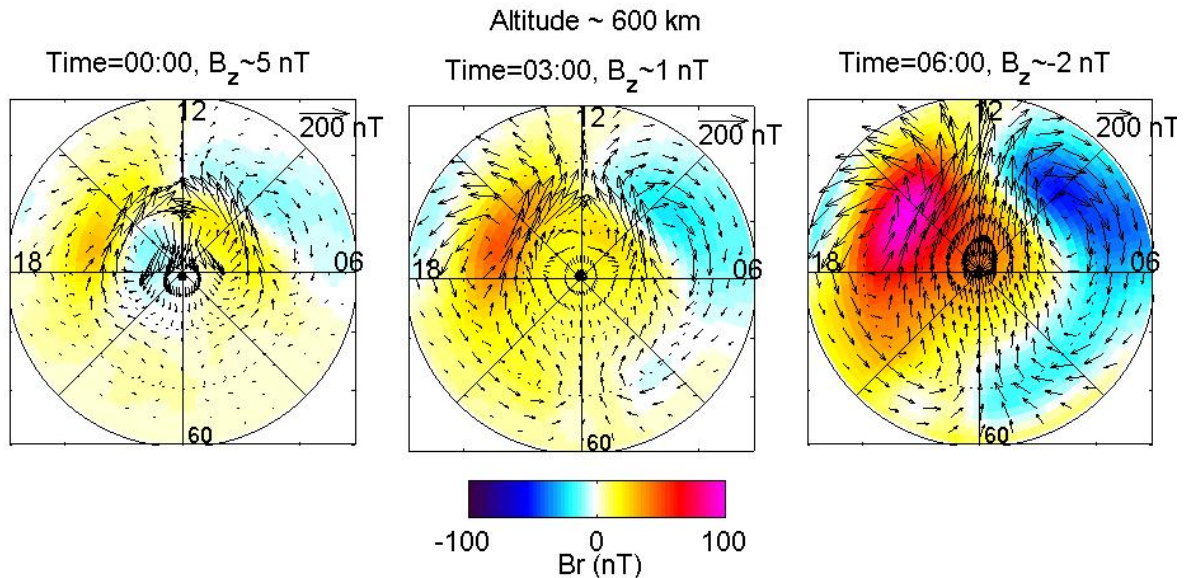


Figure 2.19: Magnetic perturbation (in nT) in 600 km's altitude due to the ionospheric and field-aligned currents shown in Figure (2.17)

the radial component  $B_r$  undergoes the most dramatic change, exhibiting a reduction of almost 50%.

Figure (2.20) shows the simultaneous horizontal electric fields (arrows) and the electric field intensity. For the polar region seen as an entity it is clear that there is a close correlation between the magnetic field disturbance and the electric field at satellite altitudes. For positive IMF  $B_z$  both the electric fields and the magnetic disturbance are confined to the near-pole region, while both becomes much more distributed when the IMF  $B_z$  is negative. In addition the electric field in the polar cap reverse direction. It should therefore be possible to distinguish between the two types of current systems based on the electric field measurements from a single satellite pass. It should however be noted that the significant variations in ionospheric conductivity makes a direct translation from the locally measured electric field to the magnetic disturbance quite difficult.

The ionospheric and field-aligned currents generated by the model are restricted to the polar regions. However, due to the intensity of the ionospheric currents and the large-scale nature of the FACs, some signal also penetrates to lower latitudes. To give an impression of the size of this effect, Figure (2.21) shows the intensity of each of the three magnetic field components in the northern hemisphere low latitude region. The three components are shown for the same three times during run 1 that was used for the earlier figures in this section. It should be noted, that due to a not quite realistic modeling of the region 2 currents, which are expected to grow for increasing negative IMF  $B_z$  and which are expected to have a shielding effect, the magnitude of the disturbances in the lower panels, likely, are not completely realistic.

### Seasonal variations

Due to the dominant contribution from solar EUV radiation, the ionospheric conductivity in the polar regions changes dramatically from summer to winter. In addition, the magnetospheric reconnection processes are more efficient in the hemisphere tilted towards the sun (for positive

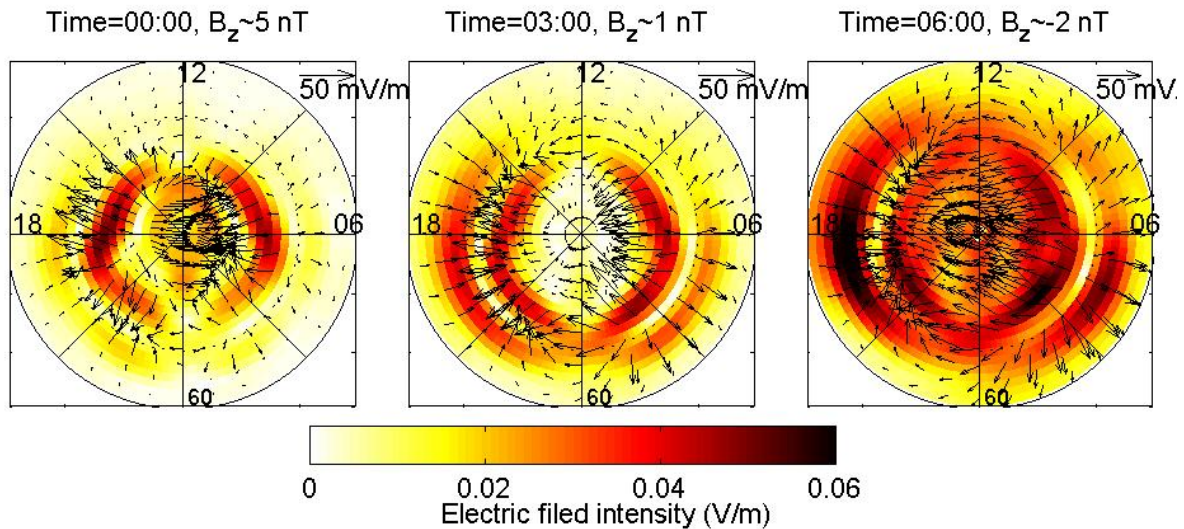


Figure 2.20: Horizontal electric fields (arrows) and electric field intensity (colorscale) in 600 km's altitude corresponding to the ionospheric and field-aligned currents shown in Figure (2.17).

IMF  $B_Z$ ). Figure (2.22) illustrates this effect by comparing the ionospheric and field-aligned currents for conditions with significant northward IMF  $B_Z$  component during summer, equinox and winter (time 00:00 in run 1 and run 2), respectively. It is evident that seasonal variations are substantial.

### Real event simulation

The day March 9, 2002 was selected for a real event simulation, because it contains both very quiet and moderately disturbed intervals, as measured by the global geomagnetic activity index  $K_p$ . In addition, the IMF  $B_Y$  and  $B_Z$  components both attain both positive and slightly negative values during the course of the day. The dipole tilt in the X-Z plane for this run is kept at  $-16.1^\circ$  and, consequently, we observe significant differences between the currents and magnetic perturbations in the two hemispheres. Figures (2.23) and (2.24) show the ionospheric current densities and the corresponding magnetic perturbations at 450 km altitude. The top panels show the northern hemisphere and the bottom panels the southern hemisphere. The patterns are shown for three selected snapshots during the time interval of the simulation. The main difference between this run and the former ones is the presence of a significant IMF  $B_Y$  component. The most obvious effect of this is that it creates a strong dawn-dusk asymmetry. Since an IMF  $B_Y$  component of at least 3 nT is by far the most commonly observed condition for the IMF, this definitely is a more realistic condition than the IMF  $B_Y = 0$  that was used in run 1. The three selected times were chosen to illustrate the kind of time-variations that can be realistically expected.

### 2.5.2 The Contributions From the Distant Magnetosphere

The contribution from the distant magnetosphere is dominated by two current systems, the magnetopause currents, which are most intense on the dayside, and the cross tail current in the center of the magnetospheric tail. Figure 2.25 shows the contribution from these currents

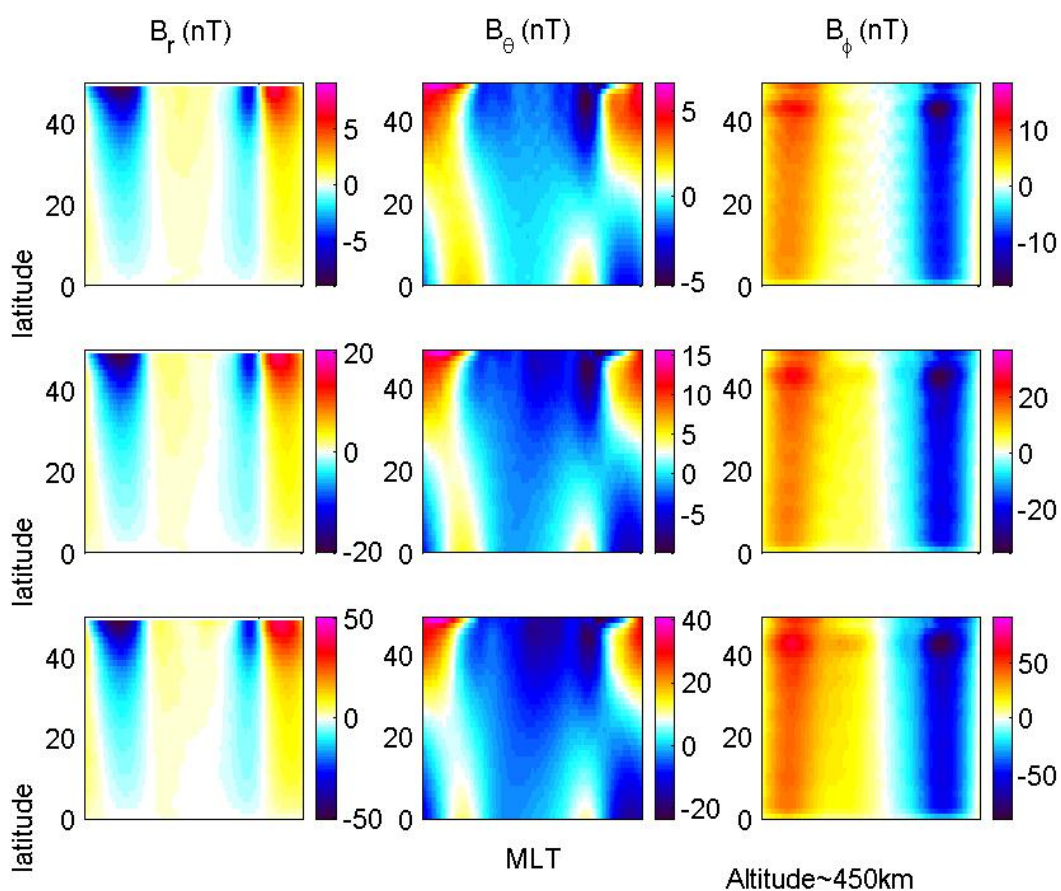


Figure 2.21: Magnetic perturbation (in nT) as a function of local time and latitude at mid- and low latitudes in the northern hemisphere. Note that the color-scale varies from panel to panel. Midnight is at the center of each panel. The result are for the three selected times of run 1. (2.17)

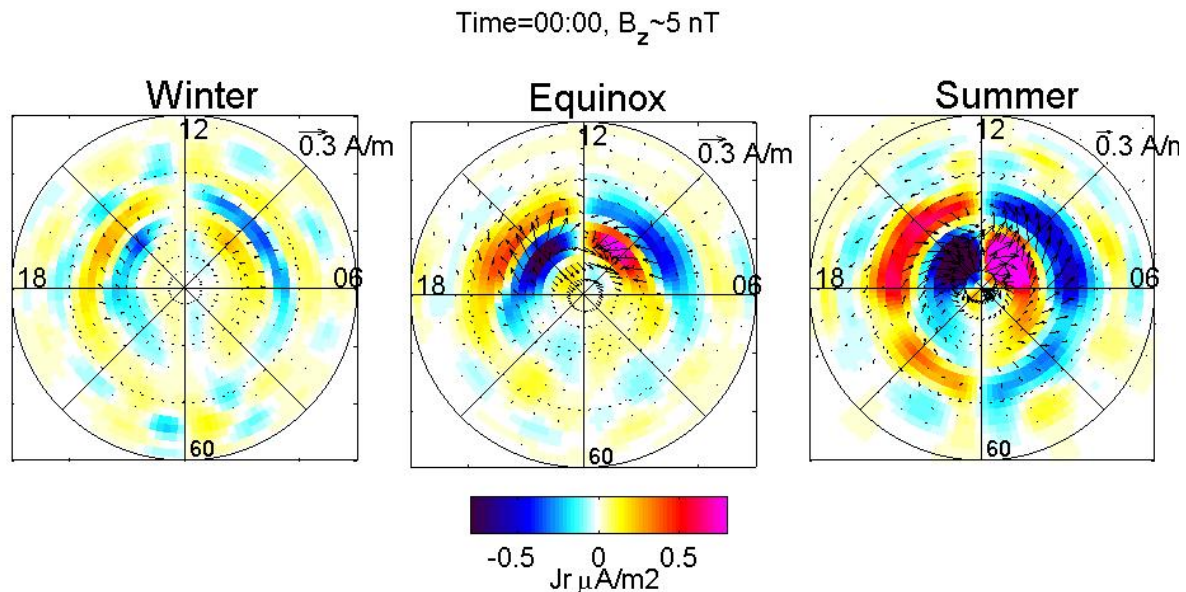


Figure 2.22: Horizontal and vertical currents in the ionosphere, for the three different seasons. Note that the horizontal scale changes from frame to frame, while the colorscale is constant.

as a function of local time and angular distance to the north pole. The computation was based on output from the first simulation run at a time when the IMF  $B_z$  was significantly positive. The largest contribution is observed in the  $B_r$  and  $B_\theta$ -component on the nightside and originates mainly from the tail. On the dayside the sign reverses due to the contribution from the Chapman Ferraro currents on the day-side magnetopause. When the IMF  $B_z$  turns negative the tail will be stretched, and the cross-tail current intensifies correspondingly, but also the Chapman Ferraro currents intensify, particularly in the subsolar region. The resulting magnetic perturbations are shown in Figure 2.26, computed on the basis of the current-densities at the end of run 1.

## 2.6 Comparison with observations

In order to investigate to which extent the simulated data compares with reality, we have compared the real event simulation results with Ørsted and CHAMP observations. Figures 2.27-2.29 show the simulated field-aligned currents and the corresponding simulated horizontal magnetic perturbation at satellite altitude together with the observed horizontal perturbation at satellite altitude. Figures (2.27) and (2.28) show passes of respectively CHAMP and Ørsted over the northern hemisphere dayside. We find a very good correspondence between model and observations. Note however, that the modeled field-aligned currents are located slightly more equatorward than observed. This difference is found at all the satellite crossings throughout the event.

Figure (2.29) shows a pass of CHAMP over the southern hemisphere night-side. Here the modeled and observed data compare less well. In the CCMC implementation of the MHD model the dipole tilt is kept fixed throughout the run at the value it had at the beginning of the run. Due to the large dipole-tilt in the beginning of the event at 6 UT the ionospheric conductivity in the southern hemisphere is significantly larger than in the northern hemisphere. Consequently the modeled field-aligned currents and the associated magnetic perturbation is also significantly

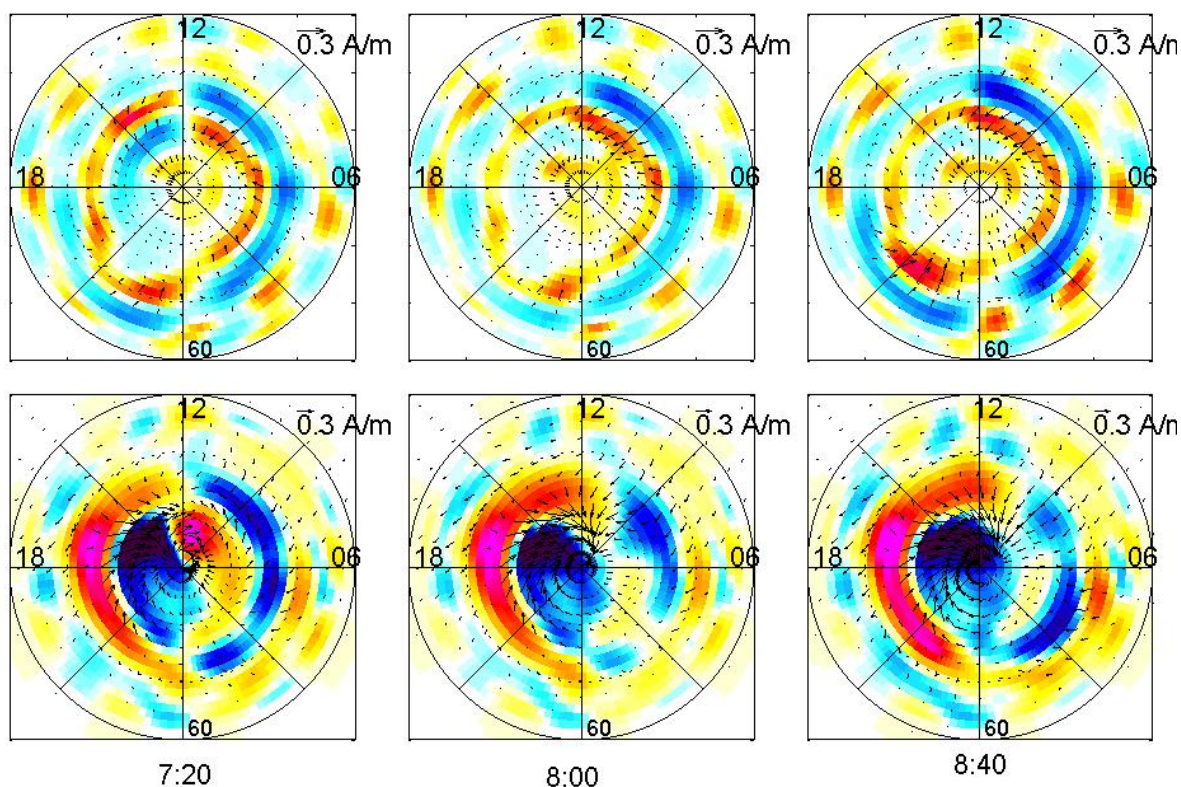


Figure 2.23: Horizontal and vertical currents in the ionosphere, for three selected times during the real event simulation. Note that the horizontal scale changes from frame to frame, while the colorscale is constant and the same as in the previous figures of this section. The top panel is for the northern hemisphere, and the bottom panel is for the southern hemisphere.

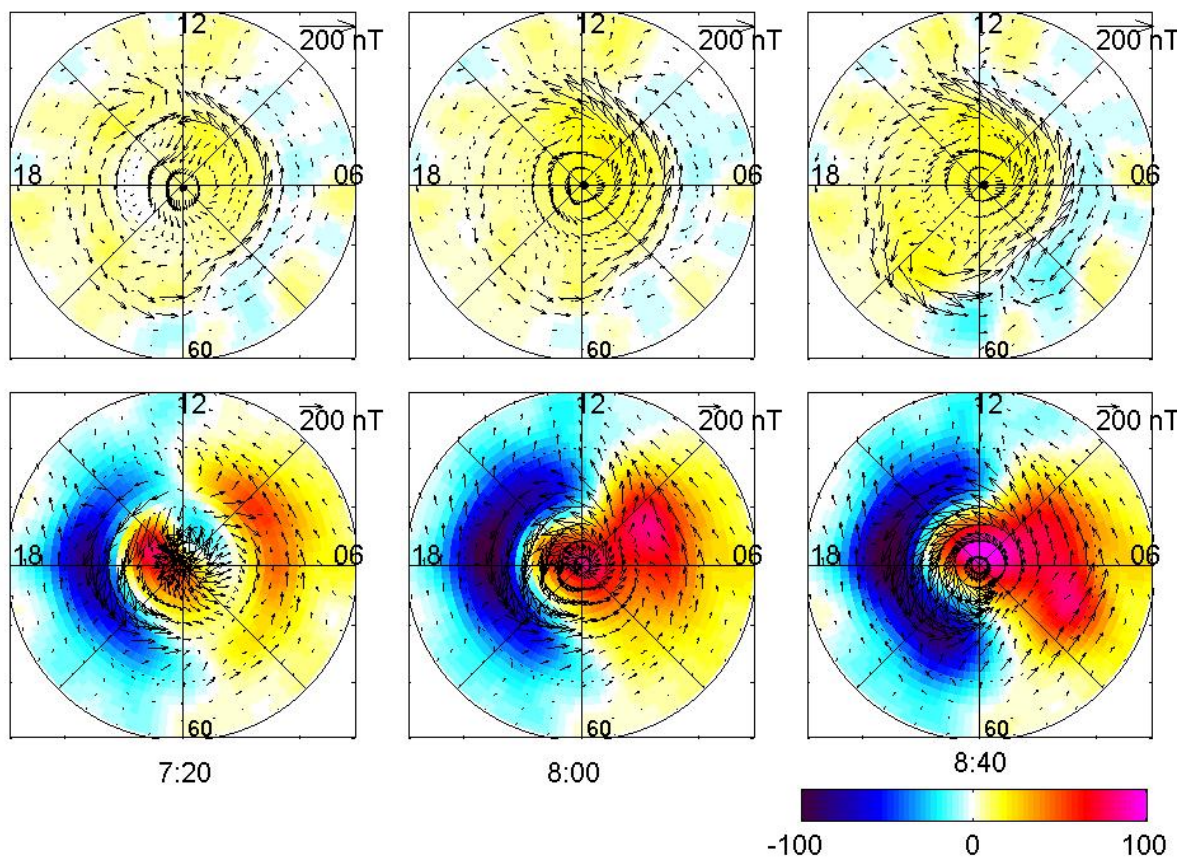


Figure 2.24: Magnetic perturbations at the altitude 450 km, calculated on the basis of the current densities displayed at Figure 2.23. Note that the horizontal scale changes from panel to panel, while the vertical scale remains constant.

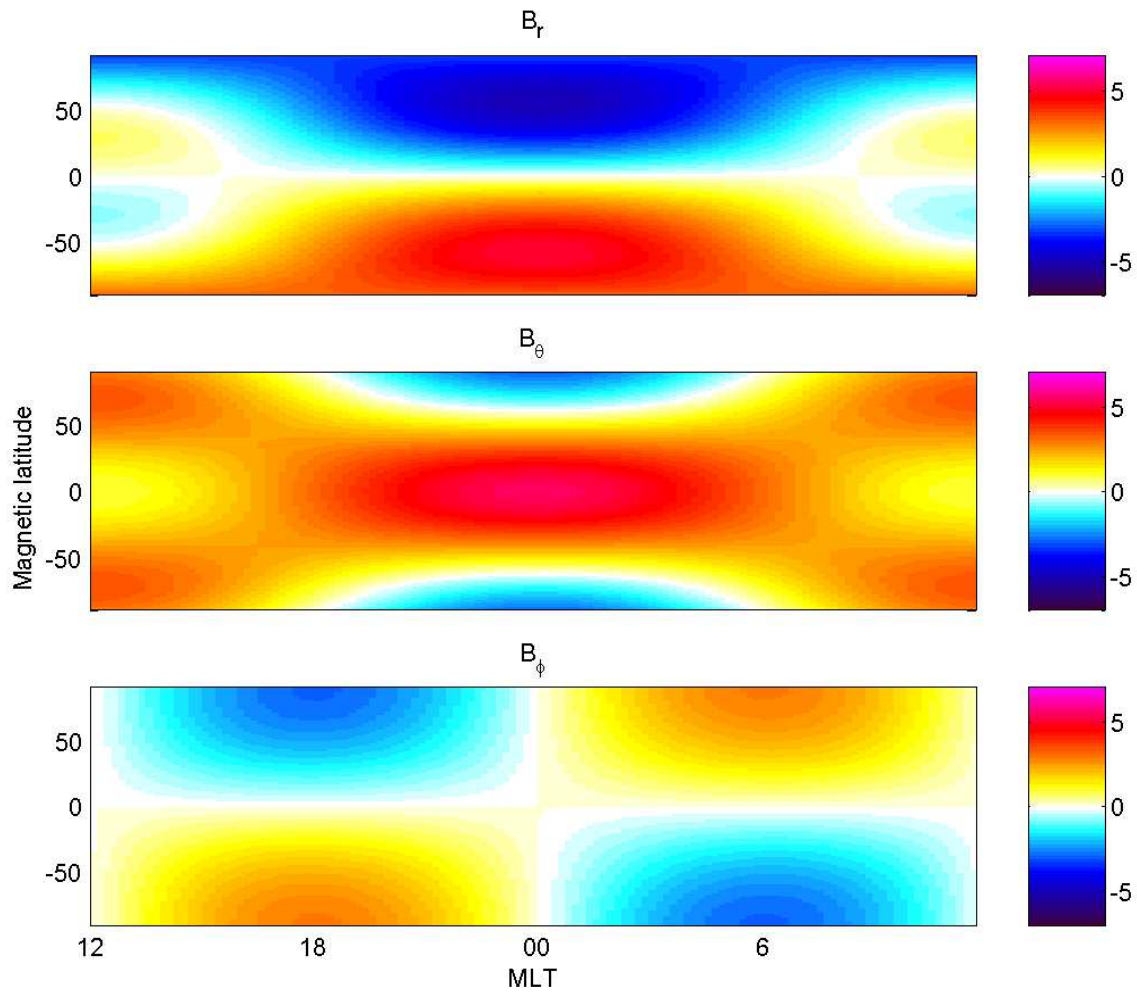


Figure 2.25: Magnetic perturbation (in nT) due to the simulated currents in the distant magnetosphere. The diagrams are (local time, north polar distance) and midnight is in the center of each diagram. The perturbations are calculated based on the currents of run1 at the time 00:00 when IMF  $B_z$  is significantly positive.

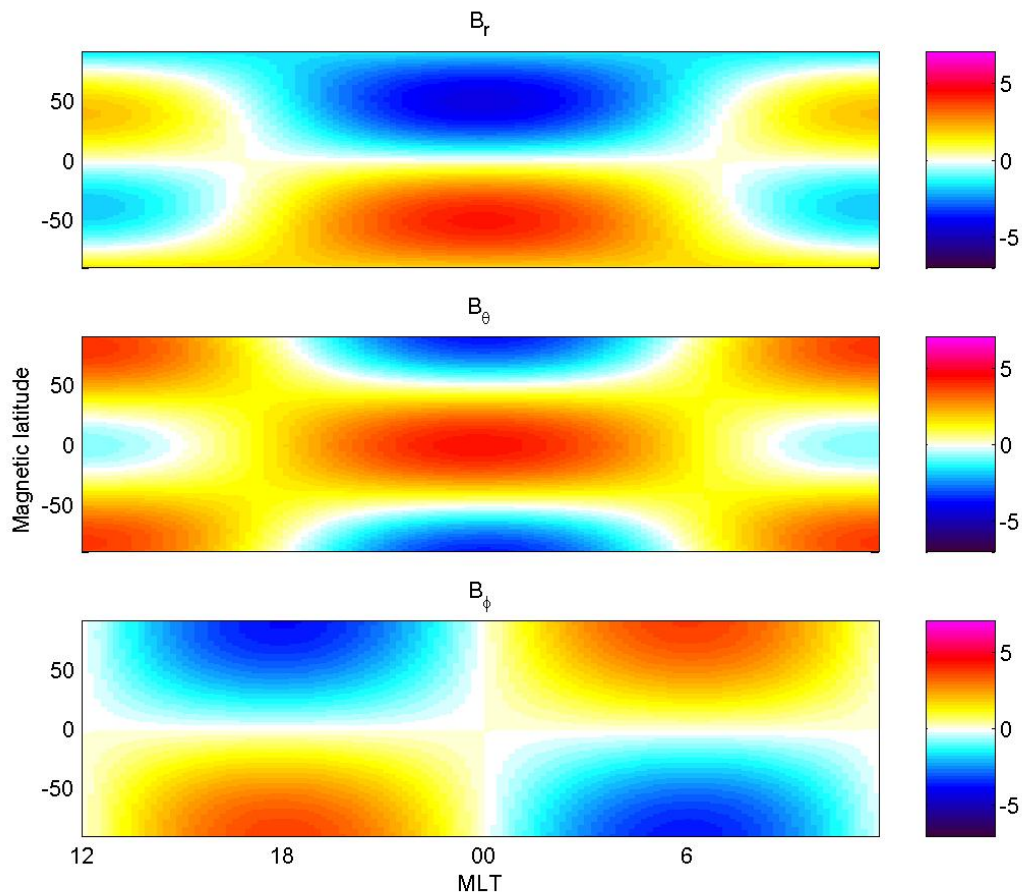


Figure 2.26: As Figure 2.25, but based on the currents of run 1 at the time 06:00 when IMF  $B_z$  is negative.

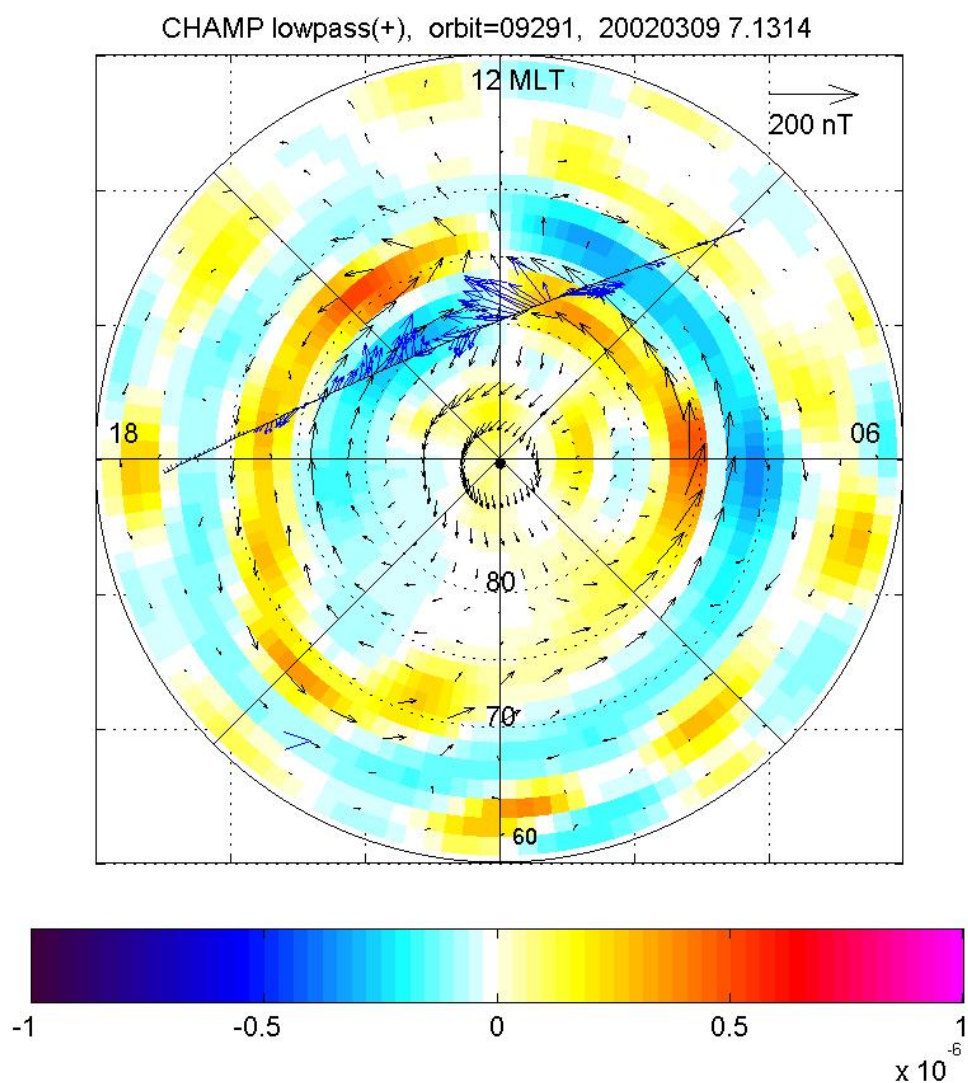


Figure 2.27: Horizontal magnetic perturbations measured by the CHAMP satellite (blue arrows), during a pass over the northern hemisphere polar region, compared with the simulated magnetic perturbations (black arrows). The colorscale shows the simulated field-aligned current intensity.

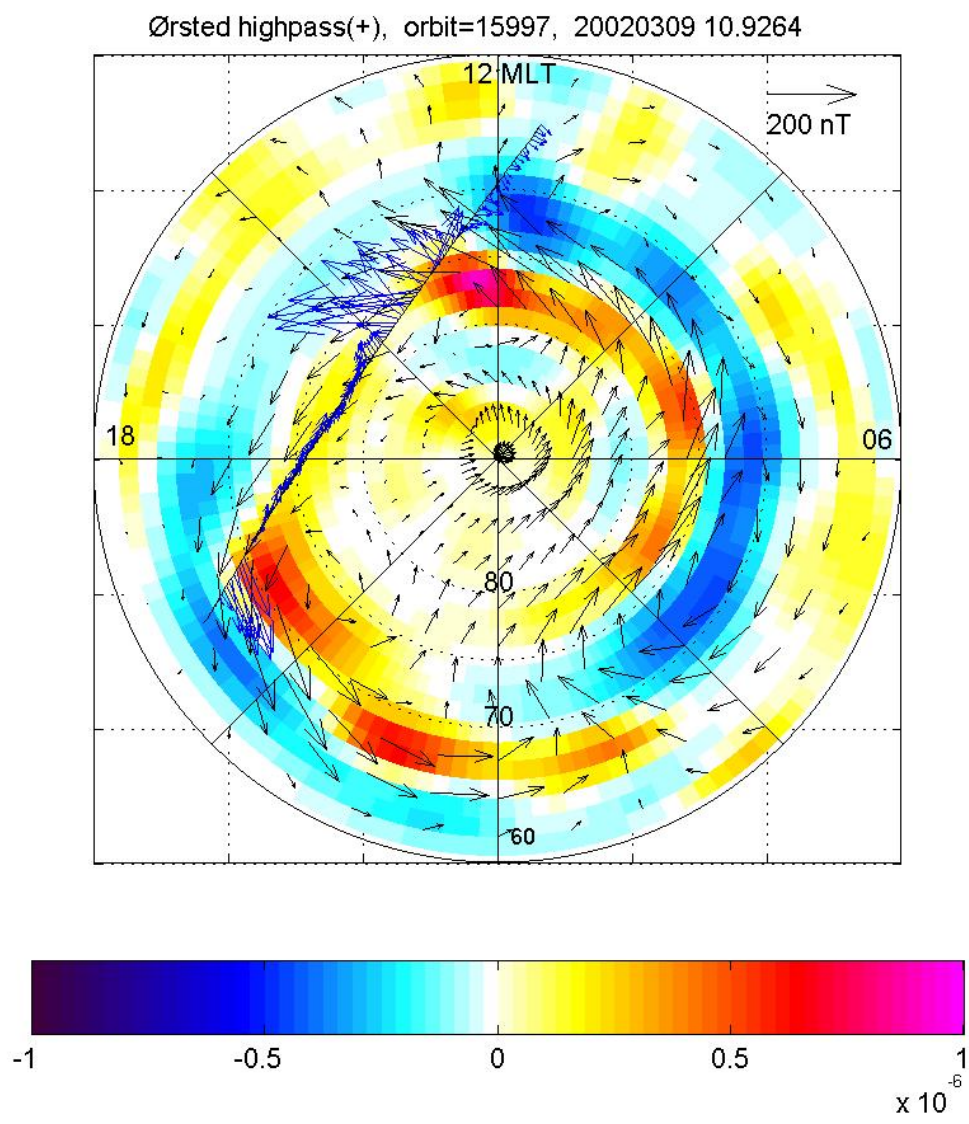


Figure 2.28: Horizontal magnetic perturbations measured by the CHAMP satellite (blue arrows), during a pass over the northern hemisphere polar region, compared with the simulated magnetic perturbations (black arrows). The colorscale shows the simulated field-aligned current intensity.

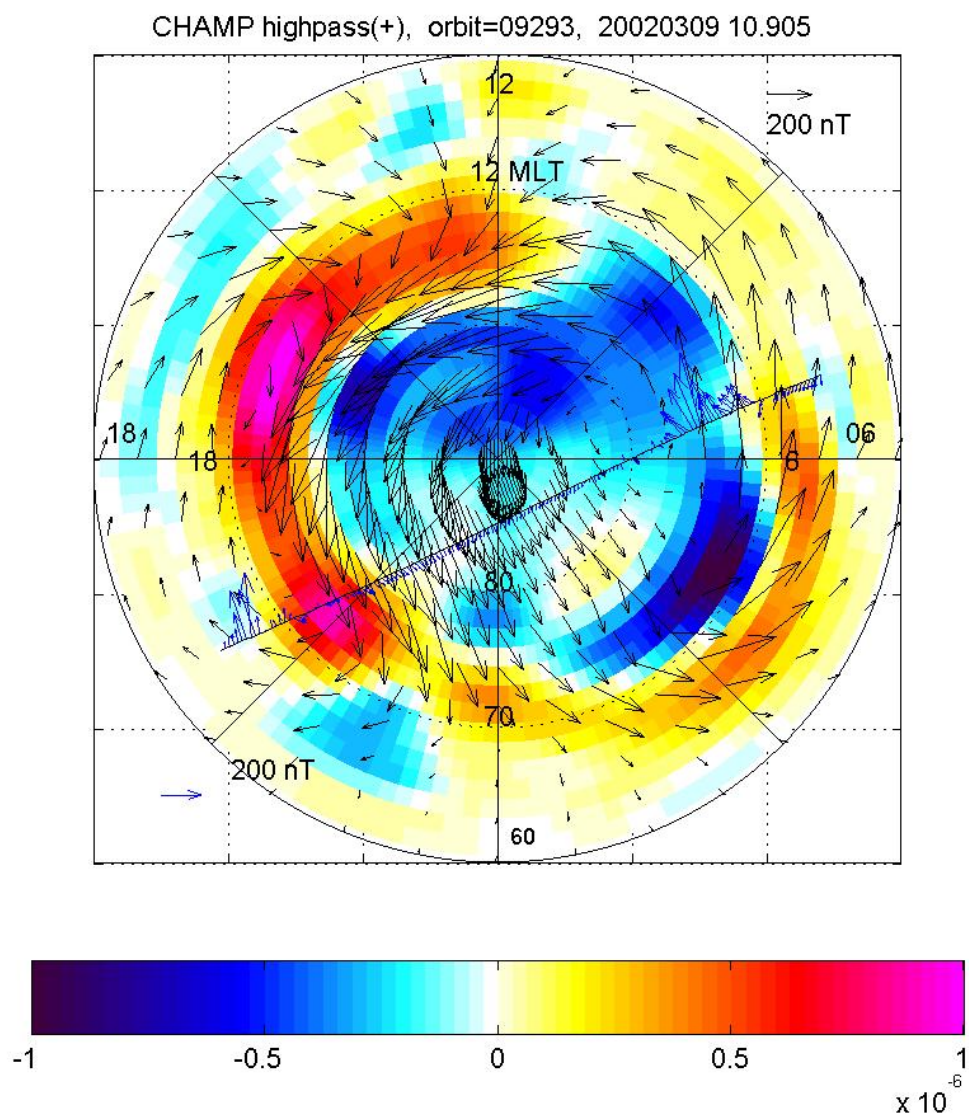
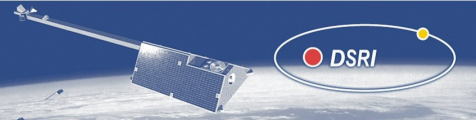


Figure 2.29: Horizontal magnetic perturbations measured by the CHAMP satellite (blue arrows), during a pass over the northern hemisphere polar region, compared with the simulated magnetic perturbations (black arrows). The colorscale shows the simulated field-aligned current intensity.

larger in the southern hemisphere (note the change of scale of the black arrows). The comparison with the observations in the central polar region shows that this hemispherical asymmetry is not realistic at the time of the pass at 10:50 UT. An update of the dipole-tilt during the simulation would most likely yield an improvement.



## 2.7 Summary and conclusions of the forward modeling

- We have developed and implemented an algorithm for fast computation of the magnetic field due to a general 3-D distribution of current density on a spherical grid.
- The algorithm has been tested against another method of calculation and against an analytical solution.
- We have selected three sets of solar wind variations and season, relevant for modeling of geomagnetic quiet and moderately disturbed conditions, and performed three corresponding runs of a state-of-the-art model of solar wind - magnetosphere - ionosphere interaction. For each time instant in each run, we have calculated the 3D-distribution of current and on the basis of this the magnetic and electric fields at *Swarm* altitudes.
- For a real event simulation we have compared the simulated magnetic fields with CHAMP and Ørsted data with good results. An update of the dipole tilt-angle during the course of the simulation, however, most likely will yield an improvement.
- As expected the field-aligned and ionospheric currents provide the main contribution to the magnetic field perturbation at *Swarm* altitudes, but also the Chapman-Ferraro and tail currents provide a significant disturbance. In particular, it has been found that the intensity of the large-scale magnetic field disturbance due to these magnetospheric currents varies considerably with the IMF  $B_z$ .
- Due to the highly variable ionospheric conductivity there is no one-to-one correspondence between the electric field and the magnetic field disturbance, however quiet intervals can be distinguished by the global pattern (in the polar region) of both fields.

## 2.8 Retrieval of Ionospheric Currents. Physical interpretation and assumptions

Before starting to retrieve ionospheric currents from the synthetic electric and magnetic field data it is useful to outline the physical properties of these input data. The understanding of the data is required for a proper assessment of the results derived.

The electrical conductivity of the ionosphere is highly anisotropic. The resistivity along the field lines can be regarded as negligible. Therefore the magnetic field lines are treated as equipotential lines and no electric field parallel to  $\mathbf{B}$  exists. E-fields measured by a satellite can be mapped up or down to any altitude. An appreciable conductivity perpendicular to the B-field exists only in the ionospheric E-layer which has a thickness of some tens of kilometres. The two possible components in this layer are split up into the Hall and Pedersen conductivity. Since the transverse currents are limited to a fairly thin layer, it is not possible to resolve the altitude distribution from remote observations. For that reason, it is common practice to use height-integrated quantities for the conductivities and currents. They are represented by capital letters ( $\Sigma_H, \Sigma_P$ : Hall and Pedersen conductance;  $\mathbf{J}_H, \mathbf{J}_P$ : Hall and Pedersen sheet current density).

These currents can be calculated as follows

$$\mathbf{J}_P = \Sigma_P \mathbf{E}_\perp, \quad \mathbf{J}_H = \Sigma_H \frac{\mathbf{B} \times \mathbf{E}}{|\mathbf{B}|} \quad (2.30)$$

For completeness it may be mentioned here that only Pedersen currents, flowing along the electric field, contribute to atmospheric heating. In case of the other two current components the dot product with the electric field representing the Joule heating vanishes.

From current continuity considerations it follows that the divergence of the sheet currents has to be balanced by field-aligned currents,  $j_\parallel$ , flowing into or out of the sheet.

$$\nabla_{hor} \cdot (\mathbf{J}_P + \mathbf{J}_H) = -j_\parallel \cdot \sin I \quad (2.31)$$

Inserting (2.30) into (2.31) and considering negligible conductivity gradients we may write

$$\nabla_{hor} \cdot (\Sigma_P \mathbf{E}_{hor}) = -j_\parallel \cdot \sin I \quad (2.32)$$

where  $I$  is the local inclination of the magnetic field,

$$\tan I = \frac{B_r}{B_\theta} = \frac{1}{2 \tan \theta}$$

and  $\theta$  is the magnetic colatitude.

Under these conditions field-aligned currents are closed exclusively by Pedersen currents in the ionosphere. Hall currents, on the other hand, close entirely in the ionosphere. Regarding the magnetic fields caused by these currents, we may state that Hall currents give rise to poloidal fields and the field-aligned plus Pedersen current circuit generates toroidal fields. We will make use of these features in the later steps when estimating the various current components.

The representation of the synthetic data set is not linked directly to the physical nature of the current system, rather it is guided by geometrical considerations. According to equation 2.2 the potential distribution in the sheet-like ionospheric E-layer is determined from the radial current components flowing into and out of this shell. Together with a model of the conductance this allows to estimate the horizontal components of the electric field in the sheet.

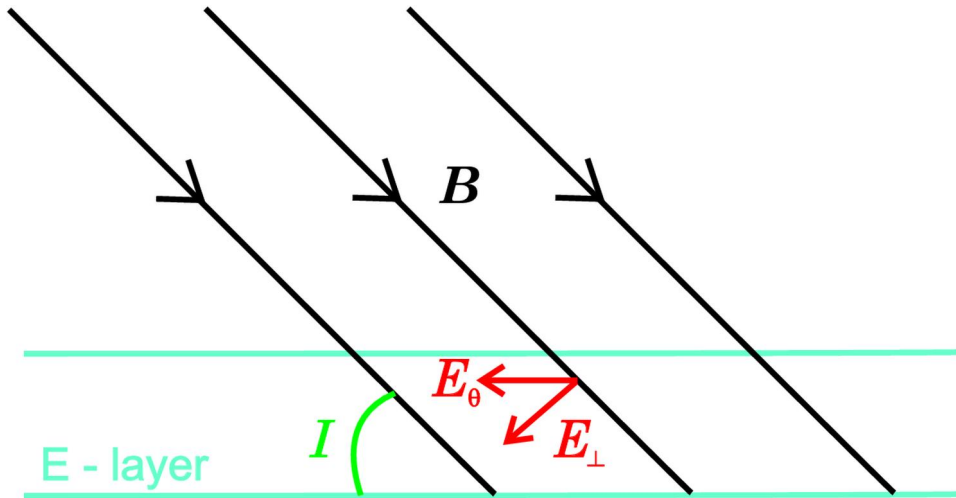


Figure 2.30: Field configuration in the ionospheric E-layer.

The electric field, which can be downloaded from the CCMC web-interface, gives the horizontal field components in the current sheet. For the representation Geocentric-Solar-Magnetospheric (SM) coordinates are used (for definition see Sect. 1.6). For convenience we have transformed them into spherical coordinates with  $E_\theta$  and  $E_\phi$  in the SM frame.  $E_r$  is zero by design.

For the calculation of the Hall and Pedersen currents according to eq. (2.30) the electric field perpendicular to  $B$  rather than the horizontal components of the E-field are needed. In the SM centred dipole geometry used here we may write

$$\mathbf{E}_\perp = \begin{pmatrix} \frac{1}{\sin I} E_\theta \\ E_\phi \end{pmatrix} \quad (2.33)$$

Using eq. (2.30) and implying the conductance and electric field from the files mentioned above the model Hall and Pedersen currents can be computed.

The synthetic values for the current density and the magnetic field are contained in the files following the name convention `J+B.iof_yeardate_hhmmss.bin`. For altitudes above the ionospheric E-layer only field-aligned currents exist comprising components  $j_r, j_\theta$ . Here,  $j_\phi = 0$  by design. At the lowest level (at 90 km) these numbers represent horizontal sheet current densities,  $J_r$  and  $J_\theta$ , which are height-integrated over the E-layer. There is no radial current component at this level,  $J_r(90km) = 0$ .

A third type of data file, `E.iof_yeardate_hhmmss .bin`, contains the electric field at satellite level. The E-field is given in spherical components ( $E_r, E_\theta, E_\phi$ ) in a centred dipole, local time frame (hereafter referred to as Solar-Magnetic (SM)). By design only the components perpendicular to the magnetic dipole field are non-vanishing. These electric fields at satellite altitude can be used to estimate the E-field in the ionospheric E-layer.

## 2.9 Determination of the field-aligned currents

The basic equation for determining electric current density  $\mathbf{j}$  from magnetic field observations is Ampere's law

$$\text{curl } \mathbf{B} = \mu_0 \mathbf{j} \quad (2.34)$$

In the auroral region only field-aligned currents are expected at satellite altitude. Therefore only one component of  $\text{curl } \mathbf{B}$  is of importance

$$j_z = \frac{1}{\mu_0} \left( \frac{\partial B_y}{\partial x} - \frac{\partial B_x}{\partial y} \right) \quad (2.35)$$

where  $x, y, z$  are components of a local Cartesian coordinate system.

As can be seen from eq. (2.35), the spatial gradients are needed for deriving the current. The *Swarm* constellation with its closely spaced pair *SwA* and *SwB* provides a suitable set-up for this purpose. As shown in Figure 2.31, the two satellites are separated in east-west direction. Flying side-by-side they provide the cross-track gradient of  $B_x$ , while the difference of readings taken at two points in time ( $t_1$  and  $t_2$ ) are used as the along-track gradient of  $B_y$ . Combining these gradients allows to determine the current density  $j_z$  according to eq. (2.34) at the centre of the four measurement points (see Figure 2.31).

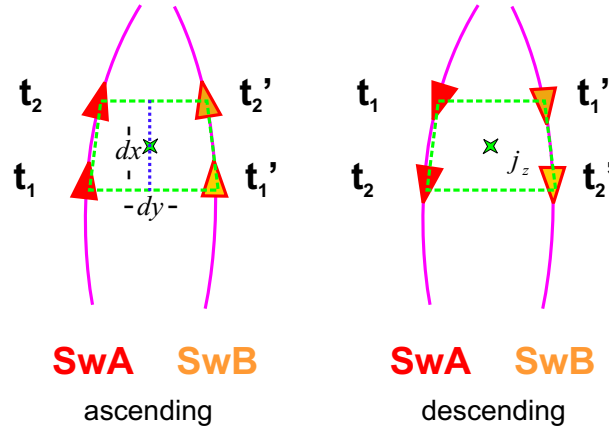


Figure 2.31: Schematic drawing of the orbit configuration for determining the radial currents.

In the following we describe the retrieval of the field-aligned current density in some details. The B-field in the synthetic data is given in a centred dipole coordinate system where longitude is related to the local time (SM). This frame is suited for presenting the ionospheric current systems. For the determination of the currents we make use of readings which are sampled along the orbits of the *Swarm* satellites. Orbit data for the initially four *Swarm* spacecraft were computed as part of the End-to-End Simulator Study (Olsen et al. [2004]). The position and velocity data are given in an Earth-fixed system (ITRF)(see Section A). For practical reasons it was decided to do all the calculations in the SM frame. Therefore the ephemerides are transformed into the dipole system using a geographic location of the dipole axis at  $78.68^\circ$  latitude and  $289.6^\circ$  longitude based on the dipole terms of a recent magnetic field model (e.g. Holme et al. [2003]).

In a real-world application one would prefer to do the current calculations in geocentric coordinates and transform the results into a suitable geomagnetic field system. The actual geomagnetic field contains significant higher degree terms beyond the dipole and thus the transformation into the Corrected Geomagnetic - Magnetic Local Time frame becomes non-orthogonal.

The curl  $\mathbf{B}$  operation is done in a local Cartesian frame called Velocity-Zenith (VZ) frame (see Section A). The origin is the midpoint between the four sampling positions shown in Figure 2.31. For this set-up the spacecraft *SwA* is selected as the reference satellite. The corresponding readings are taken from *SwB* at a time  $t'$ , when the positions of the spacecraft form a symmetric quad with the related positions of *SwA*. In our sample orbits the time difference between  $t$  and  $t'$  is 1.302 sec. Since the model activity changes gradually by 10nT in 8 h, this difference can be regarded negligible (0.0005nT). The  $x$  component of the VZ system is defined by the mean velocity vector of the two spacecraft,  $z$  points radially outward and the  $y$  component completes the triad.

The magnetic field given in the synthetic data set is the disturbance field caused by the currents. No geomagnetic main field has been added to it. Thus it can be used directly in the current retrieval. The B-field is given in spherical components  $(B_r, B_\theta, B_\phi)$  in the SM frame on a grid spaced by  $\Delta\theta = 1.4^\circ$ ,  $\Delta\phi = 2.8^\circ$  in latitude and longitude, respectively. The gridding in radial direction,  $\Delta r$ , assumes values ranging from 1 km to 50 km (increasing spacing) with  $r$  reaching from 90 km to 700 km. For the determination of the currents we interpolate the synthetic magnetic components linearly between the grid points along the orbits of the *Swarm* satellites to obtain a continuous, steady sampling with  $\Delta t = 5$ s. For convenience and in association to real applications the sampling rate was chosen to be uniform in the region of interest  $\pm 45^\circ$  around the poles.

The horizontal components  $(B_\theta, B_\phi)$  at both spacecraft are then rotated locally about the radial axis into the VZ frame giving  $B_x$  and  $B_y$ . This is done in two steps. First, the  $B_\theta$  component is rotated into the flight direction using the angle  $\alpha$ , which is calculated individually at the four sampling points

$$\alpha = \begin{cases} \sin^{-1} \left( \frac{\sin \theta_m}{\sin \theta_j} \right) & \text{for descending tracks} \\ 180^\circ - \sin^{-1} \left( \frac{\sin \theta_m}{\sin \theta_j} \right) & \text{for ascending tracks} \end{cases} \quad (2.36)$$

where  $\theta_m$  is the co-latitude of the orbit's closest approach to the pole and  $\theta_j$  are the co-latitudes of the sampling points. In the second step, the horizontal components are rotated further by half of the orbit separation angle,  $\pm 0.8^\circ$ , for *SwA* and *SwB*, respectively, to align them with the  $x$  and  $y$  axes.

For the execution of eq. (2.35) we have to employ the spatial derivatives of the magnetic field. The along-track gradient of the transverse magnetic field,  $dB_y$ , is derived from successive readings that are 5s apart. The cross-track gradient of the field component,  $dB_x$  is obtained from the difference of corresponding readings of the two spacecraft. The separation between these points varies in this example from about 100 km at  $30^\circ$  colatitude to zero at the crossover points (see Figure 2.32). While the separation of the measurement points in cross-track direction,  $d_y$ , is given by the orbital geometry, we have tested several spacings in the along-track direction. The 5s, giving a distance of about 38 km for  $d_x$ , turned out to be a good compromise. When using larger separations an undesirable damping of the current signature resulted. Smaller steps did not yield any improvement. In the vicinity of the crossover points the baseline for deriving reliable cross-track gradients becomes too small. We have set a limit (here 3 km) below that the second term in eq. (2.35) is set to zero. This means, for  $\pm 15$ s around the singular point the current determination is incomplete. Fortunately, the largest contribution comes from the

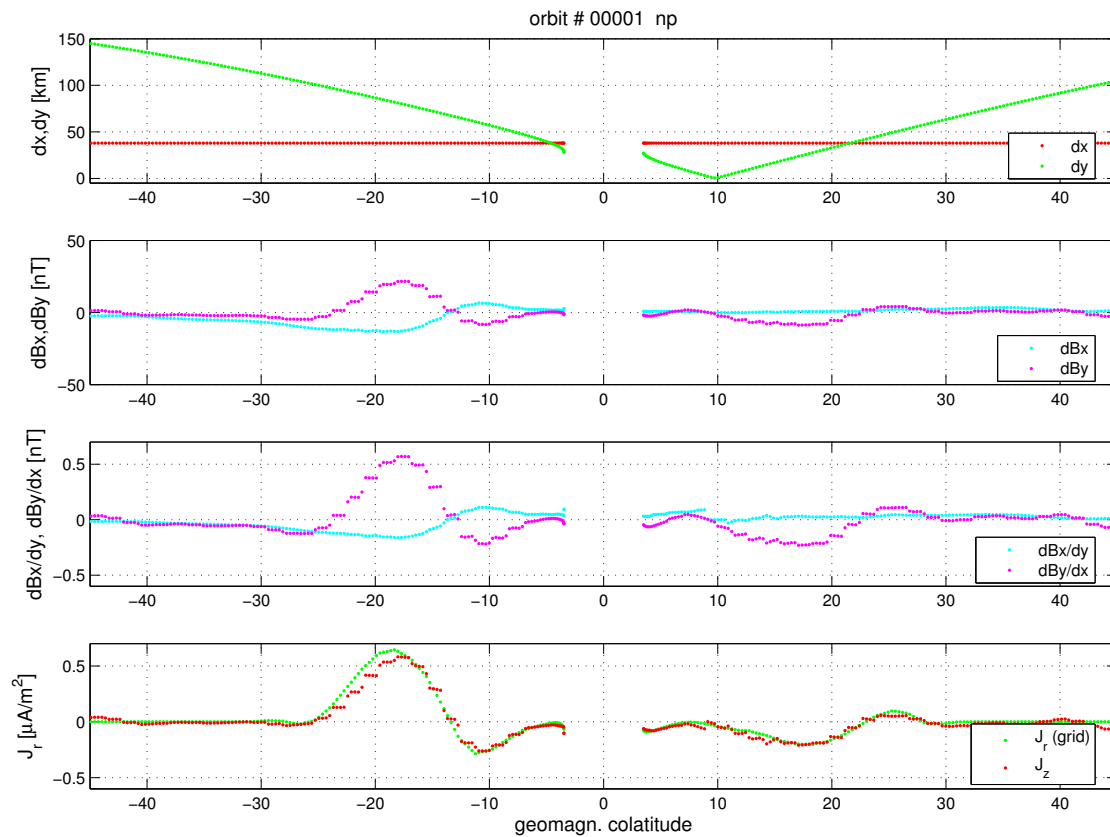


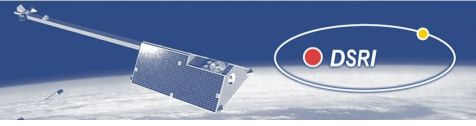
Figure 2.32: Variation of the different terms in eq. (2.35) across the pole (IMF  $B_Z = -2.5\text{nT}$ , for details see text).

along-track  $\Delta B_y$  term, therefore the results are not useless.

Figure 2.32 shows the variations of the different terms in eq. (2.35) and their contributions to the retrieved radial current density for a single pass over the north pole. In the top panel we have the distances between measurement points. The cross-track separation of the spacecraft is getting smaller towards the pole and, in this case, it passes the crossover point at  $10^\circ$  off the magnetic pole. The apparent data gap reflects the fact that the orbit does not cross the magnetic pole. In the second panel we have the magnetic field differences in the two directions. The along-track gradient of the  $B_y$  component does not vary smoothly but step-like. This is a consequence of the way the magnetic field is gridded. In the third panel the along-track and cross-track gradients are shown. It is quite evident that the largest contribution to the radial current estimate comes from the along-track gradient of the  $B_y$  component. As mentioned before, the cross-track gradient has been set to zero in the vicinity of the crossover point ( $dy < 3\text{km}$ ).

The bottom panel contains the comparison of the derived radial current density  $j_z$  with the synthetic input values of the current component  $j_r$ . In principle there is a good agreement between these two current values. In spite of that, we want to point out that there seem to be systematic discrepancies (a small phase shift) between the two curves. Estimated current features appear closer to the pole.

We think that the reason for this phase shift could be the linear interpolation between the grid points when retrieving the samples along the orbits. The spacing of grid points is



continuously changing when approaching the pole. Large residuals show up around the closest approach to the pole. They are probably due to the singularity of the spherical components at the pole. The suppression of the  $B_x$  gradient at the crossover point does not seem to generate large spurious signals.

After going through the individual processing steps of the radial current component we now have a look at a larger number of passes. Figure 2.33 shows every second polar pass for both northern and southern hemispheres during one day. For all these cases we find an almost perfect agreement between the derived and input current densities in both hemispheres. The afore mentioned phase shift can be observed here as well, and seems to be systematic.

For a more quantitative view of the deviations we have plotted the differences between the derived and modelled currents in Figure 2.34 for the same tracks. The prominent features to be noted are: the enhanced scatter in some places due to the gridding of the B-field, the sinusoidal variations caused by the phase shift, and some discontinuous jumps the vicinity of the cross-over points (e.g. second and third frame in the right column, near  $-10^\circ$ ). All these deflections are at least one order of magnitude smaller than the current amplitudes.

To get a better impression of the capability of the applied method for deriving field-aligned currents, a series of plots has been generated showing the model and recovered distribution of the currents for different orbit local times on polar plots. Figures 2.35 through 2.38 show the radial current distribution at the north pole in a Solar-Magnetic (SM) coordinate system. Midnight is at  $0^\circ$  and noon at  $180^\circ$  longitude. The input currents are in the left column; the patterns recovered within a two-days period (assuming a static FAC distribution) are displayed in the middle, and the differences of the former two are shown in the right column. From top to bottom, three scenarios with increasing magnetic activity are considered. In Figure 2.35, the *Swarm* satellites are crossing the polar region from dusk to dawn. In Figures 2.36 and 2.37 they move from noon to midnight, and in Figure 2.38 from dawn to dusk. The purpose of this series of examples is to find out whether the orbit orientation or the activity level have an influence on the quality of the obtained results. Due to the separation between the magnetic and geographic poles the satellites cover a swath of 2500 km width in the SM system every day.

When looking at the difference plots, some systematic features show up in the residuals. Right at the pole there is an isolated deflection. Especially in Figure 2.38 a half circle of yellow dots are visible. They reflect the small phase shift. In all other cases no systematic relation can be identified.

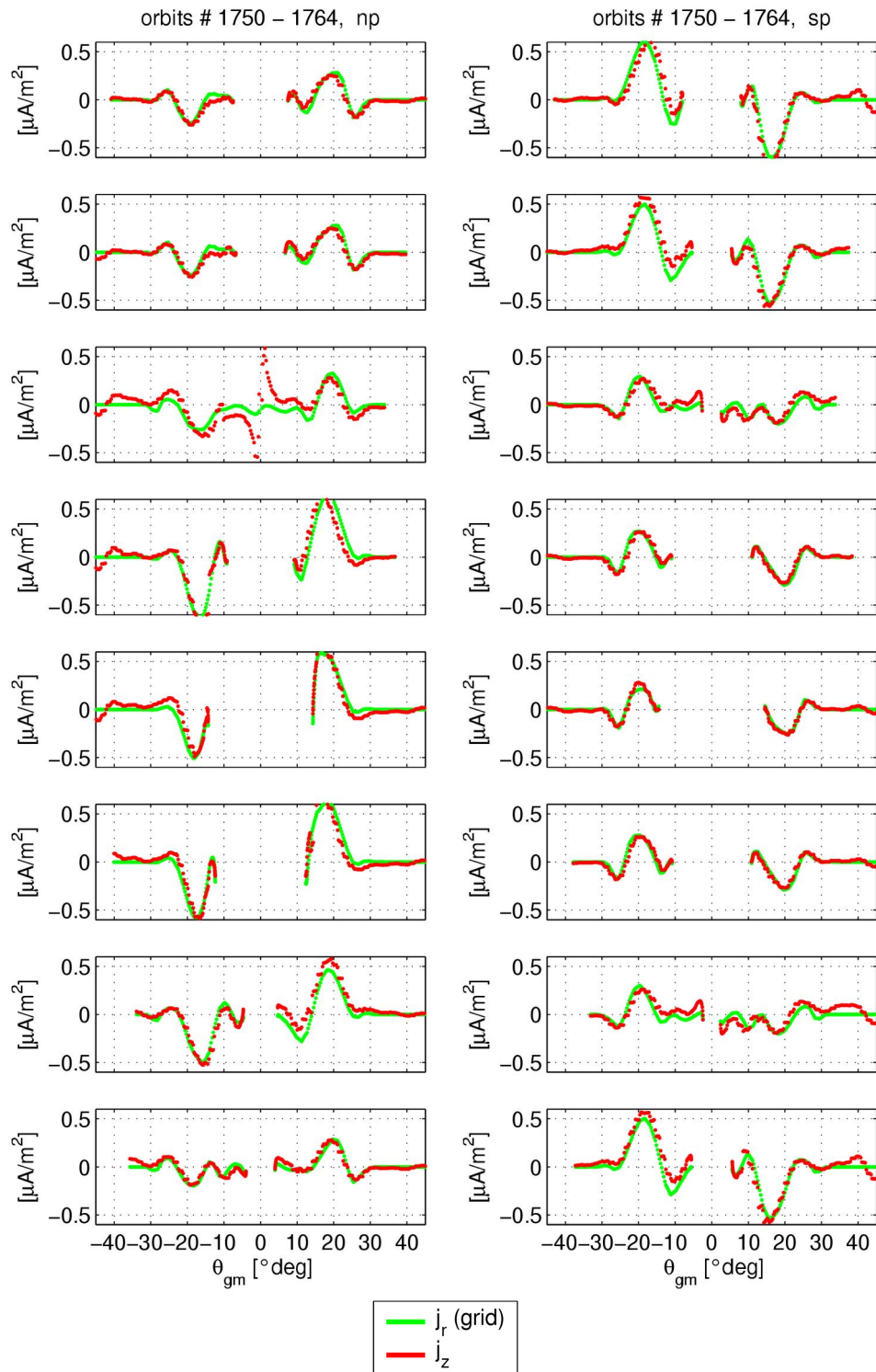


Figure 2.33: Direct comparison of derived radial current density (red) and the corresponding model input data (green) (IMF  $B_Z = -2.5\text{nT}$ ).

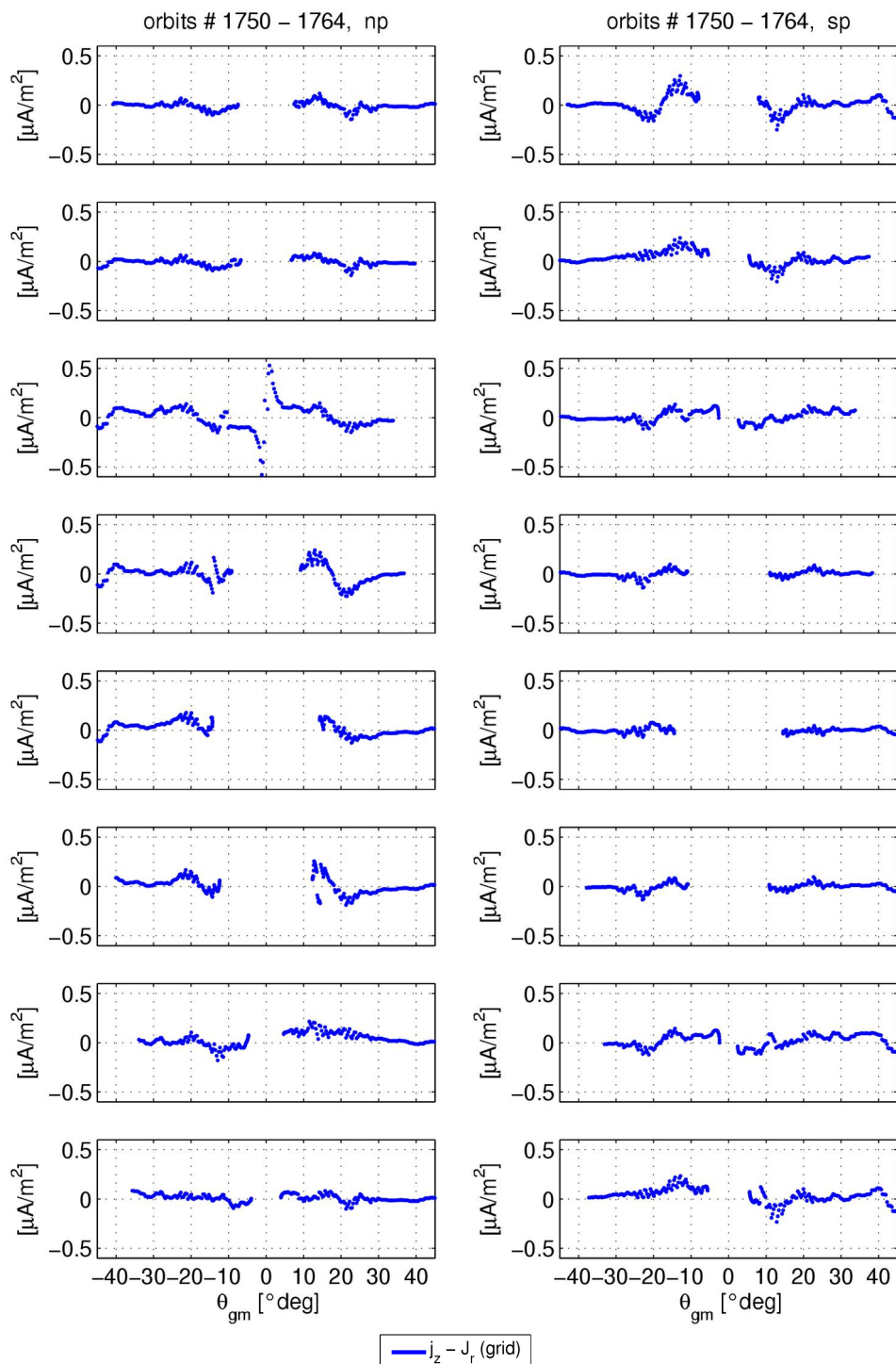


Figure 2.34: Difference between the derived radial current density and the corresponding model input data (IMF  $B_Z = -2.5\text{nT}$ ).

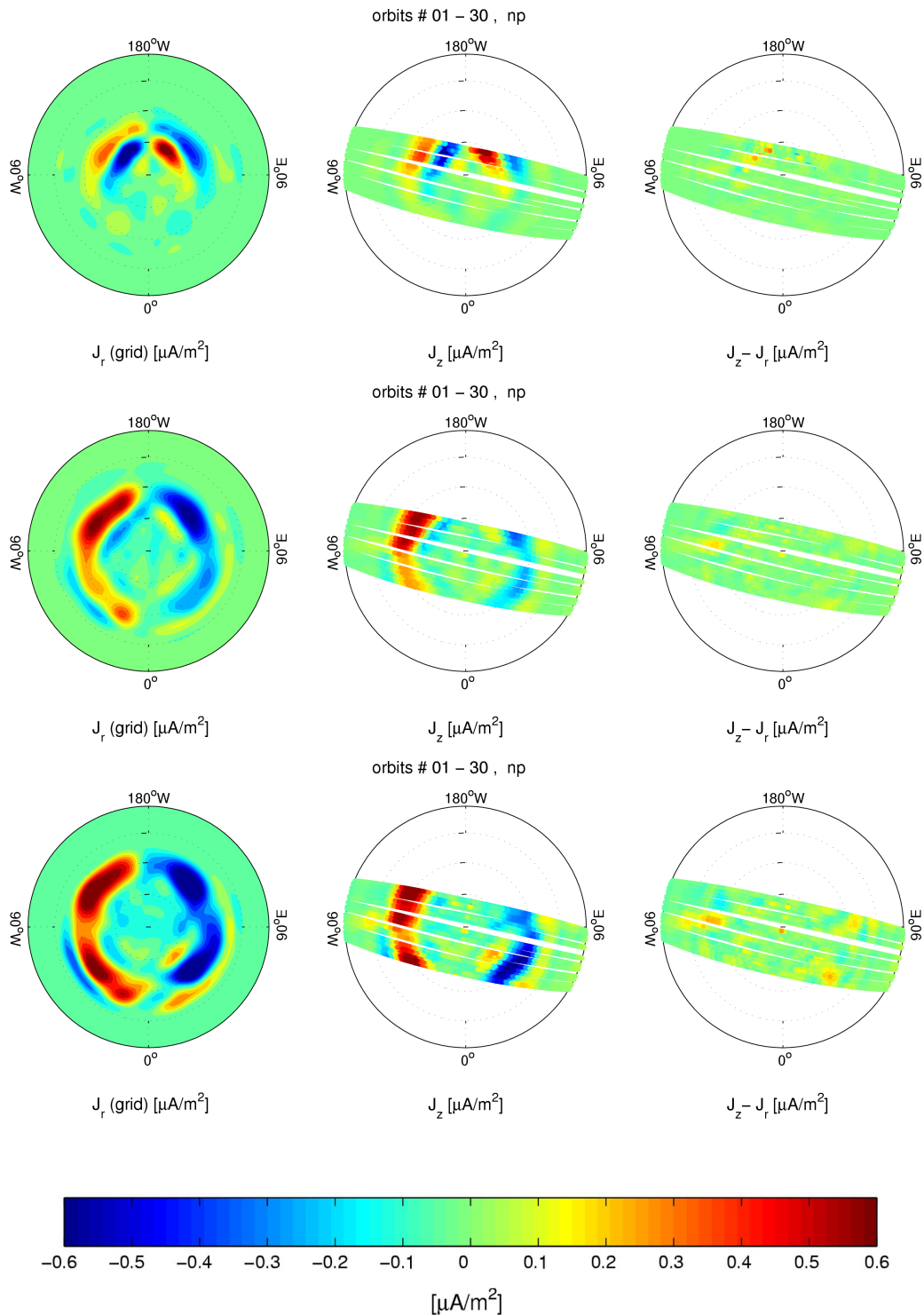
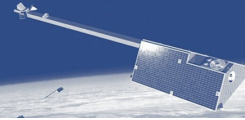


Figure 2.35: Comparison of model radial currents with the derived vertical currents from 17:00 local time orbits. (left column) distribution of radial currents from input model, (middle column) derived vertical currents from all orbits of a two-days period, (right panel) difference between derived and model currents. The rows represent different levels of activity, (top) interplanetary magnetic field:  $B_Z = 5$  nT, (middle)  $B_Z = -2.5$  nT, (bottom)  $B_Z = -5$  nT.

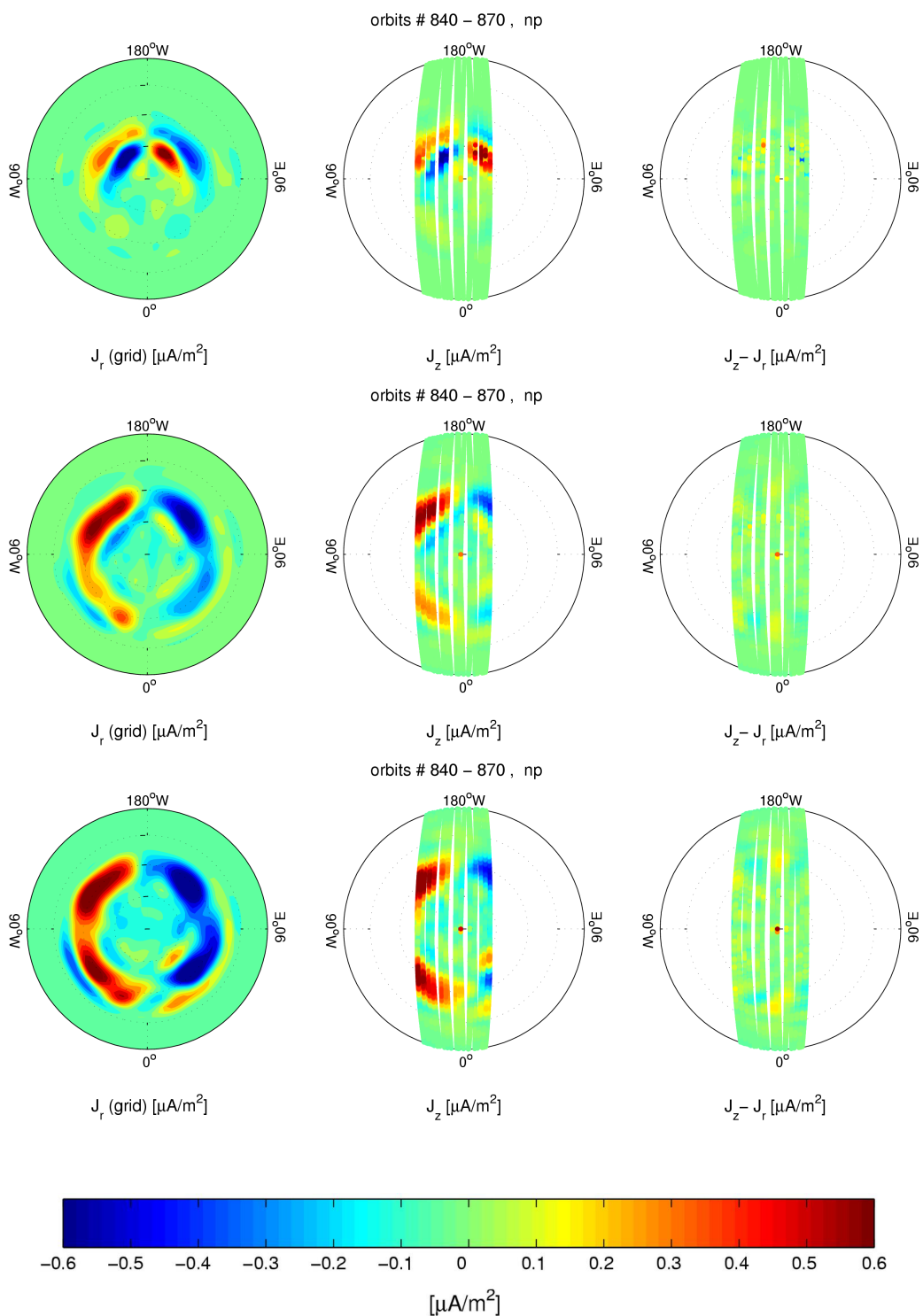


Figure 2.36: Comparison of model radial currents with the derived vertical currents from 12:00 local time orbits (format as in Fig. 2.35).

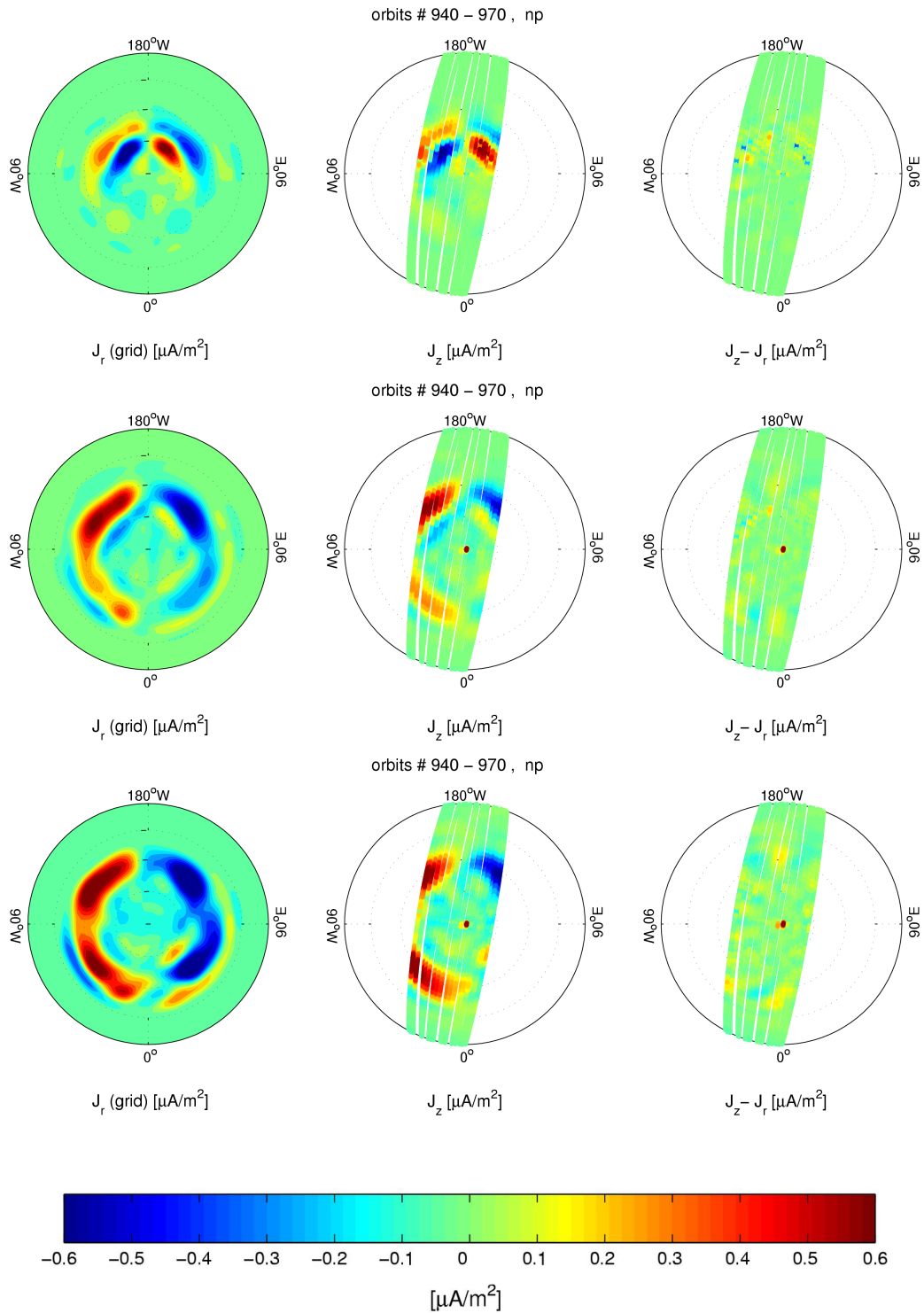


Figure 2.37: Comparison of model radial currents with the derived vertical currents from 11:00 local time orbits (format as in Fig. 2.35).

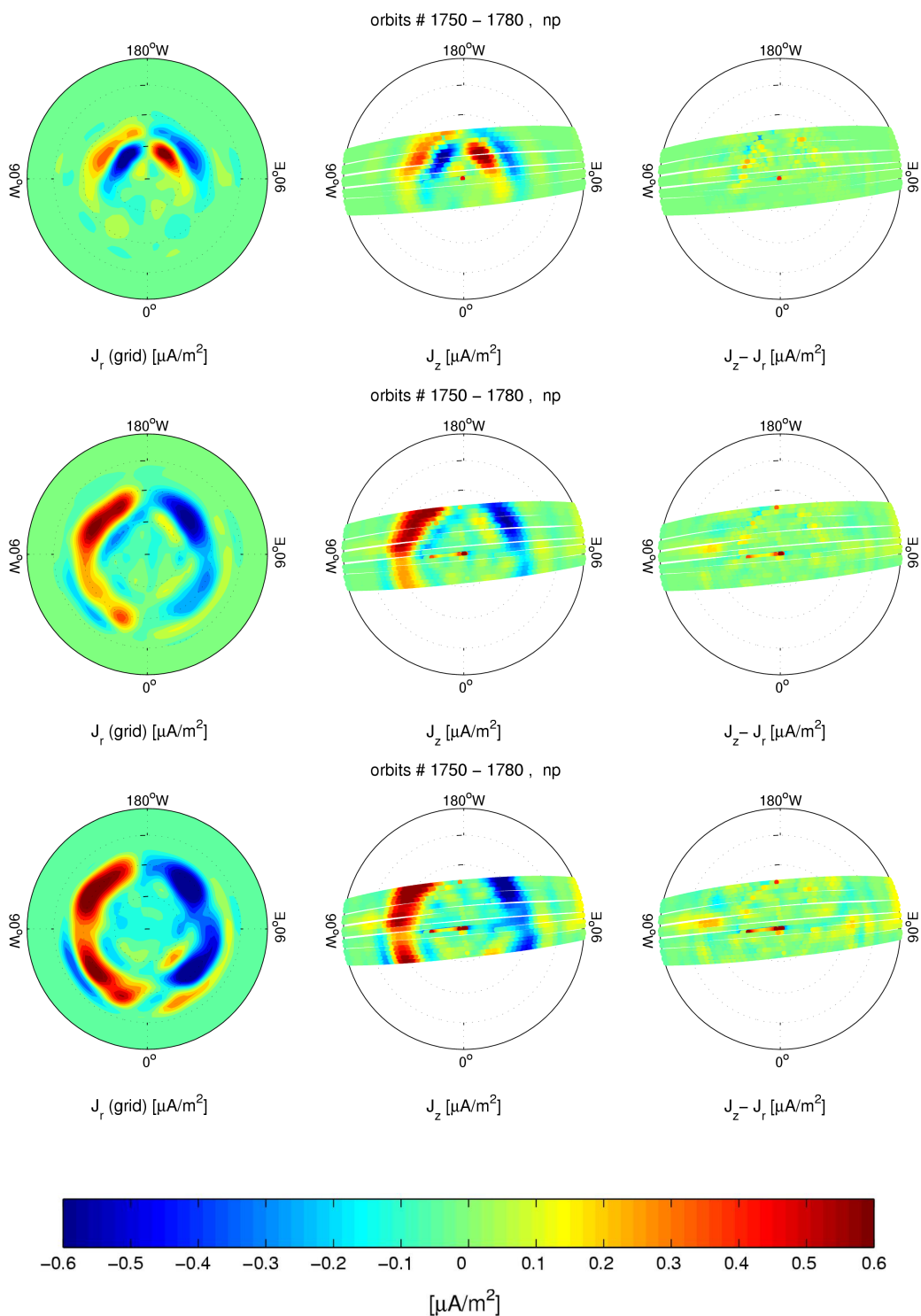
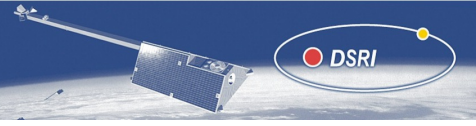


Figure 2.38: Comparison of model radial currents with the derived vertical currents from 06:00 local time orbits (format as in Fig. 2.35).



## Field-aligned current estimates from a single satellite

Up to date, the estimates of field-aligned currents have to rely on single satellite measurements. In that case the results depend on a number of assumptions. The most important one concerns the geometry of the currents (Lühr et al. [1996]). Generally it is assumed that the spacecraft crosses a sheet of field-aligned currents at a right angle. In that case eq. (2.35) can be reduced to

$$j_z = \frac{1}{\mu_0} \frac{\partial B_y}{\partial x} \quad (2.37)$$

Since the  $x$  component is aligned with the velocity vector one may write

$$j_z = \frac{1}{\mu_0} \frac{1}{v} \frac{\partial B_y}{\partial t} \quad (2.38)$$

where  $v$  is the orbital speed of the satellite.

There is another *caveat* concerning the single satellite approach. Field-aligned currents cause toroidal magnetic fields. The curl  $\mathbf{B}$  approach, as outlined in eq. (2.35), rejects poloidal field components. The reduced version, as given in eq. (2.38), is sensitive to both poloidal and toroidal fields. Thus fields from horizontal currents or crustal anomalies may cause spurious field-aligned current readings. The importance of this aspect becomes increasingly relevant the lower the spacecraft flies. As part of this *Swarm* Science Study we test also the reliability of the single satellite approach by using the synthetic data set of auroral zone fields and currents. Magnetic field data sampled along the orbit of *SwA* were applied to eq. (2.38). The calculations are performed in the local Cartesian, VZ frame. The transformations into this frame are the same as described in the previous section.

A comparison between the estimated radial current densities and the model data is shown in Figure 2.39 for a selection of tracks of one day both for the north and south pole. For many of the frames a reasonable agreement of the two curves results. There are, however, some passes where the current density is badly underestimated (lower left and upper right). Also in this approach we find a slight phase shift of the estimated current features towards the pole. We take this as a further indication that the shift is not caused by our curl  $\mathbf{B}$  method described above, but rather a mapping effect.

Figures 2.40 and 2.41 show the comparison of input and estimated current distribution on polar plots, as presented before for the multi-satellite approach. For the two local times of the orbit plane we get quite different results. As expected, the residuals are small in regions where the angle of attack between the flight direction and the current system is close to  $90^\circ$ . At the fringes of the swath, however, where this angle becomes smaller, the deficit in estimated current density is severe and reaches a factor of 2. The residuals of the dawn/dusk and the noon/midnight orbits look quite different now. From the comparison of the curl  $\mathbf{B}$  technique with the single satellite approach we may get an idea of the uncertainty involved in present-day field-aligned current estimates.

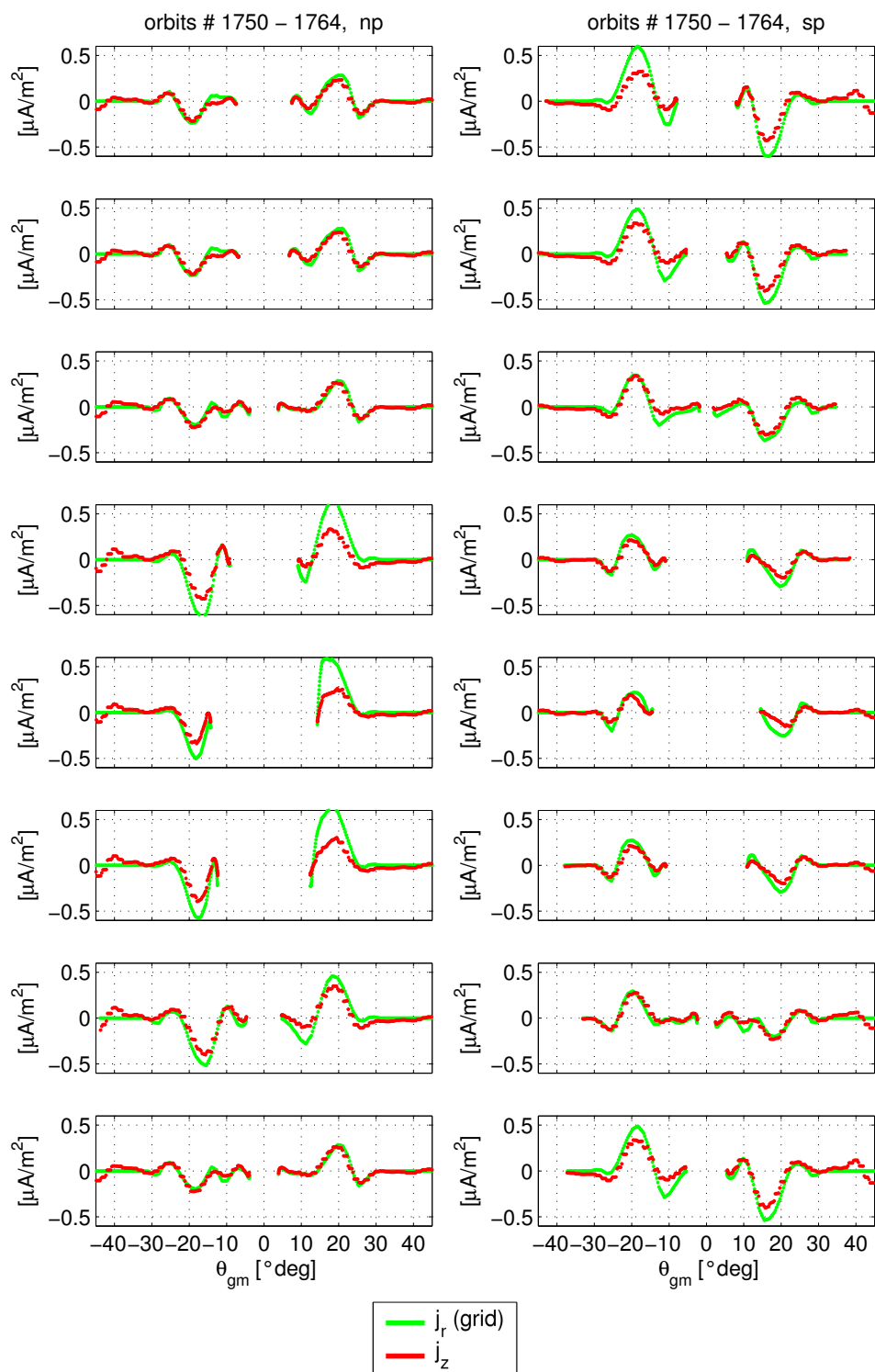


Figure 2.39: Direct comparison of derived radial current density using the single satellite (*SwA*) method (red) and the corresponding model input data (green) (IMF  $B_Z = -2.5\text{nT}$ ).

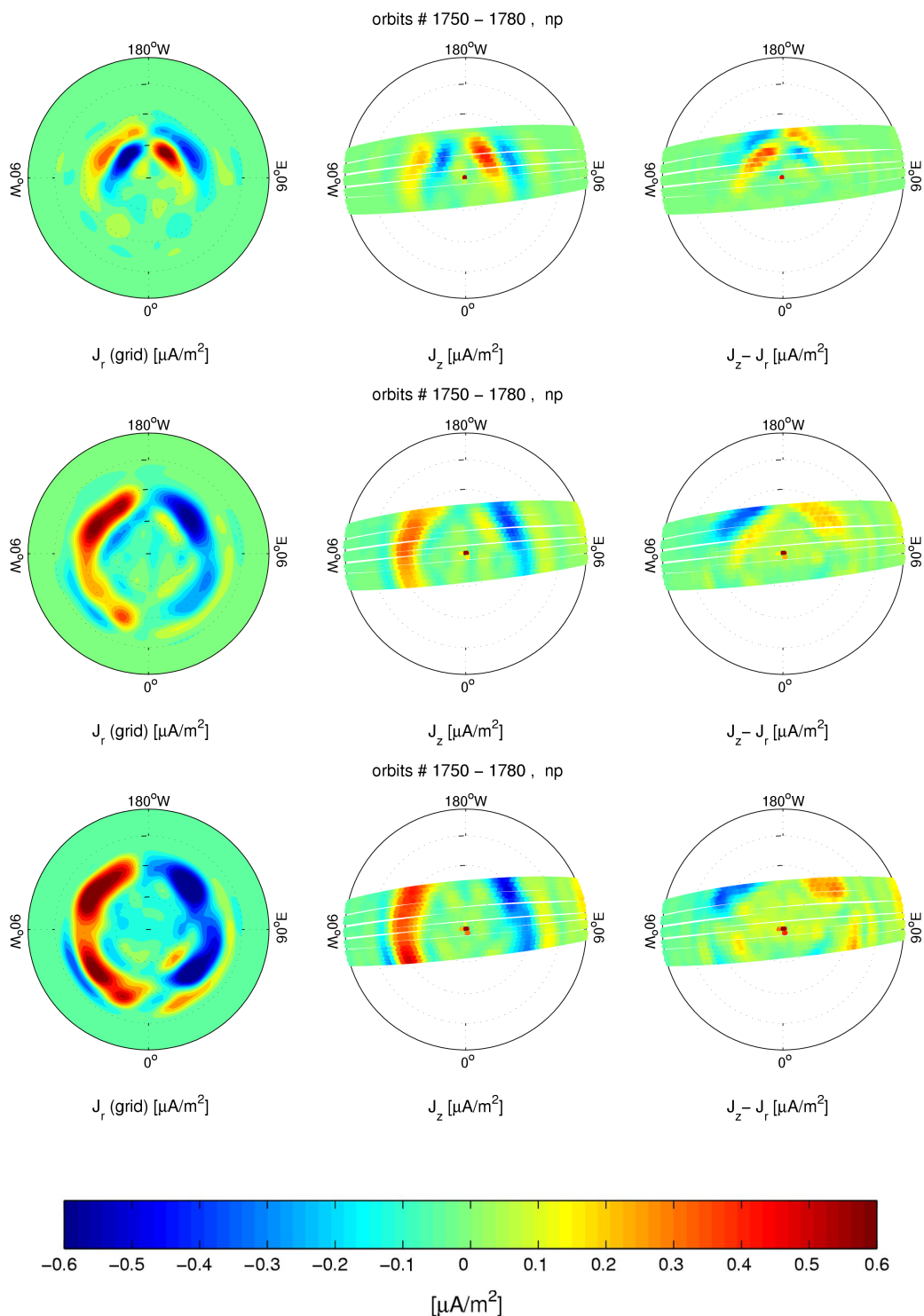


Figure 2.40: Comparison of model radial currents with the single satellite (*SwA*) derived vertical currents from 06:00 local time orbits. (left column) distribution of radial currents from input model, (middle column) derived vertical currents from all orbits of a two-days period, (right panel) difference between derived and model currents. The rows represent different levels of activity, (top) inter planetary magnetic field:  $B_Z = 5$  nT, (middle)  $B_Z = -2.5$  nT, (bottom)  $B_Z = -5$  nT.

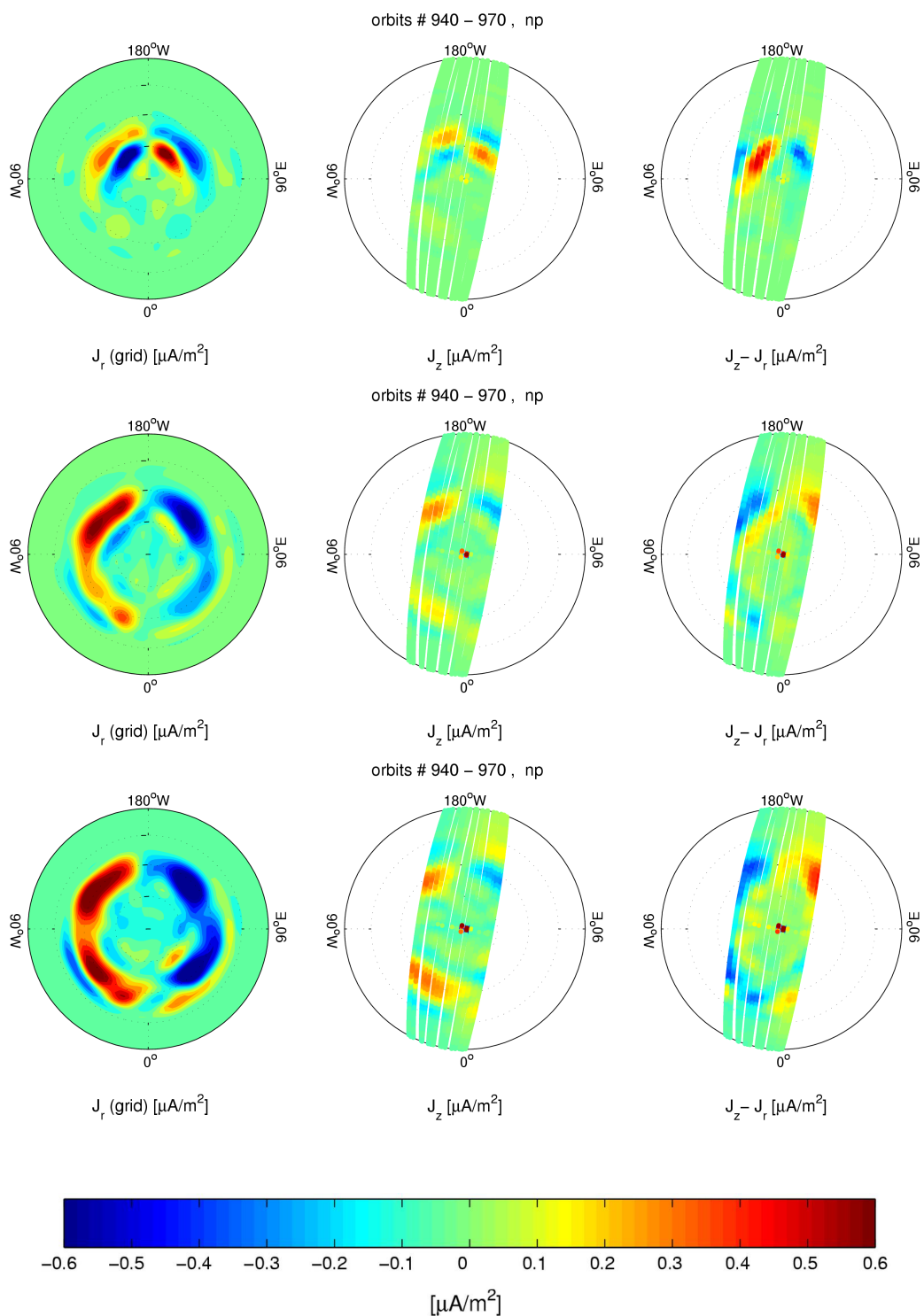


Figure 2.41: Comparison of model radial currents with the derived vertical currents from 011:00 local time orbits (format as in Fig. 2.40).

## 2.10 Retrieval of horizontal ionospheric currents

After having demonstrated the ability of the *Swarm* constellation to determine the field-aligned current density reliably, we will, in this section, propose and test techniques to estimate horizontal currents in the ionospheric E-layer, in particular the Hall currents. As has been stated in Section 2.8, Hall currents generate predominantly poloidal magnetic fields. These fields contribute also to the field magnitude. Field-aligned currents on the other hand do not influence the magnitude. For the estimation of the Hall current we therefore make use only of the variation in the total field.

The approach used here is based in principle on the original work of Olsen [1996]. In a later version it has been refined by Ritter et al. [2004b]. The Hall currents are approximated by a series of horizontal line currents. These line currents are placed in the ionospheric E-layer, here at 90 km altitude and separated by 110 km along the orbit track.

The magnetic effect at orbital altitude caused by a line current flowing in  $y$ -direction can be written as

$$b_x = -\frac{\mu_0 J d}{2\pi} \frac{h}{x^2 + h^2} \quad b_z = \frac{\mu_0 J d}{2\pi} \frac{x}{x^2 + h^2} \quad (2.39)$$

where  $b_x$  and  $b_z$  are the perpendicular and vertical components of the generated magnetic field, respectively.  $J$  is the sheet current density,  $d$  the distance between the lines,  $h$  denotes the height above the currents and  $x$  is the horizontal distance to the current.  $x, y, z$  are coordinates in a local Cartesian frame, where  $z$  is pointing to the zenith; the directions of  $x$  and  $y$  are defined by the orientation of the current. Since we want to derive the current density from the variation in the total field, we take a look at the magnetic signature,  $\Delta F$ , in the field magnitude.

$$\Delta F = |\mathbf{B} + \mathbf{b}| - |\mathbf{B}| \quad (2.40)$$

where  $\mathbf{B}$  is the ambient magnetic field, in this case a centric dipole. Since the field caused by the currents,  $\mathbf{b}$ , is much smaller than the background field, eq. (2.40) may be approximated by a normalised dot product of  $\mathbf{B}$  and  $\mathbf{b}$

$$\Delta F = \frac{\mathbf{B} \cdot \mathbf{b}}{|\mathbf{B}|} \quad (2.41)$$

With this equation we obtain a linear relation between the variation in the total field and the line current density.

For the inversion a series of 60 line currents to each side of the closest approach to the pole is used. The magnetic field readings are available at intervals of 5 s giving 3 measurements per degree (per line). With the available 120 free parameters the current system is severely under-determined. For that reason the individual current densities have to be constrained. On both edges the currents are suppressed by cosine bells extending over  $30^\circ$ . The variability of current intensity from line-to-line is kept low by solving for a minimum of the second differences in adjacent line current strength. For the estimate of the current density distribution the following equation has to be solved

$$\mathbf{J} = (\mathbf{G}^T \mathbf{G} + \mathbf{D}^T \mathbf{A}^T \mathbf{A} \mathbf{D})^{-1} \mathbf{G}^T \Delta \mathbf{F} \quad (2.42)$$

where  $\mathbf{J}$  is the column vector containing the resulting current densities,  $\mathbf{G}$  is the design matrix,  $\mathbf{D}$  contains the cosine bell taper,  $\mathbf{A}$  the second difference constraint and  $\Delta \mathbf{F}$  is the vector of observations.

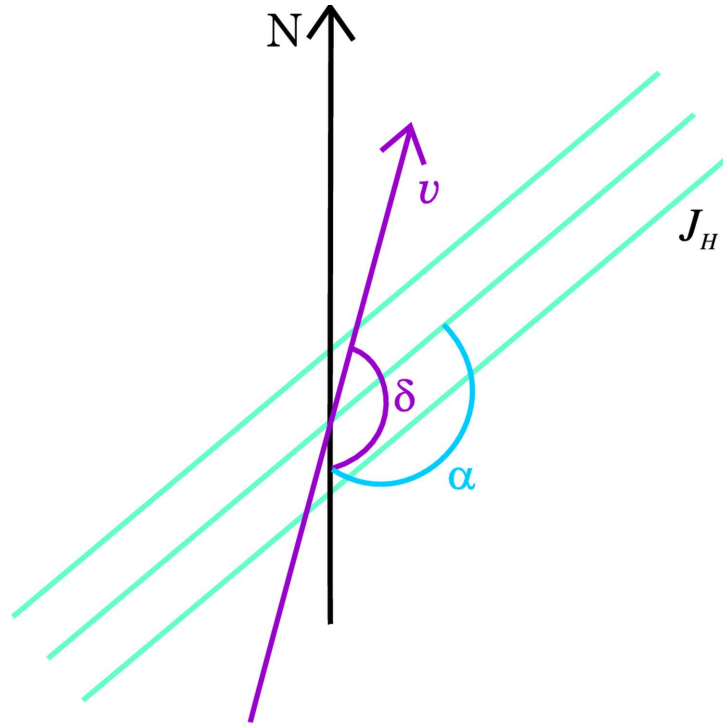


Figure 2.42: Relative orientation of the model line (Hall) currents with respect to the flight pass.

Before starting to apply the synthetic ionospheric data set to the above outlined formalism we will have a look at the measurement geometry (see Figure 2.42).

The angle  $\alpha$  representing the orientation of the Hall current can be calculated from its components in the E-layer:

$$\tan \alpha = \frac{|J_{H\phi}|}{J_{H\theta}} \quad (2.43)$$

Equally, the angle  $\delta$ , the deviation of the flight pass from the southward direction, can be computed as follows

$$\tan \delta = \frac{\Delta\phi \sin \theta}{\Delta\theta} \quad (2.44)$$

$\theta$  and  $\phi$  are the colatitude and longitude of the orbit position in the SM system (see Section A). The  $\sin |\delta - \alpha|$  has been used to scale the separation between the measurement point and the line current. These angles may differ for each line current element. As an example, Figure 2.43 shows the distribution of Hall currents (arrows) around the vertical currents centres (colour coded) for a scenario with medium activity, IMF  $B_z = -2.5$  nT.

An orbit track has been added for reference. It can be seen that all kinds of relative angles occur. The example orbit crosses from dawn, 07 MLT, to dawn, about 18 MLT. On the dawn and dusk sides we find homogeneous fields of westward and eastward flowing currents, respectively. Their intensity is reduced strongly behind the sun light terminator coinciding approximately with the 06/18 MLT datum line.

In the first step of computation, we assume that the angle of attack between Hall current and velocity is always  $90^\circ$ . This is the underlying assumption in all previous single-satellite

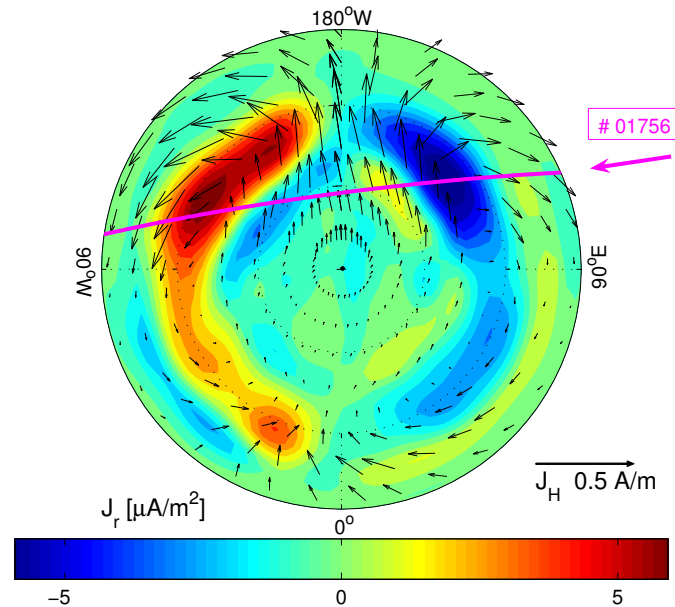


Figure 2.43: Distribution of Hall currents (arrows) around the patches of field aligned currents (color coded). Medium activity with IMF  $B_Z = -2.5$  nT is reflected. For reference, the orbit track # 01756 is overlaid.

studies of this kind (e.g., Olsen [2002], Ritter et al. [2004b]), since no information about the orientation of the current is available. For one polar pass the different products of computation are plotted in Figure 2.44. The top panel shows the retrieved Hall current in red. The two current components, as contained in the input data set, are in green and light blue. In the second panel we show the current flowing in each of the model lines. This is the prime product of the inversion. The current strength varies quiet smoothly with latitude reflecting the effect of the constraints. The diagram below presents the variation of the magnetic field magnitude ( $dF$ ) where the current estimate is based upon, and the forward calculation of the magnetic field produced by the estimated current ( $dF_{synth}$ ). The input data and the fitted field values are virtually identical. At least, they cannot be distinguished in the plot. Finally, in the bottom panel we show the angles  $\alpha$  and  $\delta$  as defined in eqs. (2.43) and (2.44). In this run they are kept at fixed values.

When looking at the curves in the top panel we see that there is a qualitative agreement between the derived current density (red) and the model Hall current components. In some parts, however, systematic deviations exist. In order to find out how significant the results of the one pass are, we show polar passes of a whole day in Figure 2.45 for the north pole (np). There is a systematically positive bias in all ascending arcs. The descending arcs give better results.

Since we have information about the electric field in the *Swarm* mission, it is possible to include the orientation of the Hall currents into the inversion. The results of such an advanced inversion approach are shown for one polar pass in Figure 2.46. The bottom panel presents the variations of the angles  $\alpha$ ,  $\delta$  and  $|\delta - \alpha|$ . The intensity of the current strength in the series of lines is displayed in the second panel. There is hardly any discernible difference to the corresponding panel in Figure 2.44. Obviously, the orientation of the line currents has little influence on the obtained current intensity. This is not surprising, since we make only use of

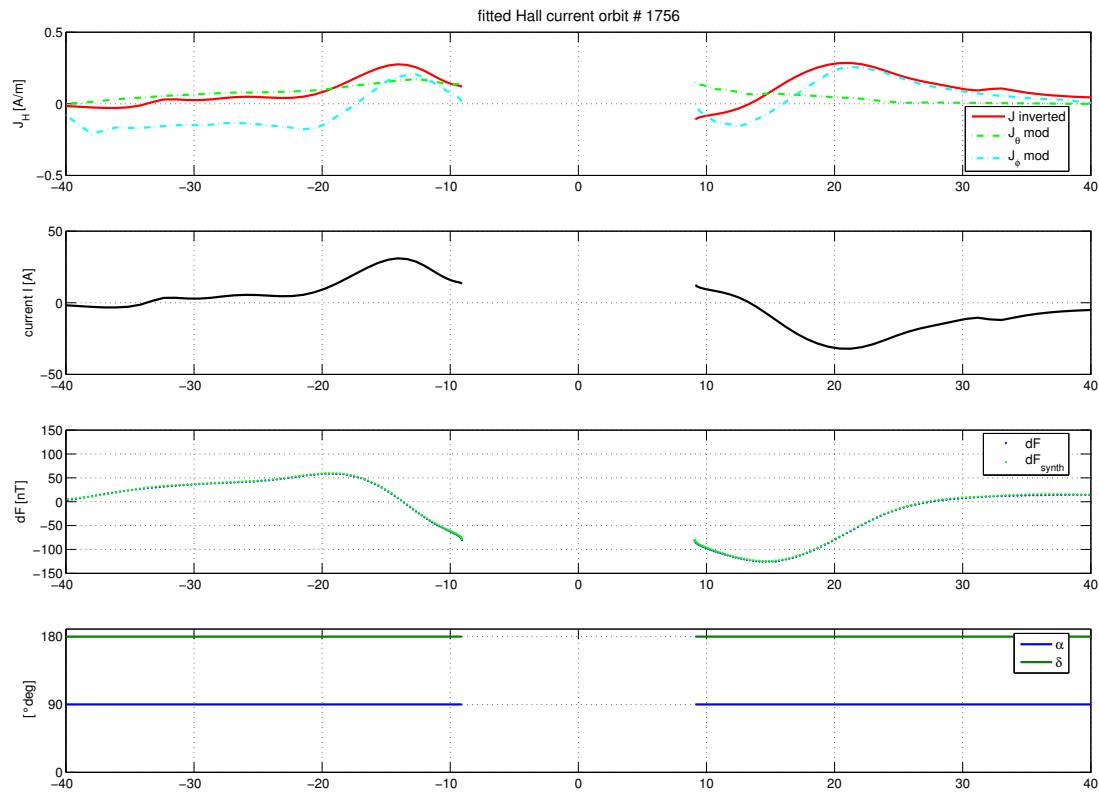


Figure 2.44: Estimate of Hall current density according to eq. (2.42) from deflections of the magnetic field magnitude (for details of the panels see text).

the field-aligned component of the magnetic field. As it is almost vertical in the polar region, it is invariant to rotations about the vertical direction.

The top panel contains the direct comparison between the input Hall current and the derived current components. Over large parts of the descending arc (right part of the graph) there is an almost perfect match between model and estimate. Clear deficiencies are apparent in the ascending part of the track (left part). The overall characteristics of the Hall current, however, is recovered.

In order to get a feeling for the significance of this single polar pass, again orbits of a whole day at the north pole are considered in Figure 2.47. We can state a satisfying agreement of all descending passes. Equally, we find a systematic underestimation of the current density for the ascending arcs.

For the explanation of the discrepancies at the ascending arcs we may have a look at the full current distribution in Figure 2.43. The ascending part of the orbit is on the dawn side where we have the area of homogeneous currents. Our method is quite insensitive to cases of such current distributions. Homogeneous sheet currents develop vertical magnetic field only at their edges. We regard this as the prime cause for the deficit in this area.

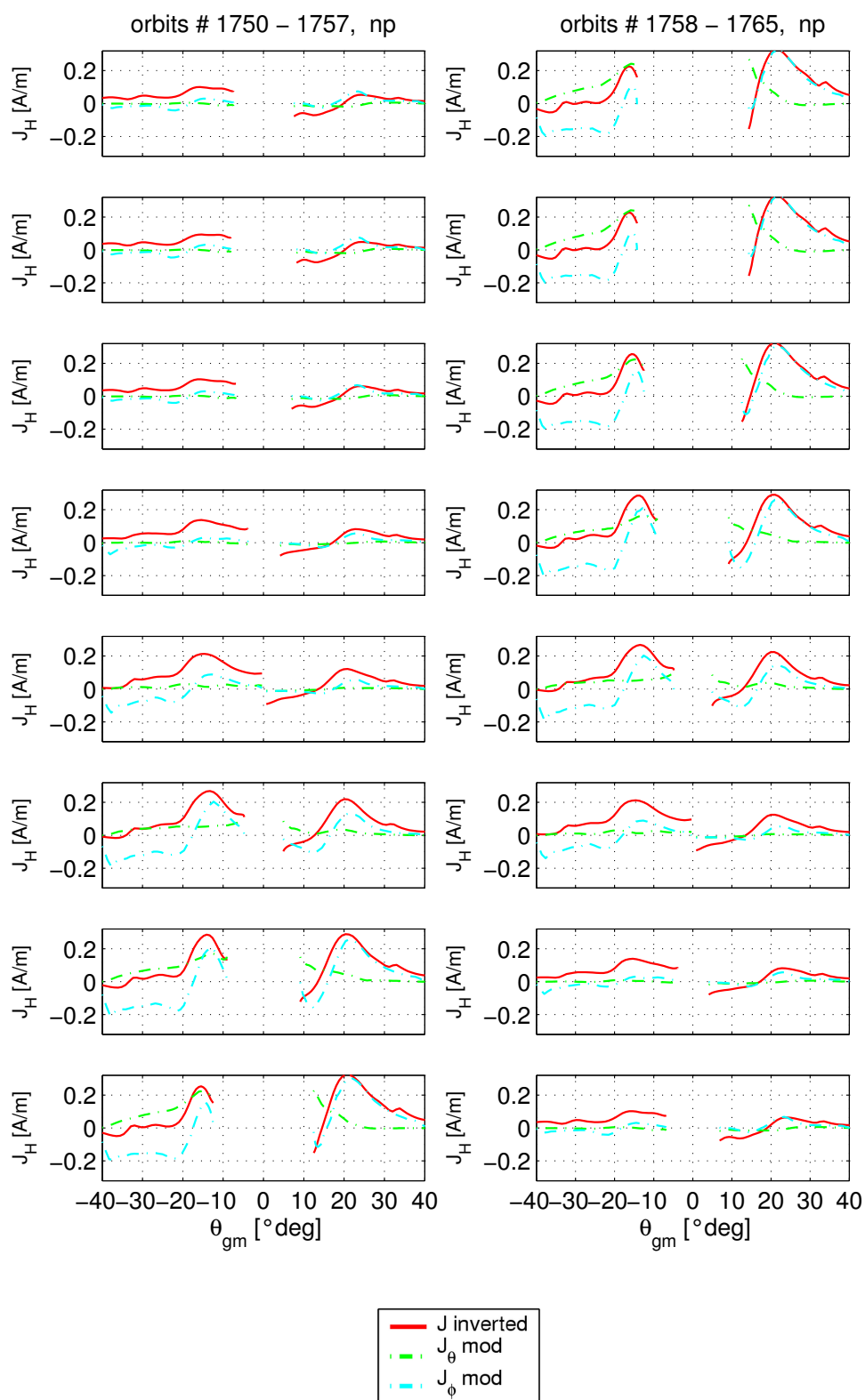


Figure 2.45: Direct comparison of derived Hall current density (red) with current components from the model data (blue and green) for one full day (IMF  $B_z = -2.5$  nT).

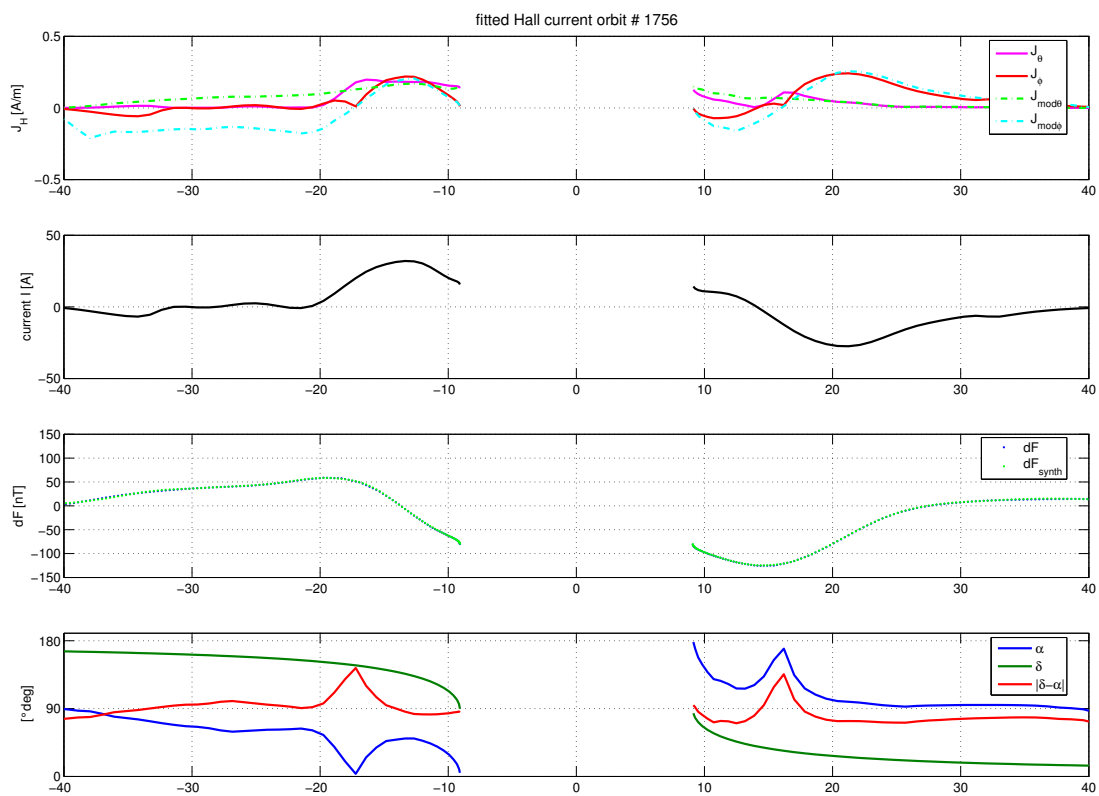
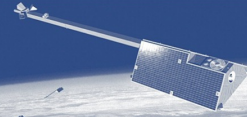
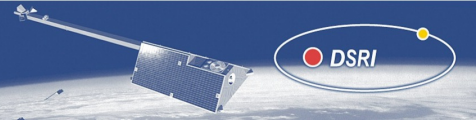


Figure 2.46: Same format as in Figure 2.44, but with the component of the Hall current retrieved separately.





## 2.11 New Auroral Region Index for Improved Data Selection

It is good practice in geomagnetic main field modelling to make use exclusively of the field magnitude at high latitudes. The reason for that are the large transverse magnetic field deflections caused by the ever-flowing field-aligned currents (FAC). Fortunately, these FACs do not contribute significantly to the field magnitude.

There have been different approaches in use for a dedicated data selection. For the purpose of main field modelling Olsen [2002] selected the data according to the following conditions:  $K_P < 1.3$  at the time of the observation,  $K_P < 2.0$  for the preceding 3 hours,  $|D_{ST}| < 10$  nT,  $|dD_{ST}/dt| < 3$  nT/h and IMF  $|B_Y| < 3$  nT. A rather different approach was applied by Maus et al. [2002] for their modelling of the lithospheric magnetisation. Their criterion is the rms-value of the scalar residuals after subtracting a main field and a high-degree crustal field model. Passes with an rms-value below a certain threshold were classified as quiet.

In a statistical study Ritter et al. [2004a] showed that the magnetic activity indices  $K_P$  and  $D_{ST}$  are not efficient in predicting magnetically quiet times at high latitudes. Also the dependence on the interplanetary magnetic field (IMF)  $B_Y$  component was not convincing. The success of the approach used by Maus et al. (2002) depends strongly on the quality of the before-mentioned models. Ideally, the index should be derived locally, but independent of any *a priori* field model.

*Swarm* with its advanced instrumentation and the dedicated constellation may help to provide such an index. In Section 2.8 we have shown that variation in the field magnitude are predominantly caused by the Hall currents. The intensity of these currents can be calculated from the electric field and the corresponding conductivity

$$J_H = \Sigma_H E_{\perp} \quad (2.45)$$

While the electric field will be measured by the *Swarm* spacecraft, the Hall conductance  $\Sigma_H$  has to be derived from models, which enhances the uncertainty. On the dayside, the ionospheric conductivity caused by the photoionisation can be estimated reasonably well depending primarily on the solar zenith angle (Wang et al. [2005]). On the nightside, the conductivity is mainly caused by the precipitation of energetic electrons. Here, the resulting Hall conductance can range from 0.1 to 20 S even on quiet days .

### Total field variations from Pedersen current estimates

Here we are going to introduce and test another method, estimating the maximum amplitude of magnitude variations from the derived field-aligned currents. As has been shown in Section 2.9, FACs can be determined very reliably by the pair of satellites *SwA* and *SwB*, and the result is virtually independent of the quality of the models for removing the internal contributions. From Section 2.8 we know that the divergence of the horizontal currents in the ionospheric E-layer are equal to the field-aligned currents. In case of negligible conductivity gradients which is a reasonable assumption during magnetically quiet conditions, the field-aligned current density equals the divergence of the Pedersen current (cf. eq. (2.32)). Subsequently we will make use of this relation. For our application we may write

$$\int j_{\parallel} dl = -\frac{1}{\sin I} J_P \quad (2.46)$$

where  $dl$  is the integration path aligned with the electric field. The aim is, however, to estimate the Hall current density. The two current components are related to each other by the ratio of

the conductances

$$J_H = \frac{\Sigma_H}{\Sigma_P} J_P \quad (2.47)$$

From literature it is known (e.g. Schlegel [1988]) that the ratio  $\Sigma_H/\Sigma_P$  varies generally only between 1 and 2, tending towards 1 during quiet conditions. For that reason the integrated field-aligned current density may be regarded as a suitable quantity for estimating the magnetic activity. For the implementation of this approach we used the method outlined in Section 2.9 to derive the radial current component. At satellite altitude all currents are field-aligned. Therefore, they can be derived from the radial current

$$j_{\parallel} = \frac{1}{\sin I} j_r \quad (2.48)$$

where  $I$  is the inclination of the magnetic field

$$\tan I = -\frac{B_r}{\sqrt{B_{\theta}^2 + B_{\phi}^2}} \quad (2.49)$$

and  $B_r, B_{\theta}, B_{\phi}$  are the components of the main field. For the estimation of the Pedersen current  $J_P$ , we apply the synthetic data to eq. 2.46 and get in practice the corresponding expression,

$$J_P = \sum j_{\parallel} \frac{\mathbf{v}_s \cdot \mathbf{E}}{|\mathbf{E}|} \Delta t \quad (2.50)$$

where  $\mathbf{v}_s = 7.6$  km/s is the velocity of the satellite and  $\Delta t$  the time interval between readings, here  $\Delta t = 5$ s. The summation is started at the current-free mid-latitude and continued to the point of interest.

Figure 2.48 shows the different steps of computation for a single pass. In the top panel we present the derived field-aligned current (red) and the model current (green). By integration of these two FAC-types according to eq. (2.50), we obtain the proxy for the Pedersen current. The second panel shows a comparison between the two estimated Pedersen currents and the calculated Pedersen current (blue) according to eq. (2.30). All three curves track each other quite well. This means the approximation of eq. (2.50) is reasonably valid. The direction cosine between the velocity vector and the electric field is plotted in the third panel. Here, the importance of the electric field for this method becomes evident. The variation of the magnetic field magnitude due to the ionospheric currents is shown in the bottom panel. These variations seem to reflect mainly the spatial derivative of the Pedersen current curve.

The example shown in Figure 2.48 is from a quiet period with the interplanetary magnetic field (IMF)  $B_Z = 5$  nT. We also applied this method to more active scenarios. Figure 2.49 shows the same series of curves for larger activities with IMF  $B_Z = -2.5$  nT and  $B_Z = -5$  nT. Unfortunately, the agreement between the predicted and the model Pedersen current is much worse here. This is particularly evident for the descending arc. Possible reasons for that will be discussed in Section 2.12.

The purpose of this section is to use the estimated Pedersen currents as an indicator for the level of magnetic disturbances. In the approach chosen, the peak current density is compared with the peak deflection of the total field. To derive an activity index, the relation between the two quantities is determined in a correlation analysis.

Figure 2.50 contains the results of the correlation obtained for the quiet period, separately for ascending and descending tracks. For the selected orbits the satellite passes first dusk on its

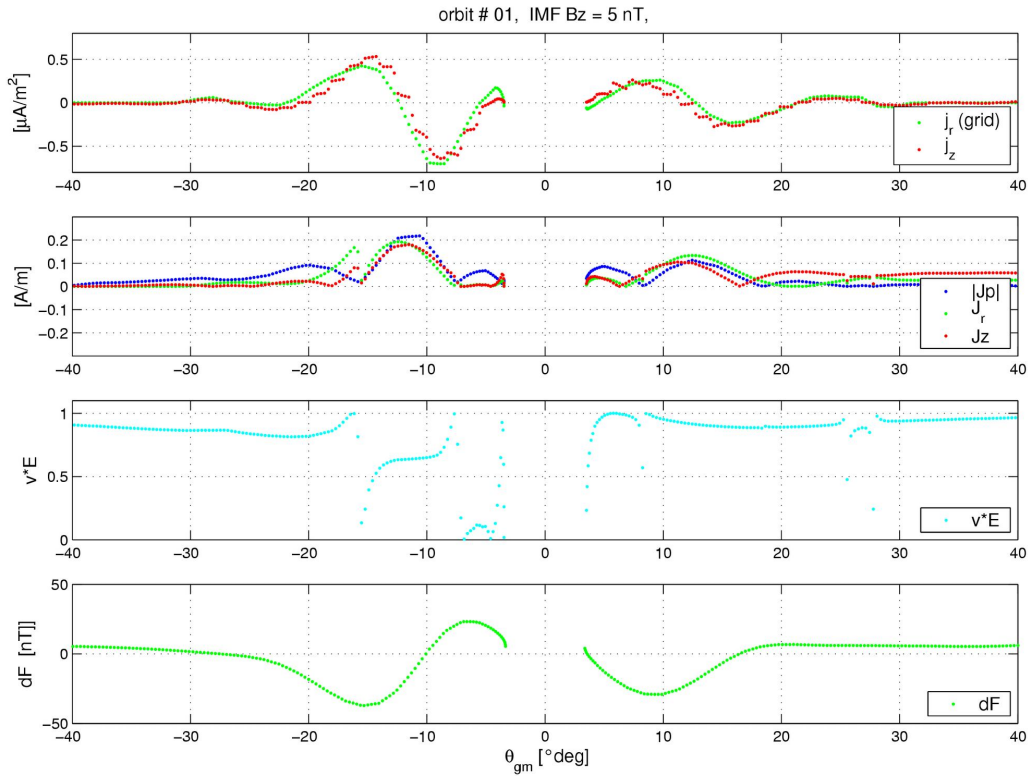


Figure 2.48: Estimation of Pedersen current density according to eq. (2.50) from integration of field aligned currents (for details of the different panels see text).

ascending part, then down on its descending part. In case of the ascending tracks, a good linear relation with a correlation coefficient above 0.9 emerges. The descending tracks give a much less convincing result. We have extended the correlation to all levels of activity. As can be seen in Figure 2.51, the impression gained in the previous figure is confirmed here. For the ascending tracks we get a very convincing correlation result, whereas the correlation of the descending tracks cannot be regarded as significant.

From the physical point of view there is no good reason for a difference between the two orbital arcs. A plausible argument could be an asymmetry in the model. Using the results of the good correlation we may predict the variation in the field magnitude,  $dF$ , from the amplitude of the Pedersen current density,  $J_P$ . From the slope of the regression line we obtain

$$dF = 220 J_P \quad (2.51)$$

where  $dF$  is in nT and  $J_P$  in A/m. This number is valid for a height of about 350 km above the E-layer. For larger altitudes the factor will be smaller.

Nevertheless, we have obtained on average a quite satisfying linear relation between the estimated Pedersen current and the associated magnetic deflections. However, when using eq. (2.51) to predict the scalar disturbance field on a track-by-track basis, a rather large uncertainty is expected.

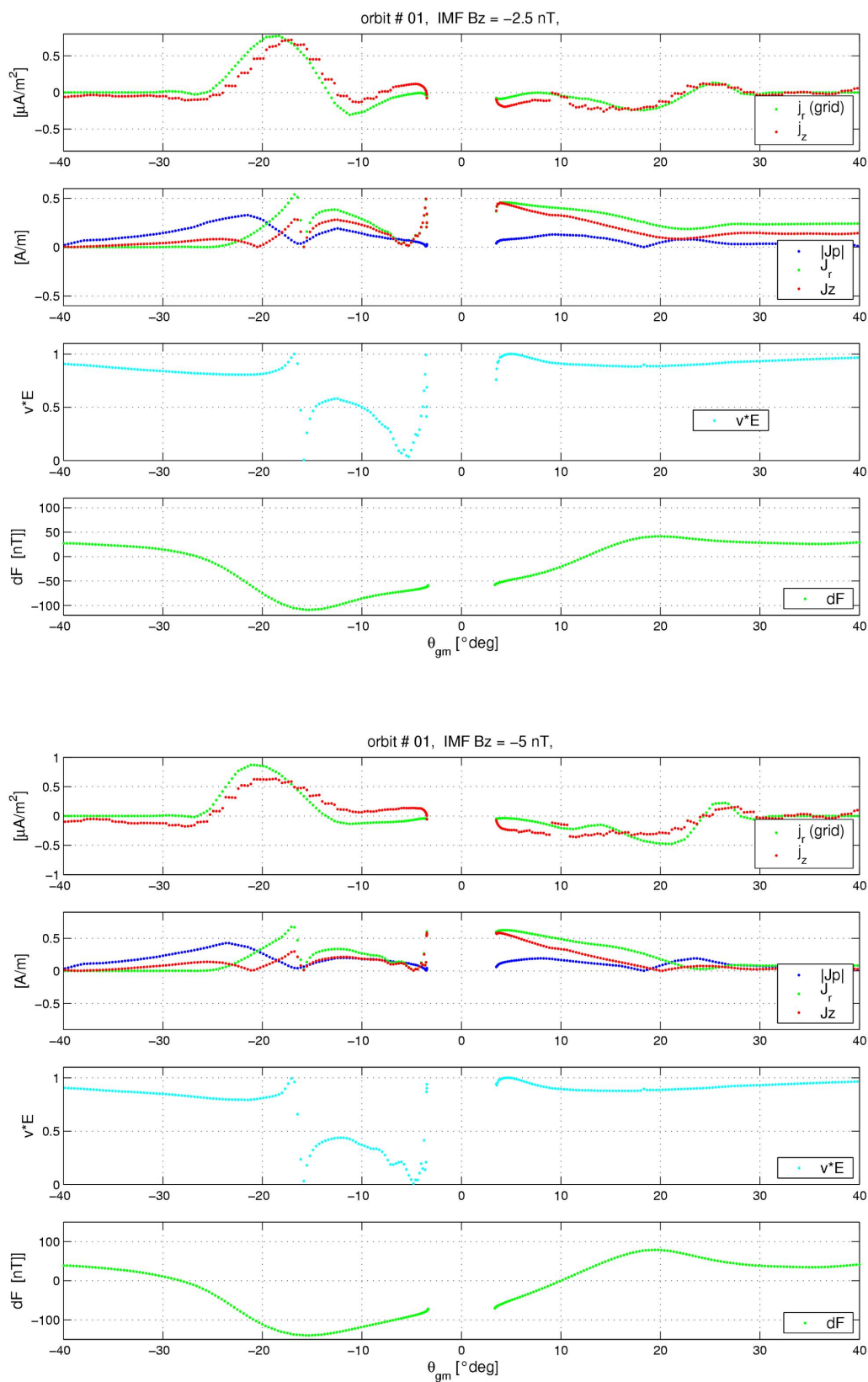


Figure 2.49: Same quantities as in Figure 2.48, medium activity (top), high activity (bottom).

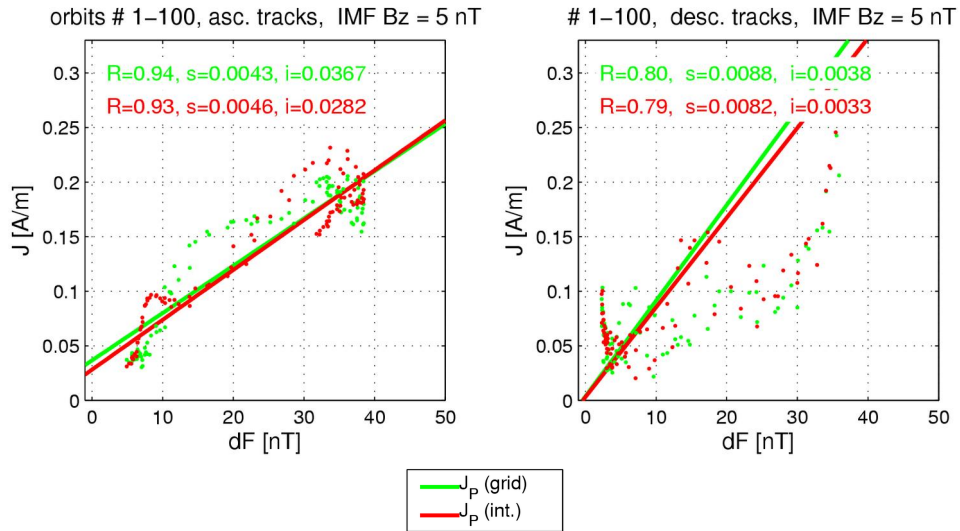


Figure 2.50: Correlation analysis between the peak Pedersen current density and the peak deflection in the total magnetic field for quiet conditions. Separate analysis for ascending and descending tracks.

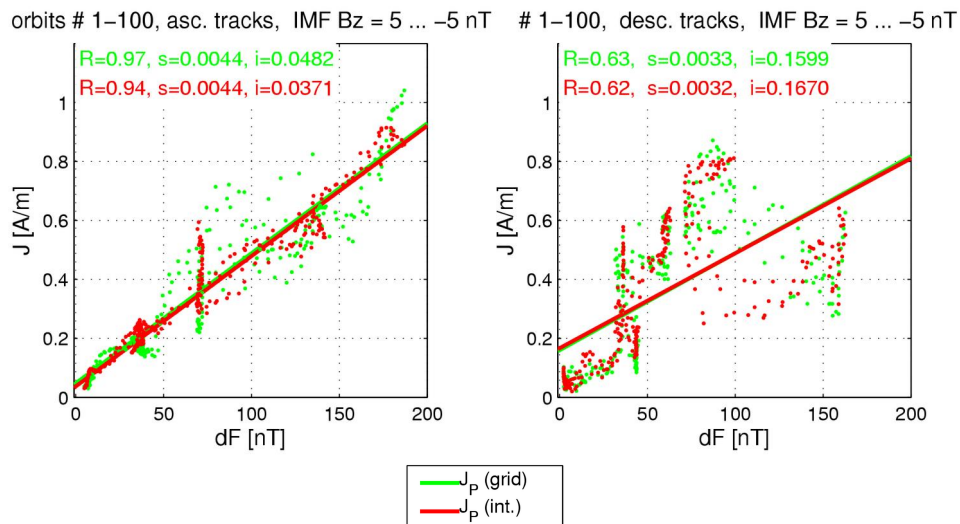


Figure 2.51: The same analysis as above, for all levels of activity.

## Direct comparison of FAC density and scalar residuals

Here, we want to present and test another approach to derive a disturbance index for the polar regions. It is based on the direct comparison between the signatures of the field-aligned currents and the residuals of the field magnitude. As can be seen from the top and bottom panels of Figure 2.48 these two quantities tend to vary in anti-phase. The physics behind this relation will be described in the following paragraphs.

An elementary field-aligned current filament carries charges into the ionosphere. These charges will set up a radial electric field. As a consequence, Hall currents flowing perpendicular to the  $E$  and  $B$ -field will circulate around the filament. These current circles, in return, generate a vertical magnetic field which is aligned with the FAC filament. Figure 2.52 shows schematically the distribution of these currents and fields for the reasonable case of vertical FAC geometry.

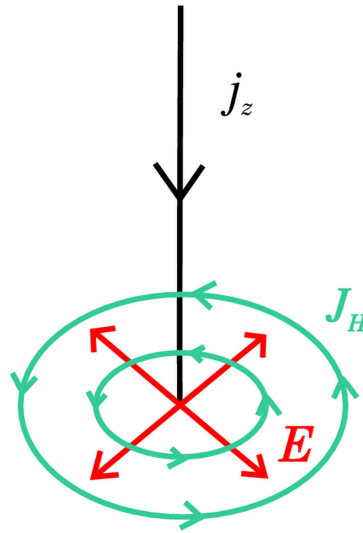


Figure 2.52: Schematic drawing of a vertical current flowing into the ionosphere. As a consequence, a radial electric field and circular Hall currents will be set up.

Using plane geometry and assuming a homogeneous conductivity distribution in the ionosphere we may rewrite eq. (2.32) in cylindric coordinates

$$j_z = \nabla \cdot (\Sigma_P \mathbf{E}(r)) = -2 \Sigma_P E_0 \frac{r_0^2}{r^3} \quad (2.52)$$

where  $E_0$  is the electric field at the radius  $r_0$  of the FAC tube. Here we made use of the  $E$ -field distribution around a band source

$$E(r) = E_0 \left( \frac{r_0}{r} \right)^2 \quad (2.53)$$

This electric field drives a Hall current

$$J_H(r) = \Sigma_H E(r) \quad (2.54)$$

An elementary Hall current loop generates a vertical magnetic field

$$b_z(r) = \frac{\mu_0}{2} \frac{J_H(r) r^2 dr}{\sqrt{r^2 + h^2}^3} \quad (2.55)$$

where  $dr$  is the width of current sheet and  $h$  the height of the measurement point above the current.

We can substitute  $J_H$  in eq. (2.55) by the electric field  $E(r)$ . To get the total magnetic effect of this current circuit we have to integrate over all radii

$$B_z(r) = \frac{\mu_0}{2} \int_0^\infty \Sigma_H E_0 \frac{r_0 dr}{\sqrt{r^2 + h^2}^3} \quad (2.56)$$

There is an analytical solution to this integral

$$B_z(r) = \frac{\mu_0}{2} \Sigma_H E_0 r_0^2 \frac{1}{h^2} \quad (2.57)$$

According to eq. (2.52) the electric field is caused by the field-aligned current. Therefore we can make use of the relation

$$E_0 = -\frac{r_0}{2 \Sigma_P} j_z \quad (2.58)$$

When inserting eq. (2.58) into eq. (2.57) we obtain

$$B_z(r) = -\frac{\mu_0}{4} \frac{\Sigma_H}{\Sigma_P} j_z \frac{r_0^3}{h^2} \quad (2.59)$$

As can be seen from eq. (2.59) there is a linear relation between the vertical current density  $j_z$  and the associated magnetic effect  $B_z$ . It decreases by the inverse of the square of the height above the current layer. The ratio between the conductances, on the other hand, can be regarded as rather constant.

The actual scaling factor between the FAC density and the deflection of the field magnitude is determined by a correlation analysis. Figure 2.53 shows the results for the quiet time conditions, separately for ascending and descending arcs. We find, as expected, a very good linear relation between the FAC density and the magnetic deflection for the ascending arcs. Results are less convincing for the descending arcs. In the next step we have again considered data from all levels of activity. Correlation results are shown in Figure 2.54. In this case we obtain a good linear relation for both ascending and descending tracks. Also the slopes and offsets of the regression lines are quite similar.

From these numbers we can deduce a relation to predict the amplitude of the field magnitude deflection,  $dF$ , from the vertical current density  $j_z$

$$dF = 280 j_z \quad (2.60)$$

where  $dF$  is in nT and  $j_z$  in  $\mu A/m^2$ . For a highly accurate modelling effort the peak deflection of the field magnitude should probably be smaller than 5 nT. This requires a resolution of the field-aligned currents of  $0.018 \mu A/m^2$ . As has been shown in Section 2.9 the major contribution in the FAC calculation comes from the along-track gradient of the cross-track component  $dB_y/dx$ . With a baseline of 38 km, as applied in Section 2.9, the field difference has to be determined to be better than 0.85 nT. The required accuracy of the vector magnetometer in this frequency range is 0.1 nT. Thus, the required resolution of field-aligned current density is compliant with the specification of the magnetometer.

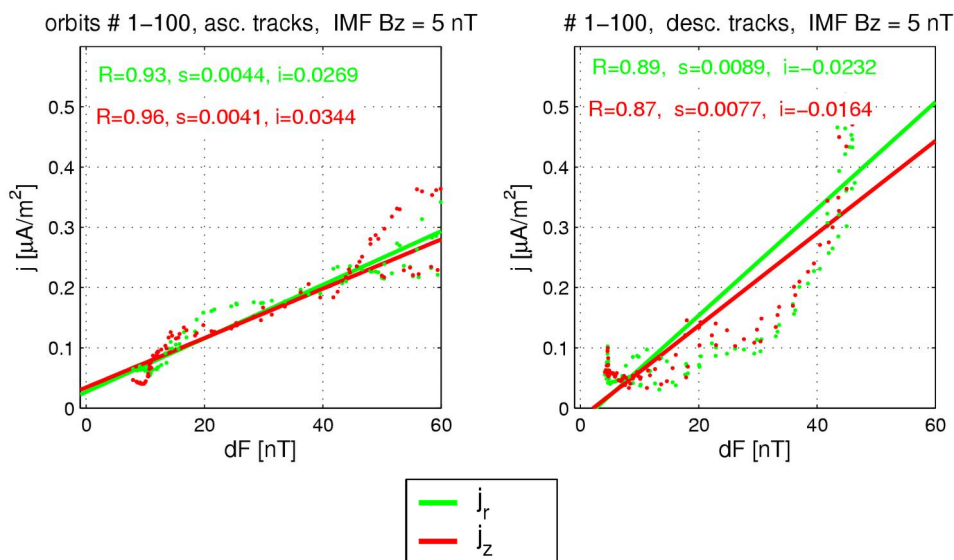


Figure 2.53: Correlation analysis between the peak FAC density and the field magnitude in the total magnetic field for quiet conditions. Separate analysis for ascending and descending tracks.

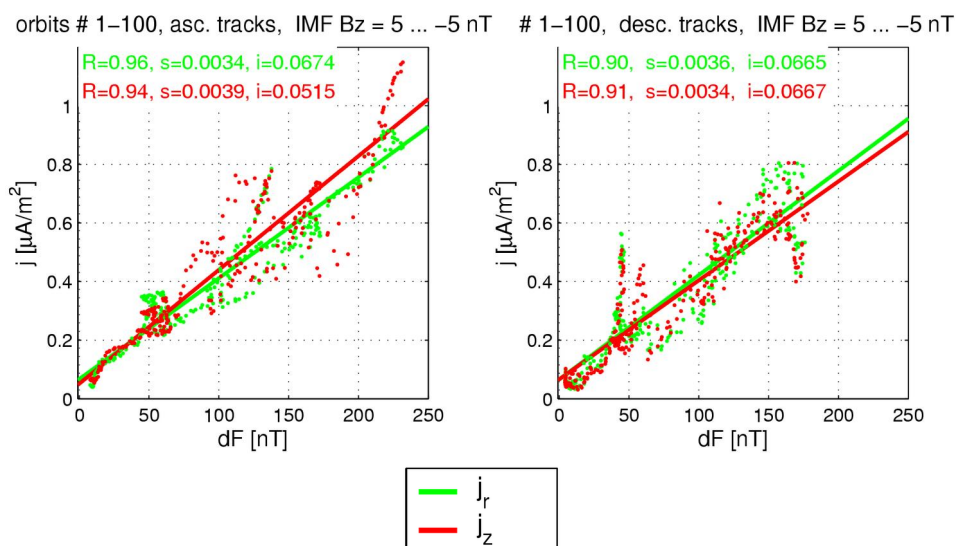
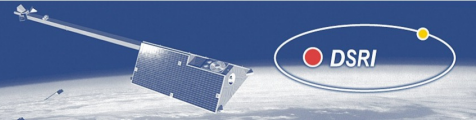


Figure 2.54: The same analysis as above, but for all levels of activity.



## Design of the activity index

In this section we have presented two approaches for deriving a local activity index for the polar region. The second technique, based directly on the FAC density, seems to be more promising. A proposal would be to take the predicted peak-to-peak amplitude of the field magnitude variation in nanoTesla and use it as the index value,  $AF$ . These estimates should be determined separately for the ascending and descending part of the track across the pole, because the two parts of the orbit sample very different local times.

The scaling factor between FAC and magnetic field deflection given in eq. (2.60) depends on the satellite altitude. It is, however, not expected to vary as rapidly as  $1/h^2$ , as suggested by eq. (2.59), since also  $j_z$  gets weaker at higher altitudes. This scaling factor has to be determined experimentally during different phases of the mission.

## Example with CHAMP data

For validation of the activity index  $AF$  we make use of CHAMP magnetic field data. The standard one-satellite approach was used to estimate the field-aligned current density (cf. eq. (2.38)). In order to mitigate the problem of underestimating the current density due to a small angle between the current sheet and the velocity vector (cf. Figures 2.40 and 2.41) we have rejected certain tracks from the analysis. The criterion for being accepted was an angle of attack larger than  $45^\circ$  between the mean auroral oval and the flight direction. The time interval chosen is December 2002. During the winter solstice the largest part of the auroral ionosphere in the northern hemisphere is in darkness. This is the time when quiet periods are expected.

For the calculation of the FAC density we have used magnetic field data averaged over 40s (equiv. to 300 km) to suppress the effects of small-scale features. A direct comparison between the FAC density and the variations in field magnitude is shown in Figure 2.55 for a few polar passes. As predicted by eq. (2.59) they are varying in antiphase. These plots can be compared directly with the associated curves in Figure 2.48. Both data sets are from similar local times.

The scaling factor between the FAC density and the field magnitude deflection is determined again by a correlation analysis. Figure 2.56 shows the results for ascending and descending tracks. There is quite some scatter of points, but a correlation coefficient of  $R = 0.76$  can still be regarded as significant. The regression algorithm used here provides the linear regression line with the lowest slope consistent with the uncertainty band. Therefore we have used the factor of the descending tracks. The amplitude of magnitude deflection  $dF$  may be predicted by

$$dF = 125 j_z \quad (2.61)$$

where  $dF$  is in nT and  $j_{\parallel}$  in  $\mu\text{A}/\text{m}^2$ . The scaling factor found here is only 45% of the one determined from the model data (cf. eq. (2.60)). This may be seen as an indication that the scales and shapes of typical FAC tubes, as represented by  $r_0$  in eq. (2.59), are larger in the model than in reality.

In order to test the reliability of the activity index we calculated  $AF$  for a quiet day and compared it with the actually observed peak-to-peak deflections of the scalar residuals. Using the derived scaling factor of eq. (2.61) yields results that are systematically too large. To obtain a reasonable distribution of differences for this quiet day we had to use  $dF = 80 j_z$ . Table 2.4 presents a comparison of the activity index with observed deflections for all orbits of that quiet day. As mentioned earlier, the accuracy of the index should be better than 10 nT. For the majority of the cases the differences are well below this limit. There are only a few outstanding

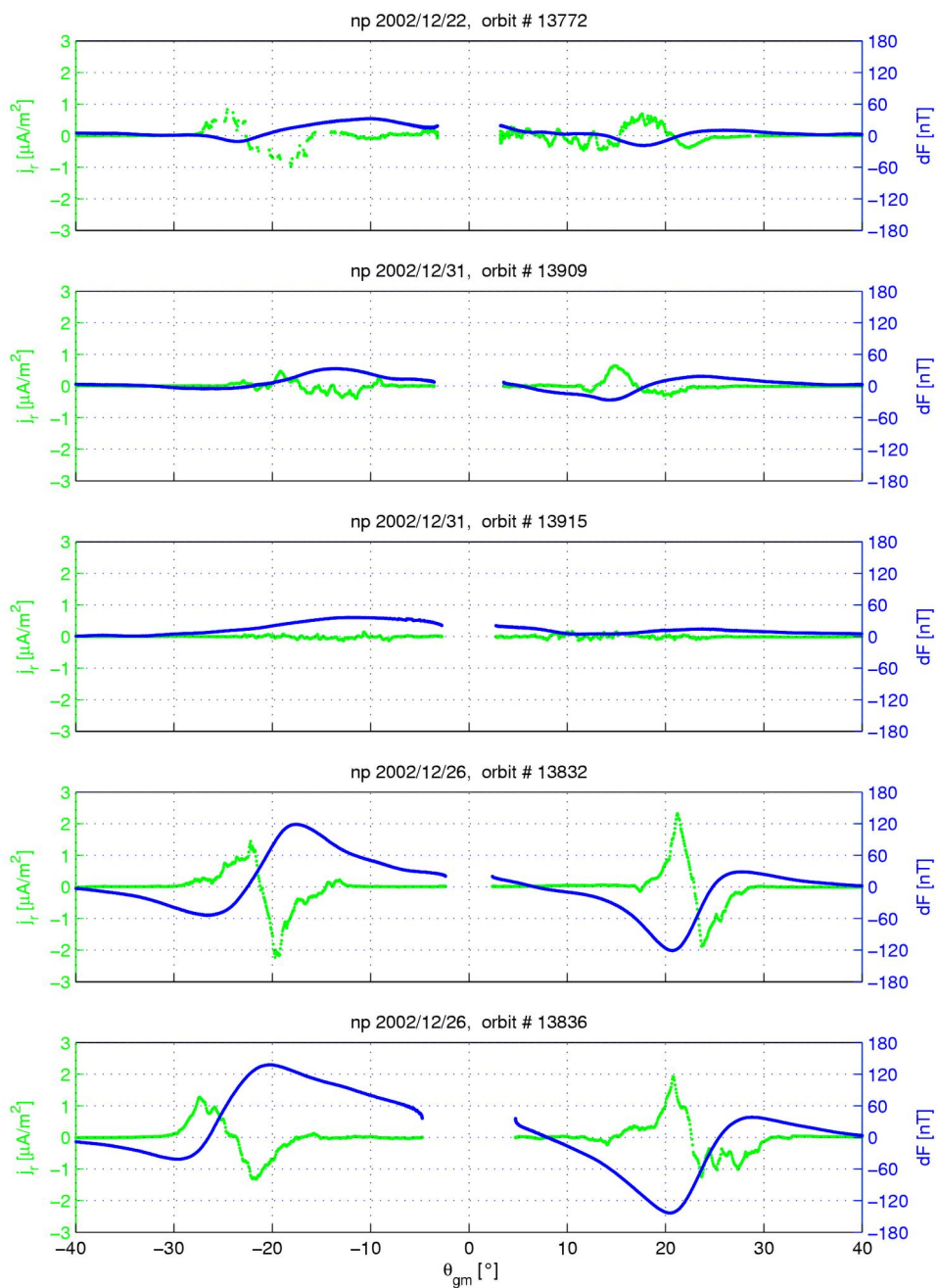


Figure 2.55: Direct comparison between field-aligned current density (green) and variations of the field magnitude (blue).

exceptions. It may be noted that, even on this quiet day, none of the orbits would have passed the  $AF < 10$  nT criterion.

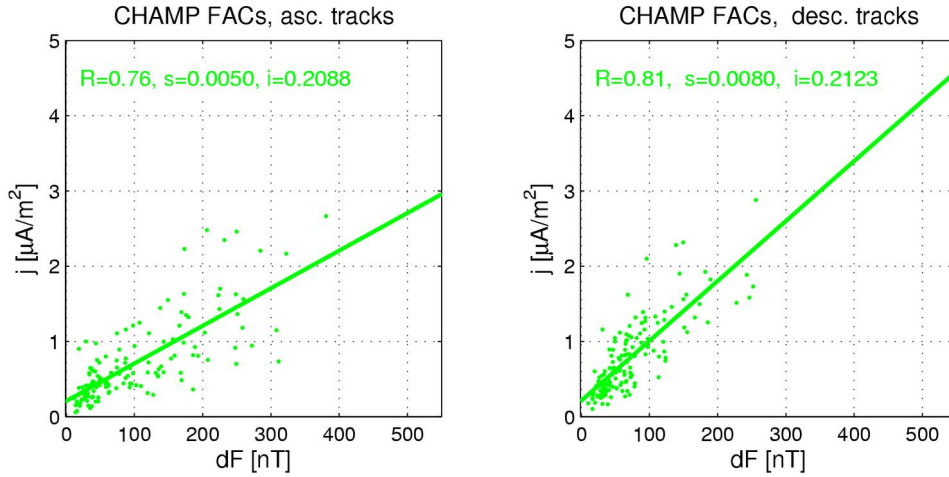


Figure 2.56: Correlation analysis of the peak FAC density and the field magnitude derived from CHAMP data.

orbit #	ascending tracks				descending tracks			
	$j_{\parallel}$	$AF$	$dF$	$\Delta$	$j_{\parallel}$	$AF$	$dF$	$\Delta$
1	0.4138	33.10	31.51	1.59	0.3778	30.22	33.68	-3.46
2	0.3438	27.51	26.58	0.92	0.3549	28.39	32.41	-4.02
3	0.1806	14.45	20.75	-6.30	0.2368	18.94	26.74	-7.80
4	0.2945	23.56	20.04	3.52	0.4331	34.65	20.46	14.19
5	0.2051	16.41	19.70	-3.29	0.1755	14.04	18.59	-4.55
6	0.2635	21.08	15.75	5.33	0.5439	43.51	13.20	30.31
7	0.2591	20.73	12.62	8.11	0.2372	18.97	16.57	2.41
8	0.1732	13.85	18.93	-5.07	0.6514	52.11	47.95	4.16
9	0.2047	16.38	15.45	0.93	0.2560	20.48	29.91	-9.43
10	0.3175	25.40	25.30	0.10	0.3447	27.58	28.17	-0.59
11	0.3743	29.94	31.80	-1.86	0.4554	36.43	42.40	-5.96
12	0.2576	20.60	46.97	-26.37	0.4303	34.42	39.91	-5.48
13	0.3954	31.63	58.40	-26.77	0.8928	71.42	41.15	30.27
14	0.3179	25.43	29.17	-3.74	0.2359	18.87	16.67	2.21
15	0.2907	23.26	26.65	-3.39	0.4141	33.13	24.76	8.37
16	0.3135	25.08	31.68	-6.60	0.4450	35.60	40.13	-4.53

Table 2.4: Comparison of the auroral activity index  $AF$  with the actually observed deflection in field magnitude  $dF$  using a scaling factor of 80.



## 2.12 Assessment of current estimates and conclusions

In the previous sections we have made use of the synthetic data set containing ionospheric currents and fields to develop and test methods for estimating ionospheric currents from *Swarm*-type observations at satellite altitude. The synthetic data are derived from global magneto-hydrodynamics (MHD) simulation runs of the near-Earth plasma dynamics. The underlying models represent the present state of the art. This data set provides the opportunity to develop and test new interpretation techniques by making use of the new opportunities provided by the *Swarm* constellation of satellites. The advanced results are compared with single-satellite retrievals to demonstrate the expected gain in accuracy.

A lot of attention has been paid to the determination of field-aligned currents (FAC). This is appropriate for two reasons:

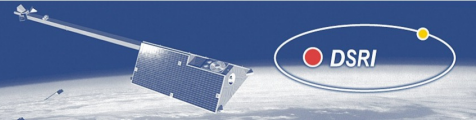
1. The FACs are the prime driver for the magnetic activity and heating in the auroral ionosphere, thermosphere. Knowing their distribution and intensity is of paramount importance for several kinds of upper atmospheric studies.
2. The *Swarm* constellation provides for the first time the opportunity to derive FAC densities uniquely from satellite observations. Results obtained from previous missions may be revised to check their validity.

The purpose of this study is to find out the quality of retrieved currents when using realistic *Swarm* orbit configurations. The current estimates are based on simulated measurements taken by the two lower satellites flying side-by-side separated in east-west direction. Since the sampling geometry is changing continuously, the quality of the curl-B method may also change.

The results presented in Section 2.9 are very promising. Reliable current densities can be obtained all along the orbit, as close as a few kilometres around the crossover point. From the comparison between the derived vertical currents and the associated model currents we find a small but systematic phase shift. Derived current features appear shifted poleward by a fraction of one degree in latitude. We believe that this effect is caused by the fairly large grid spacing which is 160 km in latitude ( $\theta$ ) and  $320 \text{ km} \cdot \sin(\theta)$  in longitude. These distances are significantly larger than the sampling (38 km along-track and  $\approx 165 \text{ km} \cdot \sin(\theta)$  cross-track). The linear interpolation of sampling points cannot restore the details of the signal. A denser gridding of the synthetic data may solve the problem. The investigation of this effect could be the topic of a follow-on study.

Prominent discrepancies occur close to the poles. This is probably due to the singularity of the spherical components at the poles. Here, the horizontal components,  $B_\theta$  and  $B_\phi$ , switch sign. When interpolating across the pole spurious values are obtained. The choice of a different coordinate system for the synthetic data can solve this problem. In a real application the computation will be done in geocentric coordinates. The immediate vicinity of the singular point at the geographic pole will then be left unsampled with the present orbit configuration and the cross-over points coincide with the closest approaches to the poles. Omitting data in the vicinity of those points will enlarge the uncovered area at the poles only slightly, but would cure both problems.

There is another point that should be stressed here. The curl-B technique interprets only the toroidal part of the magnetic field. For that reason, the results of the field-aligned currents will only marginally be influenced by spurious residuals of the main and crustal fields and from the ring current. Those kinds of field components can be described by a scalar potential and



thus do not contain toroidal fields. This characteristic will be of importance in the later part when designing an activity index.

For comparison, the same data have been used in a single-satellite approach for estimating field-aligned currents. In many cases the obtained FAC densities compare very well with the model currents. As expected, the computed values fall short, 50% in some cases, when the angle of attack between the satellite velocity vector and the orientation of the FAC sheet is significantly smaller than  $90^\circ$ . This indicates the degree of uncertainty inherent in present-day field-aligned current studies.

In Section 2.10 the capability of the *Swarm* mission is explored to recover the horizontal ionospheric currents. This task is more demanding, since the satellites do not fly through the currents. For that reason a model for the currents is required. Here, a series of line currents is employed. This approach has been demonstrated to provide very reliable results when applied to CHAMP magnetic field data and compared to current estimates from ground-based observations (Ritter et al. [2004b]).

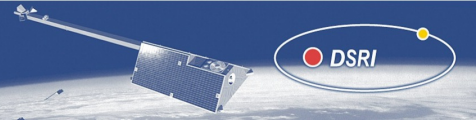
Applying this approach to our synthetic data set of currents and fields reveals mixed results. In some parts of a polar pass the agreement between retrieved and model current is good, in others there are large deficits. In this *Swarm* simulation we have also the electric field available. This allows to determine not only the current intensity but also its direction. Generally, it may be stated that, when the total current estimate is good, the two current components also agree well between model and estimate. For that reason we have to find out why the current estimates do fall short in some areas.

There are a number of assumptions entering the retrieval approach. Some of them may not be satisfied. One of them is the expected current closure of the Hall currents in the E-layer. It is quite obvious from the model current distribution in Figure 2.43 that this is not fulfilled in the simulated case. Another reason may be that the inversion sometimes is an ill posed problem. This is the case when our approach is applied to a region of fairly homogeneous current distribution. In Figure 2.43 it can be seen that the orbit crosses such a region in the pre-noon/dawn sector. Just on that ascending part of the tracks a poor agreement is reached between estimate and input.

The difference in quality between the results obtained here and in the study by Ritter et al. [2004b] may probably be attributed to deficiencies of the employed MHD model. The so-called Region 2 field-aligned currents, another ring of FACs just equatorward of the present ring, is missing in the model. This additional field-aligned current system causes a much stronger confinement of the currents in the polar regions. In such a case our current inversion problem is conditioned much better. Global MHD models that include the Region 2 field-aligned currents are presently in development and may be employed in a later simulation study.

A quite important topic is addressed in Section 2.11, the design of an activity index for the auroral region. Using an appropriate data selection strategy for the main and crustal field modelling will help to improve the accuracy. Up to now there is no effective indicator available for a suitable data selection at high-latitudes. Here we present two possible alternatives which could be used for this purpose. Both make use of the reliably-determined field-aligned current densities.

In the first case the FAC density is integrated along the orbit trajectory. Scaling the integral with the direction cosine between satellite velocity and electric field reveals an estimate of the Pedersen current. Pedersen currents are related to Hall currents by the ratios of the respective conductances. From Section 1.3 we know that a linear relation between the total field deflection and the Hall current density can be assumed (cf. eq. (2.41)). Therefore, an activity index can be derived from the integrated FAC density. In a statistical analysis the correlation between the



peak deflection of the field magnitude and the maximum in estimated Pedersen current density was determined. When considering only quiet conditions we obtained good results from data of the ascending arcs and poor ones from the descending parts. When taking all levels of activity into account satisfying and consistent results are obtained again for the ascending branch, but not for the descending. The descending tracks in this case are sampling the dawn side of the polar region (cf. Figure 2.43). In this area also the Hall current estimates fell short. Here the expected relations between vertical and horizontal currents are obviously not well satisfied.

The second approach for deriving an activity index is even more elegant. It relates the field-aligned current density directly with the deflection of the magnetic field magnitude. An analytical expression for that is given in eq. (2.59). For a derivation of an index peak-to-peak values of the FAC density are compared with that of the magnitude variations. In a correlation analysis we find a good linear relationship between these two quantities when taking all activity levels into account. Here again we get a slightly worse result from the data of the descending arcs. Supporting the afore mentioned suspicion of a somewhat unphysical relation between horizontal and vertical currents in that area.

The virtue of this index is that it relies entirely on the derived field-aligned currents. As has been mentioned before, the quality of this quantity does in principle not dependent on the accuracy of the models that have been used to subtract the internal and external field contributions. Therefore, no feedback effect is expected. The linear scaling factor derived in the correlation analysis can be used to predict the amplitude of the field variations at high latitudes. It is proposed to use the predicted peak-to-peak deflection in field magnitude as the value for the index. Separate numbers should be derived for the ascending and descending arcs and for both hemispheres. By setting a certain threshold for the activity quiet orbit segments can be selected from the predictions.

As a test of this index real data of the CHAMP magnetometers have been used. In spite of the limitations of field-aligned current density estimates from single satellites, interesting results could be obtained. First of all, the predicted, antiphase variation of the FAC density and field magnitude could be confirmed. The correlation analysis, on the other hand, revealed a much smaller factor between magnitude variation and the FAC density as had been calculated from the synthetic model data. This is good, since it reduces the required accuracy of the FAC density for obtaining proper index values,  $AF$ .

The reason for this difference of the factors may partly be due to the lower altitude of CHAMP at that time ( $\approx 400$  km), and, to a larger extend, it may also be due to the scale sizes of the FAC tubes as observed by CHAMP compared to the ones in the MHD model.

Quite a strong scatter of points can be seen in the correlation between the FAC density and the field magnitude variation. The scatter may probably be reduced by choosing the filter for the FAC density data in a way that the same wavelength is considered to be present in the magnitude deflections. This is, however, a topic that cannot be accomplished with model data, but has to be fitted to the spectrum of the real observations.

The amount of variability in the field magnitude even on a very quiet day is shown in Figure 2.57. If we accept arcs with a peak-to-peak variation of 10 nT, only few are left. A reliable activity index is required to pick out these valuable tracks. At present, the uncertainty of the index  $AF$  is only slightly below the threshold value of 10 nT and the yield is presently not optimal. We may conclude that the calculation of the activity index  $AF$  needs further refinement. However, the approach of making use of FAC density data seems to be promising.

2002/12/12 north pole

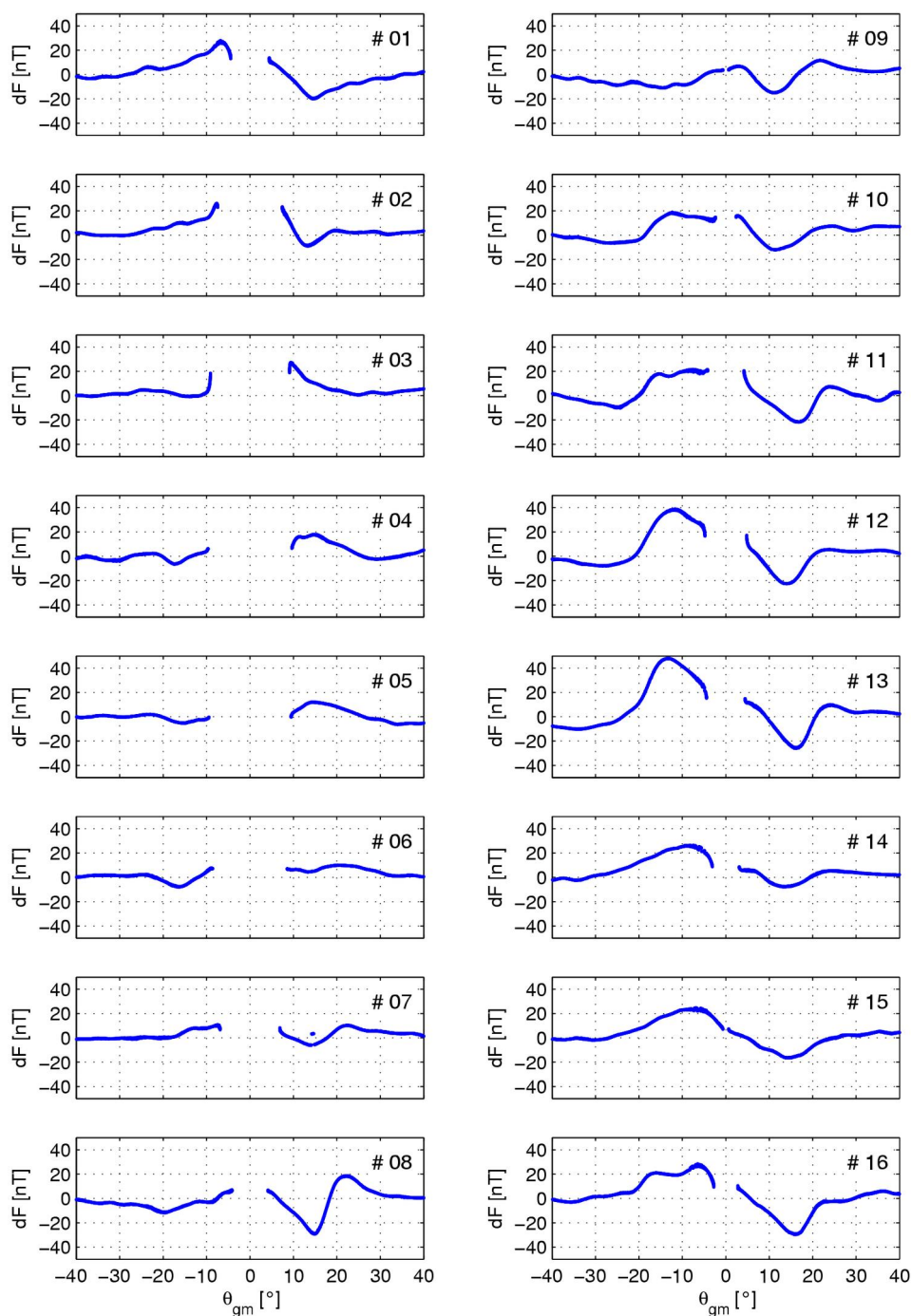


Figure 2.57: Variations of the total magnetic field on a very quiet day measured by CHAMP at the north pole during winter.

Objective	Used method	Achievement	Impact on field modelling	Suggested improvements
Field-aligned current determination	curl-B method applied to the pair of spacecraft flying side-by-side.	Unique determination of field-aligned currents; excellent agreement with input currents.	Indicator of magnetic activity since field-aligned currents are the prime drivers for the electrodynamic at auroral latitudes.	Further tests with the curl-B method should be performed including synthetic data in a more suitable coordinate system and denser gridding.
Estimation of horizontal ionospheric currents	Fitting of a discrete line current model by inversion of scalar magnetic field residuals; current direction deduced from electric field.	Determination of source-free current distribution in ionosphere; satisfying results in active regions, deficits in areas of large-scale homogenous currents.	The locally determined current densities can be used for parameterisation of auroral current models.	Development of a comprehensive approach which solves for the field-aligned and horizontal currents at the same time by interpreting the magnetic and electric fields at both spacecraft.
Auroral activity index AF a) based on ionospheric closure currents b) based on field-aligned current intensity.	Integration of field-aligned current density along electric field direction; peak values is the measure for AF.  Direct correlation of averaged field-aligned density and scalar residuals.	Estimation of ionospheric closure current; a reasonable correlation with scalar residuals is achieved.  Generation of activity index AF from well-determined field-aligned currents.	The new auroral activity index AF will be used for high latitude data selection.	No further development of method considered.  Further development of this promising method; tests with real data; comparison with other activity indicators.

Table 2.5: Summary.

## 2.13 Suggestions for further studies

### Global Pattern of Field-Aligned and Ionospheric Currents in the Polar Regions

In the present study it has been shown that the *Swarm* constellation and instrumentation can be used to determine local field-aligned current intensities, and to some extent also the intensity of the accompanying ionospheric currents at the satellite path. However, in order to estimate properly the contribution to the magnetic field caused by the external current system, it is necessary, not only to estimate the currents traversed by the satellite, but to estimate the global pattern of field-aligned and ionospheric currents in the polar region. Such an estimate would also be a highly relevant contribution to space-weather studies.

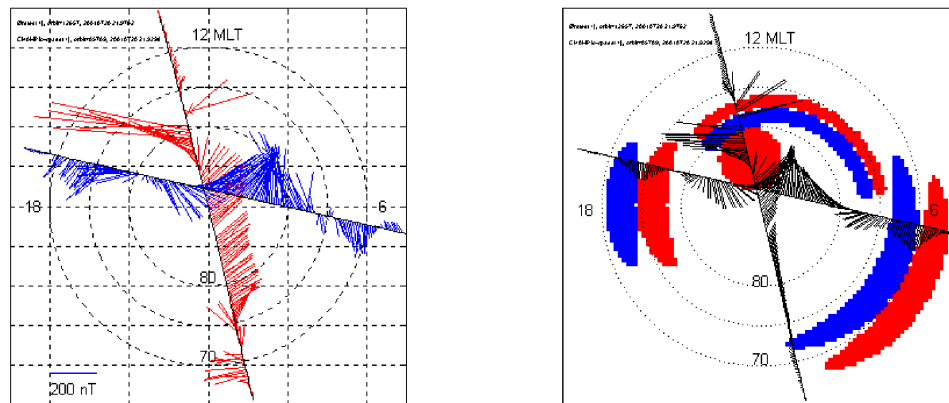


Figure 2.58: An example of a simple modeling of the global current system in the polar region, based on data from crossing tracks of the Ørsted and CHAMP satellites [Vennerstrøm et al., 2002].

A natural and highly interesting extension of the present study would therefore be to examine the possibility to use the *Swarm* constellation and instrumentation to assess the global pattern of field-aligned and ionospheric currents in the polar regions. Statistical studies have shown that the field-aligned currents can be divided into a number different parts, most importantly region 1 and region 2 currents and NBZ-currents, and that the intensity, location and extension of these currents vary both with the solar wind parameters, the state of the magnetosphere and with season. Two important questions arise:

- To what extent is it possible to parametrize the field-aligned and accompanying ionospheric currents, for example based on parameters such as intensity and location of the separate parts of the system? Is this parametrization possible at an instantaneous basis, corresponding to a satellite pass of the polar region? How many, and which parameters are necessary?
- Is it possible to use the *Swarm* magnetic and electric field measurements to retrieve these parameters for each polar pass? Will the ability be significantly improved if the swarm data are combined with additional data as for example solar wind data, and/or groundbased geomagnetic activity measures?

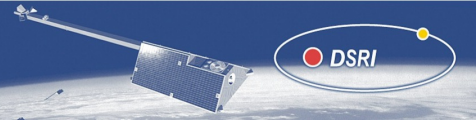


Figure (2.58) shows a simple example of such a parametrization, here of the field-aligned currents. Crossing tracks of the Ørsted and CHAMP satellites (right) are interpreted in terms of a simple model of field-aligned currents. Separate FAC's are parametrized by their intensity, width and location, and the resulting magnetic perturbation along the satellite tracks is computed. The parameters are then varied until the observed and modeled magnetic perturbation compare. The tools developed in the present study, i.e. the programs for a fast computation of the magnetic field perturbation due to a 3-D current pattern on a spherical grid, would be perfectly suited to extend such studies beyond the single event study. The inclusion of the ionospheric currents in the modeling, in a consistent way, would be another natural extension.

A successful parametrization of the global pattern of currents in the polar region would form a strong basis for monitoring geomagnetic activity in this region.

### Space weather model validation and development

The present study has benefited greatly from a very fruitful collaboration with the Community Coordinated Modeling Center. Through this collaboration we have access to state-of-the-art space weather models that can provide us with global predictions for the ionospheric fields and currents. In return, the current study has provided valuable feedback to the model developers regarding the consistency and accuracy of the models. The development of realistic and precise predictive models is the main goal of current space weather research activities. Model validation through comparisons with observations is a very important component hereof. Another important objective is the development of methods to further constrain the models by assimilation of observational data. It is obvious that *Swarm* can make valuable contributions to both of these tasks. In preparation hereof, it would be very useful to continue the collaborative efforts with the modeling center that was initiated in the present study. Using observations from the current Ørsted and CHAMP missions as well as simulated future *Swarm* data we can address the following questions:

What are the most important factors determining how well the model output match the measurements of magnetic fields and currents? How do we best define quantitative measures for the agreement to monitor improvements? Can the *Swarm* measurements be used in a systematic way to drive space weather prediction models? How can the *Swarm* observations be used to further model development?

Figure 2.59 shows an example of a comparison between magnetic field measurements and model predictions for a single CHAMP orbit, similar to the previously shown figures comparing model and satellite data, but for a more active period.

### Night-time Ionospheric Currents at Mid and Low-Latitude

Another topic, more related to the accurate determination of the core and lithospheric field, concerns night-side ionospheric currents at middle and low latitudes.

Data used in modelling the core and lithospheric field are typically taken from the nightside orbital arcs on magnetically quiet days, in order to minimize external contributions. However, ionospheric currents flowing predominantly below the satellite generate magnetic fields which can hardly be separated from the internal field sources. During the dark hours conductivity of the ionospheric *E*-region – the layer where most of the horizontal currents are flowing, located at about 100-150 km altitude – is reduced by about two orders of magnitude.

However, the situation is somewhat different when taking also the *F*-region (altitude 150 - 1000 km, i.e. *Swarm* satellite altitude) into consideration. More than 30 years ago [Rishbeth \[1971, 1981\]](#) has proposed a *F*-region dynamo which is expected to be particularly effective at

## CHAMP orbit 9296 March 9, 2002

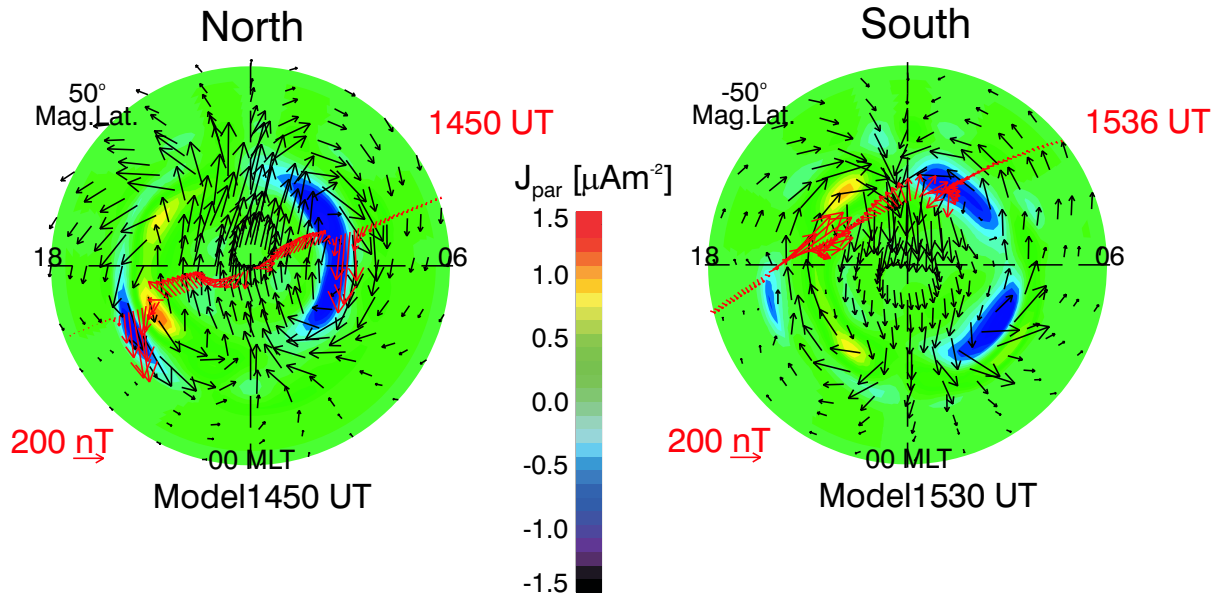


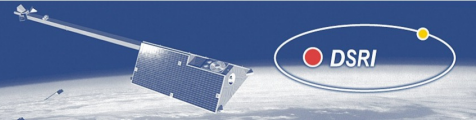
Figure 2.59: The model field-aligned current density (background color scale) and horizontal magnetic field variation vectors (black arrows) over the high latitude polar regions at two times corresponding to the passage over the North and South pole, respectively, of the CHAMP satellite. Overlaid are the horizontal magnetic variation vectors measured by the CHAMP satellite (red arrows) along the satellite track.

low latitudes during the night-time. Up to now, however, there is little observational evidence of the importance of these currents.

In a recent study, Lühr et al. [2002] have found evidence for  $F$ -region currents in the equatorial region during the post-sunset hours. Fairly small-scale current circuits (some 100 km) are set up along the Appleton electron density anomaly appearing on both sides of the dip equator. These currents are associated with plasma instabilities such as the so-called plasma bubbles. The magnetic effect caused by these currents is of the order of 5 nT in the satellite data. So far there has never been a comprehensive study published on the occurrence of currents on the nightside and their implications on field modelling - a research topic that should be investigated for optimal use of the *Swarm* data.

## Chapter 3

# Magnetic Field Contributions Produced by Ocean Flow



## 3.1 Introduction

This section details the results of modelling of motionally induced magnetic fields from global oceanic circulation as part of the Task 1: Forward modelling of external and oceanographic contributions to *Swarm* observations. It relates in particular to work packages (WP) WP-2100 and WP2200.

Several modelling studies on motionally induced magnetic fields in ocean were carried out in the past three decades (Sanford [1971], Larsen [1973, 1992], Junge [1988], Chave and Luther [1990], Lilley et al. [2001], Stephenson and Bryan [1992], Flosadottir and Smith [1997], Tyler [1992], Tyler et al. [1999]). Most of them were theoretical predictions and/or observationally supported in a regional scale. Land based magnetic and electric field measurements and under-sea-cable voltage measurements were used to validate the predictions. Recently, Tyler et al. [2003] correlated M2 tide induced magnetic signals with CHAMP magnetic measurements, on a global scale. The scope for the present simulation comes from these advances - 1) The increased reliability and resolution of global oceanic circulation models, 2) High precision satellite magnetic field measurements and 3) Better understanding of internal and external contributions to the Earth's magnetic field.

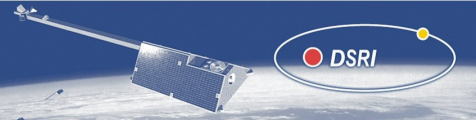
Vector magnetic field components are computed at *Swarm* satellite altitude (430 km from sea level) from oceanic circulation data by employing a 3D global EM induction code. The magnetic field signatures related to oceanic circulation, and their variation are in the range  $\pm 1.5$  nT. The global oceanic circulation model used for the present study, basic inputs and the model outputs are described in section 3.2. Section 3.3 deals with the basic assumptions, equations and derivations relevant to motional EM induction problem. Section 3.4 describes the results of the simulations. Here the effects of seasonal variation (3.4.1) and El Niño (3.4.2) on the computed magnetic fields are discussed. Conclusions and scope for further simulation studies are outlined in section 3.5.

## 3.2 Ocean circulation model

In order to compute the induced electromagnetic field generated by the ocean circulation, a reliable global ocean state estimator is required. An ocean state estimator combines ocean circulation model and incorporates a large amount of observations from diverse platforms. The ocean state estimator used for the present study is from the Consortium for Estimating the Circulation and Climate of the Ocean (ECCO) (Fukumori et al. [1999]), a scientific collaboration between Jet Propulsion Laboratory, Massachusetts Institute of Technology and Scripps Institution of Oceanography (<http://www.ecco-group.org>). The central element for this activity is a numerical circulation model that is constrained by (combined with) ocean data. To generate time varying ocean circulations is one of the aims of ECCO and is particularly suited for use with *Swarm* simulations. This allows us to compute time variability (realistic) of magnetic field associated with the ocean flow.

### 3.2.1 The ECCO 1 (1992 – 2002) model run

The ocean circulation data used for *Swarm* simulation are from ECCO 1 model run by ECCO group, assimilating observed data for the period 1992 to 2002. The ECCO model is based on the MIT general ocean circulation model, developed at the Massachusetts Institute of Technology (Marshall et al. [1997]). Using model Adjoint (Marotzke et al. [1999]) approach, ECCO model is forced to be consistent with the World Ocean Circulation Experiment (WOCE) observations,



within a specified error limit (Koehl et al. [2003]). The model run by ECCO consortium was configured globally with  $1^\circ$  horizontal resolution within  $\pm 80^\circ$  latitude with 23 levels in the vertical axis (Table 3.2.1). The model topography was taken from NOAA ETOPO2 bathymetry.

Level	Thickness	Layer Center	Level	Thickness	Layer Center
1	10	5	12	200	610
2	10	15	13	275	847.5
3	15	27.5	14	350	1160
4	20	45	15	415	1542.5
5	20	65	16	450	1975
6	25	87.5	17	500	2450
7	35	117.5	18	500	2950
8	50	160	19	500	3450
9	75	222.5	20	500	3950
10	100	310	21	500	4450
11	150	435	22	500	4950
			23	500	5450

Table 3.1: Model layer thicknesses and center depths (m)(From Koehl et al. [2003]).

### 3.2.2 Input data to the model

The ECCO 1 model was forced by daily fields of surface heat and fresh water fluxes and twice daily values of wind stress obtained from National Centre for Environmental Prediction / National Center for Atmospheric Research re-analysis project (Lu et al. [2003]). The other data assimilated to the model were river runoff, Sea Surface Height (SSH) from European Remote Sensing Satellite (ERS) and TOPEX/Poseidon satellite missions, Sea Surface Temperature (SST), WOCE hydrographic sections, Sea Surface Salinity (SSS) observations, Expendable Bathythermograph (XBT) and Tropical Ocean Global Atmosphere – Tropical Atmosphere Ocean (TOGA TAO) temperature profiles, temperature and salinity profiles from Profiling Autonomous Lagrangian Circulation Explorers (P-ALACE), ARGO (A global array of profiling floats) floats, monthly wind stress from ERS/ NSCAT/ QSCAT and mean 15 m drifter velocities. For further information on data constraints see Lu et al. [2003].

### 3.2.3 The outputs from the model

The major outputs from the ECCO 1 model run are bottom pressure, net shortwave heat flux, salinity, sea surface height, surface heatflux, surface salt flux, temperature, velocity (vertical, meridional and zonal) and wind stress (meridional and zonal). These data products (monthly) are available at a horizontal resolution of  $1^\circ$  for entire globe, within  $\pm 80^\circ$  latitude for the period 1992 to 2002. Out of these model outputs, the horizontal velocity data for the years 1997 to 2000 and 2002 were used for the present study.

### 3.2.4 Modifications of the output for *Swarm* study

As the horizontal components of velocity are computed on a ‘staggered’ grid, they were interpolated to a common  $1^\circ \times 1^\circ$  grid for all the vertical levels. Later the data were vertically

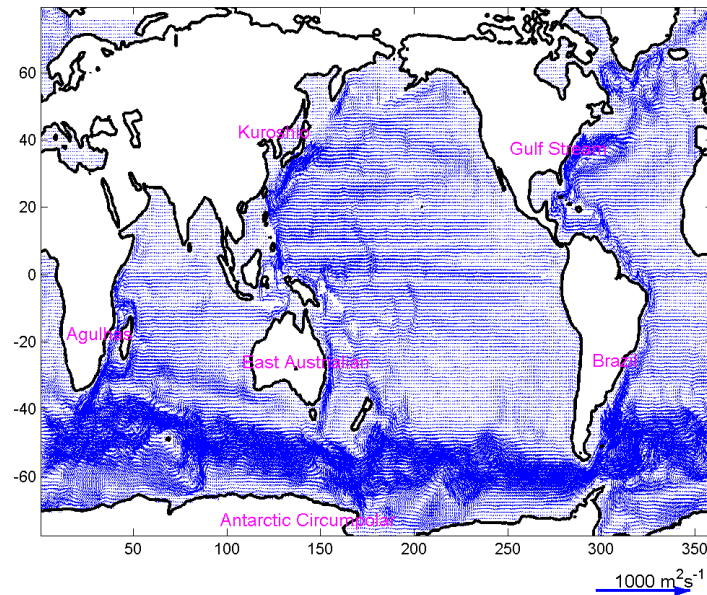


Figure 3.1: Global distribution of depth-integrated velocities for the year 2022 (in  $m^2s^{-1}$ ).

integrated. This resulted in the velocity field  $U(u,v)$  ( $m^2s^{-1}$ ) defined at the centre of every cell in the grid. Monthly data were grouped to make seasonal and event averages needed for *Swarm* simulations.

### 3.2.5 General description of the data

Integrated velocity vectors for the year 2022 are shown in Figure 3.1. The most prominent feature is the Antarctic Circumpolar current. Continental barriers prevent similar features in the Northern Hemisphere. Less prominent features are the poleward flowing western boundary currents. Kuroshio and Gulf Stream are examples from the Northern Hemisphere, whereas Brazil, East Australian and Agulhas streams are examples from the Southern Hemisphere. Figure 3.2 shows the depth distribution of the velocity data. Plotted are the zonal components of the velocity field, from a profile in the South Pacific Ocean. Velocities decrease rapidly with depth, reaching negligible values for depths  $> 2000$  m.

## 3.3 Numerical approach to calculate electromagnetic field due to ocean flow

### 3.3.1 Governing equations

To calculate the magnetic fields due to global ocean steady flow we have adopted the numerical solution described in (Kuvshinov et al. [2002], Kuvshinov and Olsen [2005], Kuvshinov et al. [2005]). The solution is based on a volume integral equation (IE) approach and allows simulating the electromagnetic (EM) fields, excited by arbitrary sources in three-dimensional (3D) spherical models of electric conductivity. These 3-D models (see Figure 3.3) consist of a number of anomalies of conductivity  $\sigma_{3D}(r, \vartheta, \varphi)$ , embedded in a host section of conductivity  $\sigma_b(r)$ . Here

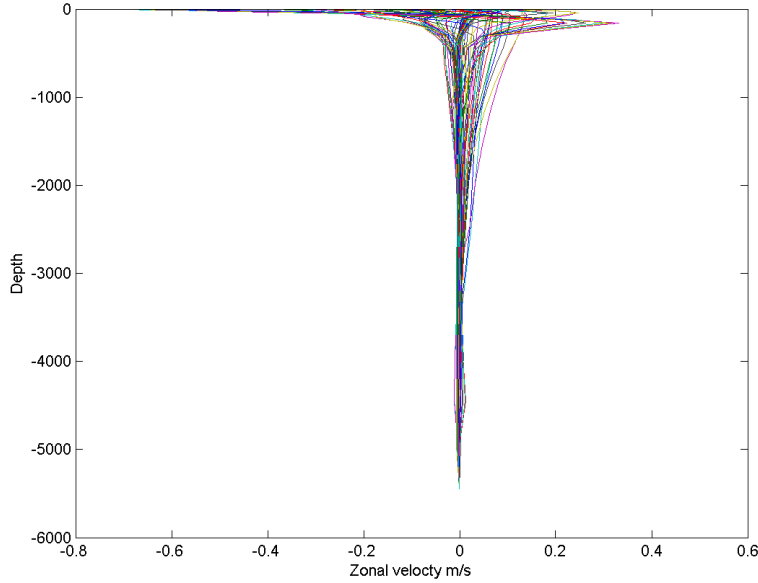


Figure 3.2: Stacked velocity (zonal) - depth profiles.

$\vartheta, \varphi$  and  $r$  are co-latitude, longitude and the distance from the Earth's centre, respectively. Within this approach Maxwell's equations in the frequency domain,

$$\nabla \times \mathbf{H} = \sigma \mathbf{E} + \mathbf{j}^{ext}, \quad (3.1)$$

$$\nabla \times \mathbf{E} = i\omega \mu_o \mathbf{H}, \quad (3.2)$$

are reduced, in accordance with the modified iterative-dissipative method [Singer, 1995], to a scattering equation of specific type (cf. Pankratov et al. [1997])

$$\chi(\mathbf{r}) - \int_{V^{mod}} K(\mathbf{r}, \mathbf{r}') R(\mathbf{r}') \chi(\mathbf{r}') dv' = \chi_o(\mathbf{r}), \quad (3.3)$$

which is solved by the generalized bi-conjugate gradient (BCG) method [Zhang, 1997]. In the equations above  $\mathbf{j}^{ext}$  is the exciting current, its time-harmonic dependency is  $e^{-i\omega t}$ ,  $\mu_o$  is the magnetic permeability of free space,  $i = \sqrt{-1}$ ,  $\omega = 2\pi/T$  is the angular frequency,  $T$  is the period of variations,  $\sigma$  is the conductivity distribution of the model,  $\mathbf{r} = (r, \vartheta, \varphi)$ ,  $\mathbf{r}' = (r', \vartheta', \varphi')$ ,  $V^{mod}$  is the modelling region and

$$R = \frac{\sigma - \sigma_o}{\sigma + \sigma_o} \quad (3.4)$$

$$K(\mathbf{r}, \mathbf{r}') = \delta(\mathbf{r} - \mathbf{r}')I + 2\sqrt{\sigma_o(r)}G_o^e(\mathbf{r}, \mathbf{r}')\sqrt{\sigma_o(r')}, \quad (3.5)$$

$$\chi = \frac{1}{2\sqrt{\sigma_o}}((\sigma + \sigma_o)\mathbf{E}^s + \mathbf{j}^s), \quad (3.6)$$

$$\mathbf{j}^s = (\sigma - \sigma_o)\mathbf{E}^o, \quad (3.7)$$

$$\mathbf{E}^o = \int_{V^{ext}} G_o^e(\mathbf{r}, \mathbf{r}') \mathbf{j}^{ext}(\mathbf{r}') dv', \quad (3.8)$$

where  $\delta(\mathbf{r} - \mathbf{r}')$  is Dirac's delta function,  $I$  is the identity operator,  $V^{ext}$  is the volume occupied by the exciting current  $\mathbf{j}^{ext}$ ,  $\mathbf{E}^s = \mathbf{E} - \mathbf{E}^o$  is the scattered electric field,  $G_o^e$  is the  $3 \times 3$  Green's tensor of the 1-D reference conductivity  $\sigma_o(r)$ . Note that, in order to provide optimum efficiency of the scattering equation solution (3.3), which in operator form can be written as

$$A\chi = \chi_o, \quad (3.9)$$

with  $A = I - KR$ , the reference conductivity  $\sigma_o(r)$  is chosen in a special way (cf. Singer [1995]). More specifically, outside the depths occupied by the inhomogeneities,  $\sigma_o(r)$  is equal to the conductivity of the host section,  $\sigma_b(r)$ , but at depths with laterally inhomogeneous conductivity distribution it is,

$$\sigma_o(r) = \sqrt{\min_{\vartheta, \varphi} \sigma(r, \vartheta, \varphi) \max_{\vartheta, \varphi} \sigma(r, \vartheta, \varphi)}. \quad (3.10)$$

Note that the choice of the reference conductivity in the form of (3.10) delivers optimal preconditioning of the equation (3.9). For example, if one chooses the reference conductivity to be the same as the host conductivity  $\sigma_b(r)$ , the condition number of the operator  $A$  becomes proportional to  $C$ . In such cases, the solution of the resulting linear system would suffer from numerical instability, especially for models with high lateral conductivity contrasts. With this choice of  $\sigma_o(r)$ , the condition number of the operator  $A$ ,  $\kappa(A) = \|A\| \cdot \|A^{-1}\|$ , can be estimated as

$$\kappa(A) \simeq \sqrt{C}, \quad (3.11)$$

where  $C$  is the maximum lateral contrast of conductivity in the 3-D model. From this estimate it follows that even for models with extremely large lateral conductivity contrasts (which easily might exceed 30000 for 3-D models with realistic oceans), the operator  $A$  remains well conditioned, which means that after discretization of the scattering equation (3.9), the resulting linear system can be efficiently solved by BCG iterations.

Once  $\chi$  is determined from the solution of the scattering equation (3.9), the magnetic field,  $\mathbf{H}$ , at the observation points,  $\mathbf{r} \in V^{obs}$  (in our case  $V^{obs}$  is the surface of the Earth) is calculated as

$$\mathbf{H} = \int_{V^{ext}} G_o^h(\mathbf{r}, \mathbf{r}') \mathbf{j}^{ext}(\mathbf{r}') dv' + \int_{V^{mod}} G_o^h(\mathbf{r}, \mathbf{r}') \mathbf{j}^q(\mathbf{r}') dv', \quad (3.12)$$

with

$$\mathbf{j}^q = (\sigma - \sigma_o)(\mathbf{E}^o + \mathbf{E}^s), \quad (3.13)$$

$$\mathbf{E}^s = \frac{1}{\sigma + \sigma_o} (2\sqrt{\sigma_o}\chi - \mathbf{j}^s). \quad (3.14)$$

The explicit expressions to calculate the elements of Green's tensors,  $G_o^e$  and  $G_o^h$ , are presented in the next subsection. Having the magnetic field at the surface of the Earth one can easily recalculate the magnetic field at the satellite altitude.

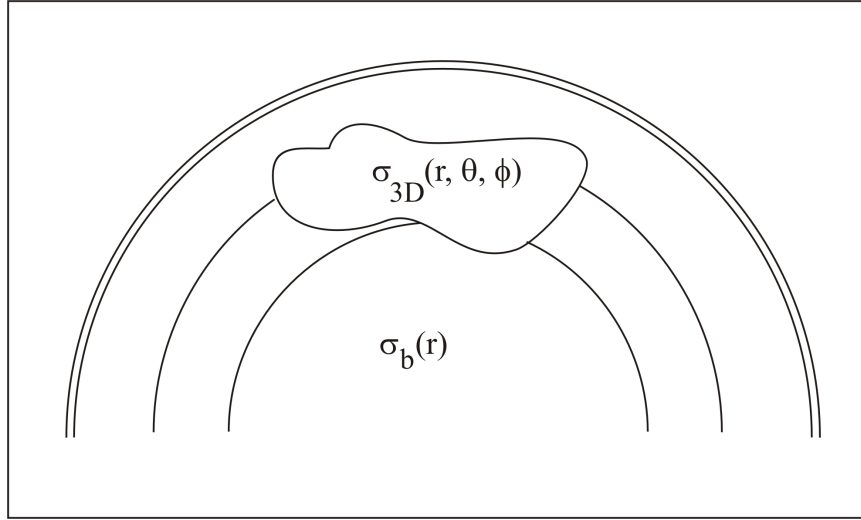


Figure 3.3: Sketch of 3-D model.

As the present study focuses on the steady state ocean flow and the conductivity model assumes a thin surface layer of variable conductance, the period of simulation is set to a large value (10,000 years). This value approximates the DC limit in our EM induction code. At the DC limit the imaginary components of the predicted fields should be zero. We found the value 10,000 years sufficiently large to make the imaginary parts of the predicted fields negligible as compared to the real parts. Now  $\mathbf{j}^{ext}$  is reduced to the sheet current density,  $\mathbf{J}^{ext}$ , which is calculated as

$$\mathbf{J}^{ext} = \sigma_w(\mathbf{U} \times \mathbf{B}^m), \quad (3.15)$$

where  $\times$  denotes the vector product,  $\sigma_w = 3.2$  S/m is the mean sea water conductivity,  $U$  is depth integrated velocity of global ocean steady flow, and  $B^m$  is the main magnetic field derived from IGRF 2000.

### 3.3.2 Green's tensors of the reference radially-symmetric section

Here we present the explicit forms of the  $3 \times 3$  dyadic Green's functions. These forms express electric and magnetic fields induced in a radially symmetric section with conductivity  $\sigma_o(r)$  by an impressed current  $\mathbf{j}$

$$\mathbf{E}(r, \vartheta, \varphi) = \int_{\Omega} \int_0^{\infty} G^e(r, r', \vartheta, \vartheta', \varphi - \varphi') \mathbf{j}(r', \vartheta', \varphi') dv', \quad (3.16)$$

$$\mathbf{H}(r, \vartheta, \varphi) = \int_{\Omega} \int_0^{\infty} G^h(r, r', \vartheta, \vartheta', \varphi - \varphi') \mathbf{j}(r', \vartheta', \varphi') dv'. \quad (3.17)$$

Here  $dv' = r'^2 \sin \vartheta' d\vartheta' d\varphi'$ . The  $3 \times 3$  Green's function tensors  $G^{e(h)}$  can be written in the following form

$$G^{e(h)} = \mathbf{e}_{\vartheta} g_{\vartheta\vartheta'}^{e(h)} \mathbf{e}_{\vartheta'} + \mathbf{e}_{\vartheta} g_{\vartheta\varphi'}^{e(h)} \mathbf{e}_{\varphi'} + \dots + \mathbf{e}_r g_{rr'}^{e(h)} \mathbf{e}_{r'} \quad (3.18)$$

where  $\mathbf{e}_\vartheta$ ,  $\mathbf{e}_\varphi$ ,  $\mathbf{e}_r$  and  $\mathbf{e}_{\vartheta'}$ ,  $\mathbf{e}_{\varphi'}$ ,  $\mathbf{e}_{r'}$  are the spherical coordinate system unit vectors in points  $\mathbf{r} = (\vartheta, \varphi, r)$ ,  $\mathbf{r}' = (\vartheta', \varphi', r')$ , respectively, and the components of  $G^e$  are written as

$$\begin{aligned}
 g_{\vartheta\vartheta'}^e &= \frac{1}{\sin \vartheta} \frac{1}{\sin \vartheta'} \partial_\varphi \partial_{\varphi'} \mathcal{P} \left[ \frac{1}{r'r} \frac{G^t}{n(n+1)} \right] + \partial_\vartheta \partial_{\vartheta'} \mathcal{P} \left[ \frac{1}{r'r} \frac{G^p}{n(n+1)} \right], \\
 g_{\vartheta\varphi'}^e &= -\frac{1}{\sin \vartheta} \partial_\varphi \partial_{\vartheta'} \mathcal{P} \left[ \frac{1}{r'r} \frac{G^t}{n(n+1)} \right] + \frac{1}{\sin \vartheta'} \partial_\vartheta \partial_{\varphi'} \mathcal{P} \left[ \frac{1}{r'r} \frac{G^p}{n(n+1)} \right], \\
 g_{\vartheta r'}^e &= -\partial_\vartheta \mathcal{P} \left[ \frac{1}{r'^2 r} \frac{\beta^p G^p}{\sigma_o(r')} \right], \\
 g_{\varphi\vartheta'}^e &= -\frac{1}{\sin \vartheta'} \partial_\vartheta \partial_{\varphi'} \mathcal{P} \left[ \frac{1}{r'r} \frac{G^t}{n(n+1)} \right] + \frac{1}{\sin \vartheta} \partial_\varphi \partial_{\vartheta'} \mathcal{P} \left[ \frac{1}{r'r} \frac{G^p}{n(n+1)} \right], \\
 g_{\varphi\varphi'}^e &= \partial_\vartheta \partial_{\vartheta'} \mathcal{P} \left[ \frac{1}{r'r} \frac{G^t}{n(n+1)} \right] + \frac{1}{\sin \vartheta} \frac{1}{\sin \vartheta'} \partial_\varphi \partial_{\varphi'} \mathcal{P} \left[ \frac{1}{r'r} \frac{G^p}{n(n+1)} \right], \\
 g_{\varphi r'}^e &= -\frac{1}{\sin \vartheta} \partial_\varphi \mathcal{P} \left[ \frac{1}{r'^2 r} \frac{\beta^p G^p}{\sigma_o(r')} \right], \\
 g_{r\vartheta'}^e &= \partial_{\vartheta'} \mathcal{P} \left[ \frac{1}{r'r^2} \frac{\alpha^p G^p}{\sigma_o(r)} \right], \\
 g_{r\varphi'}^e &= \frac{1}{\sin \vartheta'} \partial_{\varphi'} \mathcal{P} \left[ \frac{1}{r'r^2} \frac{\alpha^p G^p}{\sigma_o(r)} \right], \\
 g_{rr'}^e &= -\frac{\delta(r-r')\delta(\vartheta-\vartheta')\delta(\varphi-\varphi')}{r'^2 \sin \vartheta' \sigma_o(r)} + \mathcal{P} \left[ \frac{1}{r^2} \frac{n(n+1)\alpha^p \beta^p G^p}{\sigma_o(r)\sigma_o(r')} \right],
 \end{aligned} \tag{3.19}$$

whereas the components of  $G^h$  are

$$\begin{aligned}
 g_{\vartheta\vartheta'}^h &= -\frac{1}{\sin \vartheta'} \partial_\vartheta \partial_{\varphi'} \mathcal{P} \left[ \frac{1}{r'r} \frac{\alpha^t G^t}{n(n+1)} \right] - \frac{1}{\sin \vartheta} \partial_\varphi \partial_{\vartheta'} \mathcal{P} \left[ \frac{1}{r'r} \frac{\alpha^p G^p}{n(n+1)} \right], \\
 g_{\varphi\vartheta'}^h &= \partial_\vartheta \partial_{\vartheta'} \mathcal{P} \left[ \frac{1}{r'r} \frac{\alpha^t G^t}{n(n+1)} \right] - \frac{1}{\sin \vartheta'} \partial_\vartheta \partial_{\varphi'} \mathcal{P} \left[ \frac{1}{r'r} \frac{\alpha^p G^p}{n(n+1)} \right], \\
 g_{\vartheta\varphi'}^h &= -\frac{1}{\sin \vartheta} \frac{1}{\sin \vartheta'} \partial_\varphi \partial_{\varphi'} \mathcal{P} \left[ \frac{1}{r'r} \frac{\alpha^t G^t}{n(n+1)} \right] + \partial_\vartheta \partial_{\vartheta'} \mathcal{P} \left[ \frac{1}{r'r} \frac{\alpha^p G^p}{n(n+1)} \right], \\
 g_{\varphi\varphi'}^h &= \frac{1}{\sin \vartheta} \partial_\varphi \partial_{\vartheta'} \mathcal{P} \left[ \frac{1}{r'r} \frac{\alpha^t G^t}{n(n+1)} \right] + \frac{1}{\sin \vartheta'} \partial_\vartheta \partial_{\varphi'} \mathcal{P} \left[ \frac{1}{r'r} \frac{\alpha^p G^p}{n(n+1)} \right], \\
 g_{\vartheta r'}^h &= -\frac{1}{\sin \vartheta} \partial_\varphi \mathcal{P} \left[ \frac{1}{r'^2 r} \frac{\alpha^p \beta^p G^p}{\sigma_o(r')} \right], \\
 g_{\varphi r'}^h &= \partial_\vartheta \mathcal{P} \left[ \frac{1}{r'^2 r} \frac{\alpha^p \beta^p G^p}{\sigma_o(r')} \right], \\
 g_{r\vartheta'}^h &= \frac{1}{\sin \vartheta'} \partial_{\varphi'} \mathcal{P} \left[ \frac{1}{r'r^2} \frac{G^t}{i\omega\mu_o} \right], \\
 g_{r\varphi'}^h &= -\partial_{\vartheta'} \mathcal{P} \left[ \frac{1}{r'r^2} \frac{G^t}{i\omega\mu_o} \right], \\
 g_{rr'}^h &= 0.
 \end{aligned} \tag{3.20}$$

Note, that all components of Eqs. (3.19) and (3.20) depend on  $(r, r', \vartheta, \vartheta', \varphi - \varphi')$ . Also, the transform

$$\mathcal{P}[f](\cos \gamma, r, r') = \sum_{n=1}^{\infty} \frac{2n+1}{4\pi} f(n, r, r') P_n(\cos \gamma) \quad (3.21)$$

converts a function of spectral number  $n$  into a function of  $\cos \gamma$ , where  $\cos \gamma = \cos \vartheta \cos \vartheta' + \sin \vartheta \sin \vartheta' \cos(\varphi - \varphi')$  and  $P_n$  is the Legendre polynomial of degree  $n$ . The spectral functions  $\alpha^t, \alpha^p$  are determined via four admittances  $Y^{l,t}, Y^{u,t}, Y^{l,p}$  and  $Y^{u,p}$  as

$$\alpha(n, r, r') = \beta(n, r', r) = \begin{cases} -Y^u(n, r), & r > r' \\ Y^l(n, r), & r < r' \end{cases} \quad (3.22)$$

The scalar Green's functions  $G^t, G^p$  of Eqs. (3.19) and (3.20) are determined as

$$G(n, r, r') = -\frac{1}{Y^l(n, r') + Y^u(n, r')} \exp\left(\int_{r'}^r p(n, \xi) \alpha(n, \xi, r') d\xi\right), \quad (3.23)$$

where  $p^t = -i\omega\mu_o$ ,  $p^p = -i\omega\mu_o + \frac{n(n+1)}{r^2\sigma_o(r)}$ . The four admittances  $Y^{l,t}(n, r), Y^{u,t}(n, r), Y^{l,p}(n, r), Y^{u,p}(n, r)$ , and two factors  $F^t(n, r, r') = \exp\left(\int_{r'}^r p^t(\xi) \alpha^t(n, \xi, r') d\xi\right)$ ,  $F^p(n, r, r') = \exp\left(\int_{r'}^r p^p(n, \xi) \alpha^p(n, \xi, r') d\xi\right)$  are calculated by a unified procedure described below.

We assume that the radially symmetric reference section consists of  $N$  layers  $\{r_{k+1} < r \leq r_k\}_{k=1,2,\dots,N}$ . We construct the set  $\{r_k\}_{k=1,2,\dots,N}$  in such a way that it includes all levels  $r_j$ , where we will calculate the admittances and the Green's scalar functions. We assume that within each layer the conductivity varies as (cf. Fainberg et al. [1990])

$$\sigma_o(r) = \sigma_k \left(\frac{r_k}{r}\right)^2, \quad r_{k+1} < r \leq r_k, \quad (3.24)$$

where  $r_1 = r_e$  is the Earth's radius,  $r_{N+1} = 0$ ,  $\sigma_k$  is an appropriate constant. Since  $N$  can be taken as large as necessary, the distribution (3.24) allows the approximation of any radially symmetric conductivity section. Distribution (3.24) is chosen to make the recurrence formulae as simple as possible. We express these formulae in the following form

$$Y_k^{l,t} = \frac{1}{q_k} \frac{q_{k+1} Y_{k+1}^{l,t} (b_k - 0.5\tau_k) + b_k^+ b_k^- \tau_k}{(b_k + 0.5\tau_k) + q_{k+1} \tau_k Y_{k+1}^{l,t}}, \quad k = N-1, N-2, \dots, 1, \quad Y_N^{l,t} = -\frac{b_N^+}{q_N}, \quad (3.25)$$

$$Y_{k+1}^{u,t} = \frac{1}{q_{k+1}} \frac{q_k Y_k^{u,t} (b_k + 0.5\tau_k) + b_k^+ b_k^- \tau_k}{(b_k - 0.5\tau_k) + q_k \tau_k Y_k^{u,t}}, \quad k = 1, 2, \dots, N-1, \quad Y_1^{u,t} = -\frac{n}{q_1}, \quad (3.26)$$

$$Y_{k+1}^{u,p} = g_k \eta_k \frac{Y_k^{u,p} (b_k + 0.5\tau_k) - g_k \tau_k}{g_k (b_k - 0.5\tau_k) - b_k^+ b_k^- \tau_k Y_k^{u,p}}, \quad k = 1, 2, \dots, N-1, \quad Y_1^{u,p} = 0, \quad (3.27)$$

$$Y_k^{l,p} = g_k \frac{Y_{k+1}^{l,p} (b_k - 0.5\tau_k) - g_k \eta_k \tau_k}{g_k \eta_k (b_k + 0.5\tau_k) - b_k^+ b_k^- \tau_k Y_{k+1}^{l,p}}, \quad k = N-1, N-2, \dots, 1, \quad Y_N^{l,p} = \frac{\sigma_N r_N}{b_N^-}, \quad (3.28)$$

where  $Y_k$  stands for  $Y(n, r_k)$ , the layer number  $k$  is the index of recurrence,  $n$  is the spectral number and

$$\eta_k = \frac{r_k}{r_{k+1}}, \quad \tau_k = \frac{1 - \zeta_k}{1 + \zeta_k}, \quad \zeta_k = \eta_k^{2b_k}, \quad g_k = \sigma_k r_k, \quad q_k = i\omega\mu_o r_k.$$

$$b_k^- = b_k - \frac{1}{2}, \quad b_k^+ = b_k + \frac{1}{2}, \quad b_k = \left\{ (n + \frac{1}{2})^2 - i\omega\mu_o\sigma_k r_k^2 \right\}^{\frac{1}{2}}.$$

Finally the recurrence formulae for the scalar Green's functions  $G^t, G^p$  are given by

$$G(r_i, r_j) = -\frac{1}{Y_j^l + Y_j^u} \prod_{m=j}^{i-1} F_m, \quad r_i \leq r_j, \quad (3.29)$$

$$G(r_i, r_j) = G(r_j, r_i), \quad r_i > r_j.$$

where the factors  $F_m$  are

$$F_m^t = \frac{1}{1 + \zeta_m} \frac{2b_m \eta_m^{b_m^-}}{(b_m + 0.5\tau_m) + q_m \tau_m Y_{m+1}^{l,t}}. \quad (3.30)$$

for a toroidal mode and

$$F_m^p = \frac{1}{1 + \zeta_m} \frac{2g_m b_m \eta_m^{b_m^-}}{g_m \eta_m (b_m + 0.5\tau_m) - b_m^+ b_m^- \tau_m Y_{m+1}^{l,p}}. \quad (3.31)$$

for a poloidal mode. Note, that in Eqs. (3.25)-(3.31) a dependence on the spectral number  $n$  is omitted but implied.

### 3.3.3 Validation of numerical solution

We compare our IE solution with the finite difference solution of Tyler et al. [2003] to validate our numerical approach. In both cases the conductivity models consist of a thin surface shell of variable conductance and an insulating mantle underneath. A realistic distribution of the shell conductance was obtained by merging the contributions from the sea water and from the sediments (As described in subsection 3.3.4). Depth integrated velocity is taken from the TPXO.6.1 global tidal flow model (Erofeeva and Egbert [2002]). Fig. 3.4 presents the vertical component of the magnetic field due to the  $M_2$  tide (period = 12.42 hours) at sea-level as given by Tyler et al. [2003] (upper panel) and by the IE solution (lower panel). Tylers results have a resolution of  $2^\circ \times 2^\circ$ , while our results have a resolution of  $1^\circ \times 1^\circ$ . The good agreement between the two results verifies both approaches. The similarity of the global patterns is particularly remarkable. However, minor differences also exist between the two predictions and we believe that it is due to the difference in the numerical approaches (FD and IE). It is difficult to be in favor of one or the other solution as only two approaches are compared.

As a second test of our approach, we compare the spherical IE solution against the Cartesian IE solution described in (Avdeev et al. [1997, 2002]) for a simplified ocean circulation. We consider a radially symmetric (1-D) Earth model that consists of a uniform ocean with a conductance of 20000 S and with a 1-D mantle underneath. The 1D mantle consists of following layers (ordered top to bottom): 1) A resistive (10,000 Ohm-m) Lithosphere of thickness 100 km, 2) Moderately resistive (100 Ohm-m) layer (100 to 500 km), 3) A transition zone of resistivity 10 Ohm-m (500 to 750 km) and finally 4) An inner uniform sphere of 0.5 Ohm-m. For

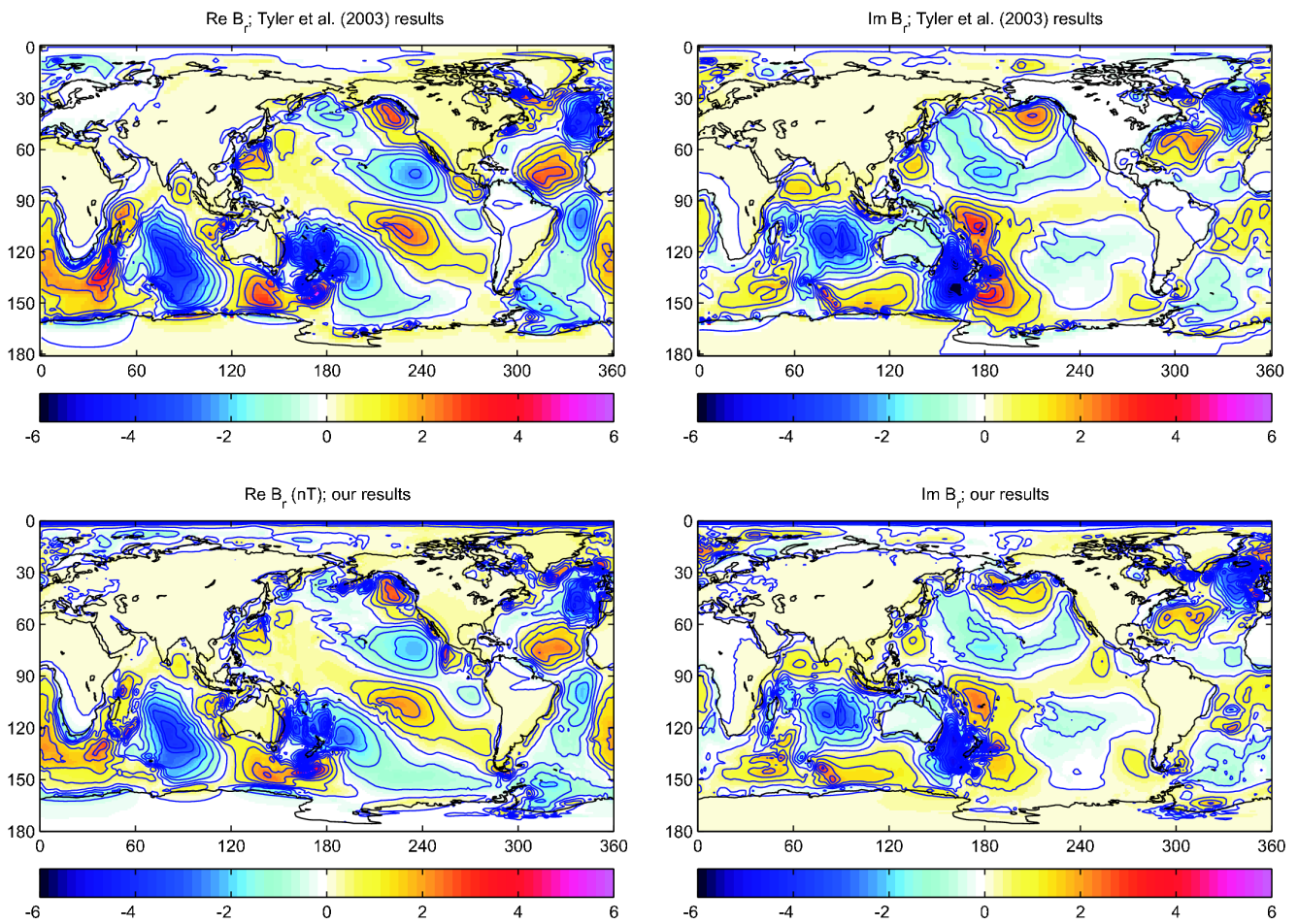
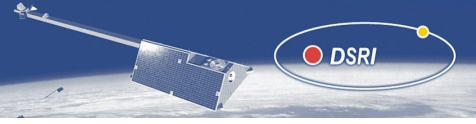


Figure 3.4:  $B_r$  (nT) at sea level from  $M_2$  tide obtained by Tyler et al. [2003] (upper panels) and with our IE solution (lower panels).

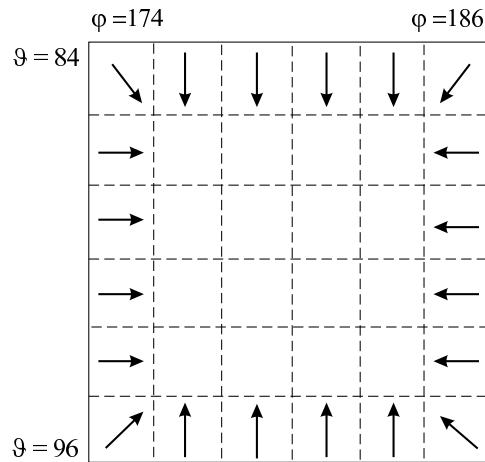


Figure 3.5: The geometry of inducing currents from the test circulation model.

the trial flow, a medium-size circulation model in the equatorial region was adopted. Fig. 3.5 demonstrates the geometry of the inducing currents for this circulation model. The inducing currents are described by an array of electric dipoles with the moments of 1 A-m. Calculations are in a mesh with a cell size of  $2^\circ \times 2^\circ$  for the Spherical solution and with a cell size of  $222 \text{ km} \times 222 \text{ km}$  for the Cartesian solution. Fig. 3.6 demonstrates vertical magnetic field at sea level obtained by Cartesian (left panel) and by spherical (right panel) solutions. It is evident from these figures that there exists good agreement between the two solutions.

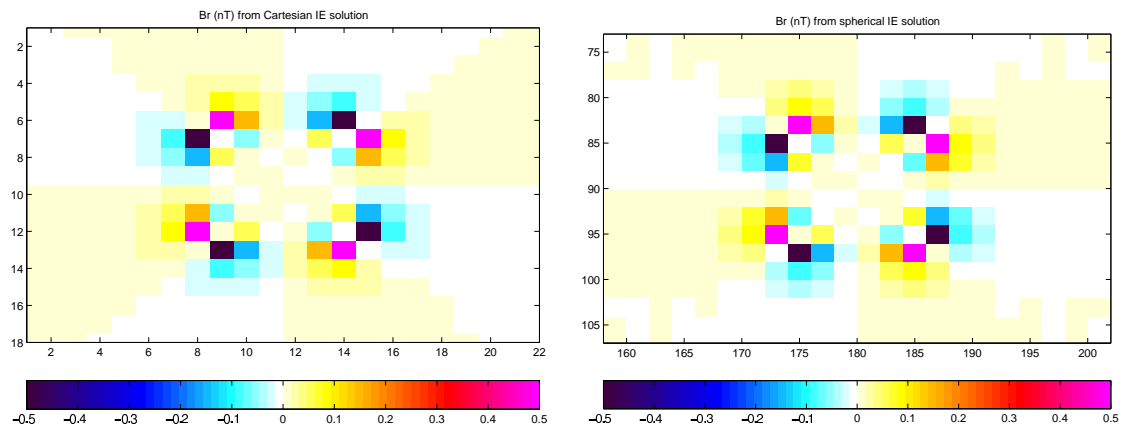


Figure 3.6:  $B_r$  (nT) at sea level obtained from the Cartesian IE solution (left panel) and from our spherical IE solution (right panel).

### 3.3.4 3-D conductivity model

The 3-D model consists of a thin spherical shell of conductance  $S(\theta, \varphi)$  at the Earth's surface, underlaid by a radially symmetric spherical conductivity  $\sigma(r)$ . The shell conductance  $S(\theta, \varphi)$  was chosen as realistic as possible, and consists of contributions from sea water and from sediments. The conductance of the sea water has been derived from the global  $5' \times 5'$  NOAA ETOPO map of bathymetry, multiplying the water depth by a mean seawater conductivity of  $3.2 \text{ S/m}$ . The conductance of the sediments has been derived from the global sediment thickness

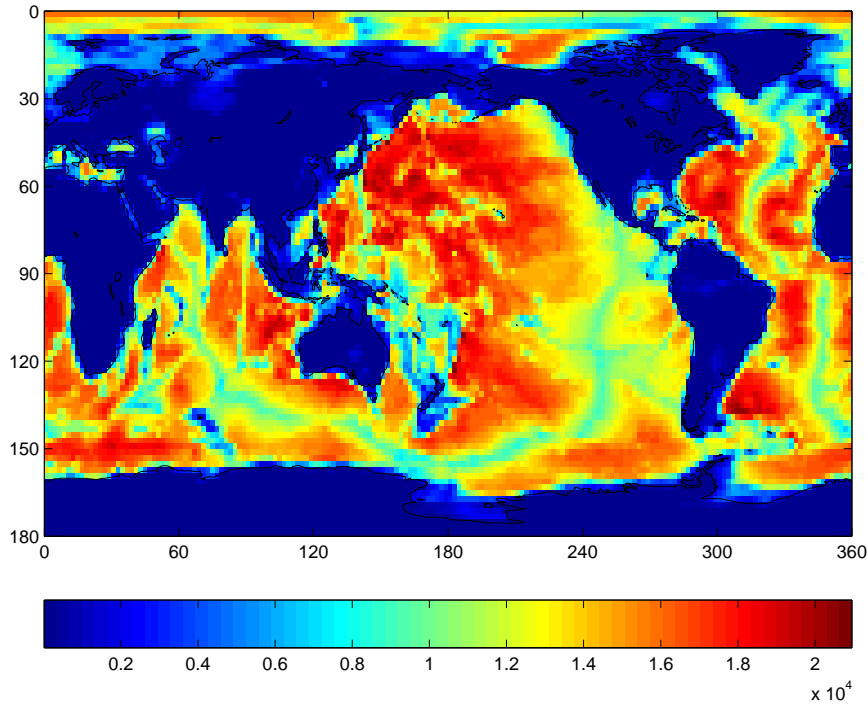


Figure 3.7: Map of the adopted surface shell conductance (in S).

given by the  $1^\circ \times 1^\circ$  map of [Laske and Masters \[1997\]](#) by using a heuristic procedure similar to that described in [Everett et al. \[2003\]](#). Figure 3.7 presents the map of the adopted surface shell conductance. It is seen that the conductance varies from tens of S inland up to 35000 S in the oceans. For the underlying spherical conductor we chose three-layer Earth model from [Schmucker \[1985\]](#). It consists of a moderately resistive first layer of 70 Ohm-m down to 500 km, a second transition layer of 16 Ohm-m from 500 km to 750 km, followed by an inner uniform sphere of 0.42 Ohm-m. We have modified the model slightly by subdividing the first layer into an upper part of 100 km thickness resembling a more resistive lithosphere with a resistivity of 3000 Ohm-m.

### 3.3.5 Computational aspects

Each simulation (for a given model of ocean flow) takes 1.2 hours of CPU on one processor of the type SunFire V8800 for an adopted shell discretization of  $N_\theta \times N_\phi = 180 \times 360$  with an angular dimensions of  $1^\circ \times 1^\circ$ .

## 3.4 Results of simulation

The distribution of exciting electric current density  $\mathbf{J}^{ext}$  (3.15) in the ocean, computed from the averaged velocity data for the year 2002, is shown in Figure 3.8. The resolution is reduced for clarity. The current density vectors point to the left of the flow direction in Southern Hemisphere and vice versa in the Northern Hemisphere. This follows the observation by [Stephenson and Bryan \[1992\]](#), wherein they comment the maximum flow generated electric potential should be on the left, as one faces downstream in the Northern Hemisphere. As expected, the distribution of  $\mathbf{J}^{ext}$  is predominantly influenced by the Antarctic Circumpolar Current (ACC). Three com-

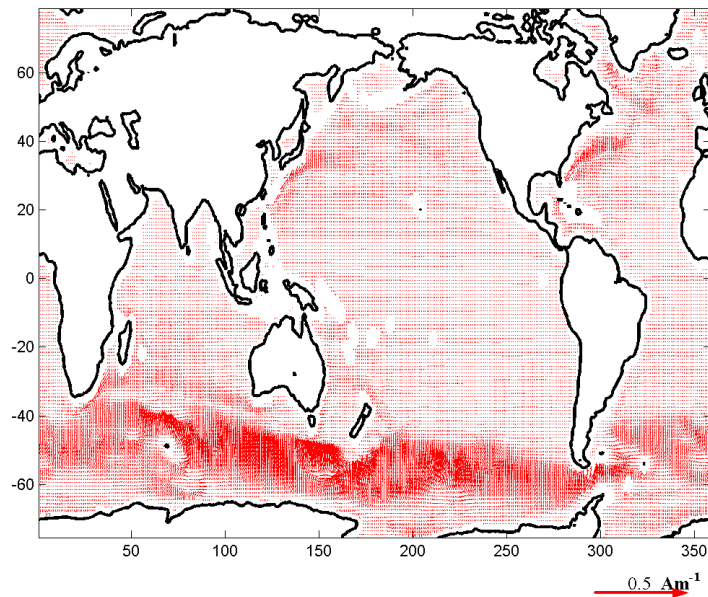


Figure 3.8: Distribution of exciting current  $\mathbf{J}^{ext}$  (in  $\mathbf{A}m^{-1}$ ) for the year 2002.

ponents of induced magnetic field computed from velocity data for the year 2002 are presented in Figure 3.9. The left panel gives the field at sea level and the right panel gives the field at an altitude of 430 km from sea level. At sea level, the magnetic fields are in the ranges -6 to 4 nT for  $B_r$  (a), -3 to 2 nT for  $B_\theta$  (c) and -4 to 6 nT for  $B_\phi$  (e). These ranges roughly agree with some of the earlier predictions by Stephenson and Bryan [1992], Tyler [1992] which are in the range from 1 to 10 nT. The dominant ocean induced magnetic signal is the vertical component,  $B_r$  and the horizontal components have about half of that strength. Note that these arguments are relevant only outside the ocean. Within the ocean the vertical field component may have lower amplitude than the horizontal components (Tyler [1992]). In the following sections we use only the vertical component to represent the magnetic field. At an altitude of 430 km, the predicted magnetic fields describe the large scale features of ocean circulation and are void of shorter wavelength features which are observed at the sea level (Right panel of Figure 3.9). Here,  $B_r$  has a range of -1.5 to 1.0 nT. The most predominant contribution comes from ACC, with a maximum strength of -1.5 nT in the Southern Indian ocean. The Western boundary currents, especially Kuroshio and Gulf Stream are reflected in all the predicted components, though with a lesser amplitude. The effect of Agulhas and Brazil currents are not so clear, perhaps masked by ACC (comparing the fields at sea level and at 430 km altitude). The predicted amplitude of the magnetic fields at satellite altitude are in agreement with the computations by Tyler et al. [1999].

As the satellite observed magnetic data are influenced by several other sources of internal and external origin, it will be worthwhile to study the variability of circulation generated magnetic fields. A similar study for ocean tides was reported by Tyler et al. [2003]. In the following section, the seasonal and interannual variability of predicted magnetic fields are discussed.

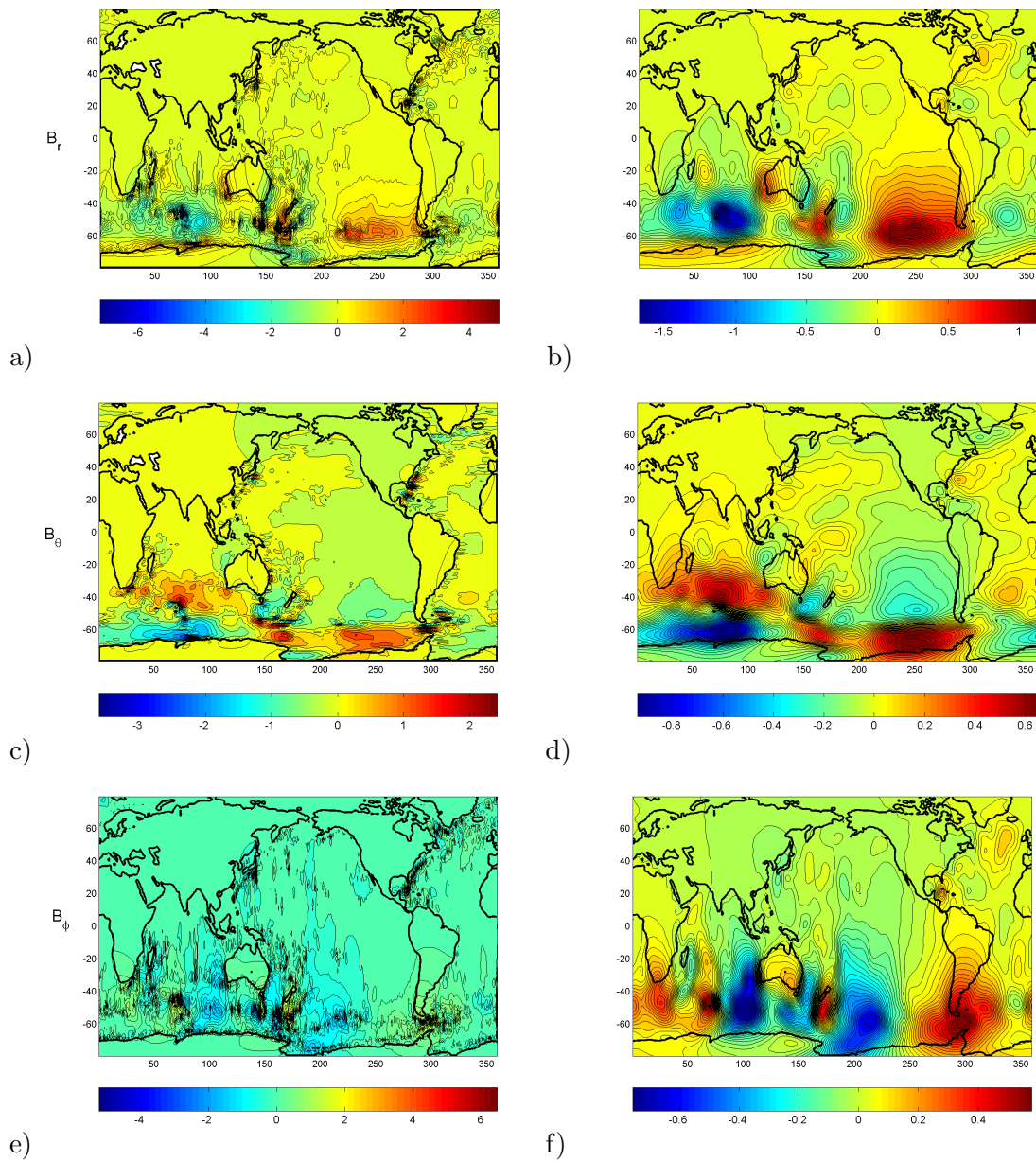
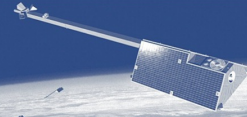


Figure 3.9: Predicted components of the ocean induced magnetic field ( $B_r$ ,  $B_\theta$ ,  $B_\phi$ ; from up to bottom) at sea level (left panels) and at 430 km above sea level (right panels) (in nT).

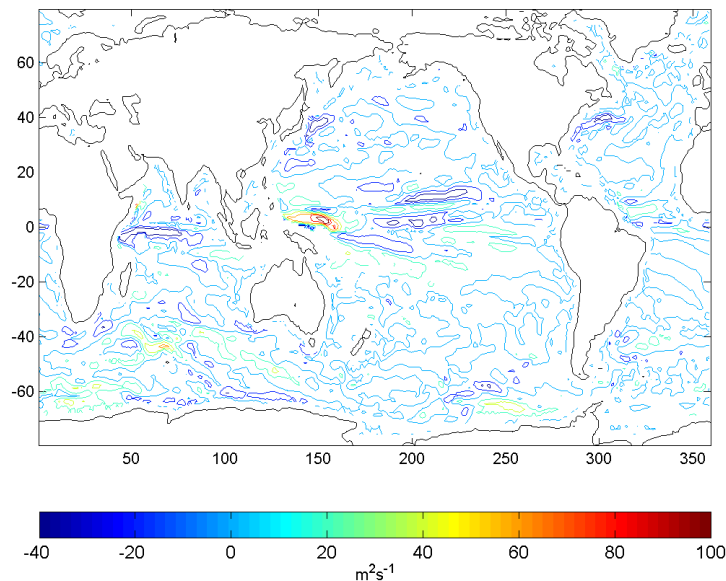


Figure 3.10: Difference between Summer and Winter (2002) ocean velocity data. Units in  $m^2s^{-1}$ .

### 3.4.1 Seasonal variation

Ocean circulation is driven by winds on the surface and the cooling and sinking of water in the polar region. The depth integrated velocities used for our study are affected by the time variations in these factors. The difference between Summer and Winter flow velocity data for the year 2002 (Figure 3.10) shows strong variability along the equatorial region, possibly due to ocean flow vigorously responses to changes in the wind field at low altitude. However changes of lesser order can also be found over most of the oceans. In order to study the seasonal variability of the ocean generated magnetic field at sea level Stephenson and Bryan [1992] used the first annual harmonic of total water transport stream function. With a simpler approach, we estimated mean flow velocities of Winter (January to March) and Summer (June to August) months for the year 2002. The predicted vertical components of the magnetic field for Summer and Winter are given in Figure 3.11. As the amplitude of fluctuation in circulations are lower than that of the mean circulation, the variations in the magnetic fields are not obvious. The difference between Summer and Winter predictions (Figure 3.12) shows strong variability in the Indian Ocean, probably connected to the South Asian monsoon. In addition, variations in the Western boundary currents and ACC are also evident. The difference field has a range of  $\pm 0.2$  nT.

### 3.4.2 El Niño / Interannual variability

The global oceanic circulation also exhibits interannual to interdecadal variability. Most prominent being the variation associated with El Niño and Southern Oscillation (ENSO). It is a change in the ocean-atmosphere system in the eastern Pacific which contributes to a significant weather changes around the world. In normal conditions, the trade winds blow towards west and pile up warm water in the Western Pacific. During these conditions (called La Niña), the sea level is 0.5 m higher at Indonesia than at Ecuador. During El Niño, the trade wind relaxes

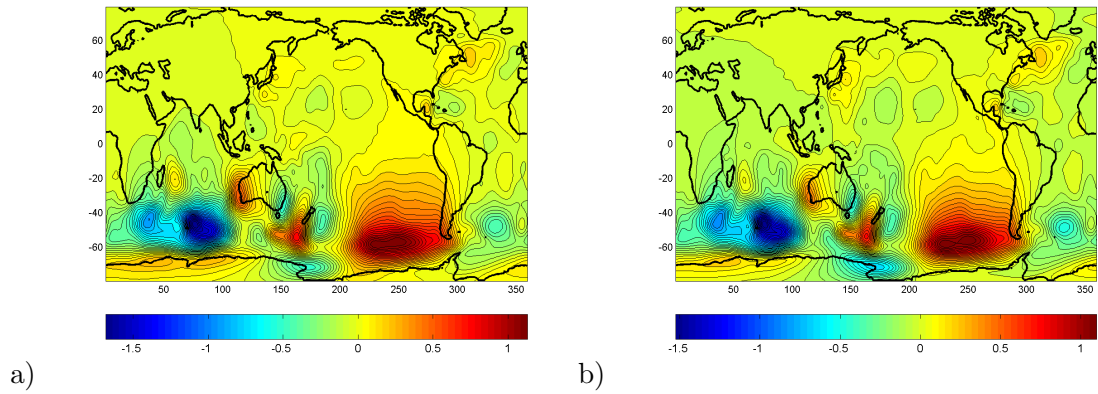


Figure 3.11: Predicted vertical component of magnetic field at 430 km (a) Summer and (b) Winter, 2002 (in nT).

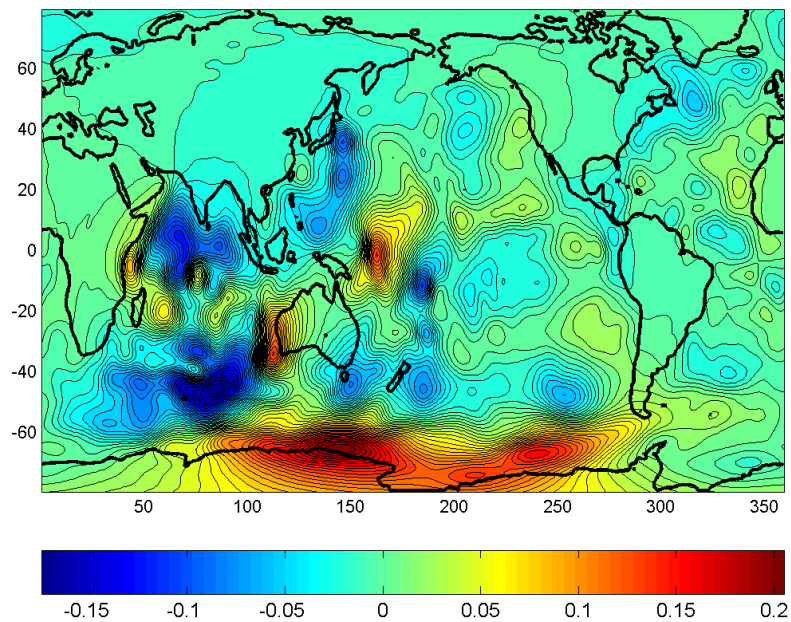


Figure 3.12: Difference map ( $B_r$ ) between Summer and Winter predictions (in nT).

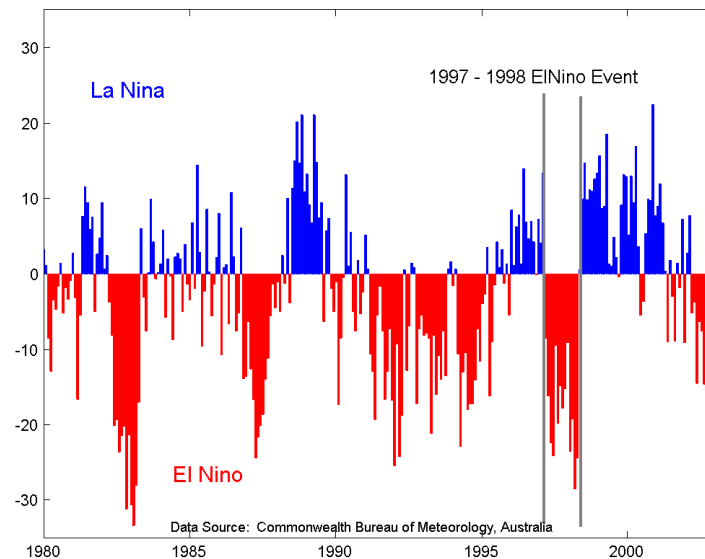


Figure 3.13: The monthly southern oscillation indexes from 1980 to 2003. Gray lines indicate period of 1997 - 1998 El Niño.

allowing the warm equatorial current to flow towards the South American coast. This occurs roughly once in every 4-5 years. Figure 3.13 shows the monthly Southern Oscillation Indexes from 1980 to 2003. The recent El Niño event of 2002-2003, was weaker than the previous event during 1997-1998. We selected the El Niño during June 1997 to May 1998 for the simulations studies. Changed sea level gradient and relaxed trade winds reverse the surface currents along the equatorial region during an El Niño. This perhaps is best illustrated by the surface velocity data from ECCO simulations as given in Figure 3.14. The mean velocity vectors for surface layers (levels 1 to 4, Table 3.1) for November 1997 (El Niño) and November 1999 (La Niña) period shows a dramatic reversal in its direction. The depth extent of these currents is given in a stacked velocity plot (Figure 3.15) for a rectangular area of latitude  $0^{\circ} - 5^{\circ}$  and longitude  $200^{\circ} - 212^{\circ}$ . The influence of El Niño on the velocity seems to exist only in the upper 250 meters of the ocean. The velocities are within a range of  $\pm 0.2$  m/s and have negligible magnitude for depth  $> 250$ m.

We averaged the circulation velocity data from June 1997 to May 1998 to represent the flow during El Niño period. In addition we computed the annual mean velocity for the Year 1999 to represent La Niña period (ref: Figure 3.13). The predicted magnetic fields for the El Niño and La Niña period (Figure 3.16) are dominated by the gradients associated with ACC, with a weak amplitude range of  $\pm 0.2$  nT. The difference of these two predictions, though weak, show an anomaly trending EW, as one would have expected from currents reversal, is dominated by velocity fluctuations associated with some other phenomena (Figure 3.17). In any case, the variability in the magnetic field has very low amplitude, as compared to seasonal variation. The reasons for such small variation could be: 1) El Niño affects only a thin surface layer in the ocean, and the surface current reversal fails to produce appreciable change in the depth integrated velocity and 2) The low strength of the vertical component of the Earth's magnetic field at low geomagnetic latitudes.

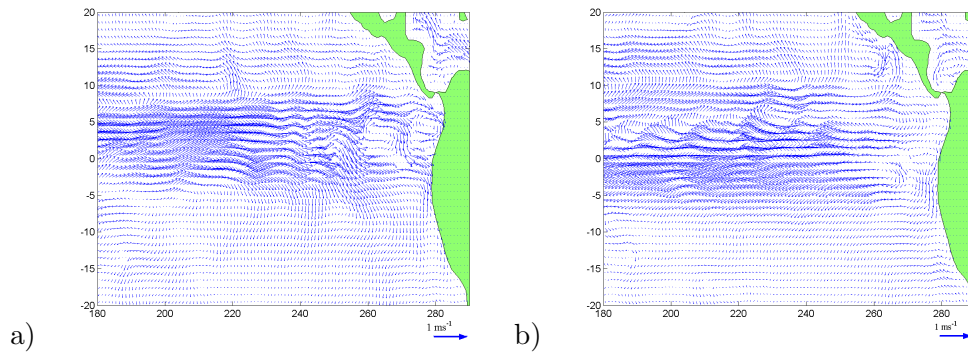


Figure 3.14: Surface current (depth < 60 m) velocity data from ECCO model (a) November 1997 (El Niño ) and (b) November 1999 (La Niña). Units in  $m s^{-1}$

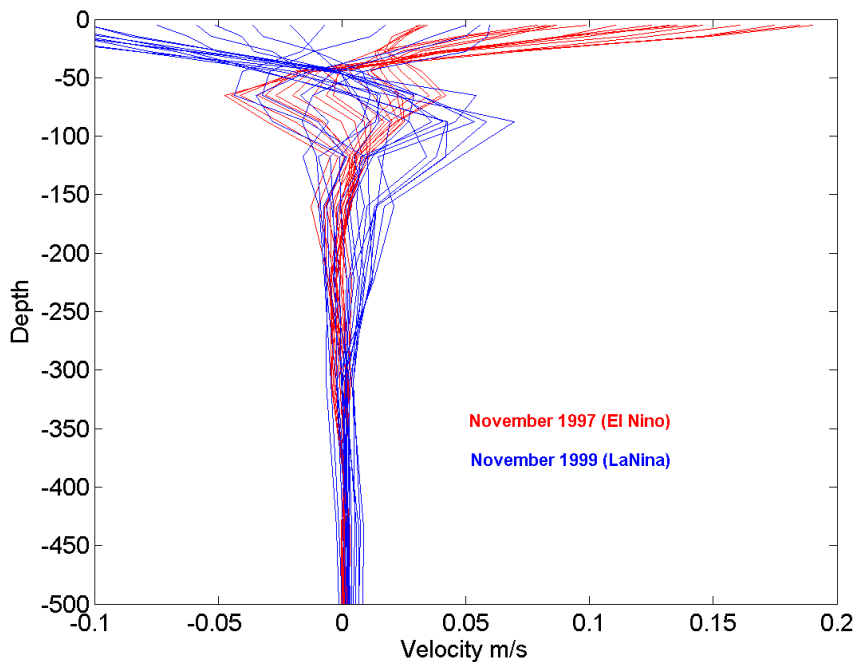
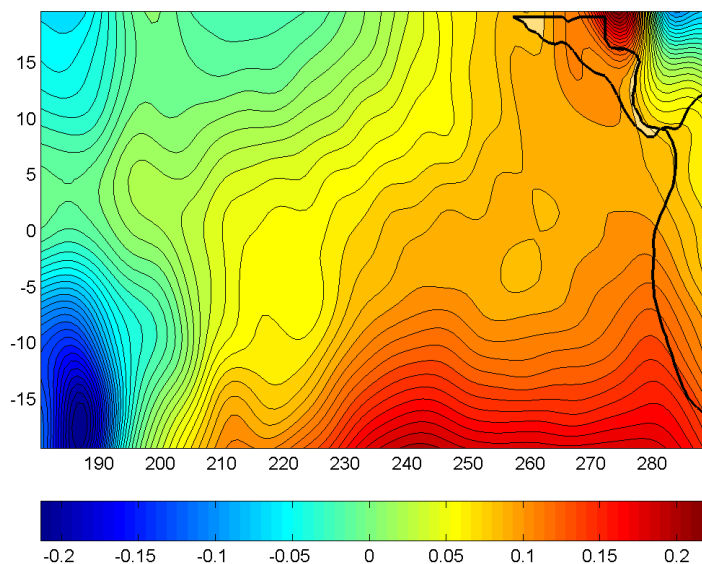
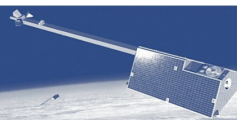
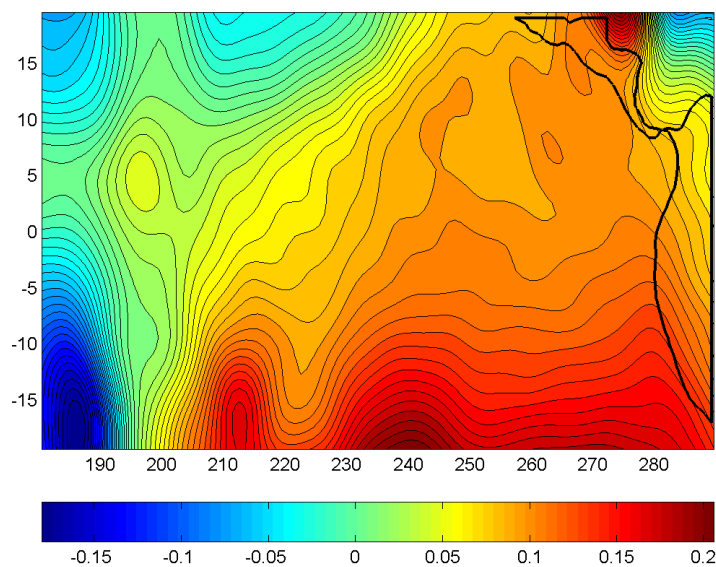


Figure 3.15: Stacked velocity (Zonal) depth profiles for La Niña and El Niño periods (depth in m).



a)



b)

Figure 3.16: Predicted vertical component of ocean induced magnetic field in nT for the Equatorial Eastern Pacific ocean (latitude:  $\pm 20^\circ$ , longitude:  $180^\circ - 300^\circ$  E). (a) El Niño (June 1997 to May 1998) and (b) La Niña (Year 1999).

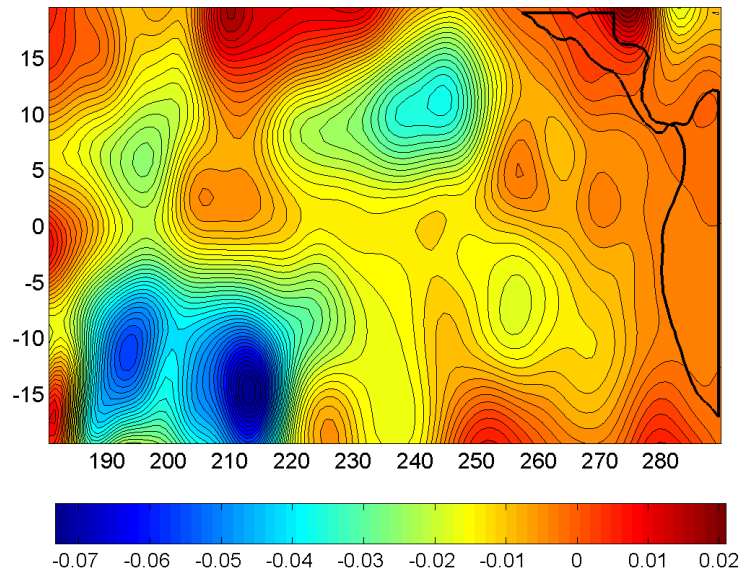


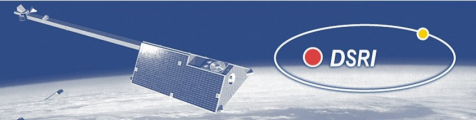
Figure 3.17: The same format as above, but difference of predicted magnetic fields between El Niño and La Niña periods.

### 3.5 Conclusions and scope for future work

Predicted magnetic field components from oceanic circulations are dominated by the Antarctic Circumpolar Current and the Western boundary currents. The vertical component of the generated field has higher strength, compared to the other components, ranging between -6 to 4 nT at sea level and -1.5 to 1.0 nT at an altitude of 430 km above the sea level. Seasonal variations in the magnetic field have an amplitude range  $\pm 0.2$  nT. An interesting region is the Indian Ocean. The variations in the magnetic field related to the surface current reversal during the 1997-1998 El Niño event is smaller in comparison with seasonal variation. As a next step, we will study the magnetic fields generated by small but more energetic phenomena like ocean eddies. A higher resolution ocean model will be required for this purpose. In addition, a sensitivity analysis will be done for different ocean flow components on the predicted magnetic field.

### Acknowledgement

We used ECCO adjoint experiment result. This is a contribution of the Consortium for Estimating the Circulation and Climate of the Ocean (ECCO) funded by the National Oceanographic Partnership Program, USA.



## 3.6 Introduction

In this section, we discuss the results from the simulation of ocean generated magnetic signals, analysis of their sensitivity to Earth's main field and its surface conductance distribution and finally a scheme to recover ocean flow from satellite observations. The work forms a part of the Task 2: *Forward modeling of external and oceanographic contributions to Swarm observations*. It relates in particular to work packages (WP) WP 2100, 2200, 2300 and 2400. Results from computation of ocean induced signals using a  $0.25^\circ \times 0.25^\circ$  resolution ocean circulation model (OCCAM) are described in the section 3.7. A description on the new velocity data, discussions on the results and a comparison of the results with our earlier simulations using ECCO are included in this section. Section 3.8 details a sensitivity analysis performed to study the influence of two of the major model inputs for simulations, namely the main magnetic field and the 3D conductivity distribution on the ocean generated magnetic fields. A least square inversion scheme is proposed to recover the ocean circulation from satellite magnetic observations. Numerical approach and the preliminary results of this inversion scheme are presented in the last section 3.9.

## 3.7 Simulations with high resolution ocean circulation data

Computation of ocean magnetic signals from ECCO  $1^\circ \times 1^\circ$  degree resolution gave an amplitude range within  $\pm 6$  nT at sea surface and  $\pm 2$  nT, at satellite altitude (3.3). Coarser ocean circulation models (such as ECCO) will tend to get overall water transports correct but will achieve this with broader, more sluggish currents. Though signals from simulations using ECCO data described the major global water transports, it could not represent many of the smaller scale features of ocean circulation such as eddies. Magnetic fields produced by these smaller, but intense flows may have higher amplitudes, and thus it is important to be studied. To resolve the meso-scale ocean features such as eddies and narrow boundary currents, the ocean model should have certain resolution, depending on stratification and latitude. A typical number is 40 km for mid latitude (Andrew Coward, personal communication, 2004). OCCAM global ocean model (Saunders et al. [1999], Webb et al. [1998]) with a resolution  $0.25^\circ \times 0.25^\circ$  is a suitable candidate for such simulations. Subsections 3.7.1-3.7.2 describe the OCCAM model and its output. Results from simulations are discussed in 3.7.4.

### 3.7.1 OCCAM Model

Ocean Circulation and Climate Advanced Modeling Project (OCCAM) (<http://www.soc.soton.ac.uk/JRD/OCCAM>) is a Community Research Project set up by the UK Natural Environment Research Council (NERC), the core group is located at the Southampton Oceanographic Centre, UK. The aim of the project was to develop a high resolution global ocean model to study the large scale ocean circulation. The primary model variables are temperature, salinity, horizontal velocity and sea surface elevation. The model has 36 levels in the vertical starting with a thickness of 20 m at the surface and increasing to 250 m at depth. The spatial resolution of the model is  $0.25^\circ$ . Surface wind forcing is provided by stress vectors interpolated from an annual cycle of 12 monthly fields, derived from European Centre for Medium-Range Weather Forecasts (ECMWF) winds for the year 1986-1988. With a baroclinic time step of 15 minutes, the model ran for 14 "model years" (5118 days). Webb et al. [1998] recommend to use the model outputs between day 2922 and 4383 of the model

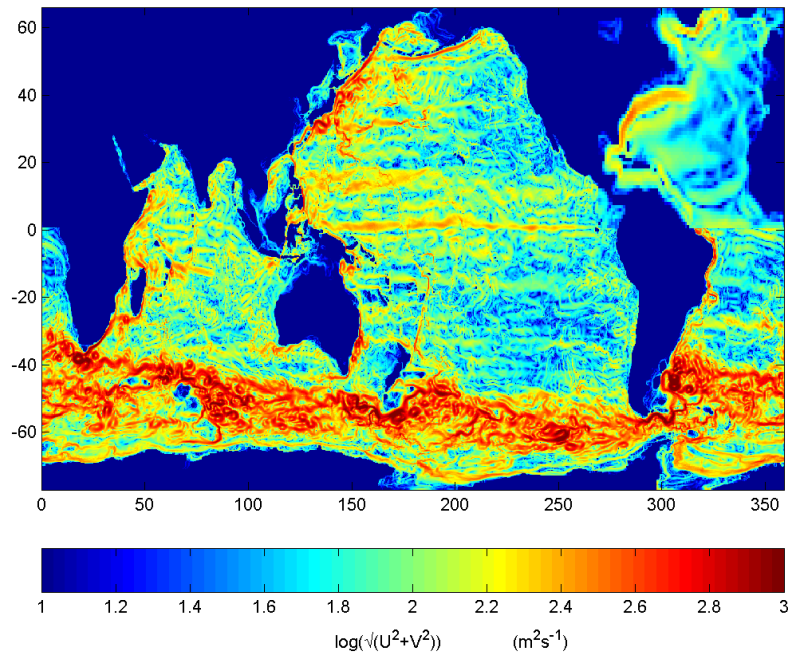


Figure 3.18: Magnitude distribution of the integrated velocity data from OCCAM (in  $m^2s^{-1}$ ).

run for analysis purpose. Archived data of the variable are available for every 15 days for most of the analysis period within the latitudinal limits  $+66$  to  $-77$  degrees. However, velocity data are not available for North Atlantic region. For the *Swarm* simulations we used the average horizontal velocity fields from the 2985 and 3000 days of model run.

### 3.7.2 OCCAM velocity data

The velocity fields were vertically integrated and subsequently interpolated to a common grid. For the North Atlantic area, where the OCCAM data are not available, velocity data from ECCO (for the year 2002) were interpolated to fill the gap. The velocities outside the latitudinal limits  $+66^\circ$  to  $-77^\circ$  degrees were set to zero. The magnitude of the velocity data with  $0.25^\circ \times 0.25^\circ$  resolution is shown in the Figure 3.18. Narrow, intense currents and eddies are evident especially along the Antarctic Circum Polar current and the western boundaries. An exception is the Gulf Stream region in the North Atlantic, where ECCO data were used to fill the gap. A plot of zonal velocity data for the Drake Passage (south of South America) (Figure 3.19) shows the smooth nature of ECCO model (year 2002) as compared to OCCAM. Moreover, OCCAM gives a higher value for zonal water transport across the Passage than ECCO.

### 3.7.3 Forward Computation of ocean magnetic fields

We compute the magnetic fields due to ocean flow following the approach elaborated in the Task I studies (see sections 3.3). This approach is based on volume integral equations and allows simulating electromagnetic (EM) fields, excited by arbitrary sources in three-dimensional spherical model of conductivity. The 3D electrical conductivity model consists of a surface shell of variable conductance, underlain by a 1D mantle. An improvement of the conductivity model

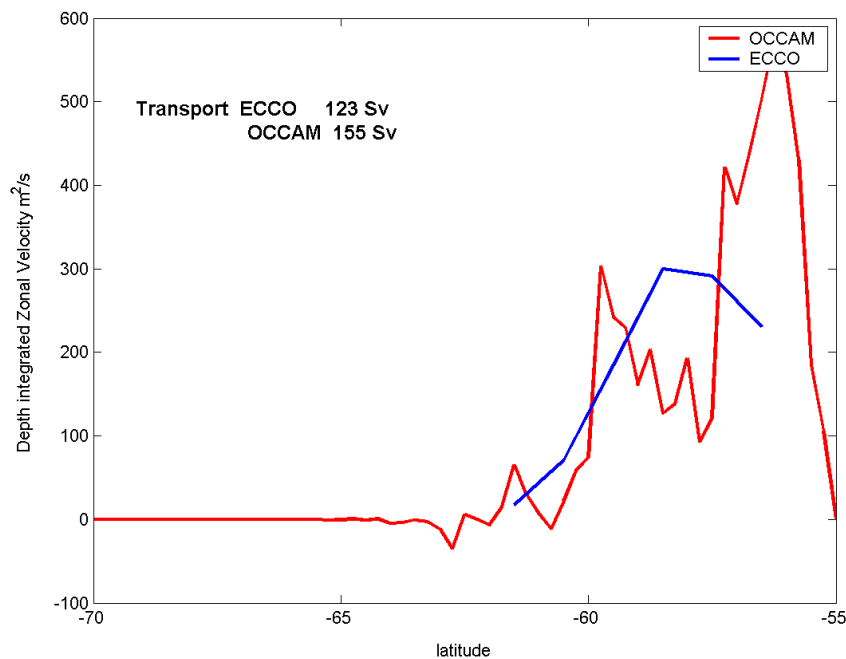


Figure 3.19: Comparison of OCCAM and ECCO model outputs across Drake Passage.

over the previous simulation has been done as follows. The sea water conductance was computed at a  $0.25^\circ \times 0.25^\circ$  resolution (Figure 3.20) using depth data derived from  $5' \times 5'$  NOAA ETOPO bathymetry. The conductance map for sediments was essentially the same, however interpolated to a  $0.25^\circ \times 0.25^\circ$  mesh. Simulations using the velocity grid of dimension  $720 \times 1440$  took 20 hours on one processor of type SunFire V8800.

### 3.7.4 Results of simulation

The predicted magnetic fields are presented on Figure 3.21. The left panels show the fields at sea level and the right panels show the fields at *Swarm* altitude (430 km above sea level). At sea level the predicted magnetic fields have a range of  $\pm 10$  nT. The effect of small-scale ocean circulation features are clearly visible in the vertical magnetic field component. The Kuroshio Current region, off the coast of Japan is an example. The strong positive and negative anomalies are probably due to the presence of eddy currents (see Figure 3.21). We will have a closer look at this region later in this section. Compared to the vertical magnetic field components, the horizontal fields have lesser strength. The large spatial scale of ocean generated magnetic fields allows the information about major water transport to reach the satellite altitude, though with reduced amplitude (see right panels of Figure 3.21). The predicted magnetic fields at *Swarm* altitude have an amplitude ranges of  $\pm 2$  nT. As we have shown in our previous simulations, the magnetic fields are predominated by the Antarctic Circumpolar Current (ACC) and western boundaries. In the following sections, we use only the vertical component of the magnetic fields. Since all fields are poloidal, their horizontal components do not contain independent information.

A detailed map of the Kuroshio Current region is given in Figure 3.22. The bottom panel shows the vertical component of the predicted magnetic field at sea level, and the upper panel

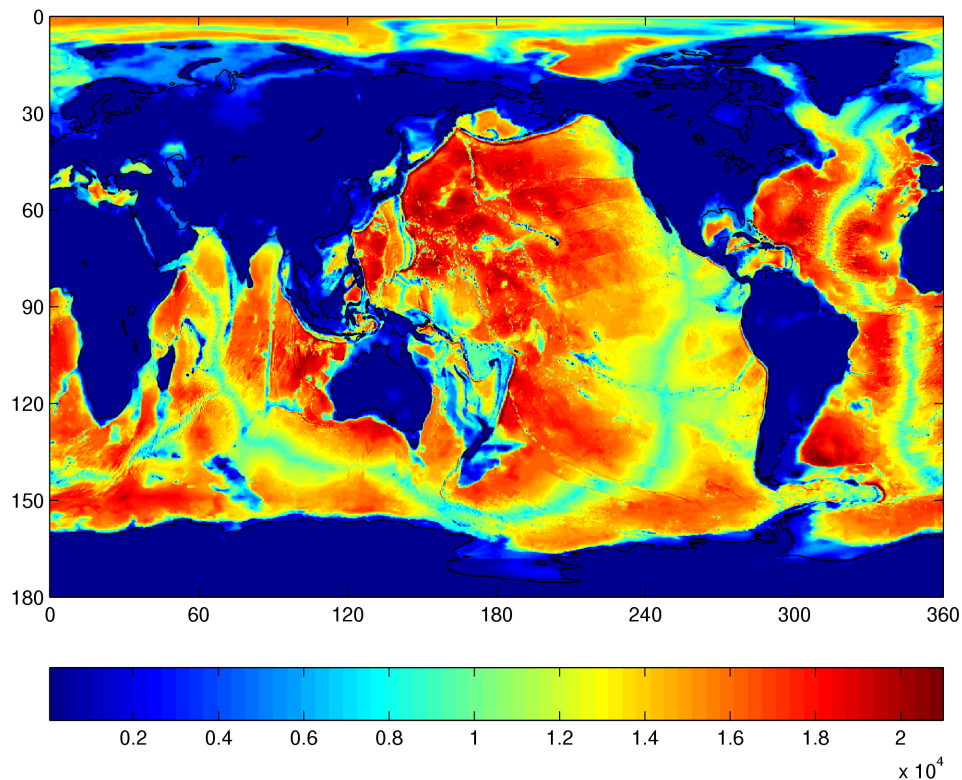


Figure 3.20: Improved conductance map on  $0.25^\circ \times 0.25^\circ$  resolution (in S).

the magnetic field at satellite altitude. Both maps are superimposed by the velocity vectors from OCCAM results. The induced magnetic fields due to eddies are evident at sea level, with a large amplitude range of  $\pm 10$  nT. These anomalies can be considered as a compounded effect of magnetic fields generated by individual eddies. As the ocean-continent boundary represents a large lateral contrast in conductance, the variation in sensitivity of the magnetic fields with respect to the conductance also must be taken into account. The one-to-one relationships between eddies and predicted anomalies are difficult to explain considering these complications. We will discuss this issue later in this document. At satellite altitude the magnetic fields of individual eddies are not resolved (upper panel of Figure 3.22). Here, the magnetic signatures of the Kuroshio Current exist as weak elongated anomalies running parallel to the coast.

### 3.7.5 Comparison of results using ECCO and OCCAM models

The idea behind the new simulations with high resolution OCCAM velocity data is to study the magnetic effect of small scale features of the ocean circulation like eddy currents. Since ECCO outputs are in  $1^\circ \times 1^\circ$  degree resolution, they cannot include the small scale features in ocean circulation. It was expected that in large scale maps, the flows will be more intense and may produce higher amplitudes for predicted magnetic fields at *Swarm* altitude. The results from simulations using OCCAM and ECCO data are presented in Figure 3.23 for comparison. The left panels show the results from OCCAM data and the right, show the results from ECCO data. The vertical components of the predicted magnetic fields at sea level are given in the bottom panel. The effect due to eddies are clearly visible in the simulations from OCCAM data. Other than Kuroshio Current region, eddy magnetic signals can also be seen along ACC,

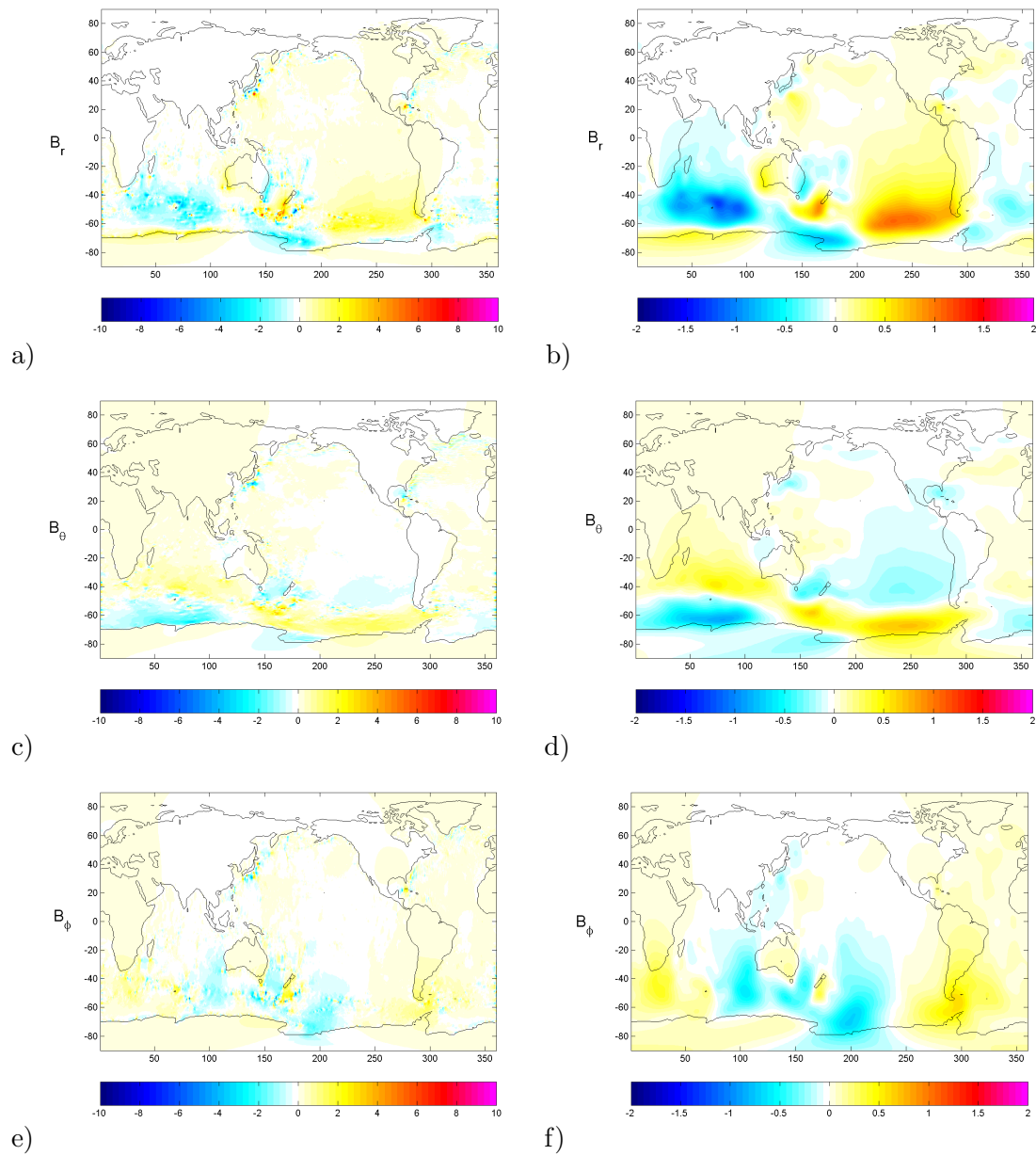
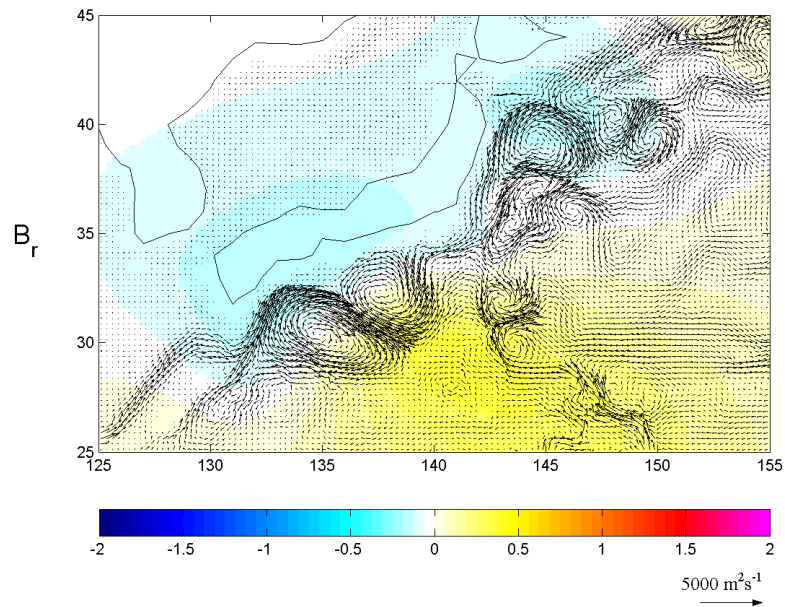
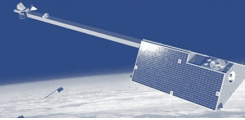
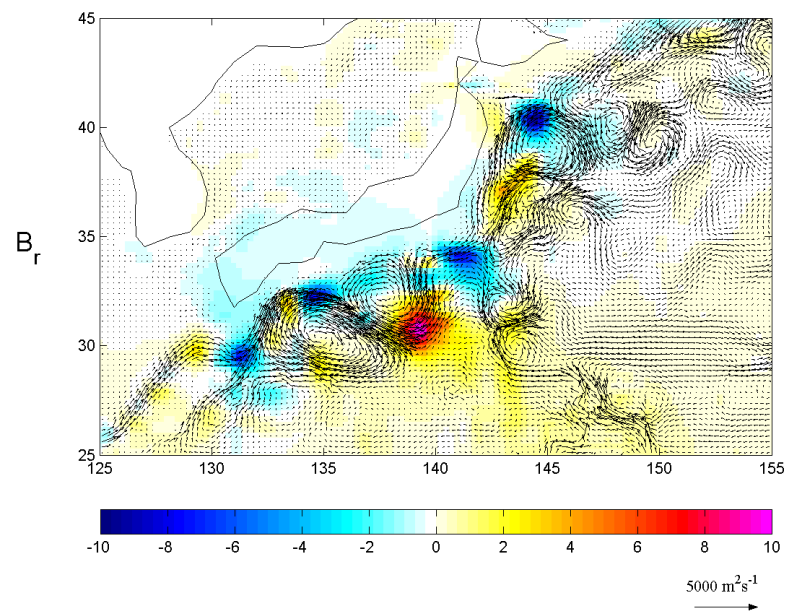


Figure 3.21: Predicted components of the ocean induced magnetic field ( $B_r$ ,  $B_\theta$ ,  $B_\phi$ ; from top to bottom) at sea level (left panels) and at 430 km above sea level (right panels) (in nT).



a)



b)

Figure 3.22: Predicted vertical component of ocean induced magnetic field in nT for the Kuroshio Current Region (magnetic field in nT). (a) At *Swarm* altitude (430 km) and (b) at sea level.

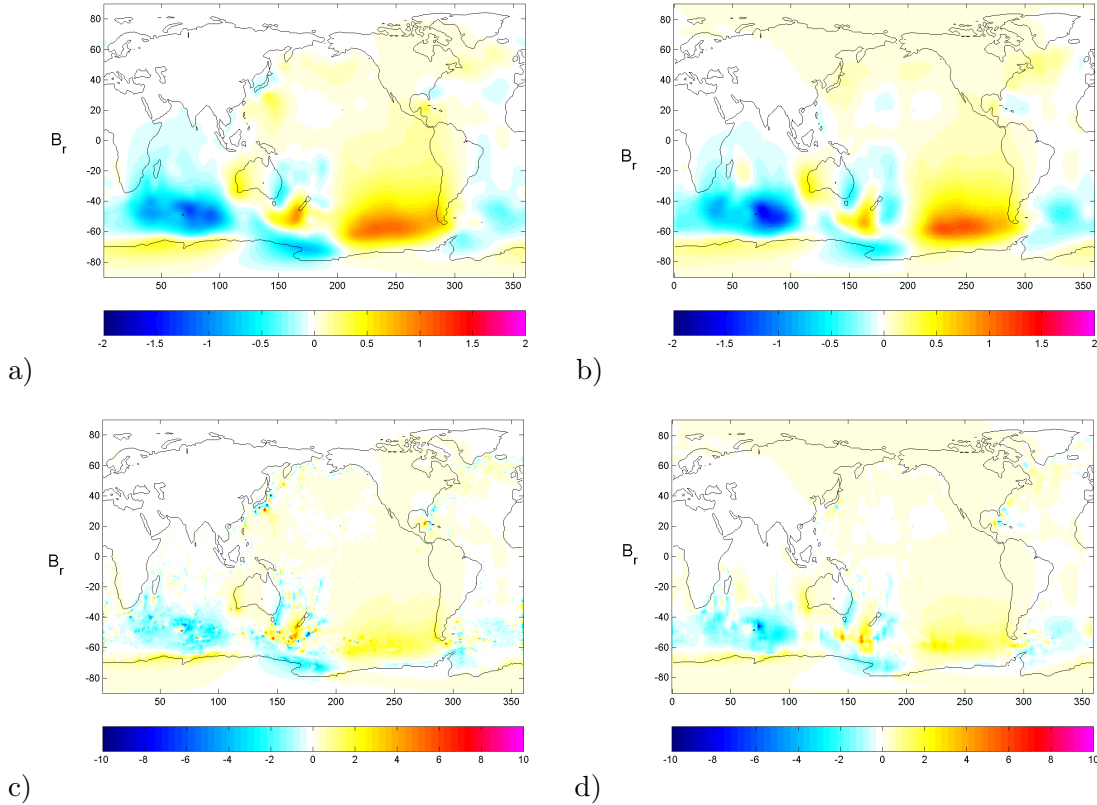


Figure 3.23: Comparison of simulations using OCCAM (left panels) and ECCO (right panels) results at sea level and at 430 km above sea level (in nT).

especially south of Australia. The smaller, but intense flows resulted in an increased amplitude range for signals simulated by OCCAM velocity data at sea level. Where as, ECCO predictions at sea level have an amplitude range between  $\pm 6$  nT, OCCAM results give a range of  $\pm 10$  nT. However such differences do not show up when the predicted fields are upwardly continued to *Swarm* altitude. In the upper panels of Figure 3.23, both predictions look very much the same. Both the predictions for vertical components of magnetic fields are within an amplitude range  $\pm 2$  nT. The predicted vertical magnetic fields from ECCO data have a slightly higher amplitude above the ACC in the Southern Indian ocean. (ECCO: -1.5 nT and OCCAM: -1.2 nT).

### 3.8 Sensitivity analysis

In this section we estimate the spatial distribution of the sensitivity of the ocean magnetic signals with respect to the Earth's main magnetic field and its 3D conductivity distribution. This scheme consists of the following three steps.

1. On a mesh  $S_{kl}$ ,  $\{S_{kl} : \vartheta_k = \Delta\vartheta_k, \varphi_l = \Delta\varphi_{(l-1)}, \Delta\vartheta = \frac{\pi}{N_\vartheta}, \Delta\varphi = \frac{2\pi}{N_\varphi}, k = 0, 1, \dots, N_\vartheta, l = 1, 2, \dots, N_\varphi\}$  the elementary vortex flows,  $\mathbf{U}_{kl}$ , are introduced in the form

$$\mathbf{U}_{kl} = \mathbf{e}_r \times \nabla_\perp \Psi_{kl}, \quad (3.32)$$

where  $\mathbf{e}_r$  is the radial unit vector, subscript  $\perp$  denotes the tangential vector,  $\nabla_{\perp}\Psi_{kl} = \mathbf{e}_{\vartheta} \frac{\partial \Psi_{kl}}{\partial \vartheta} + \mathbf{e}_{\varphi} \frac{1}{\sin \vartheta} \frac{\partial \Psi_{kl}}{\partial \varphi}$  is the tangential gradient of scalar function  $\Psi_{kl}$ , and  $\mathbf{e}_{\vartheta}$  and  $\mathbf{e}_{\varphi}$  are the unit tangential vectors. Such presentation follows from steady flow incompressibility,

$$\nabla_{\perp} \cdot \mathbf{U}_{kl} = 0. \quad (3.33)$$

2. For each elementary vortex flow  $\mathbf{U}_{kl}$  the EM simulations (with  $N = (N_{\vartheta} - 1) \times N_{\varphi} + 2$  simulations) are performed with a realistic conductivity model for the Earth by using the numerical solution described above. The model is excited by an inducing current deduced from elementary vortex flow with the use of equation (3.15). As a result we obtain  $3N$  maps of the magnetic field  $\mathbf{B}^{(kl)}$  on a mesh,  $S_{mn} = \{\vartheta_m = \Delta_{\vartheta}(m - 0.5), \varphi_n = \Delta_{\varphi}(n - 0.5), m = 1, 2, \dots, N_{\vartheta}, n = 1, 2, \dots, N_{\varphi}, \}$  at satellite altitude  $h$ .
3. Since  $\mathbf{B}^{(kl)}$  decays quite rapidly with horizontal distance from the centre of an elementary vortex flow, we can combine  $3N$  maps of the magnetic fields into one map of the combined magnetic fields. This map will give an idea about the relative strength of the magnetic signal due to ocean flow in different regions above the Earth.

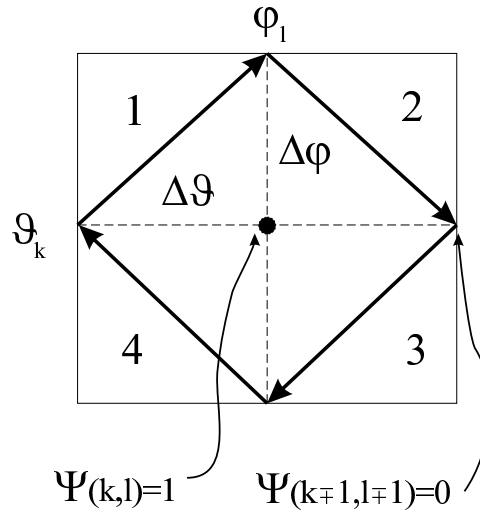


Figure 3.24: The sketch of the geometry of an elementary vortex flow.

Fig. 3.24 shows the geometry of elementary vortex flow used in the implemented scheme.

The geometry of the velocity components,  $\mathbf{U}_{kl}$ , in the four sub-cells occupied by vortex flow is determined as

$$U_{\vartheta}^{1,kl} = -\frac{1}{\sin \vartheta_k} \frac{1}{\Delta_{\varphi}}, \quad U_{\vartheta}^{2,kl} = \frac{1}{\sin \vartheta_k} \frac{1}{\Delta_{\varphi}}, \quad U_{\vartheta}^{3,kl} = \frac{1}{\sin \vartheta_k} \frac{1}{\Delta_{\varphi}}, \quad U_{\vartheta}^{4,kl} = -\frac{1}{\sin \vartheta_k} \frac{1}{\Delta_{\varphi}}, \quad (3.34)$$

$$U_{\varphi}^{1,kl} = \frac{1}{\Delta_{\vartheta}}, \quad U_{\varphi}^{2,kl} = \frac{1}{\Delta_{\vartheta}}, \quad U_{\varphi}^{3,kl} = -\frac{1}{\Delta_{\vartheta}}, \quad U_{\varphi}^{4,kl} = -\frac{1}{\Delta_{\vartheta}}. \quad (3.35)$$

Here superscripts 1, 2, ... are the respective cell numbers (see Fig. 3.24). Note that these expressions are valid for all locations of vortex flows on the mesh except at the north and south poles,

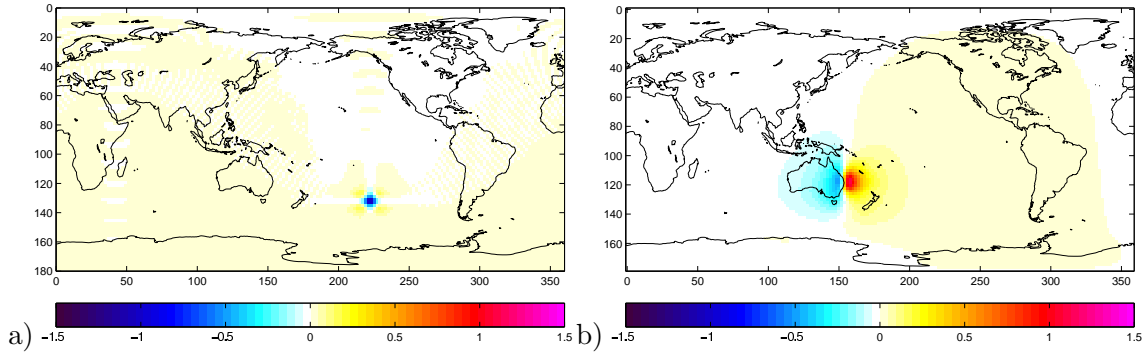


Figure 3.25: Predicted vertical component of the magnetic field (in nT) due to a single vortex flow at two locations (a) South Pacific ( $\vartheta = 134^\circ$ ,  $\varphi = 224^\circ$ ) and (b) east coast of Australia ( $\vartheta = 120^\circ$ ,  $\varphi = 156^\circ$ ).

where the meridional component,  $U_\vartheta$ , becomes zero and the vortex flow occupies  $N_\varphi$  cells with  $U_\varphi^i = \frac{1}{\Delta\varphi}$ ,  $i = 1, 2, \dots, N_\varphi$ .

For modelling, the grid dimensions  $N_\vartheta$  and  $N_\varphi$  have been chosen to be 90 and 180 respectively which gives an effective spatial resolution of  $2^\circ \times 2^\circ$ . Further,  $(N_\vartheta - 1) \times N_\varphi + 2$  simulations have been conducted in a 3-D conductivity model of the Earth. The 3-D conductivity model was taken to be the same, as used in the previous model studies.

Figure 3.25 shows as examples, the magnetic fields at satellite altitude for two vortex flows at locations in the southern hemisphere. In order to make the results comparable, the locations of vortex flows are chosen to have approximately the same strength of the geomagnetic field vertical component. The left panel shows the vertical magnetic field from a vortex at the centre of South Pacific ocean. The right panel shows the magnetic signature from a vortex near the east coast of Australia. For these two locations the vortex flows produce different magnetic signals. The first one is consistent with the magnetic of a star-like geometry (which follows from the geometry of the elementary vortex flow). Whereas the second example resembles the vertical magnetic field of dipole oriented along the coast. The reason for change in magnetic field signature is the contrast between the sea water and the poorly conducting continent which prevents inland penetration of the electric currents. This leads to the reconfiguration of the inducing currents, and the resulting currents get oriented along the ocean-continent boundary. Since the 3D conductivity model assumes a highly resistive lithosphere, the magnetic fields gets more pronounced (Figure 3.25b).

Magnetic fields, calculated at the Earth's surface were upward continued to satellite altitude at  $h = 430$  km. Finally,  $(N_\vartheta - 1) \times N_\varphi + 2$  maps of the vertical magnetic field were obtained. The computation with the grid spacing of  $89 \times 180 + 2$  points took 10 days on two processors of the type SunFire V8800. These maps have been combined into one map that depicts the accumulated absolute value of  $B_r$ , determined as

$$F(\vartheta_k, \varphi_l) = \sum_{\vartheta_m, \varphi_n \in S_{mn}} |B_r^{(kl)}(r = a + h, \vartheta_m, \varphi_n)|. \quad (3.36)$$

We have chosen the vertical magnetic component for our analysis. Previous studies showed that this component has larger (compared to other components) amplitude of the modelled signals due to ocean steady flow. Fig. 3.26 demonstrates the map of  $F$  in logarithmic scale. As is expected, the accumulated signal,  $F$  has low values above the continents, while above the oceans,  $F$  resembles the distribution of the vertical component of the main magnetic field,

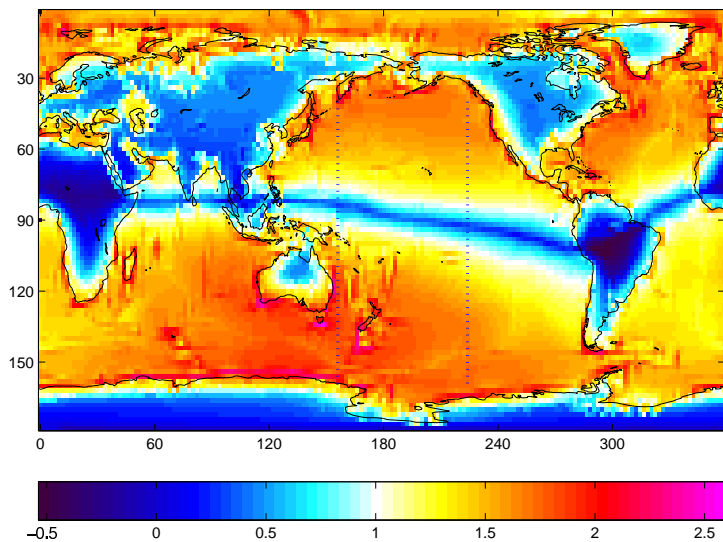


Figure 3.26: Accumulated absolute value of vertical magnetic field,  $F$  at *Swarm* altitude (in nT; on logarithmic (base 10) scale).

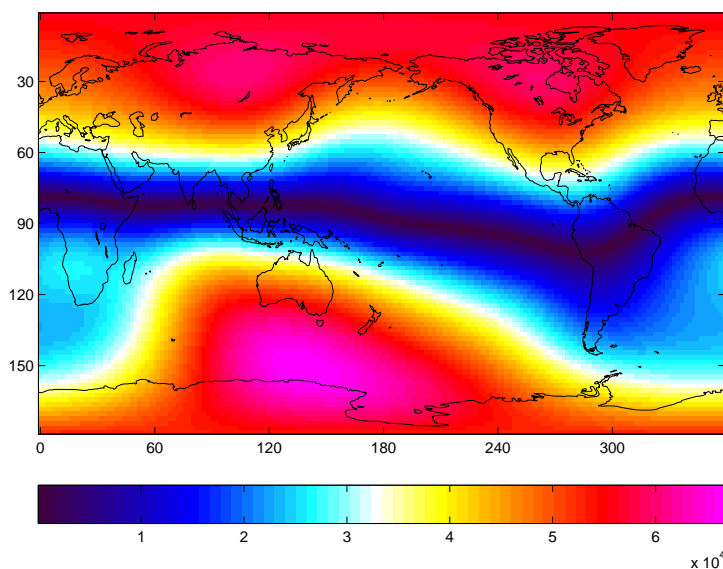


Figure 3.27: Absolute value of main field vertical component (in nT).

$B_r^m$  (cf. Fig. 3.27). The latter is due to the fact that the induced electric current is directly proportional to  $B_r^m$  (equation 3.15).

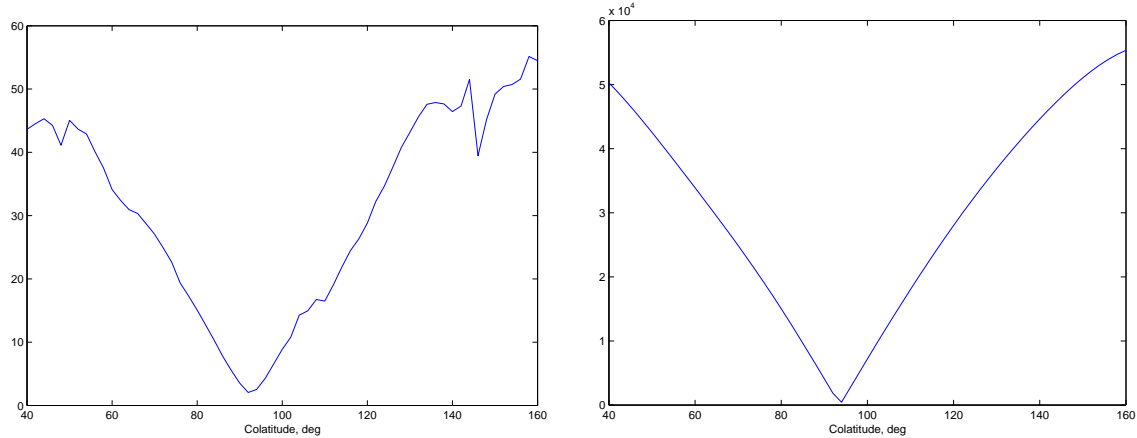


Figure 3.28: The accumulated absolute value,  $F$  (left panel) and geomagnetic field vertical component,  $|B_r^m|$  (right panel) along longitudinal profile of  $\varphi = 224^\circ$  (in nT).

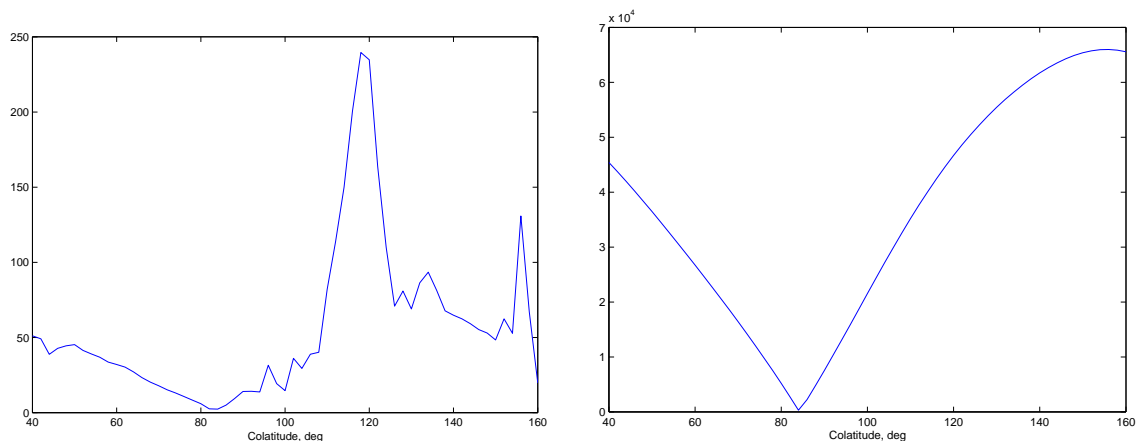


Figure 3.29: Same as above but along longitudinal profile of  $\varphi = 156^\circ$  (in nT).

In addition to the dependence on the geomagnetic field, the signal  $F$  attains high values along the ocean-continent boundaries. To illustrate this in more details, Fig. 3.28 presents  $F$  (left panel) and  $|B_r^m|$  (right panel) along a longitudinal profile at  $\varphi = 224^\circ$ . This profile crosses the Pacific ocean at its central part, (see Figure 3.26 for location) where the distribution of surface conductance in lateral directions is almost uniform. Along this profile the correlation coefficient between  $F$  and  $|B_r^m|$  is 0.97. However, over regions with the large lateral contrasts of surface conductance (i.e. over the coasts and deep trenches) one can observe enhancement of  $F$ . It is possibly due to the anomalous behavior of vertical component of induced magnetic field over these regions. Fig. 3.29 shows  $F$  and  $|B_r^m|$  along the longitudinal profile of  $\varphi = 156^\circ$  that crosses Pacific ocean in its eastern part (see Figure 3.26 for location). Along this profile the correspondence between  $F$  and  $|B_r^m|$  is not so evident (the correlation coefficient is 0.52). A prominent enhancement of  $F$  is observed in the the southern part of the profile, close to the eastern coast of Australia.

### 3.9 Recovery of the ocean circulation from satellite magnetic signals

In this section we introduce a scheme to recover ocean circulation from satellite magnetic signals and present preliminary results of it. The scheme is based on two considerations: (1) An arbitrary ocean steady flow can be represented as a superposition of elementary vortex flows and (2) Maxwell's equations which describe the behavior of the magnetic field due to global ocean flow (ocean circulation) are linear with respect to the exciting electric currents. Then the magnetic signal at any altitude caused by ocean circulation,  $\mathbf{U}$ , can be written as,

$$\mathbf{B}_{\mathbf{U}} = \sum_i a_i \mathbf{B}_{\mathbf{U}_i}, \quad (3.37)$$

where  $\mathbf{U}$  is given via elementary vortex flows  $\mathbf{U}_i$  as

$$\mathbf{U} = \sum_i a_i \mathbf{U}_i. \quad (3.38)$$

In the numerical implementation,  $\mathbf{U}_i$  differs from 0 only in  $i$ -th cell of the mesh in which the elementary vortex flows are introduced. It means that the coefficients  $a_i$  determine the intensities of elementary vortex flows  $\mathbf{U}_i$ .

To solve equation 3.37, let  $L$  be a linear operator that acts on an external electric current,  $\mathbf{J}^{ext}$  causing the magnetic field,  $\mathbf{B}$ , at some altitude is

$$L : \mathbf{B} = L\{\mathbf{J}^{ext}\}. \quad (3.39)$$

For a specific ocean flow  $\mathbf{U}$  determined by equation (3.38) we have,

$$\begin{aligned} \mathbf{B}_{\mathbf{U}} &= L\{\mathbf{J}_{\mathbf{U}}^{ext}\} = L\{\sigma \mathbf{U} \times \mathbf{B}^m\} = L\{\sigma (\sum_i a_i \mathbf{U}_i) \times \mathbf{B}^m\} \\ &= L\{\sum_i a_i \mathbf{J}_{\mathbf{U}_i}^{ext}\} = \sum_i a_i L\{\mathbf{J}_{\mathbf{U}_i}^{ext}\} = \sum_i a_i \mathbf{B}_{\mathbf{U}_i}, \end{aligned} \quad (3.40)$$

where  $\mathbf{B}_{\mathbf{U}_i} = L\{\mathbf{J}_{\mathbf{U}_i}^{ext}\}$  with  $\mathbf{J}_{\mathbf{U}_i}^{ext}$  determined as

$$\mathbf{J}_{\mathbf{U}_i}^{ext} = \sigma_i \mathbf{U}_i \times \mathbf{B}_i^m. \quad (3.41)$$

Here  $\sigma_i$  and  $\mathbf{B}_i^m$  are the conductivity and main magnetic field in  $i$ -th cell of the mesh.

From equations 3.37-3.41 it follows that the proposed scheme implies the calculation of  $\mathbf{B}_{\mathbf{U}_i}$  for a preselected set of elementary vortex flows  $\mathbf{U}_i$  and then the determination of the intensities  $a_i$  from the equation (3.37) by applying the least squares approach.

As a test for the scheme, we consider a radially symmetric (1-D) Earth model that consists of a uniform ocean with a conductance of 20000 S and 1-D mantle underneath. The parameters of the 1-D mantle are the same as used for the 3-D modelling performed in the previous sections. For ocean flow, we adopt a simplified circulation model which is described by an array of  $3 \times 3$  adjacent  $4^\circ \times 4^\circ$  elementary vortex flows. The vortex flows occupy the region which is bounded by the colatitudes  $\vartheta = 126^\circ$  and  $\vartheta = 138^\circ$ , and longitudes  $\varphi = 196^\circ$  and  $\varphi = 208^\circ$  (see Fig. 3.30). The geometry of vortex flows are the same as used in the previous section. The intensities  $a_i=1$ , for the ocean flow were assigned to all vortexes. For this distribution of vortexes and for

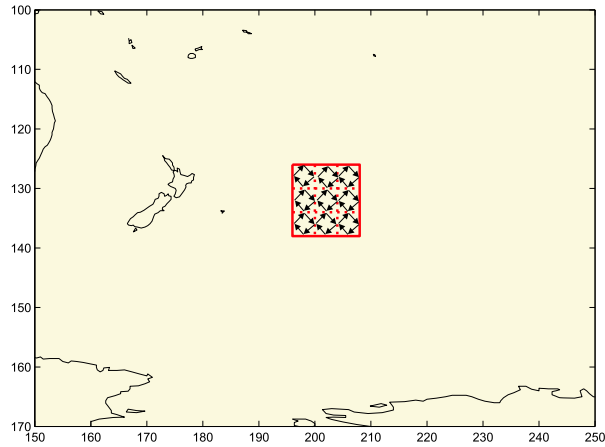
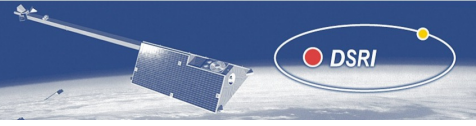


Figure 3.30: Location of test ocean flow pattern.

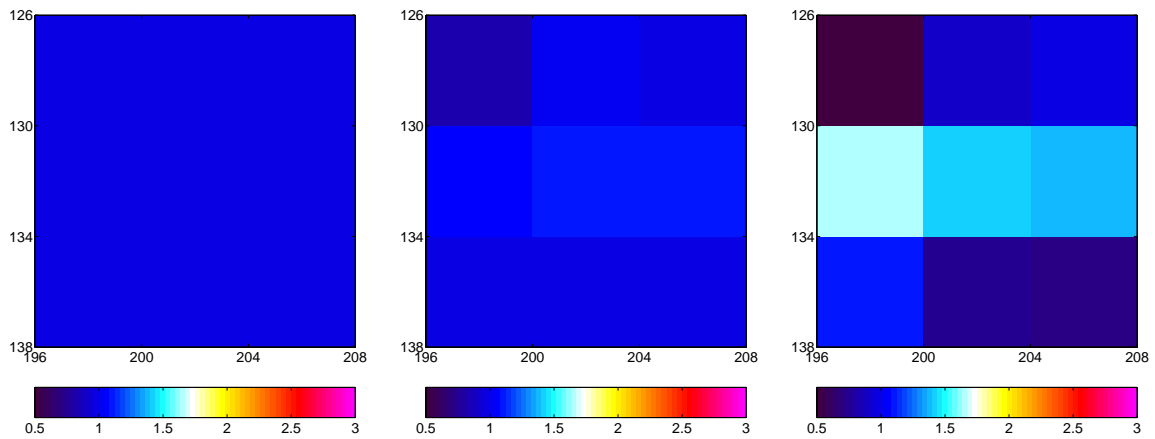


Figure 3.31: Ocean flow intensities: Original (left panel), and results of LS inversion from predicted magnetic fields at sea level (middle panel) and at *Swarm* altitude (right panel).

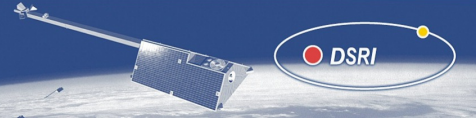


each elementary vortex, the vertical magnetic field at sea level and at an altitude of 430 km were calculated. Further, using the least square (LS) procedure, the estimates of the intensities,  $a_i$  have been determined from the modelled magnetic fields at sea-level and, separately, from the fields at satellite altitude. For the application of LS approach, the vertical magnetic fields over an area bounded by colatitudes  $\vartheta = 90^\circ$  and  $\vartheta = 178^\circ$ , and longitudes  $\varphi = 100^\circ$  and  $\varphi = 300^\circ$  were used.

Left panel of Fig. 3.31 shows the intensities of the test ocean flow ( $a_i = 1$ ). The predicted magnetic fields (at sea level and satellite altitude) from this ocean flow were inverted using the LS approach previously described. The middle and right panels of Fig. 3.31 show the ocean flow intensities obtained from the inversions of magnetic fields at sea level and satellite altitude respectively. It can be seen from these figures that there is a good agreement exists between original flow and the ocean flow inverted from magnetic field at sea level (their relative differences vary from 0 % to 20 %). In addition, a reasonable agreement exists between the original flow and the ocean flow inverted from magnetic fields at satellite altitude (their relative differences vary from 2 % to 100 %).

### 3.10 Conclusions

The high resolution simulations using OCCAM data brought out the effect of ocean eddies in ocean generated magnetic fields. In general, OCCAM simulations ( $0.25^\circ \times 0.25^\circ$ ) resulted in higher amplitudes compared to ECCO ( $1^\circ \times 1^\circ$ ) simulations, for the magnetic fields at the sea level. However at *Swarm* altitude, both predictions have almost the same magnitude. Here the predictions lack short wavelength features and describe the major water transport features in the ocean circulation. A sensitivity analysis of ocean magnetic signals showed two interesting results. The spatial distribution of the relative strength of magnetic field produced by the ocean circulation is mainly influenced by the vertical component of the geomagnetic field. One should expect maximum magnetic signals from the ocean flow close to the geomagnetic poles and least signals from the geomagnetic equator. We have shown using our previous simulations, that the temporal variations in ocean magnetic fields associated with Monsoon and El Niño have very small amplitudes. Considering the geographical proximity of both these ocean phenomena to the geomagnetic dip equator, the low amplitude for the magnetic field variations may be explained. A relatively high sensitivity for ocean-magnetic signals over the southern hemisphere improves the prospect to detect signals from the Antarctic Circumpolar Currents as well. Another inference from the analysis is the high sensitivity for regions where large lateral contrast in surface conductance exist. As ocean-continent boundaries offer such contrasts, it is a promising area for detecting western boundary currents. However, a rugged bathymetry may produce a random distribution of the sensitivity and can complicate the ocean magnetic fields. The least square approach introduced for recovery of ocean flow from satellite magnetic observations exploits the linear relation between ocean flow and ocean generated magnetic fields. With the assumptions of noise-free magnetic fields and 1D conductivity model for the Earth, a good agreement was reached between original and inverted flows using fields at sea level. However such agreement was not observed when the magnetic fields at *Swarm* altitude were inverted.



### 3.11 Suggestions for further studies

The high sensitivity of ocean-magnetic signals to the surface conductance distribution demands improvements to the existing conductance map. This may be achieved by computing a realistic distribution of ocean water conductance from the salinity and temperature data and by using a more realistic 3D Earth model. As ocean generated magnetic signals have small amplitudes at satellite altitude, it would be worthwhile to study their statistical properties. This means a serial computation of ocean-magnetic signals using a long and realistic time series of ocean circulation. Our simulations show a significant contribution of the ocean-magnetic signals to the geomagnetic fields. As *Swarm* intends to bring out more precise crustal magnetic models, the contributions from the steady state ocean flow should be considered while filtering the non-crustal part of the geomagnetic field. Recovery of ocean circulations and its temporal variations from satellite observations is a possibility, but should be further studied.

# Appendix A

## Coordinate systems

In this part of the report on the ionospheric currents, a number of different coordinate systems have been used. Definitions and references are given within this section.

### A.1 Geocentric Solar Magnetic (GSM) Frame

The GSM is a Cartesian coordinate system which is preferably used to describe the interaction of the solar wind with the magnetosphere. The origin of the frame is the centre of the Earth. The  $x$  axis is pointing towards the sun; the  $z$  axis lies in the plane formed by the  $x$  axis and the geomagnetic pole and points northward; the  $y$  axis completes the right-handed triad. A detailed definition is given in [Kivelson and Russell \[1995\]](#).

### A.2 Solar Magnetic (SM) Frame

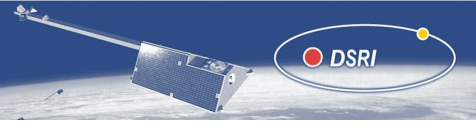
The SM frame is in particular useful to describe the electrodynamics in the near-Earth space. In this report it is a spherical coordinate system - with the components  $r, \theta, \phi$ . The origin of the frame is the centre of the Earth. The radial component  $r$  is the distance to the Earth's centre. The colatitude  $\theta$  describes the angular distance to the geomagnetic dipole axis in the northern hemisphere. The  $\phi = 0^\circ$ -meridian lies on the night-side, defined by the plane containing the magnetic dipole axis and the direction to the sun. The angle of the azimuthal component  $\phi$  increases towards east.

### A.3 IERS Conventional Terrestrial Reference Frame (ITRF)

The ITRF is an Earth-fixed Cartesian system used in this report for describing the orbit ephemeris. The origin of the frame is the Earth's centre of mass. The  $x$  axis points towards the IERS Reference Meridian (close to Greenwich); the  $z$  axis points to the Reference North Pole; the  $y$  axis completes the triad. A detailed description of this frame can be found in the IERS Technical Note 21 ([McCarthy \[1996\]](#)).

### A.4 Velocity Zenith (VZ) Frame

The Velocity-Zenith frame is a locally horizontal cartesian system. The origin is the measurement point, generally, moving along the orbit. The  $z$  axis points radially outward; the  $x$  axis



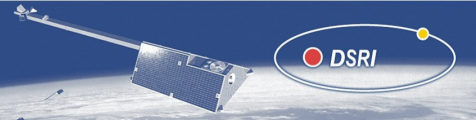
lies in the plane containing the  $z$  axis and the mean velocity vector, pointing in flight direction; the  $y$  axis completes the right-handed triad.

## A.5 Mean Field Aligned (MFA) Frame

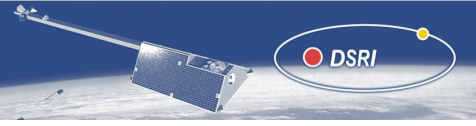
The MFA frame is a local coordinate system defined by the ambient magnetic field. It is particularly useful for describing electric currents in the topside ionosphere. The origin is the local measurement point of the magnetic field. The  $z$  axis is aligned with the unperturbed magnetic field which points from the southern to the northern hemisphere; the  $y$  axis is perpendicular to the magnetic meridian pointing predominantly eastward; the  $x$  axis completes the triad having an outward component.

# Bibliography

- G. Arfken. *Mathematical Methods for Physicists*. Academic Press, 3 edition, 1985.
- D. Avdeev, A. Kuvshinov, O. Pankratov, and G. Newman. High-performance three-dimensional electromagnetic modeling using modified Neumann series. Wide-band numerical solution and examples. *J. Geomagn. Geoelectr.*, 49:1519–1539, 1997.
- D. Avdeev, A. Kuvshinov, O. Pankratov, and G. Newman. Three-dimensional induction logging problems, Part I: An integral equation solution and model comparisons. *Geophysics*, 67:413–426, 2002.
- G. Backus. Poloidal and toroidal fields in geomagnetic field modeling. *Rev. Geophys.*, 24:75–109, 1986.
- S. Chapman and J. Bartels. *Geomagnetism*, volume I+II. Clarendon Press, Oxford, 1940.
- A. Chave and D. Luther. Low-frequency, motionally-induced electromagnetic fields in the ocean: 1. Theory. *J. Geophys. Res.*, 95:957185–957200, 1990.
- U. Engels and N. Olsen. Computation of magnetic fields within source regions of ionospheric and magnetospheric currents. *J. Atmosph. Solar-Terr. Phys.*, 60:1585–1592, 1998.
- S. Erofeeva and G. Egbert. Efficient inverse modelling of barotropic ocean tides. *J. Ocean. Atmosph. Technol.*, 19:183–204, 2002.
- M. Everett, S. Constable, and C. Constable. Effects of near-surface conductance on global satellite induction responses. *Geophys. J. Int.*, 153:277–286, 2003.
- E. Fainberg, A. Kuvshinov, and B. Singer. Electromagnetic induction in a spherical earth with non-uniform oceans and continents in electric contact with the underlying medium, I. Theory, method and example. *Geophys. J. Int.*, 102:273–281, 1990.
- J. Flosadottir, A.H. and J. Smith. Large-scale electric and magnetic fields generated by the oceans. *J. Geophys. Res.*, 102:10353–10372, 1997.
- I. Fukumori, R. Raghunath, L. Fu, and Y. Chao. Assimilation of TOPEX/POSEIDON data into a global ocean circulation model: How good are the results? *J. Geophys. Res.*, 104:25647–25665, 1999.
- R. Holme, N. Olsen, M. Rother, and H. Lühr. CO2 - a CHAMP magnetic field model. In C. Reigber, H. Lühr, and P. Schwintzer, editors, *First CHAMP Mission Results for Gravity, Magnetic and Atmospheric Studies*, pages 220–225, Berlin, 2003. Springer.



- A. Junge. The telluric field in northern Germany induced by tidal motion in the North Sea. *Geophys. J.*, 95:523–533, 1988.
- M. G. Kivelson and C. Russell. *Introduction to Space Physics*. Cambridge University Press, 1995.
- S. Knight. Parallel electric fields. *Planet. Space Sci.*, 21:741, 1972.
- A. Koehl, D. Stammer, B. Cornuelle, E. Remy, Y. Lu, P. Heimbach, , and C. Wunsch. The global 1° WOCE Synthesis: 1992–2001. The ECCO Report Series 1 Number 20, Jet Propulsion Laboratory, The Massachusetts Institute of Technology and the Scripps Institution of Oceanography, 2003.
- A. V. Kuvshinov, D. B. Avdeev, O. V. Pankratov, S. A. Golyshev, and N. Olsen. Modelling electromagnetic fields in 3D spherical Earth using fast integral equation approach. In M. S. Zhdanov and P. E. Wannamaker, editors, *3D Electromagnetics*, chapter 3, pages 43–54. Elsevier, Holland, 2002.
- A. V. Kuvshinov and N. Olsen. 3D modelling of the magnetic field due to ocean flow. In C. Reigber, H. Lühr, P. Schwintzer, and J. Wickert, editors, *Earth Observation with CHAMP, Results from Three Years in Orbit*. Springer Verlag, 2005.
- A. V. Kuvshinov, H. Utada, D. Avdeev, and T. Koyama. 3-D modelling and analysis of *Dst* *C*-responses in the North Pacific ocean region, revisited. *Geoph. J. Int.*, 60 (2):505–526, doi: 10.1111/j.1365-246X.2005.02477.x, 2005.
- H. Lühr, S. Maus, M. Rother, and D. Cooke. First in-situ observation of night-time F region currents with the CHAMP satellite. *Geophys. Res. Lett.*, 29:127–1, May 2002.
- J. C. Larsen. An introduction to electromagnetic induction in the ocean. *Phys. Earth Planet. Int.*, 7:389398, 1973.
- J. C. Larsen. Transport and heat flux of the Florida Current at 27°N derived from cross-stream voltages and profiling data: Theory and observations. *Phys. Earth Planet. Int.*, 338: 169–236, 1992.
- G. Laske and G. Masters. A global digital map of sediment thickness. *EOS Trans. AGU*, 78: F483, 1997.
- F. Lilley, A. White, and G. Heinson. Earth’s magnetic field: ocean current contributions to vertical profiles in deep oceans. *Geophys. J. Int.*, 147:163–175, 2001.
- Y. Lu, K. Ueyoshi, A. Koehl, R. E., K. Lorbacher, and D. Stammer. Input data sets for the ECCO global 1° WOCE synthesis. The ECCO Report Series 1 Number 18, Jet Propulsion Laboratory, The Massachusetts Institute of Technology and the Scripps Institution of Oceanography, 2003.
- H. Lühr, J. J. Warnecke, and M. Rother. An algorithm for estimating field-aligned currents from single spacecraft magnetic field measurements: a diagnostic tool applied to Freja satellite data. *IEEE Trans Geosci. Remote Sens.*, 34:1369–1376, 1996.
- J. Marotzke, R. Giering, Q. K. Zhang, D. Stammer, C. N. Hill, and T. Lee. Construction of the adjoint MIT ocean general circulation model and application to Atlantic heat transport sensitivity. *J. Geophys. Res.*, 104:29,529–29,548, 1999.



- A. Marshall, J., C. Adcroft, L. Hill, Perelman, and C. Heisey. A finite-volume, incompressible navier-stokes model for studies of the ocean on parallel computers. *J. Geophys. Res.*, 102: 5753–5766, 1997.
- S. Maus, M. Rother, R. Holme, H. Lühr, N. Olsen, and V. Haak. First scalar magnetic anomaly map from CHAMP satellite indicates weak lithospheric field. *Geophys. Res. Lett.*, 29(10), 2002.
- D. D. Mc Carthy. IERS technical note 21, IERS conventions. Technical report, IERS, 1996.
- J. Moen and A. Brekke. The solar flux influence on quiet time conductances in the auroral ionosphere. *Geoph. Res. Lett.*, 20:971, 1993.
- N. Olsen. A new tool for determining of ionospheric currents from satellite data. *Geophys. Res. Lett.*, 23:3635–3638, 1996.
- N. Olsen. A model of the geomagnetic main field and its secular variation for epoch 2000 estimated from Ørsted data. *Geophys. J. Int.*, 149:454–462, 2002.
- N. Olsen, E. Friis-Christensen, G. Hulot, M. Korte, A. Kuvshinov, V. Lesur, H. Lühr, S. Macmillan, M. Manda, S. Maus, M. Purucker, C. Reigber, P. Ritter, M. Rother, T. Sabaka, P. Tarits, and A. Thomson. *Swarm End-to-End Mission Performance Simulator Study, February 2004*. ESA Contract No. 17263/03/NL/CB, DSRI Report 1/2004, 2004.
- O. Pankratov, A. Kuvshinov, and D. Avdeev. High-performance three-dimensional electromagnetic modeling using modified Neumann series. Anisotropic case. *J. Geomagn. Geoelectr.*, 49: 1541–1547, 1997.
- J. Raeder. *in: Space Plasma Simulation*, volume 615 of *Lecture Notes in Physics*. Springer Verlag, Heidelberg, 2003.
- J. Raeder and V. Angelopoulos. Using global simulations of the magnetosphere for multi-satellite mission planning and analysis, in: Science closure and enabling technologies for constellation class missions. Technical Report 78, UCB and NASA GSFC, 1998.
- J. Raeder, J. Berchem, and M. Ashour-Abdalla. The geospace environment grand challenge: Results from a global geospace circulation model. *Jour. Geoph. Res.*, 103:14787, 1998.
- H. Rishbeth. The *F*-layer dynamo. *Planet. Space Sci.*, 19:263–267, 1971.
- H. Rishbeth. The *F*-region dynamo. *J. Atmos. Terr. Phys.*, 43:387–392, 1981.
- P. Ritter, H. Lühr, S. Maus, and A. Viljanen. High latitude ionospheric currents during very quiet times: their characteristics and predictabilities. *Ann. Geophys.*, 22:2001–2014, 2004a.
- P. Ritter, H. Lühr, A. Viljanen, O. Amm, A. Pulkkinen, and I. Sillanpää. Ionospheric currents estimated simultaneously from CHAMP satellite and IMAGE ground-based magnetic field measurements: A statistical study at auroral latitudes. *Ann. Geophys.*, 22:417–430, 2004b.
- R. Robinson, R. Vondrak, K. Miller, T. Dabbs, and D. Hardy. On calculating ionospheric conductances from the flux and energy of precipitating electrons. *Jour. Geoph. Res.*, 92:2565, 1987.



- T. Sanford. Motionally-induced electric and magnetic fields in the sea. *J. Geophys. Res.*, 76: 3476–3492, 1971.
- P. Saunders, A. C. Coward, and B. A. de Cuevas. The Circulation of the Pacific Ocean seen in a Global Ocean Model (OCCAM). *J. Geophys. Res.*, 104:18281–18299, 1999.
- K. Schlegel. Auroral zone E-region conductivities during solar minimum derived from EISCAT data. *Ann Geophys.*, 6:129–138, 1988.
- U. Schmucker. Electrical properties of the Earth's interior. In *Landolt-Börnstein, New-Series, 5/2b*, pages 370–397. Springer-Verlag, Berlin-Heidelberg, 1985.
- B. Singer. Method for solution of Maxwell's equations in non-uniform media. *Geophys. J. Int.*, 120:590–598, 1995.
- D. Stephenson and K. Bryan. Large-scale electric and magnetic fields generated by the oceans. *J. Geophys. Res.*, 97:15467–15480, 1992.
- D. P. Stern. Representation of magnetic fields in space. *Rev. Geophys.*, 14:199–214, 1976.
- R. Tyler. Electromagnetic fields generated by a three-dimensional global ocean. *J. Geophys. Res.*, 102:5531–5551, 1992.
- R. Tyler, S. Maus, and H. Luehr. Satellite observations of magnetic fields due to ocean tidal flow. *Science*, 299:239–240, 2003.
- R. Tyler, J. Oberhuber, and T. Stanford. The potential for using ocean generated electromagnetic field to remotely sense ocean variability. *Phys. Chem. Earth (A)*, 24:429–432, 1999.
- S. Vennerstrøm, T. Moretto, N. Olsen, E. Friis-Christensen, A. M. Stampe, and J. Watermann. Field-aligned currents in the dayside cusp and polar cap region during northward IMF. *J. Geophys. Res.*, 107:10.1029, 2002.
- H. Wang, H. Lüher, and S. Y. Ma. Solar zenith angle and merging electric field control of field-aligned currents: A statistical study of the southern hemisphere. *J. Geophys. Res.*, 110: 10.1029/2004JA010530, 2005.
- D. J. Webb, B. A. de Cuevas, and A. C. Coward. The first main run of the OCCAM global ocean model. Internal Document 34, Southampton Oceanography Centre, U.K., 1998.
- S.-L. Zhang. GPBi-CG: generalized product-type methods based on Bi-CG for solving nonsymmetric linear systems. *SIAM J. Sci. Comput.*, 18:537–551, 1997.